Beoordeling van de weerstand van turbofan-compressorschoepen
tegen vogelimpact door middel van geavanceerde numerieke modellering
en uitgebreide kalibratietesten

Assessment of the Bird Strike Robustness of Turbofan Compressor Vanes
through Advanced Numerical Modelling and Extensive Calibration Testing

Frederik Allaeys

Promotoren: prof. dr. ir. W. Van Paepegem, dr. ir. G. Luyckx
Proefschrift ingediend tot het behalen van de graad van
Doctor in de ingenieurswetenschappen: werktuigkunde-elektrotechniek

UNIVERSITEIT
GENT

Vakgroep Toegepaste Materiaalwetenschappen
Voorzitter: prof. dr. ir. L. Kestens
Faculteit Ingenieurswetenschappen en Architectuur
Academiejaar 2016 - 2017

ISBN 978-90-8578-954-3
NUR 978, 971
Wettelijk depot: D/2016/10.500/86

Promoters

Prof. Wim Van Paepegem
Ghent University
Faculty of Engineering and Architecture
Department of Materials Science and Engineering

Dr. Geert Luyckx
Ghent University
Faculty of Engineering and Architecture
Department of Materials Science and Engineering

Examination Committee

Prof. Luc Taerwe	(chairman)
Prof. Wim Van Paepegem (*promotor*)	(Ghent University)
Dr. Geert Luyckx (*promotor*)	(Ghent University)
Prof. Joris Degrieck	(Ghent University)
Prof. Stijn Hertelé	(Ghent University)
Ir. Jean-Sébastien Ruess	(Safran Aero Boosters)
Prof. Wouter Wilson	(Technische Universiteit Eindhoven), (Fokker Landing Gear)
Prof. Rade Vignjevic	(Brunel University, London)

Research Institute

Ghent University
Department of Materials Science and Engineering
Tech Lane Ghent Science Park - Campus A
Technologiepark-Zwijnaarde 903
9052 Zwijnaarde, Belgium

Acknowledgements

De keuze om zich vier jaar toe te leggen op een bepaald onderzoek is niet vanzelfsprekend. Wat ik onderschat had, is de doorzetting die het vergt gezien de tegenslagen èn de ambities die soms teruggeschroefd moesten worden. Gelukkig zijn er ook heel wat troeven: het is de ultieme kans om een fenomeen diepgaand te gaan bestuderen en begrijpen, de richting van het onderzoek zelf te kiezen en te leiden en daarenboven ook een heleboel interessante mensen te leren kennen.

Wat zeker vaststaat, is dat het behalen van de resultaten beschreven in deze uiteenzetting niet mogelijk was geweest zonder de hulp van drie mensen, namelijk Geert Luyckx, Wim Van Paepegem en Joris Degrieck. Het was Geert die mij geïntroduceerd heeft tot de vogelimpacttesten en hoe deze moesten uitgevoerd worden. Zijn aanmoedigingen om sommige zaken toch te overwegen hebben geleid tot verschillende concepten in dit werk. Aan de andere kant is er Wim die gedurende vier jaar het werk van dichtbij heeft opgevolgd, zowel op experimenteel als numeriek vlak, papers meerdere keren heeft nagelezen en herwerkt en die altijd klaar stond voor problemen of vragen. Ook Joris zijn bijdrage was essentieel. Zijn kennis over bird strike, de testopstelling met de krachtmeting van de splitter en bijvoorbeeld ook de ontwikkeling van de robuuste 1D en 2D lijntjestechniek zijn mede verantwoordelijk geweest voor de resultaten in dit werk.

I also would like to thank Safran Aero Boosters for the cooperation. Much of the final experiments and simulations are partly the result of the good

work of SAB. More specifically I would like to thank Hicham Benabou for managing the start of the project and especially Jean-Sébastien with whom I had a very pleasant collaboration. I very much appreciate the hard work he did to prepare the booster targets in time and the communication concerning the numerical work.

Zoals ik al zei, is één van de troeven van een doctoraat de mensen die je ontmoet. In de vier jaar tijdens dit doctoraat heb ik heel wat collega's ontmoet waarvan ik er nu een heel deel vrienden durf noemen. In de eerste plaats zou ik graag Mathijs bedanken. In die vier jaar hebben we veel plezier gehad, ontzaglijke hoeveelheden cafeïene verwerkt, frustraties gedeeld, etc. Het was een eer om, naast die ruimtemissie, een bureau te delen. De activiteiten samen met Mathijs, Siebe, Gabriele (of was het Gabrielle?) en Ruben zal ik ook niet snel vergeten (reis naar Italië, zwemtrainingen inclusief Rodenbach, spelletjesavonden, etc.). Bedankt Sam, voor de introductie tot de wondere wereld van de opera, Joren, voor de vele bezoekjes gedurende het hele doctoraat, Mathias voor de ontdekking van de eeuw, de frazer, Nature!, Joachim, Stefan, Nicolas, Jana en Diederik voor de fijne gesprekken tijdens de koffiepauze, Ives voor de vaste waarde in de vakgroep, etc. Ook de mensen van de metaalgroep hebben gedurende deze vier jaar bijgedragen aan de leuke sfeer op het departement.

Ik zou ook mijn ouders, mijn broer, zus, familie en vrienden willen bedanken voor de ontspanning en steun doorheen de jaren. De eindeloze kansen en fundamentele waarden die ik heb gekregen hebben mee geleid tot dit resultaat. Om het in de leuze van de familie samen te vatten: vooruit is de weg!

Bij deze zou ik ook graag mijn thesisstudenten bedanken (Christophe Sarrazin, Jarre Decaestecker, Reinout D'Haene, Lander De Frene, Mathieu Putman, Tim Cogghe, Tom Van Hoorebeke, Jens Maes en Frederic Pirlot). Ik heb geluk gehad dat elk van hen zich ten volle heeft ingezet tijdens hun thesis om de testcampagne's tot een goed einde te brengen. Vogelimpact testen nemen veel tijd in beslag, zonder hen had ik nooit hetzelfde kunnen bereiken. Ik zou ook Wim De Waele en Stijn Hertelé willen bedanken om deze thesissen na te lezen en mee te beoordelen.

Finaal zou ik ook graag Luc en Pascal willen bedanken. De ombouw van de opstelling en het maken van de vele sabots was ook van essentieel belang in dit werk. Ook dank aan Willem Van De Steene en Kurt Van Houtte, die meerdere 3D-geprinte mallen vervaardigd hebben, Siebe Spronk, Klaas Allaer en Jeroen Missinne, voor de hulp bij de ontwikkeling en het testen van de 2D lijntjestechniek en Stefan Jacques voor de opstart van de vervormbare plaat-simulaties.

Frederik Allaeys
Gent, 12 augustus 2016

The research leading to these results has received funding from the European Union's Seventh Framework Programme FP7/2007-2013 under grant agreement n° ACP2-GA-2012-314366-E-BREAK. More information can be found at `http://www.e-break.eu/`.

Summary

Turbofan engines need to withstand bird strike conform certain airworthiness regulations. Since physical tests are very expensive and time-consuming, numerical simulations are increasingly being used in the design process. Certification by analysis however still requires a lot of research to be able to prove that numerical methods are fully capable for simulating bird strike. An attempt to move in the right direction is taken in the FP7 project E-Break, where a task is devoted to the development of a numerical model that is able to validate the design rules of the turbofan low pressure compressor vanes in terms of bird strike robustness. The final model is validated with experimental data obtained from a parametric study on the booster vanes.

To assure that qualitative information is achieved from the parametric study and to understand the behaviour of the model in the simulations, the objective of is extended to three main research topics:

- Understanding the behaviour of the bird: To obtain a better understanding of the bird impact phenomenon and be able to assess the final experiments and simulations.
- Development of a set-up to test booster vanes: The experimental tests on multiple booster vane configurations are expensive and require a qualitative and extensively tested and validated test set-up to obtain valuable data for numerical simulations.
- Parametric study on the booster vanes and validation of the numerical model: To execute the parametric test campaign and analyse the

obtained results. The performance of the numerical model needs to be investigated by comparing the results with the data from the experiments.

For the experimental tests, the gas gun test set-up of the research group Mechanics of Materials and Structures at Ghent University is used. Several adjustments are made to be able to launch a wider range of impact masses and optimize the test sequence. The current set-up is able to launch bird of 0.3 kg, 1.5 kg and 1.8 kg, theoretically with energies up to 42 kJ. The test set-up has a vacuum chamber which avoids unwanted influences of compressed air on the experiment. Data acquisition is done using high speed cameras, displacement, acceleration and pressure transducers, lasers, oscilloscopes and strain gauges.

As a part of the data acquisition, several optical measurement techniques are developed, which are used to acquire displacement data in the experiments. An optical measurement has several benefits above transducers. Since it is per definition a non-contact method, the following issues cannot occur: no wires that can detach during movement, no triboelectric effect on the wires, no resonance frequencies, electrical current leakage, etc. Four optical techniques are discussed in this work. Apart from the existing DIC technique and a 1D line grating technique, significant contributions are made to a 3D shape measurement technique and a 2D line pattern technique. In the 3D shape measurement technique, a stereo vision technique is developed that is able to calculate 3D shape maps from specimens containing a line pattern. The main focus is to enhance the images to some extent, when excessive blurring occurs. A 2D line pattern technique developed at the department is further enhanced to extract more data from the refined Fourier transform and improve the accuracy of the method in certain conditions. Some of these techniques were essential to obtain the necessary data from the experiments.

The work on bird strike in this PhD starts with an introduction to bird modelling. The impact of a bird is generally characterized by a shock and steady state regime. A shocked region can be created when the material is suddenly stopped at impact. The shocked regime is characterized by a very short very high pressure. After this, the shocked region is entirely converted

into kinetic energy and heat, a steady state regime starts to form. This second regime is characterized by a much longer much lower pressure. Both regimes can be studied with numerical techniques such as FEM. In this work, a related technique called SPH is used to simulate the bird, because it is much better capable of handling the large deformations that are occurring during bird strike. In this first part of the work, it is shown that the shock and steady state pressures are very well predicted by the numerical models. Several influences on the shock regime are investigated: tilting the projectile and decreasing the mass or the stiffness of the target. The elastic energy as a measure for the presence of the shock regime is also introduced. The results of several experimental pressure measurements are covered, showing a good correlation with the theory and the simulations.

After the introduction of the bird modelling, the bird strike phenomenon is investigated in a much broader sense by considering the impact on rigid targets, experimentally and numerically. The impact of gelatine substitute birds with multiple mixing ratios as well as ducks and pigeons on a plate, a wedge and a splitter target are considered. In this study, the momentum transfer is used as measure for the force. In the experiments and simulations, this momentum transfer is derived from the unconstrained 1-dimensional translation of the targets. Additionally, several analytical models are introduced based on the momentum balance. This study shows that in general, the impactor material has a negligible influence in terms of momentum transfer. A theoretical model for the momentum transfer of the wedge is developed, which reveals the ability of this target to asses the performance of a numerical material model. The performed experiments and simulations show that likely deviatoric and/or dissipating constitutive behaviour is missing to improve the underestimation of the momentum transfer obtained from the current state-of-the art bird model. Several numerical aspects such as the artificial dissipation, splashing of the bird and mesh convergence are also investigated. Finally, the concept to measure the residual energy of a bird after impact using a rigid plate is introduced, which makes use of the fact that the momentum transfer is 100% for the rigid plate.

In a transition towards deformable targets, the impact on a thin aluminium flat plate imposed on a thick steel frame with a square opening is consid-

ered. This type of test allows to look at the performance of the model in case of large bird and target deformation. Four tests are performed and simulated. The correlation of the final shape of the plate is quite good. The influence of several input conditions are investigated, which gives a first indication that the impact location has a large influence on the results.

In the development of the set-up to test booster vanes, a method that is able to measure the reaction forces is developed. In literature, reaction forces were already measured in multiple directions by allowing a rigid object to pivot around one point, which gives the transferred rotational momentum. In this work, this concept is further refined. In contrast to the technique found in literature, the required kinematics are derived from a robust optical measurement. An algorithm is developed which is able to derive the kinematics from a 2D line pattern measurement. The error on the momentum obtained from this optical measurement is quantified with DIC measurements in quasi-static experiments and dynamic bird impact experiments and showed to be less than 5%. A simplified steel vane is used to test the set-up dynamically and to serve as an intermediate step towards the booster vane experiments and simulations. A very good correlation of these experiments with the simulations is achieved, in terms of momentum transfer and measured strain. Together with the rigid plate, a set-up is obtained to test booster vanes.

For the booster vane experiments and simulations, a fixture is developed which allows to test a subset of the entire booster including the inner and outer shroud, the welds in the outer shroud, the silicon, abradable and the retaining plate. A parametric study is performed on such fixtures, where the influence of the stacking and the radius of the vanes, the impact speed and angle of the bird and the size of the vanes is investigated. For each of these parameters, two tests are performed. Additionally, three tests on a reference configuration are performed. These tests on the reference configuration were instrumented with 12 strain gauges each, once on the vanes, once mainly on the inner shroud and once mainly on the reinforcements.

In the results of the parametric study, the visible damage is categorized. Damage generally ranges from small cracks or a pull out movement of the

grey silicon up to cracks in the black abradable and vanes entirely pulled out from the inner shroud. The most damage can be observed for the test at higher impact speeds. Apart from the visible observations, the transferred multi-axial momentum, strain signals and residual energy is measured. The data obtained from the reference tests is used to validate numerical models.

For the numerical model, solid elements are chosen for all the parts in the assembly. An extensive mesh convergence study showed that for the vanes, 3 elements through the thickness with an in-plane mesh size of 0.5 mm is sufficiently refined to obtain good results. It is shown that the bird to vane mesh size ratio can have a significant impact on the result. A too high ratio can result in an unrealistic distorted leading edge and high mesh distortions when damage is modelled. A significant mesh refinement can eliminate this issue. The performance of the numerical model is investigated by comparing momentum transfer, strain signals and residual energy with the experimental data. The global and local behaviour of the bird and the vane is captured quite well by the model. However, the deformation of the retaining plate, though realistic at first, is too large. The material model of the abradable and silicon needs to be improved to obtain better results. For impact directions aligned with the chord of the vanes, it is shown that a very fine mesh is needed to obtain a good correlation.

Samenvatting

Turbofan motoren moeten bestand zijn tegen vogelimpact conform bepaalde regulaties. Omdat het fysisch testen behoorlijk duur en tijdrovend is, wordt steeds meer gebruik gemaakt van numerieke simulaties tijdens het design proces. Er is echter nog veel onderzoek nodig om te kunnen aantonen dat de numerieke methoden werkelijk capabel zijn om vogelimpact te simuleren, ten einde certificatie te doen enkel op basis van simulaties en analyses. Een poging om een stap in de juiste richting te doen, wordt genomen in het FP7 project genaamd E-Break, waar een taak zich toespitst op de ontwikkeling van een numeriek model dat de ontwerp regels van een booster bij vogelimpact kan valideren. Om hierin te slagen wordt een experimentele parametrische studie uitgevoerd op de booster.

Om te kunnen garanderen dat bruikbare informatie verkregen kan worden uit de parametrische studie wordt het vooropgestelde doel uitgebreid naar:

- Het gedrag van de vogel begrijpen via kalibratietesten, ten einde de experimenten en simulaties op de booster beter te kunnen beoordelen.
- Ontwikkeling van een opstelling om boostersecties te testen: Experimentele testen op een booster zijn zeer duur. Daarom is een gevalideerde opstelling nodig zodat bruikbare data gegenereerd kan worden voor de vogelimpactsimulaties.
- Experimentele parametrische studie op een boostersectie en de performantie van het numeriek model evalueren: Het uitvoeren van de parametrische studie. De resultaten hiervan worden geanalyseerd en

bijgevolg gebruikt om de performantie van het numeriek model te onderzoeken.

Voor de experimentele testen is een door perslucht aangedreven kanon ter beschikking. Deze opstelling werd door het departement Toegepaste Materiaalwetenschappen van Universiteit Gent doorheen de jaren ontwikkeld. Gedurende het doctoraat werden ook enkele aanpassingen gemaakt, zoals bijvoorbeeld het vervangen van de lanceringsbuis en specifieke aanpassingen die de test procedure vergemakkelijken. Met de huidige opstelling kunnen vogels van 0.3 kg, 1.5 kg en 1.8 kg, met een energie van theoretisch 42 kJ geschoten worden. Voor elke test wordt de testkamer eerst vacuüm gezogen om ongewenste invloeden van lucht op het experiment te minimaliseren. Data acquisitie wordt gedaan met behulp van hogesnelheidscamera's, verplaatsing, acceleratie en druksensoren, lasers, oscilloscopen en rekstrookjes.

Als onderdeel van de data acquisitie zijn ook enkele optische meettechnieken ontwikkeld. Deze worden gebruikt in de experimenten om verplaatsingen te bepalen. Een optische techniek heeft meerdere voordelen ten opzichte van sensoren. Omdat de methode per definitie geen contact vereist zijn de volgende problemen niet aan de orde: draden die loskomen tijdens de beweging, geen tribo-elektrisch effect op de draden, geen resonantie frequenties van de sensor, geen lekstroom, etc. Vier optische technieken worden behandeld. Naast de reeds bestaande DIC techniek en een 1D lijntjespatroon meettechniek worden de significante bijdragen bij een 3D hoogtemap meettechniek en een 2D lijntjespatroon techniek besproken. De 3D hoogtemap meettechniek is in essentie een stereo visie techniek die in staat is om 3D hoogtemappen te berekenen van specimens met een 1D lijntjespatroon. De focus bij deze techniek ligt op het verbeteren van het contrast in wazige beelden. Een 2D lijntjespatroon techniek die reeds werd ontwikkeld aan het departement is verder geoptimaliseerd zodat nu meer informatie kan gehaald worden uit de Fourier transformatie. De accuraatheid onder specifieke condities is ook verbeterd. Sommige van deze technieken zijn essentieel om de nodige data te verkrijgen uit de experimenten.

Het werk rond vogelimpact in dit doctoraat start met een introductie tot het modelleren van de vogel. De impact van een vogel kan gekarakteriseerd

worden door een schok (*shock*) en een stationair (*steady state*) regime. Een schok wordt gecreëerd wanneer materiaal tegen hoge snelheid abrupt gestopt wordt. Het schok regime heeft karakteristiek een zeer korte zeer hoge druk. Nadat de energie in de schok volledig is omgezet naar kinetische energie en warmte begint een stationair regime zich te vormen. Dit tweede regime kan gekarakteriseerd worden door een veel langere en veel lagere druk. Beide regimes kunnen bestudeerd worden met numerieke technieken zoals de EEM. In dit werk wordt een gerelateerde techniek gebruikt om de vogel te simuleren (afgekort SPH), omdat deze veel beter in staat is om te gaan met de typische grote vervormingen. In dit eerste deel van het werk wordt getoond dat het schok en stationair regime zeer goed voorspeld wordt door de numerieke technieken. Verscheidene invloeden op het schok regime zijn onderzocht: het tilten van het projectiel voor impact of het lichter of minder stijf maken van het doelwit. De elastische energie als een maat voor het schok regime wordt ook geïntroduceerd. Finaal worden ook de resultaten van enkele experimentele drukmetingen behandeld. Deze komen over het algemeen vrij goed overeen met de theorie en de simulaties.

Na de introductie tot het modelleren van de vogel wordt vogelimpact in een breder perspectief geplaatst bij de experimentele testen en numeriek simulaties op rigide doelwitten. De impact van gelatine surrogaat vogels met verschillende mengverhoudingen alsook eenden en duiven op een plaat, hoekvormige structuur en een splitter worden behandeld. In deze studie wordt de overdracht van de impuls als maat voor de kracht gezien. Zowel in de experimenten als in de simulaties wordt deze bepaald uit de ongedwongen eendimensionale beweging van de doelen. Bijkomend werden enkele analytische modellen geïntroduceerd, afgeleid uit het impulsevenwicht. Deze studie toont dat in grote lijnen het materiaal van de impactor een verwaarloosbare invloed heeft op de impulsoverdracht. Een nieuw theoretisch model is ontwikkeld voor de hoekvormige structuur. Deze onthult het vermogen van dit doel om de performantie van een numeriek materiaal model te taxeren. De experimenten en simulaties tonen aan dat wellicht het materiaalgedrag (afschuiving en/of dissipatie) niet compleet is in het huidige state-of-the-art vogelmodel. Meerdere numerieke aspecten zoals de artificiële dissipatie, de grote vervormingen van de vogel en de convergentie van de numeriek discretisatie of vermazing worden ook bekeken. In dit stuk wordt ook het

concept om de residuele energie van de vogel te meten geïntroduceerd. Dit concept maakt gebruikt van het feit dat de impulsoverdracht bij de rigide plaat 100% is.

In een stap richting meer vervormbare doelen wordt de impact op dunne vlakke aluminium platen beschouwd, bevestigd tegen een dik stalen kader met een vierkante opening. Dit soort test laat toe om de performantie van het model te testen bij zeer grote vervormingen van zowel het doel als van de vogel. Vier testen worden uitgevoerd en achtereenvolgens gesimuleerd. De correlatie van de finale vorm van de plaat is vrij goed. De invloed van verscheidene input parameters worden onderzocht, wat al een eerste indicatie geeft dat de impact locatie een grote invloed heeft op het resultaat.

Tijdens de ontwikkeling van een opstelling om de schoepen te testen is veel aandacht besteed aan de ontwikkeling van een methode om de impact krachten te meten. In de literatuur werden reactiekrachten reeds opgemeten in meerdere richtingen door een object gecontroleerd te laten pivoteren rond een bepaald punt, waaruit vervolgens de rotationele impulsoverdracht bepaald kan worden. In dit werk is dit concept verder uitgewerkt. In tegenstelling tot de techniek beschreven in de literatuur, wordt de vereiste kinematica afgeleid uit een robuuste optische meting. Een algoritme is ontwikkeld dat in staat is om de kinematica af te leiden uit de data gegenereerd door de 2D lijntjespatroon techniek. De fout op de berekende impuls wordt bepaald uit DIC metingen in quasi-statische experimenten en dynamische vogelimpact experimenten en blijkt minder als 5% te zijn. Een vereenvoudigde stalen schoep is ontwikkeld die toelaat om deze dynamische testen uit te voeren en bovendien kan dienen als een tussenstap voor de testen en simulaties op de schoepen van de booster. Een zeer goede correlatie tussen de experimenten en de simulaties is waargenomen. Zowel het momentum als de opgemeten rekken komen goed overeen. Samen met de rigide plaat wordt een kwalitatieve opstelling bekomen waarmee de testen op de schoepen van de booster kunnen worden uitgevoerd.

Voor de testen en simulaties op de schoepen van de booster is een assemblage ontwikkeld dat het mogelijk maakt om een deel van de complete booster te testen, inclusief de binnenste en buitenste ring (inner and outer shroud), de

lassen in de buitenste ring, de silicone, het abrasief materiaal (abradable) en een plaatje dat elk paar schoepen losjes verbindt (the retaining plate). Een parametrische studie is uitgevoerd op dit design, waarbij de invloed op de geometrie van de schoepen, de impact snelheid en massa van de vogel en de grootte van de schoepen onderzocht wordt. Voor elke parameter zijn twee testen voorzien. Bijkomend zijn voor de configuratie die als referentie dient, drie testen uitgevoerd. Voor elke test op de referentie configuratie is de assemblage geïnstrumenteerd met 12 rekstrookjes, een keer op de schoepen, een keer vooral op de binnenste ring en een keer vooral op de verstevigingen.

Voor alle testen is de zichtbare schade gecategoriseerd. Schade gaat typisch van kleine scheurtjes in of een uittrek beweging van de silicone tot scheuren in het abrasief materiaal en zelfs schoepen die volledig uit de binnenste ring getrokken zijn. De meeste schade is waargenomen voor de testen tegen hogere impact snelheden. Naast de visuele waarnemingen wordt de multi-axiale impulsoverdracht, de rekken en de residuele energie ook opgemeten. De data verkregen uit deze experimenten kan gebruikt worden om numerieke modellen te valideren.

Voor alle onderdelen in het numerieke model zijn volume elementen gekozen. Een uitgebreide convergentiestudie van de vermazing toont aan dat 3 elementen door de dikte met een element grootte van 0.5 mm in het vlak voldoende is om goede resultaten te verkrijgen. De ratio van de elementgrootte van de schoep ten opzichte van de afstand tussen de partikels van de vogel kan een grote invloed hebben op de resultaten. Wanneer de afstand tussen de partikels te groot is (en dus de massa van de partikels relatief groter wordt) kunnen onrealistische distorties ontstaan aan de aanvalsboord van de schoep. Een significante verfijning van de vermazing kan dit probleem oplossen. De performantie van het numeriek model is onderzocht door de impulsoverdracht, rekken en residuele energie te vergelijken met de experimentele data. Het globaal en lokaal gedrag van de vogel en de schoepen worden goed voorspeld door het model. Maar, de vervorming van de retaining plate is na verloop van tijd te groot. Het materiaalmodel van het abrasief materiaal en de silicone moet verbeterd worden om betere resultaten te verkrijgen. Er wordt ook aangetoond dat bij impactrichtingen die sterk gealinieerd zijn met

de koorde van de schoepen, een zeer fijne vermazing van de vogel nodig is om goede resultaten te bekomen.

Curriculum

Frederik Allaeys was born on November 14, 1988 in Leuven, Belgium. In 2006 he started his education M.Sc. in Industrial Sciences - Electromechanical Engineering at Kaho Sint-Lieven in Ghent. In the final year of this four year education, he did a thesis about automated discrete event model generators for a production cell where delicate spacecraft parts are produced, as a part of an Erasmus programme at Högskolan Väst in Tröllhättan, Sweden. In 2010, he continued at Ghent University to obtain a M.Sc. degree in Electromechanical Engineering. In the thesis of this two year programme, a controller for a robot was developed using Genetic Programming, with a focus on the limitation of code growth and the development of the robot morphology.

As a result of the gained interest in scientific research in his master theses, he decided to continue to work in a scientific area in the form of a PhD. Frederik Allaeys is first author of 3 publications in the international journals of Science citation index (A1) and 4 publications in international conference proceedings.

Publications

Publications in international journal of the Science Citation Index (A1)

Allaeys, F., Luyckx, G., Sarrazin, C., Van Paepegem, W., Jovanov, L. and Philips W. (2014), 'A 3D Shape Measurement Technique That Makes Use of a Printed Line Pattern.' *Experimental Mechanics* 54 (6): 99-1009.

Allaeys, F., Luyckx, G., Van Paepegem, W. and Degrieck, J. (2017), 'Characterization of real and substitute birds through experimental and numerical analysis of momentum, average impact force and residual energy in bird strike on three rigid targets: a flat plate, a wedge and a splitter.' *International Journal of Impact Engineering* 99: 1-13.

Allaeys, F., Luyckx, G., Van Paepegem, W. and Degrieck, J. (2017), 'Development and validation of a set-up to measure the transferred multi-axial impact momentum of a bird strike on a booster vane.' *International Journal of Impact Engineering* 99: 102-110.

Publications in conference proceedings

Allaeys, F., Sarrazin, C. and Luyckx, G. (2013) Feasibility of a novel 3D shape measurement technique for test specimens subjected to bird strike using a printed line pattern. In *High Speed Imaging for Dynamic Testing of*

Materials and Structures, Proceedings, 51-54.

Allaeys, F., Luyckx, G., Van Paepegem, W., Jovanov, L. and Philips W. (2014), '3D Shape Measurement Technique Using a Printed Line Pattern.' In *16th International Conference on Experimental Mechanics, Abstracts.*

Spronk, S., Degrieck, J., Gilabert Villegas, F.A., Allaeys, F. and Van Paepegem, W. (2016), 'New Test Set-up for Measuring Rate-dependent Mode-i Delamination Properties of Unidirectional and Woven Composites.' In *17th European Conference on Composite Materials*, 1-7. European Society for Composite Materials (ESCM).

Allaeys, F., Luyckx, G., Van Paepegem, W. and Degrieck, J. (2016), 'A set-up to measure the transferred multi-axial impact momentum of a bird strike on a booster vane.' *Sampe Liège 2016*, to be presented.

Contents

CHAPTER 1

General introduction

Abstract: In this chapter, an overview of the increasing bird strike problem and an introduction to bird strike testing will be given first. After that, the broader context of this PhD in the large FP7 project E-Break will be considered, including the justification of this work. Finally, the objectives of the PhD and an outline of the book will be given.

1.1 Introduction to bird strike

1.1.1 History and statistics

The potential threat of bird strike got public awareness in 2009 after the miraculous ditching of the Airbus A320 of US Airways flight 1549 on the Hudson River in New York after at least one Canadian goose was ingested in each jet engine (NTSB, 2010). However, since the early beginnings of manned flight, birds proved to be capable of bringing aircraft down. The pioneering Wright brothers recorded a first incident in their diaries on 7 September 1905, only two years after their first powered flight in 1903. After the 4.751-metre flight near Dayton, Ohio, Wilbur Wright recorded: *"Twice passed over fences into Breads cornfield. Chased flocks of birds on two rounds and killed one which fell on top of upper surface and after a time fell off when swinging a sharp curve."* The first recorded human fatality as a result of bird strike occurred in 1912, when Perry Rodgers crashed into the sea after encountering a flock of sea gulls (Stimson, 2016). The most fatal accident took place in 1960, Boston, where a flock of starlings were ingested in three engines of a Lockheed L-188 Electra, resulting in 62 deaths (Thorpe, 2003). More recently, a Belgian Air Force C130 Hercules bringing back a Dutch army band crashed when approaching Eindhoven in 1996. The two left engines lost power after flocks of starlings and lapwings were ingested. 34 of the 41 on board died (Thorpe, 1998).

Since the first incident reported by the Wright brothers, civil and military aviation communities have been confronted with the threat of wildlife strikes on aircraft. The Federal Aviation Administration (FAA, agency of the U.S. Department of Transportation) reports that between 1990 and 2014, more than 258 people were killed and over 245 aircraft were destroyed due to aircraft collisions with wildlife. These bird strikes lead to immense monetary losses including direct costs such as repair, replacement of damaged parts and labor hours but also costs related to delays and cancellations. Associated with the indirect costs are e.g. loss of passengers confidence, fuel dumped during emergency landing, emergency response by ambulances and fire fighters,... Although these indirect costs are not well documented, a study from 2001 estimated that the total cost of bird strikes to the global

commercial airline fleet amounts 1.28 billion US dollars per year (Allan and Orosz, 2001). It is clear that collisions between birds and aircraft are an economic challenge in a highly competitive business.

13.668 annual incidents were recorded in 2014, a total of 156.114 registered strikes since 1990, in which 97 percent were related to birds (Dolbeer et al., 2015). Additionally, wildlife strike reporting is not mandatory, some countries are negligent in reporting or unwilling to report concerning negative publicity and there are no consistent worldwide standards, leading to vastly under-reported data. Therefore, it is stated that the actual statistics of accidents and fatalities must be much higher (MacKinnon, 2004).

The amount of reported strikes increases over the years. Figure 1.1 shows the increasing trend, based on the reported number of bird strikes in the USA between 1990 and 2014.

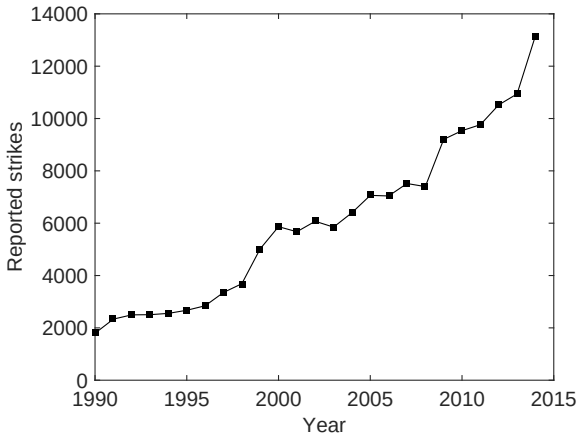

Figure 1.1: Number of reported bird strikes to civil aircraft according to the National Wildlife Strike Database of the FAA between 1990-2014 (Dolbeer et al., 2015).

There are multiple reasons for this trend, the most obvious one being that commercial air traffic passenger demand over the last 10 years has increased with an average of 5.2 percent per year (The Statistics Portal, 2016). Another reason is the increased reporting rate, as a result of encouraging airports and providing multiple tools to do the reporting (Dolbeer, 2015). A third reason is an overall increase in large bird population. Since 1970, govern-

mental organizations enacted highly successful environmental programs and legislation, such as pesticide regulation, wetlands restoration, expansion of The National Wildlife Refuge System, etc. These efforts to protect the environment resulted in a dramatic increase in populations of large bird species in North America and in Europe (Dolbeer and Eschenfelder, 2003). As a relevant example to the US Airways flight 1549, the migratory and nonmigratory population of Canadian geese grew from 1.2 million to 5.5 million birds in North America from 1970 to 2008 (Dolbeer and Seubert, 2009). Also in Western Europe, an increase of 3.10 to 5.06 million geese was noted from 1993 to 2009 (Fox et al., 2010). Another cause is the fact that modern turbofan-powered aircraft are less detectable by birds due to the more quiet engine (Burger, 1983; Lima et al., 2015). Luckely, the induced damage did stabilize or even decline since 2000, according to a study on Part 139-certified airports (Dolbeer, 2015).

Analysis of these reports shows that the majority of the strikes occurs in the vicinity of the airport (ATSB, 2003). More specifically, 91% of the departure collisions and 83% of arrival collisions occur within 9260 meters of the airport (Wang and Herricks, 2010). The European Aviation Safety Agency (EASA) reports that most of the bird strikes take place below 2500 ft or 762 m (90% - 93 %) and 64 % up to 75 % occurs at altitudes below 200 ft or 71 m (Maragakis, 2009). FAA reports that 74 % of bird strikes occur at or below 500 ft or 153 m (Dolbeer et al., 2015). Although various sources quote different percentages, these statistics are making it perfectly clear that take-off, approach and landing phases are especially critical. Only a small part of the accidents happens during en route (15 %) and manoeuvring (1 %) as can be seen in Figure 1.2 (Maragakis, 2009).

As a result, most bird strikes take place well below cruise speed. In the wildlife strike database from the FAA, 89% of the reports where the impact speed was recorded happened below 120 knots or 222 km/h (Dolbeer et al., 2015).

The cost of a collision with a bird during flight is directly related to the specific part of the aircraft which is being damaged. Especially forward facing components of aircraft are at risk of being struck by birds, as indicated

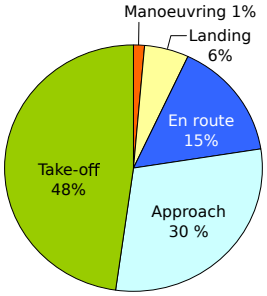

Figure 1.2: Phase of flight during which bird strike occurred and led to an accident (1999-2008) (Maragakis, 2009).

in Figure 1.3a. According to the EASA, most incidents occur with engine fan blades and inlet (44 %), followed by leading edges of the wings (31 %) and windshields (13 %). Other locations which are being damaged such as the nose and fuselage, only count for respectively 8 % and 4 % of the considered cases (Figure 1.3b) (Maragakis, 2009).

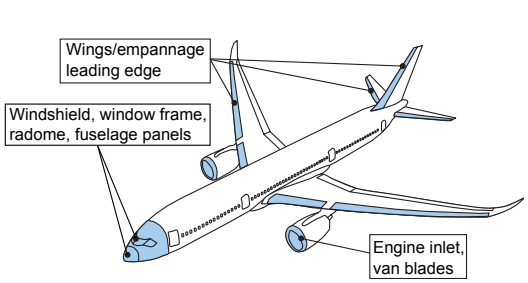

(a) Front-facing aircraft components exposed to bird strike (Heimbs, 2011*a*).

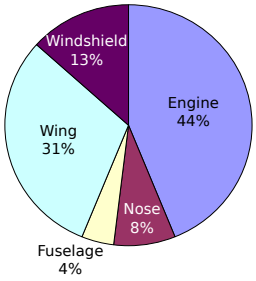

(b) Most damaged locations on an aircraft (1999-2008) (Maragakis, 2009).

Figure 1.3: Aircraft components most vulnerable to bird strike.

Sophisticated aircraft components like jet engines which are particularly vulnerable to damage from bird ingestion can cost millions of dollars in replacement, reparations and flight cancellations, despite all improvements in design following certification requirements. Extensive and detailed documentation of occurred collisions between aircraft and birds is of great importance for better assessing and controlling bird strikes. Clearly there is no single solution to this bird strike problem, which will continue to be a highly

economic loss for aviation industries worldwide. However, improvements in the number of fatal accidents and costly incidents can be achieved by focusing on bird control and avoidance methods.

From wildlife management up to removal, several efforts have been successful to reduce the probability of bird strikes (MacKinnon, 2004; Baxter and Hart, 2010; Short et al., 2000):

Passive habitat-management: Many birds have found airports (large, open grassed areas) the perfect habitat for resting, feeding and nesting. Large open areas will always attract wildlife, but there are multiple measures that can be taken to make it less attractable by eliminating or reducing food sources, shelter and safe areas.

Detection technology: To collect and detect bird activities to further evaluate the threats to aircraft operations and provide timely warnings regarding high-risk bird strike areas, visually or using advanced radar systems (Wang and Herricks, 2010; ATSB, 2003).

Deterring: Research has indicated some repelling behaviour of birds against infrasound, microwaves, pulsing lights (Blackwell and Burnhardt, 2004), brighter aircraft fuselage colors (Fernández-Juricic et al., 2011), etc ...

Removal: This includes killing and live trapping. Both options are generally short-term solutions.

These methods can reduce the probability for a birds strike. Depending on the location of the airport, different strategies and steps can be taken.

1.1.2 Certification

Consequently, the critical structures must be designed following certification requirements to assure capability of continued safe flight and landing under certain conditions. All forward facing components need approval by certification tests to be allowed for operational use. These requirements are compiled in the Federal Aviation Regulations (FAR) of the Federal Aviation Association (FAA) for the US and lately in the Certification Specifications (CS) of the European Aviation Safety Agency (EASA) for Europe. These aviation authorities describe the requirements for bird strike robustness

of the windshield panes, the general structure including e.g. empennage and wings and jet engines. The regulations for both instances are almost identical, for the category "Large (turbine powered) aeroplanes", they can be summarized as follows (the first three clauses do not apply to engines) (*Regulations and policies*, 2016; *Certification Specifications*, 2016; Dennis and Lyle, 2009):

> *FAR/CS 25.631*: The aeroplane (structure including windshield) must be designed to assure capability of continued safe flight and landing of the aeroplane after impact with a 4 lb bird when the velocity of the aeroplane (relative to the bird along the aeroplane's flight path) is equal to V_C (cruise speed) at sea-level or 0.85 V_C at 2438 m (8000 ft), whichever is the more critical (FAR 25.631 specifically requires the empennage structure to assure capability of continued safe flight and landing after an 8 lb bird impact).
>
> *FAR/CS 25.775*: Windshield panes directly in front of the pilots in the normal conduct of their duties, and the supporting structures for these panes, must withstand, without penetration, the bird impact conditions specified in CS 25.631.
>
> *FAR/CS 25.571*: The aeroplane must be capable of successfully completing a flight during which likely structural damage occurs as a result of bird impact as specified in CS 25.631.
>
> *FAR 33.76 & CS E-800*: Addresses the ingestion of single and flocks of large, medium and small birds and the effect of the impact of such birds upon the front of the engine, where the bird mass depends on the engine inlet throat area (up to 3.65 kg). For the small and medium birds, 75% thrust has to be maintained. For the large birds, a certain level of thrust is required for a certain amount of time before shut down. The engine inlet also has to withstand a medium and large bird impact. In any case, ingestion may not cause any hazardous engine effects, such as non-containment of high-energy debris, concentration of toxic products in the engine bleed air for the cabin, uncontrolled fire, complete inability to shut the engine down, etc ...

Whether these certifications cover the whole range of threats can be questioned. The increase in large-bird populations as mentioned before especially is problematic as these species exceed the standards under which most commercial aircraft components are tested and certified (cfr. the weight of a canadian goose is approximately 3.6 kg opposed to the 1.81 kg or 4 lb in the regulations). Complete loss of engine thrust after ingestion of a large bird is also acceptable if the engine can be shut down safely. The engines on the Flight 1549 Airbus 320, both of which lost power after ingesting geese, performed exactly as they were certified to perform (Dolbeer, 2009, 2002).

Physical certification tests need to be conducted to prove that aircraft components have the required level of bird strike resistance, documented in the airworthiness regulations. In these tests real birds must be used, typically dead or sedated chickens. Regulatory authorities only define the masses to be used, so species and body densities can vary, resulting in a large scatter between the individual tests. The irregular shape of real birds makes it also difficult to ensure the right target point is struck properly. It can be concluded that the use of real bird bodies in testing is not ideal. Consequently, substitute birds are widely used in the aerospace industry for in-house impact testing prior to the final certification tests (Budgey, 2000).

1.1.3 The need for substitute birds

From a biometric database, the density and shape of real birds has been investigated for commonly struck species ranging from House Sparrows at 30 g up to Mute Swans at 8 kg (Hamershock et al., 1993; Budgey, 2000). This revealed that the mean density for large birds (heavier than 200 g) is typically lower than 1000 kg/m^3. The relationship between bird mass and density (with feathers removed) for multiple birds is shown in Figure 1.4.

Birds mainly consist of water, the average density however is lower as the one of water because of internal cavities such as pneumatic bones, lungs and peculiar air sacs (Airoldi and Cacchione, 2006). This graph also shows that, even though a trend can be observed in the data, there is quite some scatter. For a Herring Gull and a domestic chicken for example (where the latter is often used for certification testing), respectively 890 kg/m^3 and 1040 kg/m^3

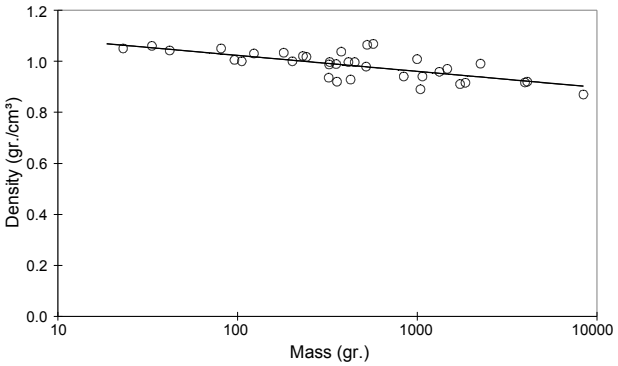

Figure 1.4: The relationship between bird mass and density for a range of commonly struck bird species. (The density is that of a bird with feathers removed) (Budgey, 2000).

can be found. The use of substitute birds for pre-certification impact testing on the other hand, leads to advantages in convenience, cost and especially consistency and reproducibility of the results. No two real birds are identical, even two individuals of the same species can have a significant different impact behaviour, making it difficult to repeat experiments. The substitute bird's function is not to make an exact copy of a real bird with its flesh and bones, but rather to reproduce the effects of an impact with a real bird (Budgey, 2000).

Extensive research programs at the end of the 20th century investigated the bird strike phenomenon with real birds. Different types however were used:

- Chickens (Jr. and Pate, 1957; Allcock and Collin, 1969; MacNaughtan, 1972; Barber et al., 1975, 1977; Wilbeck, 1978*a*,*b*; Challita and Barber, 1979; Welsh and Centonze, 1986)
- Pigeons (MacNaughtan, 1972; Steinhagen and Salemme, 1973; Johns, 1974; Premont and Stubenrauch, 1974; Challita, 1980)
- Starlings (Johns, 1974)
- Ducks (Premont and Stubenrauch, 1974; Graff et al., 1976; Martindale, 1994; Edge and Degrieck, 1999)
- Partridges (Graff et al., 1973)

In the meanwhile, the performance of multiple bird substitute materials in terms of pressure and force was investigated as well in several reference works (Allcock and Collin, 1969; Wilbeck, 1978*b*; Bertke and Barber, 1979; Wilbeck and Rand, 1981). Several tests with wax, foam, emulsions and gelatine were conducted and indicated that soft material substitutes with the specific gravity of water produced loading profiles that were very similar to that of a real bird (Allcock and Collin, 1969; Wilbeck, 1978*b*). Wilbeck and Rand determined that gelatine or porous gelatine, with the specific gravity of water, most nearly represents the impact behaviour of a real bird (Wilbeck and Rand, 1981). Consequently gelatine is the most extensively used material for artificial bird projectiles.

Gelatine is a powder derived from the hydrolyses of collagen, acquired from animal by-products such as skin, bones and tissues. The term gelatine also refers to the water solution of this powder. It is commonly used in the food industry (marshmallows, jellies,...), pharmaceutical industry (capsules, tablets,...), photographic and cosmetic industry (Aihaiti and Hemley, 2008). In the field of ballistic research, it is also used as surrogate for human tissue in bullet penetration experiments and as in this work, to replicate the constitutive behaviour of birds at high speeds (Kneubuehl et al., 2011). The term *ballistic gelatine* is also used in these applications, mostly for bullet penetration.

There is no standard for preparing gelatine substitute birds. As a result, many different processing techniques can be found in literature. Part of the techniques try to obtain a density based on the average density of a bird, indicated by a logarithmic fit to the data from Figure 1.4 (Budgey, 2000):

$$\rho = -63 \log m + 959 \tag{1.1}$$

Where m is the mass in kg and ρ the density in kg/m^3. Based on these results, a density of approximately 950 kg/m^3 is often aimed for as substitute material (masses from 2.5 lb up to 4 lb respectively correspond with an average density of 956 kg/m^3 and 943 kg/m^3).

Adding gelatine to water however increases the density above 1000 kg/m^3. To counteract that effect, the following materials can be added to the gelatine-water mixture:

Micro-balloons: This is the default technique for creating birds that weigh less than 1000 kg/m^3. Micro-balloons are very small spheres in the order of microns. The air inside these micro-balloons decrease the average density of the gelatine. Phenol is generally used as material for the spheres (Wilbeck, 1978*b*; Roberts et al., 2005; Seidt et al., 2012). Because of the lower weight of the spheres, the mould needs to be rotated throughout the solidification process (to have a homogeneous distribution of the spheres).

Other substitute materials: In (Lavoie et al., 2009), a recipe is proposed containing so-called *cinnamomum zeylanioum* for reducing the density. The advantage of this technique is that the moulds would not need to be rotated during solidification. This mixture was also used in (Orlowski, 2015).

Also in this work , the differences between a real and substitute bird and the influence of porosity will be assessed.

For the geometry of the substitute birds in the experiments or to make abstraction of the actual shape of a real bird in the simulations, in general, mostly cylinders with hemispherical and flat ends are used. In simulations, the ellipsoïd shape is often investigated as well (Heimbs, 2011*b*). The different shapes are depicted in Figure 1.5. They can be defined with a length l and diameter d. But it is rather the l/d ratio that defines the shape, the absolute values of l and d are subsequently derived from the mass.

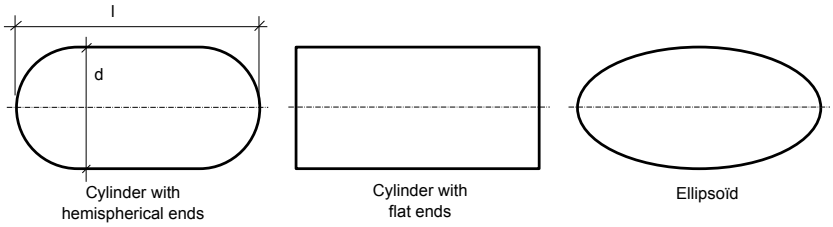

Figure 1.5: Typical substitute and numerical bird shapes.

More recently, CT-scans on bird carcasses were done as well to obtain actual bird geometries in simulations (Hedayati and Ziaei-Rad, 2013; Hedayati et al., 2014; Hedayati and Ziaei-Rad, 2014; McCallum and Constantinou, 2005; Nizampatnam, 2007).

Skeletons or structures to stiffen the gelatine bird and therefore better maintain the shape during launch and flight can also be found in literature (Ritt, 2012).

1.1.4 Introduction to bird strike testing

Depending on the velocity, the response of a projectile during impact will be elastic, plastic, hydrodynamic, sonic, or explosive. During an elastic impact, the internal stresses are below the material strength. With increasing impact velocity, plastic deformations occur but the material strength is still sufficient to prevent fluid-like behaviour. When the impact velocity increases further, the internal stresses exceed the material strength by a great amount and fluid-like flow occurs. At this velocity, it is said that it is not the material strength of the projectile that determines the response but rather the material density. This type of behaviour is typical for a bird at high impact speeds. Bird strike is also often referred to as a soft body impact, because its strength is generally well below the strength of the target structure. Because of its large deformation during impact it tends to redistribute the load on the target where hard body impact results in localised punching (Wilbeck, 1978*b*).

Several apparatus exist for testing the impact behaviour of structures, such as the drop tower, the pendulum and the ballistic set-up. Bird impact velocities however are typically between 50-250 m/s, which requires the use of a ballistic set-up. For bird strike testing specifically, a gas gun is used. In this kind of set-up, the projectile (in this case a bird), is put inside a carrier called the sabot and mounted in front of a pressure vessel which provides the necessary pressure to accelerate the bird. The purpose of the sabot is to maintain and guide the projectile during acceleration through a launching tube of several meters. At the end of the launching tube, a device separates or strips the bird from the carrier in such a way that only the bird continues

along its path and strikes the target.

Several research institutes and aircraft part manufacturers possess such a gas gun (DLR, CEAT, LAST,...). Several designs/mechanisms are used for the sabot, trigger mechanism, stripping process and test chamber (if any). Especially for the sabot, some in-house optimization of the design is typically done.

In order to mimic the impact on fast rotating blade(s) (or vane(s)), another test set-up can be used where the bird is dropped or released onto a rotating set-up (Figure 1.6), also called a whirl or whirligig impact test set-up (Martindale, 1994; Steinhagen and Salemme, 1973; Johns, 1974; Graff et al., 1976, 1973). In these tests, the velocity of the bird is rather low. The high relative velocity between the bird and the vane is therefore mainly the result of the rotating blade(s).

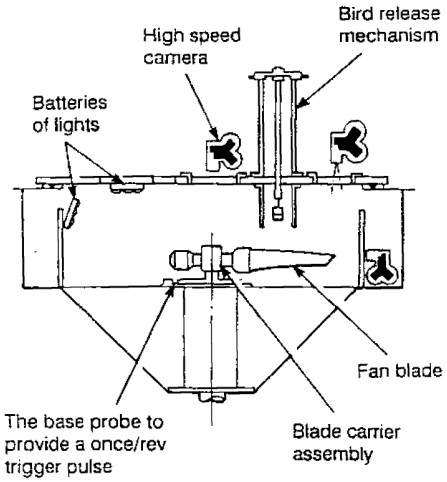

Figure 1.6: Rotating blade(s) test rig (Martindale, 1994).

Bird strike is one type of Foreign Object Damage (FOD). Test programs however are sometimes combined with other types of FOD such as impact of ice, gravel, rivets, bolts, nuts (Graff et al., 1973).

1.2 The E-Break project

This PhD is part of the FP7 project called E-Break. Since 1984, the European Union has launched several funding programmes to increase the competitiveness and boost the leadership of Europe in the global knowledge economy. These funding programmes are called framework programmes for research and technological development or FP in short. E-Break is funded by the FP7 programme, which lasted from 2007 to 2013, with a total budget of € 50 billion (*What is FP7? The basics*, 2016). More specifically, it is part of the transport area, which focusses on the development of safer, greener and smarter transport systems (*Transport (including Aeronautics)*, 2016).

The E-Break or 'Engine BREAKthrough Components and Subsystems' project is a four year large-scale European research and engineering project that started on October 2012 with 42 partners among which Rolls Royce, Safran, GKN, DLR, etc., with the ultimate goal to contribute to the development of the future aero engines. It was requested by the European Engine Industry Management Group (EIMG), a consortium consisting of the leading European aero-engine industries which pushes the development of technologies in order to further reduce the fuel burn, emissions and noise. The Advisory Council of Aeronautic Research in Europe (ACARE) aims to reduce CO2 emissions by 50% per passenger kilometer with an engine contribution of 15 to 20% of the SFC by 2020. NOX emissions would have to be reduced by 80% and efforts need to be made on other emissions as well (*E-BREAK: Engine Breakthrough Components and Subsystems*, 2016).

The focus in the E-Break project is mainly on the improvement of the different subsystems of the engine. Turboshafts, open rotors and turbofans are considered, the turbofan being the engine used in current commercial aircraft. In a turbofan, a gas turbine drives a fan blade which contributes to the air flow through the gas turbine (core air flow) and creates an additional bypass air flow (Figure 1.7). The jet formed by the bypass and the core of the engine together create the thrust of the engine.

A section cut of a turbofan engine is shown in Figure 1.8a. From left to right, the following main parts can be observed: the fan blades in blue, the low pressure compressor (LPC) or booster in blue, the high pressure

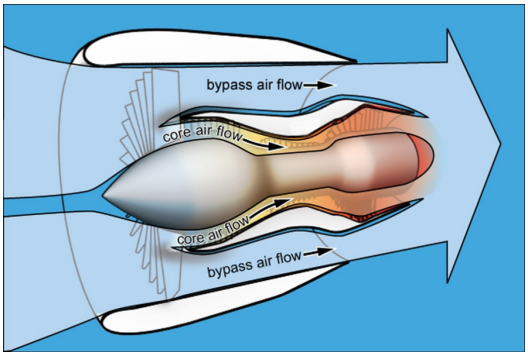

Figure 1.7: The two airflow paths through the turbofan engine (NTSB, 2010).

compressor (HPC) in red, the combustion chamber in yellow and the high and low pressure turbine (HPT and LPT) respectively in pink and green. The booster specifically consists of a sequence of stator vane and rotor blade stages (Figure 1.8b), the primary stage being a stator stage also referred to as the Inlet Guide Vanes or IGVs (number 30 in Figure 1.8b).

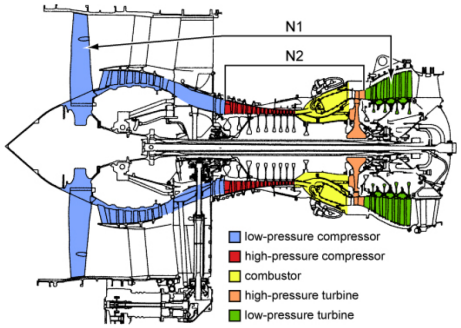

(a) Section cut (NTSB, 2010).

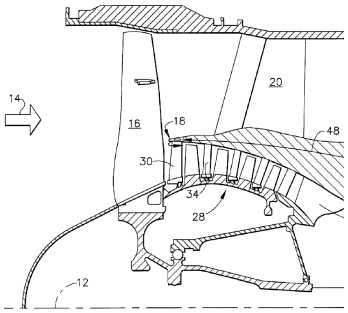

(b) Zoom booster (Wadia and Holm, 2004).

Figure 1.8: Turbofan engine.

The booster vanes are much smaller than the fan blades. A view from the front of the GEnx-2B engine is shown in Figure 1.9. The smaller IGVs can be observed behind the fan blades.

The mandatory evolution of sub-systems results from the future aero-engines which will have higher overall pressure ratios (OPR) to increase thermal efficiency and will have higher bypass ratios (BPR) to increase propulsive

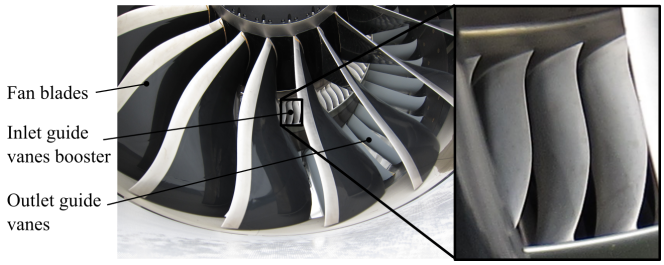

Figure 1.9: Fan blades and inlet guide vanes of GEnx-2B (Wikimedia Commons, 2011).

efficiency. These lead to smaller and hotter high pressure cores requiring the development of adequate technologies for sub-systems (*E-BREAK: Engine Breakthrough Components and Subsystems*, 2016).

The work in E-Break is divided in multiple subprojects, covering topics such as tip clearance control, advanced sealing systems, higher temperature and lightweight materials and even health monitoring (*E-BREAK: Engine Breakthrough Components and Subsystems*, 2016). This PhD is part of subproject 3 titled 'Engine variability and thermomechanical behavior to ensure stability of thermodynamical cycle' which is concerned with the development of more robust and accurate variable systems to withstand higher temperatures and pressures as well as bird debris impact during a bird ingestion event (*E-BREAK: Engine Breakthrough Components and Subsystems*, 2016). Ghent university in cooperation with Safran Aero Boosters[1], is responsible for the development of a numerical model capable of predicting the damage done to booster vanes when subjected to bird impact. Safran Aero Boosters is the world leader in low-pressure compressors for commercial turbofan engines (*Safran Aero Boosters*, 2016).

New engine architectures and materials are being used in the design of low pressure compressors for aero-engines. Additionally, new concepts arise which can have an influence on the bird strike robustness of the booster. One of these concepts are Variable Stator Vanes or VSV systems, which allow to optimize the pitch of the vanes and optimize the performance of the compressor. Another concept is the unducted fan or open rotor engine

[1]Former Techspace Aero

(Figure 1.10). In this type of engine, the fans are positioned outside the casing of the engine. The booster therefore is directly exposed to bird strike (primary impact can be on the booster, in contrast with the turbofan engine where the bird first hits the fan).

Figure 1.10: Open rotor (*Snecma Prepares For Crucial Open-rotor Tests*, 2013).

1.3 Objectives

The ultimate goal of this PhD is to perform a parametric study on the booster vane subjected to bird strike and to develop a numerical model capable of predicting the damage caused by bird strike.

To succeed, a better understanding of the phenomena needs to be obtained. This requires the consideration of multiple (simplified) impact conditions and situations which will tell something about the requirements of the numerical aspects, the importance of certain impact regimes and eventually the performance of the numerical model.

The experimental tests on multiple booster vane configurations are expensive and require a qualitative and extensively tested and validated test set-up to obtain valuable data for the numerical simulations. Different concepts need to be considered and the optimal use of the available equipment will need to be assured.

1.4 Outline of the PhD

Chapter 2 starts with a brief overview of the Ghent University bird strike test set-up and the available equipment. The complete launching procedure will be discussed, including the manufacturing of the substitute birds. Some significant changes were made to the set-up during the PhD, which will be covered here as well. A summary of the data acquistion equipment, including high speed cameras, strain, pressure and acceleration measurements, etc. is also given.

Closely related to the data acquisition in chapter 2 are the optical techniques described in **chapter 3**. The very short impact characteristic to bird strike generally results in vibrations and oscillations which proved to impede the use of transducers. Additionally, deriving the kinematics of several set-ups in this work is essential to obtain the necessary information. Therefore, multiple optical techniques are used, improved or developed to measure very specific displacements. Digital Image Correlation, a 3D shape map technique and a 2D and 1D line pattern measurement technique will be covered.

The numerical model of the bird and a study on the shock and steady state regime is covered in **chapter 4**. This chapter will start with a literature overview including the creation of the shock and steady state regime and its characteristic pressures and wave speeds, the numerical techniques with a focus on SPH and the bird material models, focussing on the equation of state and its use so far in literature. Next, the shock and steady state regime will be investigated. Specific conditions in the simulations will make it possible to accurately measure the shock pressure. The influence of the front shape (tilt angle, hemispherical end) is investigated, the elastic energy as a measure for the presence of the shock regime is introduced, together with an analytical expression for flat cylinders and the influence of the deformation of the target on the shock regime is investigated. The steady state pressures will be compared to the analytical results and a "mesh rebounce" phenomenon occurring between the shock and steady state regime observed in the simulations and in literature is discussed. Finally, the results of several impact pressure measurements will be shown and compared to the analytical

and numerical results.

Chapter 5 and 6 respectively contain the results of the experiments and simulations on rigid targets, more specifically a flat plate, a wedge and a splitter. The concept of momentum transfer is introduced, which will remain the measure for comparison of force throughout the remainder of the work. Analytical models are created for each target, which will be validated and compared in the experiments and simulations. These analytical model will allow to assess the performance of the used material model. The concept to measure the residual energy after an impact event will be introduced here as well. In the numerical simulations, the influence of the artificial dissipation is also investigated.

A step towards deformable targets is taken in **chapter 7**. A series of tests with flat thin aluminium plates simply imposed onto a square opening will be discussed. The overall deformation of the target and the bird during impact and the final shape of the plate after impact will be compared between experiment and simulations and the influence of several input conditions will be investigated.

In **chapter 8**, first the development of a set-up to measure the transferred multi-axial momentum to a vane structure will be covered. This set-up will be validated using a simplified steel vane. Except from serving as a validation for the momentum measurement set-up, the steel vane is also used as an intermediate step towards the booster vane experiments and simulations. After covering the complete set-up, the developed fixture to test the booster vanes is shown and the results of the parametric study on the booster vanes will be covered. Finally, a comparison with the simulations will be made.

A conclusion of the work and some proposals for future work will be given in **chapter 9**.

1.5 Bibliography

Aihaiti, M. and Hemley, R. J. (2008), Equation of state of ballistic gelatin, Technical Report 0704-0188, Carnegie Institution of Washington.

Airoldi, A. and Cacchione, B. (2006), 'Modelling of impact forces and pressures in Lagrangian bird strike analyses', *International Journal of Impact Engineering* **32**(10), 1651 – 1677.

Allan, J. R. and Orosz, A. P. (2001), 'The costs of birdstrikes to commercial aviation', *Proceedings of the 3rd Bird Strike Committee USA/Canada meeting* . Calgary, Canada.

Allcock, A. and Collin, D. (1969), The development of a dummy bird for use in bird strike research, Technical Report R.303-A.R.C.30697, National Gas Turbine Establishment.

ATSB (2003), The hazard posed to aircraft by birds, Technical report.

Barber, J. P., Taylor, H. R. and Wilbeck, J. S. (1975), Characterization of bird impacts on a rigid plate: Part 1, Technical Report AFFDL-TR-75-5, Dayton University.

Barber, J. P., Taylor, H. R. and Wilbeck, J. S. (1977), Bird impact forces and pressures on rigid and compliant targets, Technical Report AFFDL-TR-77-29, Air Force Flight Dynamics Laboratory, Wright-Patterson Air Force Base.

Baxter, A. and Hart, J. (2010), A review of management options for resolving conflicts with urban geese, Technical report, Food and Environment Research Agency.

Bertke, R. S. and Barber, J. P. (1979), Impact damage on titanium leading edges from small soft body impacts, Technical Report AFML-TR-79-4019, University of Dayton Research institute.

Blackwell, B. F. and Burnhardt, G. E. (2004), 'Efficacy of aircraft landing lights in stimulating avoidance behavior in birds', *USDA National Wildlife Research Center - Staff Publications* .

Budgey, R. (2000), 'The development of a substitute artificial bird by the international birdstrike research group for use in aircraft component testing', *International Bird Strike Committee ISBC25/WP-IE3* .

Burger, J. (1983), 'Jet aircraft noise and bird strikes: why more birds are being hit', *Environmental Pollution* **30**, 143–152.

Certification Specifications (2016), `https://easa.europa.eu/document-library/certification-specifications`. [Online; accessed 5-January-2016].

Challita, A. (1980), Validation of a bird substitute for development and qualification of aircraft transparenciles, Technical Report AFWAL-TR-80-3098, University of Dayton Research Institute.

Challita, A. and Barber, J. P. (1979), The scaling of bird impact loads, Technical Report AFFDL-TR-3042, University of Dayton Research Institute.

Dennis, N. and Lyle, D. (2009), Bird strike damage & windshield bird strike, Technical report, EASA.

Dolbeer, R. A. (2002), 'Population increases of large bird species in relation to impact standards for aircraft engines and airframes', *USDA National Wildlife Research Center - Staff Publications* .

Dolbeer, R. A. (2009), 'Birds and aircraft - fighting for airspace in ever more crowded skies', *Human-Wildlife Conflicts* **3**(2), 165–166.

Dolbeer, R. A. (2015), 'Trends in reporting of wildlife strikes with civil aircraft and in identification of species struck under a primarily voluntary reporting system, 1990-2013', *Federal Aviation Administration* .

Dolbeer, R. A. and Eschenfelder, P. (2003), 'Amplified bird-strike risks related to population increases of large birds in North America', *Proceedings of the International Bird Strike Committee meeting* pp. 49–67. Warsaw, Poland.

Dolbeer, R. A. and Seubert, J. L. (2009), 'Canada goose populations and strikes with civil aircraft: challenging trends for aviation industry', *U.S. Department of Agriculture, Wildlife Services* . Ohio, USA.

Dolbeer, R. A., Wright, S. E., Weller, J. R. and Begier, M. J. (2015), 'Wildlife strikes to civil aircraft in the United States 1990 - 2014', *Federal Aviation Administration National Wildlife Strike Database* (21 Serial Report).

E-BREAK: Engine Breakthrough Components and Subsystems (2016), `http://www.e-break.eu/`. [Online; accessed 9-January-2016].

Edge, C. H. and Degrieck, J. (1999), 'Derivation of a dummy bird for analysis and test of airframe', *Bird Strike Committee-USA/Canada, First Joint Annual Meeting, Vancouver, BC* .

Fernández-Juricic, E., Gaffney, J., Blackwell, B. and Baumhardt, P. (2011), 'Bird strikes and aircraft fuselage color: a correlational study', *Human-Wildlife Interactions* **5**(2), 224–234.

Fox, A., Ebbinge, B., Mitchell, C., Heinicke, T., Aarvak, T., Colhoun, K., Clausen, P., Dereliv, S., Farago, S., Koffijberg, K., Kruckenberg, H., Loonen, M., Madsen, J., Mooij, J., Musil, P., Nilsson, L., Pihl, S. and der Van Jeugd, H. (2010), 'Current estimates of goose population sizes in western Europe, a gap analysis and assessment of trends', *Ornis svecica* **20**, 115 – 127.

Graff, J., Stolze, L. and Varholak, E. (1973), Impact resistance of spar-shell composite fan blades, Technical Report NASA CR-134521, Hamilton Standard.

Graff, J., Stolze, L. and Varholak, E. (1976), Fiber composite fan blade impact improvement, Technical Report NASA CR-135001, Hamilton Standard Division.

Hamershock, D. M., Seamans, T. W. and Bernhardt, G. E. (1993), Determination of body density for twelve bird species, Technical Report WL-TR-93-3049, Wright Laboratory, Wright-Patterson Air Force Base and SUSDA, Denver Wildlife Research Center.

Hedayati, R., Sadighi, M. and Mohammadi-Aghdam, M. (2014), 'On the difference of pressure readings from the numerical, experimental and theoretical results in different bird strike studies', *Aerospace Science and Technology* **32**(1), 260–266.

Hedayati, R. and Ziaei-Rad, S. (2013), 'A new bird model and the effect of bird geometry in impacts from various orientations', *Aerospace Science and Technology* **28**(1), 9 – 20.

Hedayati, R. and Ziaei-Rad, S. (2014), 'New bird model for simulation of bird strike on various layups used in transparent components of rotorcrafts', *Journal of Aerospace Engineering* **27**(1), 76–85.

Heimbs, S. (2011*a*), 'Bird strike simulations on composite aircraft structures', *2011 SIMULIA Customer Conference* .

Heimbs, S. (2011*b*), 'Computational methods for bird strike simulations: A review', *Computers & Structures* **89**(23-24), 2093–2112. Munich, Germany.

Johns, R. (1974), 'FOD impact testing of composite fan blades', *19th National SAMPE Symposium and Exhibition* .

Jr., J. S. and Pate, R. C. (1957), Bird ingestion tests of an allison T-56 turbine engine, Technical Report 312, Civil Aeronautics Administration Technical Development Center Indianapolis.

Kneubuehl, B. P., Coupland, R. M., Rothschild, M. A. and Thali, M. J. (2011), *Wound Ballistics - Basics and Applications*, Springer-Verlag Berlin Heidelberg.

Lavoie, M., Gakwaya, A., Ensan, M. N., Zimcik, D. and Nandall, D. (2009), 'Bird's substitute tests results and evaluation of available numerical methods', *International Journal of Impact Engineering* **36**(1011), 1276 – 1287.

Lima, S. L., Blackwell, B. F., DeVault, T. L. and Fernández-Juricic, E. (2015), 'Animal reactions to oncoming vehicles: a conceptual review', *Biological Reviews* **90**(1), 60–76.

MacKinnon, B. (2004), *Sharing the Skies: Aviation Industry Guide to the Management of Wildlife Hazards*, Aviation Pub. Division of Transport Canada.

MacNaughtan, I. (1972), *The Design of Leading-edge and Intake Wall Structure to Resist Bird Impact*, number 72056.

Maragakis, I. (2009), 'Bird population trends and their impact on aviation safety 1999-2008', *European Aviation Safety Agency (EASA), Safety Analysis and Research Department* .

Martindale, I. (1994), 'Bird ingestion and the Rolls-Royce wide chord fan', *Bird Strike Committee Europe* .

McCallum, S. and Constantinou, S. (2005), 'The influence of bird-shape in bird-strike analysis', *5th European LS-DYNA Users Conference* .

Nizampatnam, L. S. (2007), Models and methods for bird strike load predictions, PhD thesis, Wichita State University.

NTSB (2010), Loss of thrust in both engines after encountering a flock of birds and subsequent ditching on the Hudson river, US airways flight 1549 airbus A320-214, N106US, Weehawken, New Jersey, January 15, 2009, Technical report.

Orlowski, M. (2015), Experimental and Numerical Investigation on the Bird Impact Resistance of Novel Composite Sandwich Panels, PhD thesis, Cranfield University.

Premont, E. and Stubenrauch, K. (1974), Impact resistance of composite fan blades, Technical Report NASA CR-134707, Aircraft Engine Group, General Electric Co.

Regulations and policies (2016), `https://www.faa.gov/aircraft/air_cert/airworthiness_certification/std_awcert/std_awcert_regs/regs/`. [Online; accessed 5-January-2016].

Ritt, S. A. (2012), 'Projectile'. US Patent 8,220,396.
URL: *https://www.google.com.ar/patents/US8220396*

Roberts, G. D., Pereira, J. M., Revilock, D. M., Binienda, W. K., Xie, M. and Braley, M. (2005), 'Ballistic impact of braided composites with a soft projectile', *Journal of Aerospace Engineering* **18**(1), 3–7.

Safran Aero Boosters (2016), `http://www.safran-aero-boosters.com/`. [Online; accessed 21-July-2016].

Seidt, J. D., Pereira, M. J., Hammer, J. T., Gilat, A. and Ruggeri, C. (2012), Dynamic load measurement of ballistic gelatin impact using an instrumented tube, *in* V. Chalivendra, B. Song and D. Casem, eds, 'Dynamic Behavior of Materials, Volume 1', Conference Proceedings of the Society for Experimental Mechanics Series, Springer New York, pp. 243–250.

Short, J. J., Kelley, M. E., Speelman, R. J., III and McCarty, R. (2000), 'Birdstrike prevention: Applying aero-science and bioscience', *International Bird Strike Committee* .

Snecma Prepares For Crucial Open-rotor Tests (2013), `http://aviationweek.com/commercial-aviation/snecma-prepares-crucial-open-rotor-tests`. [Online; accessed 21-July-2016].

Steinhagen, C. and Salemme, C. (1973), The impact resistance of current design composite fan blades tested under short haul operating conditions, Technical report, General Electric Company.

Stimson, R. (2016), 'The Wright stories, bird strikes', `http://wrightstories.com/bird-strikes/`. [Online; accessed 5-January-2016].

The Statistics Portal (2016), 'Annual growth in global air traffic passenger demand from 2005 to 2015', `http://www.statista.com/statistics/193533/growth-of-global-air-traffic-passenger-demand/`. [Online; accessed 8-January-2016].

Thorpe, J. (1998), 'The implications of recent serious birdstrike accidents and multiple engine ingestions', *International Bird Strike Committee* .

Thorpe, J. (2003), 'Fatalities and destroyed civil aircraft due to bird strikes, 1912-2002', *International Bird Strike Committee* .

Transport (including Aeronautics) (2016), `http://cordis.europa.eu/fp7/transport/home_en.html`. [Online; accessed 21-July-2016].

Wadia, A. R. and Holm, R. G. (2004), 'Turbofan engine internal anti-ice device'. US Patent App. 10/264,128.
URL: *http://www.google.com/patents/US20040065092*

Wang, J. and Herricks, E. E. (2010), 'Bird-aircraft strike threat assessment using avian radar information', *FAA worldwide airport technology transfer conference* .

Welsh, C. and Centonze, V. (1986), Aircraft transparency testing - artificial birds, Technical Report AEDC-TR-86-2, Arnold Engineering Development Center.

What is FP7? The basics (2016), `https://ec.europa.eu/research/fp7/understanding/fp7inbrief/what-is_en.html`. [Online; accessed 21-July-2016].

Wikimedia Commons (2011), 'Fan blades and inlet guide vanes of genx-2b', `https://commons.wikimedia.org/wiki/File:Fan_blades_and_inlet_guide_vanes_of_GEnx-2B.jpg`. [Online; accessed 1-August-2016].

Wilbeck, J. S. (1978*a*), 'Bird impact loading', *The shock and vibration bulletin* **48**, 115–120.

Wilbeck, J. S. (1978*b*), Impact behavior of low strenght projectiles, Technical Report AFML-TR-77-134, Air Force Materials Laboratory, Wright-Patterson Air Force Base.

Wilbeck, J. S. and Rand, J. L. (1981), 'The development of a substitute bird model', *Transactions of ASME Journal of Engineering for Gas Turbine and Power* **103**(4), 725–730.

CHAPTER 2

Bird strike testing

Abstract: Bird strike testing today is the way to test and validate concepts and designs of aerospace structures in terms of bird strike robustness. In this chapter, a brief introduction will be given to the Ghent University bird strike test set-up, capable of shooting birds with an energy up to 42 kJ. This chapter will cover the different aspects of manufacturing gelatine birds. The complete launching sequence will also be explained, including the available data acquisition equipment.

2.1 Ghent University bird strike test set-up

2.1.1 Operating principle

The research group *Mechanics of Materials and Structures* at Ghent University has developed a gas gun for bird strike measurements over the past twenty years, capable of launching birds with an energy up to 42 kJ (Figure 2.1). Basically, a pneumatic launcher is used to shoot an impacting body at the target inside the test chamber at the desired speeds.

Figure 2.1: Ghent university bird strike test set-up.

A significant difference with other set-ups found in literature is the presence of an (evacuated) test chamber. Evacuating the test chamber is done using two vacuum pumps that decrease the pressure inside the test chamber before each experiment down to an absolute pressure of roughly 0.2 bar. Using an evacuated test chamber has the following advantages:

- **A more accurate velocity measurement:** As will be explained further on, the velocity of the bird is determined from the drop of three subsequent lasers. In ambient atmosphere however, compressed air could increase the density in front of the bird, which could, due to the change in refractive index of the compressed air, deviate the laser too soon.
- **Less infuence of the air:** The air could decelerate the bird a lot less in partial vacuum. First of all, this increases the accuracy of the estimation of the impact velocity at the target. And secondly,

with more confidence, it can be said that results are not influenced by air friction and the possible error source in the correlation with the simulations is reduced by a certain extent.

- **Venting of the compressed air:** The residual compressed air behind the bird can vent into the large chamber and therefore, its influence on the results is decreased (for the short space available between stripper chamber and target).

In the following three subparagraphs, the process of launching a bird will be briefly explained by discussing the three main parts of the set-up.

The pressure vessel

Figure 2.2 gives a section cut of the pressure vessel, together with a sabot ready for testing and the start of the launching tube (the bird is not shown in this figure). At the start of every test, the projectile or sabot containing the bird (1) is mounted in front of the pressure vessel (4). The projectile or sabot essentially is a plastic cylinder closed at one side. Before launch, a lever (11) holds the internal device (12) of the pressure vessel in place, while the retaining ring (2) fixes the sabot while pressure is built up. This ring has a triangular cross-section that is clamped between the sabot (1) and the internal device, making sure the sabot is fixed in place. When the desired pressure is obtained, a software controlled actuator releases the lever. Consequently, the lever no longer retains the internal device, allowing it to be pushed backwards. A small saw cut in the retaining ring allows the ring to open and increase in diameter under influence of the high pressure acting on the free face of the sabot, thus releasing the sabot, which is then accelerated in the low-friction honed tube (3) because of the built up pressure.
The entire pressure vessel is mounted onto a linear guiding rail (13) to be able to easily and accurately close and open the heavy vessel.

The stripper chamber

In the stripper chamber (6 in Figure 2.3), the bird is separated from the sabot by a cone-shaped stripper (7a and 7b). To make sure that the bird is not hindered by the stripper, it is enveloped by a layer of foam. The foam brings

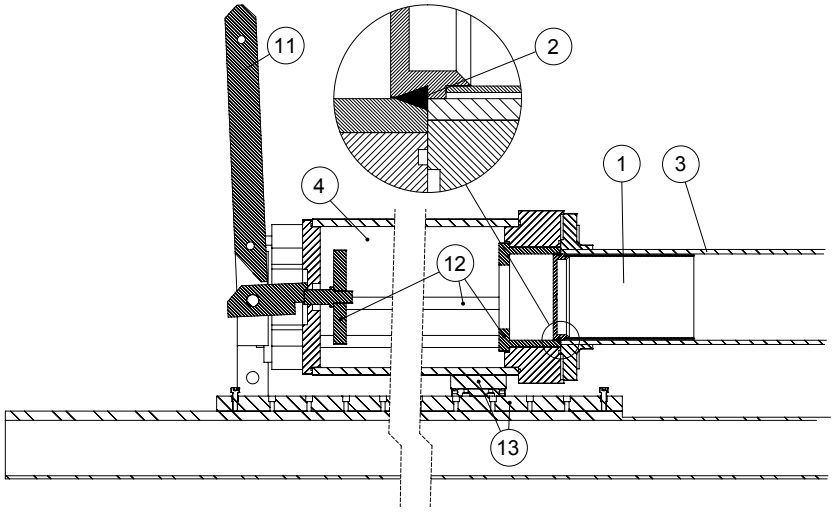

Figure 2.2: Section cut pressure vessel.

additional unwanted mass to the experiment, therefore the pass-through of foam must be minimized as much as possible. Because multiple weights have to be shot, two stripper shapes were developed: 7a for the large birds and a combination of 7a and 7b for the smaller birds. For the small birds, the clearance between the bird and the sabot is 2 mm.

The scenario with the small bird is better, because the bird is stripped from the sabot before the sabot starts crushing on stripper 7a. For the large birds, this would require a bigger diameter of the sabot and the tube. However, when a sabot reaches the stripper chamber, it has a velocity near the aimed impact velocity of the bird, at which gravity has a negligible influence on the stripping process of a large bird. The sabot is made from plastic which shows brittle behaviour at high deformation rates and breaks into small pieces during the stripping process.

For several reasons explained above, a partial vacuum has to be applied, which is why the test chamber, stripper chamber and barrel have to be airtight. On the other hand, the compressed air is unwanted at the moment after the bird is stripped from the sabot. Therefore, an air venting system was developed equivalent to a non return valve (14). With a large 120 mm

diameter rubber ball positioned on an O-ring, the stripper chamber during is sealed during evacuation and can be lifted up at high pressures. The tube on top of the chamber contains the ball when this happens, for safety reasons.

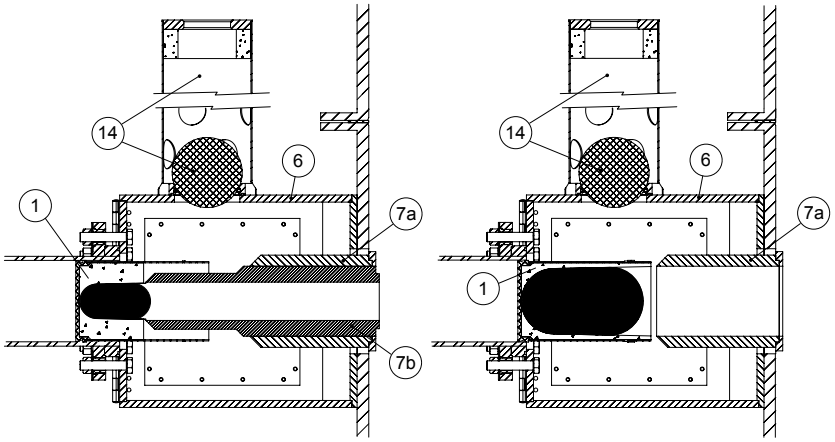

Figure 2.3: Section cut stripper chamber.

The test chamber

After the stripping process, the bird enters the test chamber (a section cut is shown in Figure 2.4). This is a 3.6 m long, 2.5 m high and 1 m wide chamber with several windows (10) for observations of the experiment and velocity measurements. The vertical mounting slats (15) provide the necessary flexibility to install any set-up, anywhere inside the chamber. Practically, the set-ups are placed rather to the back of the chamber, because the first three windows are used for the velocity measurement. The cross-beams (16) are necessary to reduce deformation when the chamber is in partial vacuum. A manhole (17) allows the user(s) to enter the chamber.

2.1.2 Preparation of the sabot and the bird

2.1.2.1 The sabot

As introduced in the previous section, the purpose of the sabot is to accelerate the bird up to speed inside the test chamber in a controlled manner. A picture of the sabot used in this work is shown in Figure 2.5. It consists of a

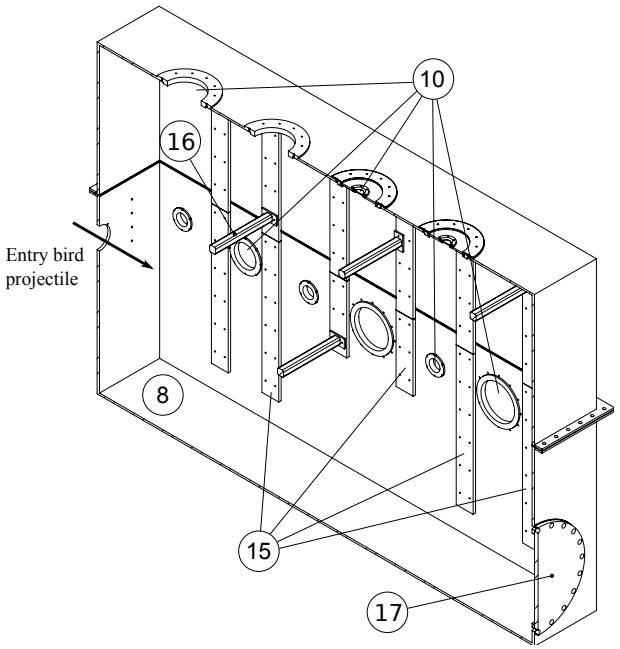

Figure 2.4: Section cut test chamber.

tube, made from PVC and a cap and a guiding ring made from the polyamide Epramid, with improved dimensional stability and grease characteristics.

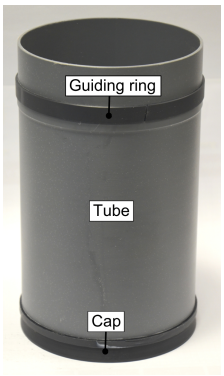

Figure 2.5: The sabot: A PVC tube with a cap and a guiding ring.

This cap and the guiding ring together guide the sabot during launch with the required precision. The cap specifically also serves as the seal between the high pressure and the vacuum and as a part of the trigger mechanism

(section 2.1.1). The three parts are manufactured on a turning machine, glued together with super glue, grinded before each test to match the tube and greased slightly to further reduce the friction.

In the current set-up, 3 masses can be shot: 0.3, 1.5 and 1.8 kg. To be able to fix the birds along the axis of the sabot and resist the high acceleration forces, material is needed that supports the bird by filling up the space between the bird and the sabot. On the other hand, the weight of the supporting material that inevitably enters the test should be minimized. A certain specific strength is therefore needed. To give an idea of the forces that are generated by the bird on the supporting material inside the sabot, the equivalent weight of the bird can be calculated from acceleration of the sabot, which is derived from the initial pressure difference over the sabot:

$$m_{eq} = \frac{\Delta P \pi d^2 m_{bird}}{4 m_{tot} g} \tag{2.1}$$

With ΔP the pressure difference or also, the relative pressure between the high pressure and vacuum in Pa, d the inner diameter of the tube in m, m_{bird} and m_{tot} respectively the mass of the bird and the total mass (sabot and bird) in kg and g the gravity coefficient in m/s^2. For a ΔP of 5 bar or 500.000 Pa, the inner diameter of the tube being 0.14 m, a 0.3 kg bird and a total mass of 0.8 kg, an equivalent mass of 295 kg can be calculated.

A two-component open-cell PUR foam proved to be capable of supporting the bird for the majority of the considered impact velocities, while having a very low density. To be able to support the bird ideally, the same but negative shape of the bird is manufactured using an equivalent mould. In this work, most substitute birds have a cylindrical shape with hemispherical ends and a l/d ratio of 2, as literature showed that this best represents the actual behaviour of a bird (Heimbs, 2011). The mould therefore has a hemispherical shape at the end. Figure 2.6 shows the three aluminium moulds that are used to create the desired foam shape, together witch a section cut showing the fixation of the moulds inside the sabot.

The big moulds are centred using a centring ring, while the mould for the 0.3 kg birds is centred using a conical ring. Before fixing the moulds inside the sabot, they are covered with a thin plastic foil or grease to make sure

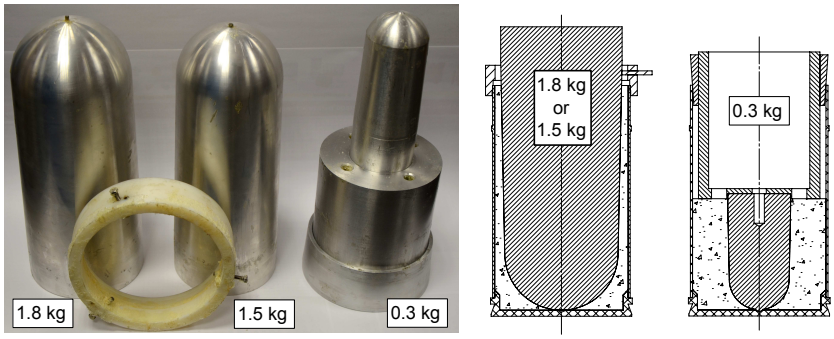

Figure 2.6: Foam moulds.

that the foam does not stick to the mould.

To get the desired shape of the gelatine bird, additional moulds are needed. The tools for that are depicted in Figure 2.7. For the 1.5 and 1.8 kg birds, the gelatine is moulded and solidified in the sabot. For the 0.3 kg bird, the gelatine is moulded and solidified in a separate shape. Also here, the parts are greased to avoid sticking of the bird to the moulds.

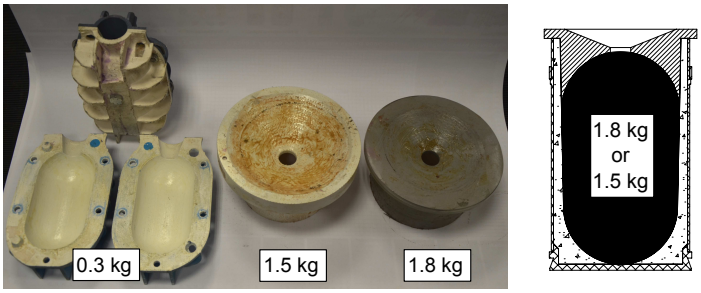

Figure 2.7: gelatine moulds.

The moulds for the 1.8 and 1.5 kg birds are manufactured with stereolitography. The 0.3 kg moulds are manufactured from polylactic acid or PLA using in-house low budget 3D printers. PLA performs well as long as the gelatine temperature is not too high. Every mould is polished and coated to have smoother surface.

The birds occasionally do not always enter the test chamber smoothly. This can be concluded from the sometimes far from perfect shape on the camera

images and the fact that sometimes, gelatine is found in the stripper chamber. There are two plausible reasons for this phenomenon. Or the foam is crushed due to the high acceleration, allowing the bird to expand in the crushed regions and therefore have a bigger diameter than the splitter. Or the sabot, including the foam, is not manufactured precisely enough. In both scenarios, the bird would hit the splitter, a piece of gelatine would be scraped off and the bird would deform due to the asymmetric splitting process, possibly sliding against the inner surface of the splitter.

2.1.2.2 Gelatine substitute birds

In this work, gelatine PBG05 mesh 20 from PB Gelatins is used. The mesh-number refers to the size of the granes (in this case similar to crystal sugar) and is determined by the way of dissolving the gelatine. PBG05 is a PB code that corresponds to 200-220 Bloom, which is a measure for the strength of the (solidified) gelatine (PB Gelatins, 2016). In the Bloom test, the gelatine sample's rigidity is evaluated by pressing a test probe on to its surface. The samples response is measured in Bloom units where each gram force response is equal to one Bloom unit (FTC, 2016).

To make gelatine birds, a certain gelatine to water weight ratio has to be chosen, further referred to as mixing ratio or MR. Typical ratios are 1:4 or 20% (1 part of gelatine with 4 parts of water) and 1:9 or 10%. In this work, mainly 1:6 was used for reasons explained in the next chapters. The procedure for preparing gelatine is as follows:

1. Fill a bowl with hot tap water (roughly 50°C), approximately 200 gram more than the aimed weight per bird.
2. Add the proper amount of gelatine according to the mixing ratio. While stirring slowly, add more gelatine until all the mass is dissolved. Try to avoid or limit clotting throughout the process.
3. Add a small amount of gouache (small teaspoon) to color the otherwise translucent bird to increase the contrast on the images (a light or a dark color depending on the color of the target and the background).
4. Fill the mould(s) (cfr. section 2.1.2.1) and pour the remaining gelatine in a same amount of cups. Be sure to fill up the neck of the mould

as well, because air bubbles will rise to the top after moulding and reduce the density locally. The cup(s) are necessary for the density measurements afterwards. Use this sequence order, to be sure to have any sediment in the cups and not in the bird.

5. Put the birds in the refrigerator for 12-24 hours.

Before each test, the moulds are removed and the weight of the bird and the total mass of bird and sabot is determined.

A key parameter that needs to be determined for the simulations of the bird strike tests is the density of the bird. The measurement of the density is done consistently each time the chamber is evacuated with a Sartorius Feinwaage type 2462 micro balance. This balance works with Archimedes' principle (buoyancy method) and is able to measure the mass of a suspended test piece weighing up to 200 g with an accuracy of 0.1 μg. Two measurements have to be done. Firstly, the scale is used to weigh a dry lump of gelatine. Secondly, the same lump is weighed again while submerged in distilled water. The difference in weight equals the buoyancy force and is proportional to the volume of the lump of gelatine and the density of water. The density of the gelatine can therefore be determined with the following formula (ASTM Standard D792-00, 2000):

$$\rho_{gel} = \frac{m_{gel}}{V_{gel}} = [(\rho_{water} + (t_w - 23) \cdot M))] \frac{m_{gel}}{m_{gel} - m_{gel,submerged}} \qquad (2.2)$$

Where m_{gel} and $m_{gel,submerged}$ are respectively the mass of the gelatine weighed in air and in water, ρ_{water} is the density of the distilled water, at 23 °C being 997.5 kg/m^3, t_w is the temperature of the water and M the density change per degree Celsius. Since the order of magnitude of M is around 0.2 kg/m^3/°C, the influence of the temperature is ignored.

For each test, at least three samples are measured from the separate cup and averaged out. The manufacturing of the gelatine was quite consistent. For the 14 booster vane experiments for example, the gelatine density was 1040.93±3.5 kg/m^3. This is a relatively high density compared to the 950kg/m ^{3} often aimed for in the experiments (see section 1.1.3). However,

1040 kg/m^3 should be a more conservative value for birds with lower mass (see Figure 1.4) and for the large scatter observed between different birds. A solid bird should also be more conservative in terms of the shock regime (see chapter 4).

Several porous birds are also tested. The lower porosity is achieved with phenolic microballoons. Because these microballoons are lighter than air, the mould needs to be rotated during solidification to achieve a homogeneous distribution of the microballoons. An aluminium mould that can be closed with a bolt is manufactured for that purpose (Figure 2.8).

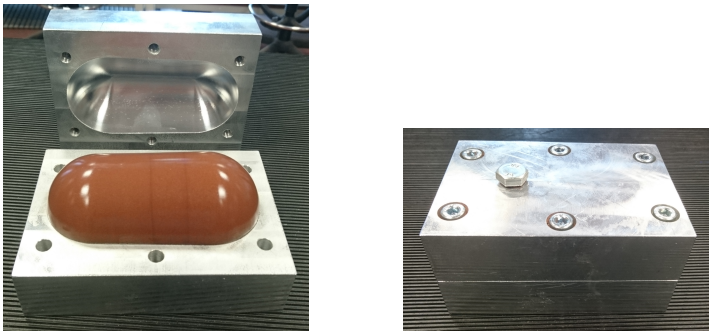

(a) Open with porous bird. **(b)** Mould closed with bolt.

Figure 2.8: Aluminium mould for porous birds.

Water cannot be used any more in the Archimedes density tests because the porous gelatine would float. Organic fluids lighter than water such as alcohol cannot be used either because it reacts with the gelatine. Therefore the density is determined from the volume of the mould, which is manufactured with an accurate CNC machine and should therefore give a good estimation. A density of 960 kg/m^3 is typically obtained, which is a good representative for most large birds (section 1.1.3).

During moulding, the microballoons tend to rise quickly. Due to the fast moulding process, consequently some air gets entrapped inside the mould. In the experiments, this is in general in the order of 1 ml, which corresponds to an error of 0.34% or 3 kg/m^3 on the density (the volume of the mould is 288.31 ml).

2.1.2.3 Real birds

Several tests are performed with real birds, more specifically with wild ducks (mallard or *Anas platyrhynchos*) and home pigeons (*Columba livia domestica*). These bird species are chosen because they are readily available and still more likely to be ingested in a jet engine than chickens.

In the performed tests, the ducks are decapitated in advance for two reasons. Keeping the neck as an extension of the body during launch is not feasible. Increasing the mass of the body by bending the neck and head and therefore adding extra mass to the body is not realistic as well, which is why the choice is made to decapitate the ducks. Because of this choice, the shape better resembles the shape of the gelatine bird. Therefore, it will be possible to make a better comparison with the gelatine birds in terms of general behaviour. Wild mallard ducks are usually lighter than 1.5 kg, as are the ones used in the four tests with ducks (see chapter 5).

Several doves are shot as well (see chapter 4 and 5). The neck of the doves are not decapitated before launch as they can more easily be launched head first. The weight of the used doves is approximately 400 gram.

In Figure 2.9, a 1.8 kg gelatine substitute bird, a 1.4 kg duck and a 0.4 kg pigeon are shown. Because of the feathers and the lower density of the duck, it occupies a lot more space. It is even questionable whether for the tests with the real birds, the total mass entered the test chamber completely because in contrary to the gelatine bird, almost no foam can be observed on the camera images. In case of the pigeon, the head and neck is bended and jammed between the sabot and the torso. During stripping, the head and neck is released and aligns with the rest of the body.

2.1.3 Retrofit

The previous two sections describe the set-up as it exists now. Throughout this PhD however, the set-up has seen some significant changes. Most importantly, birds up to 1.8 kg or 4 lb can now be tested, according to the certification standards, opposed to the 0.6 kg at the start of the project (Figure 2.10).

Figure 2.9: Gelatine substitute bird (left), wild duck (middle) and pigeon (right) inside the sabot.

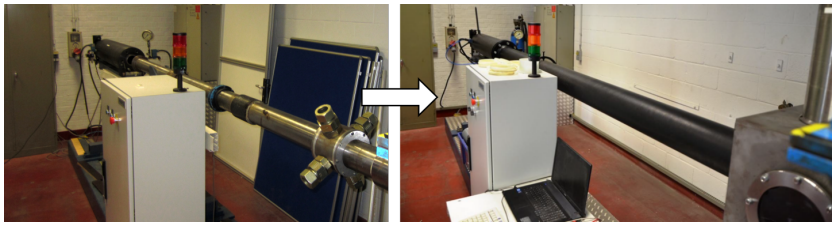

Figure 2.10: Old set-up (left) and new set-up (right).

To give a short summary, the following points were changed:

- Replacement of the launching tube system to a new tube with appropriate connections.
- Installation of a linear rail to mount the pressure vessel.
- Redesign of the sabot and the moulds for the foam and the gelatine birds with hemispherical ends.
- Development of a lighter stripper chamber with windows, a new high pressure venting system, and a new stripper for the 0.3 kg birds.
- Replacement of several polycarbonate by smaller glass windows to reduce the optical lens effect of the windows bending inwards due to the vacuum inside the test chamber.
- Some smaller changes: installation of BNC cables and shielded twisted pair (STP) cat 6e cables for data acquisition, a new platform to ease the build-up of the experiments, mounts for the lasers and optocouplers,

installation of LED lights inside the chamber for high speed imaging, etc.

At the start of the PhD, a couple of experiments were executed using the old set-up (with birds weighing approximately 0.6 kg). After that, the main retrofit of the set-up took place in the first half year of the project. Smaller adaptations were done during the course of the project when needed.

2.2 Available instrumentation

The validation of the numerical models requires a sufficient amount of data. This data can be obtained optically with cameras or on the spot using sensors or transducers. In this section, all the equipment used for the bird strike tests will be covered.

2.2.1 Optical recording

A convenient way to compare experiments with simulations is by recording the impact and deformations of the test piece. Because the actual impact only takes several milliseconds, high speed cameras (HSCs) are required. Where normal cameras generally have a framerate of 50 up to 250 frames per second (fps), a high speed camera can record up to 500.000 fps (with reduced resolution). The ability to make high speed recordings of the experiment are a requirement for several reasons:

- Images are required to visualize the impact of the bird.
- The offsets of the bird in two directions and the shape of the bird has a big influence on the simulations, the HSCs can give a rough estimate of these input parameters.
- In order to perform optical measurements, it is required to have focused images of the target structures.
- A final reason is the need for an overview of the whole set-up inside the chamber during impact. Such images can confirm if the experiment went entirely according to plan (trajectory bird, sabot debris, etc.).

The absence of HSCs would introduce a great amount of uncertainties, making it impossible to say something about the accuracy of the developed

models.

There are three HSCs available at the department: a Photron APX-RS and two Photron SA4 cameras. Some specifications relevant for the performed tests are shown in Table 2.1.

Table 2.1: Specifications high speed cameras

Specifications	**APX-RS**	**SA-4**
Memory [Gb]	8	16
Full resolution [pix]	1024 x 1024	1024 x 1024
Resolution at 10.000 fps [pix]	512 x 512	768 x 512
Record time at 10.000 fps [s]	2.5	2.91
Smallest shutter time [μs]	2	1
Bit depth [bit]	10	12
Pixel size [μm]	17	20

Because of the very high framerate, high power lights are needed. Two SSW-3015 high power LEDs with a very narrow light beam can be hung tactically inside the chamber. Two 400W Hedler D04 floodlights typically are placed on top of the chamber. A Dedolight Dedocool light system and a Hedler DF25 LED light are used as well.

The HSCs always record through the windows in the test chamber, mounted on tripods and stands on the side or above the test chamber, hanging on the ceiling. This way, vibrations due to the launch of the bird cannot disturb the images. An example of a camera set-up is shown in Figure 2.11.
A HSC uses an internal clock which directs the moment at which the frames are taken. The framerate and therefore the internal clock proved to be very accurate (in terms of ns). Synchronization of multiple cameras align the times at which frames are taken. When multiple cameras are used without synchronization, the relative time error between the cameras can be much larger: 1/(2.frame rate) maximum. For general use, this is not necessarily a problem, but for optical techniques using multiple cameras, synchronization is of utmost importance.

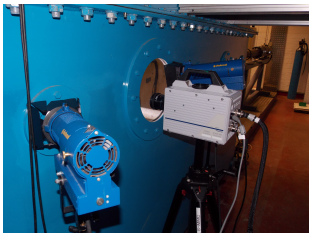

(a) A camera from the side.

(b) Two cameras hanging from the ceiling.

Figure 2.11: A typical camera set-up.

During an experiment, a TTL hardware trigger signal indicates at which time the camera should fill its memory. The trigger lies, per definition, between two subsequent frames. If the trigger would be a reference in time, an uncertainty between 0 and 1/framerate therefore is introduced.

From the images obtained from the high speed recordings, information can be extracted. Four optical measurement techniques are used, improved or developed in this PhD:

- Digital Image Correlation (DIC): the implementation of DIC in MatchID™ will be used to obtain the necessary results.
- 3D shape measurement technique: a new stereo vision technique to calculate 3D shape maps from specimens containing a line pattern.
- 2D line pattern measurement: A new technique developed by (Degrieck, 2015) that is able to do a very accurate local displacement measurement using multiple line gratings. Several case-specific improvements are developed for this technique.
- 1D line grating measurement: A very fast algorithm to derive 1D displacements from one line grating, partly based on the work of (Guelpa et al., 2014).

These techniques will be covered in more detail in chapter 3.

2.2.2 Sensors and data acquisition

2.2.2.1 Sensors for testing

Throughout the different test series performed in this work, the following quantities are measured:

- Displacement
- (Bird) velocity
- Acceleration
- Pressure
- Strain

In the following paragraphs, the sensors used to measure these quantities are briefly discussed.

Displacement

Displacements of target structures can be measured with a Kübler LIMES LI50/B2 inductive position encoder (Figure 2.12a). This sensor produces two square waves when moved over a magnetized strip with an alternating sequence of north and south poles. The two square waves are the result of a small spatial offset equal to one fourth of the period, resulting in a time offset when moving, so the lagging of one signal related to the other is an indication of the direction in which the receiver travels. The frequency of the square wave is a measure for the displacement the receiver has travelled above the magnetic strip (with a spatial period of 50μm). A picture of the sensor and a typical square wave is shown in Figure 2.12b.
The signals are sampled at 1-10 MHz and processed with a Matlab™ script that is able to account for the non-relevant noise or spurious peaks (such as the peak at 150 μs for example in Figure 2.12b).

(Bird) velocity

Three lasers (CLASS IIA) are mounted on one side of the chamber, at the same height of the launch tube (Figure 2.13a). At the other side of the

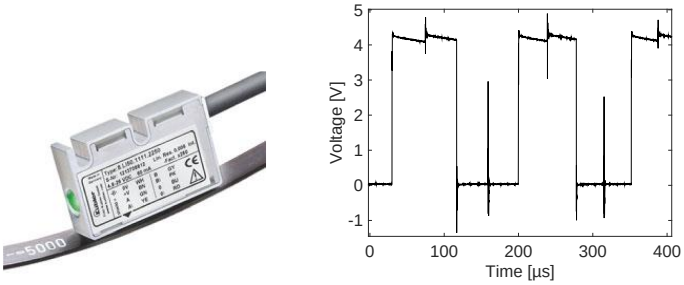

(a) The sensor (*Kübler LIMES LI50/B2 sensor*, 2016).

(b) Square wave signal.

Figure 2.12: The Kübler LIMES LI50/B2 sensor.

chamber three fast-response photodiode receptors are placed at the same height (2.13b) and sampled at 1-10 MHz.

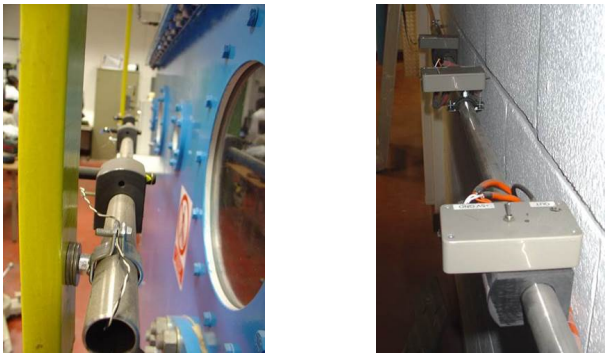

(a) Three lasers.

(b) Three receivers.

Figure 2.13: Bird velocity measurement system.

When the bird passes a laser, the corresponding receptor output voltage drops to 0 V, as shown for the three subsequent lasers in Figure 2.14.
The laser signals are not always that smooth. Foam flying at higher or lower speed than the bird can block the laser too soon for example. For some experiments, the rise of the laser signals therefore is used instead of the drop.

In theory, the drag equation taking into account the force due to the residual air inside the vacuum chamber or the pressure wave behind the bird could be fitted to the three data points in time. This proved to introduce large

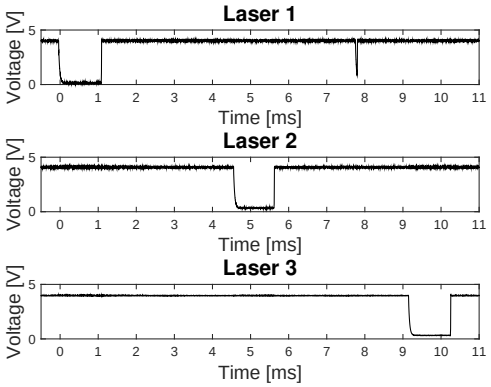

Figure 2.14: A typical set of laser signals.

errors and for future reference, this will be discussed here briefly.

The force of an object in a fluid stream is proportional to the velocity squared ($F \sim v^2$). Writing F as ma and equating a to dv/dt results in a differential equation with the following solution:

$$s = \frac{1}{K} ln(|Kt + C_1|) + C_2 \tag{2.3}$$

With K representing all the other variables in the drag equation relating the velocity squared to the force (due to the non-continuous and unknown flow, K cannot just be calculated) and C_1 and C_2 being integration constants. This equation has 3 unknowns. The three lasers give three equations, so the unknowns can be determined. This equation can be extrapolated to the location of impact, and approximated to have an expression that can be solved directly.

However, the extrapolation proved to be very dependent on small errors such as:

- The exact distance between the two lasers. Each laser beam has a diameter of several millimetres. An error of 1mm is quickly made.
- Pieces of foam flying in front of the bird.

- Vibrations of the bird (mainly the gelatine bird) due to the stripping process.

For an impact velocity of 100 m/s, a relative error in time or distance of 0.5% and -0.5% respectively between the first pair of two lasers and the second pair of two lasers would, extrapolated to a commonly used distance to the target result in an error of 6% or also 6 m/s.

Several experiments indicated that therefore, the assumption of a constant velocity is more reliable. In the remainder of the work, the velocity of the bird is assumed to be the average of the velocity calculated for the two time intervals.

Acceleration and pressure

Deriving the accelerations from displacement data can introduce a lot of noise. Accelerometers on the other hand can generate voltage signals linear to the acceleration that is applied. Similarly, the pressure exerted by the bird on a target structure can be measured with pressure sensors. The pressure sensors and several accelerometers used in this PhD are piezoelectric sensors. The core element of a piezoelectric sensor is a crystal that generates an electric potential difference when stressed. The cause of this stress can be the result of multiple phenomena, depending on the quantity to be measured. For a pressure sensor, this is the pressure of the medium outside the sensor that is stressing the crystal. For an accelerometer, this is the inertia of some well-chosen mass. In both cases an electric potential difference is generated that can be amplified and measured (*PCB: Basics Sensor Theory*, 2016).

Two ICP shock accelerometers type 350B24 with a shear sensing geometry and one ICP pressure sensor type 109C11 from PCB are available for all the experiments. Some relevant characteristics can be found in Table 2.2.
A piezoelectric sensor performs very well in dynamic conditions. But for relatively long experiments or low frequencies, leakage of the electric potential occurs. The discharge time constant is an important parameter that characterizes this leakage. The amount of output signal lost and the elapsed time as a percent of the DTC, have a one-to-one correspondence up to

Table 2.2: Specifications accelerometers and pressure sensor

Specifications	**350B24**	**109C11**
Measurement range	49000 m/s^2 g pk	552 MPa
Frequency range -3dB	0.2-25000 Hz	/
Rise time	/	$\leq$ 2 μs
Non-Linearity	$\leq$2.0 % FS	$\leq$2.0 %
Transverse sensitivity	$\leq$7.0 %	/
Resonance frequency	$\geq$ 100 kHz	$\geq$ 400 kHz
Discharge time constant	1-2 s	$\geq$ 2000 s
Sensing element	Ceramic	Quartz

approximately 10% of the DTC (*PCB: Basics Sensor Theory*, 2016). For the impact of a bird which lasts approximately 1 ms, the DTC should not be a significant error source. In some experiments, displacements are measured for 0.15 s. In that case, the signal can in theory leak up to 15% of its original value.

ICP or Integrated Circuit Piezoelectric stands for a type of sensor with built-in microelectronic amplifiers and is a trademark of the PCB group. These type of sensors produce a low-impedence voltage signal that is less susceptible to noise and easy-to-use with a general coaxial or two-wire cable (*PCB: Basics Sensor Theory*, 2016).

For the pressure sensor, an external PCB 480C02 signal conditioner is used with a frequency range up to 500 kHz and sampled at 10 MHz, which should be more than sufficient.

For the experiments on the booster vanes, Safran Aero Boosters provided a set of high amplitude MEMS shock accelerometers type 3501A1220KG with a $\pm$1dB 0-10.000 Hz frequency range and a lower transverse sensitivity of $\leq$ 3%.

Strain

To measure the local deformation or strain on the surface of an object, strain gauges can be used. A strain gauge is a conductive meandering pattern

(Figure 2.15a) that sees the same amount of deformation as the object. By deforming the object and thus the strain gauge, the resistance of the conductive pattern changes. The strain relates linearly to the measured resistance:

$$\frac{\Delta R}{R} = K\varepsilon \tag{2.4}$$

In this formula, R represent the resistance of the strain gauge in undeformed condition, ΔR represents the resistance variation and the deformation is given by the strain $\varepsilon = \frac{\Delta l}{l}$. K is the gauge factor and is a characteristic value of the strain gauge. Three different types of strain gauges are used in this works, being CEA 250UN 350 and CEA 250UT 350 from the Vishay Precision Group (the CEA 250UT 350 type consists of two strain gauges, which are rotated 90 degrees with respect to each other). The third type is applied on the booster vanes by Safran Aero Boosters.

The strain gauges only exhibit minor resistance variations, consequently a Wheatstone bridge is used to measure these small variations. A quarter bridge configuration is used in all the tests, as can be seen on the simplified electrical circuit, Figure 2.15b.

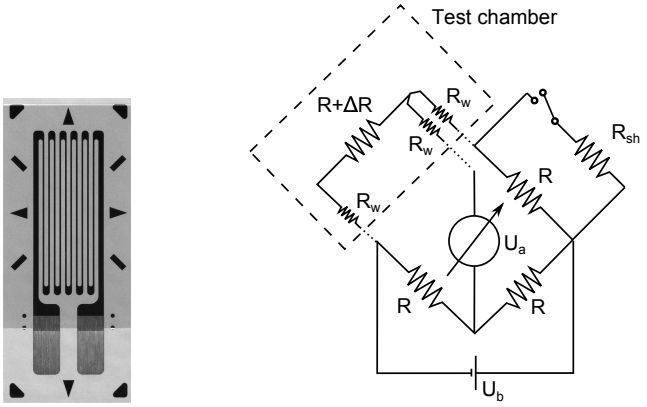

(a) Vishay strain gauge (*Strain Gage CEA-06-250UN-350*, 2016).

(b) Strain gauge in a Wheatstone bridge.

Figure 2.15: Strain gauge measurement.

In Figure 2.15b, $R + \Delta R$ represents the strain gauge. The other three resistors (R) are precision resistors with the same resistance as the strain gauge in undeformed condition, which are also referred to as the completion kit because together with the strain gauge, they complete the Wheatstone bridge. Vishay MR1-350-130 or NI 9945 quarter bridge completion kits can be used. A power supply U_b feeds the cirquit, usually around 4 V and U_a represents the measurement device. A deformation results in a change in resistance ΔR, which results consequently in a voltage output U_A:

$$U_A = \frac{1}{4}\frac{\Delta R}{R}U_B = \frac{1}{4}K\varepsilon U_B \tag{2.5}$$

A three wire configuration is adopted, to exclude the effect of the resistance of the wires connecting the completion kit with the strain gauge (R_w). As it is impossible to select identical resistors to compose this Wheatstone bridge (due to certain production tolerances), the bridge is not perfectly balanced when the sensor is undeformed, or also, U_A differs from 0 V while ΔR is still 0 Ω. Therefore it is important to balance the bridge prior to the experiment (not shown in the figure). The shunt resistor R_{sh} is used to calibrate the circuit. By simulating a known resistance variation and noting the output voltage difference, the bridge can be calibrated.

Two types of devices are used to condition the strain gauge signals: a NI 9237 with four channels (balancing, shunting, amplification and data acquisition) and a Vishay 2120B (balancing, shunting and amplification) with a frequency response of 50 kHz and in total 16 channels from Safran Aero Boosters (Figure 2.16). Contrary to the Vishay conditioner, the NI card also samples at maximum 50 kHz. The conditioned output signals from the Vishay 2120B have to be sampled externally, typically at 500 kHz to catch most of the maximum frequency response of 50 kHz (Diehl et al., 1999). Low noise shielded and twisted STP category 6e cables bring the low voltage signals from inside the test chamber to the completion kits via two serial 25-pin D-SUB connectors via an airtight sealing.

More about the data acquisition will follow in the next section.

(a) NI 2937 module (*NI 9237*, 2016).

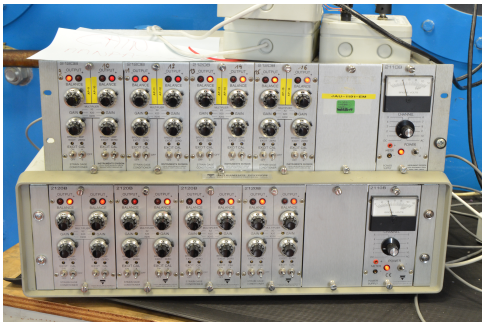

(b) Vishay 2120B.

Figure 2.16: Bridge conditioners.

2.2.2.2 Data acquisition

The main device to record the data is the HBM Gen5i oscilloscope (Figure 2.17). The Gen5i has a modular structure, acquisition cards for different applications can be easily added. It is also equipped with an internal hard disk, WLAN, Gigabit Ethernet and USB for data storage and transport. Defining the recording settings and visualizing the vast amount of data is done with the HBM software Perception.

Figure 2.17: HBM Gen5i oscilloscope.

The following acquisition cards are available in the oscilloscope:

- 1x 4 channels 100 MHz (single-ended) analog input card
- 2x 8 channels 1 MHz analog input cards

- 1x 4 channels 1 MHz ICP analog input card

These cards provide the necessary flexibility to measure all the aforementioned sensors.

2.2.3 Monitoring the test sequence

Every test starts with evacuating the test chamber. In the meanwhile, bird density measurements are performed. An analogue gauge indicates when the absolute pressure reaches approximately 0.2 bar. A pressure versus kinetic energy graph is used (and updated each test) to determine the pressure for the desired impact velocity (for all the tests, and only for the 0.3 kg tests in Figure 2.18).

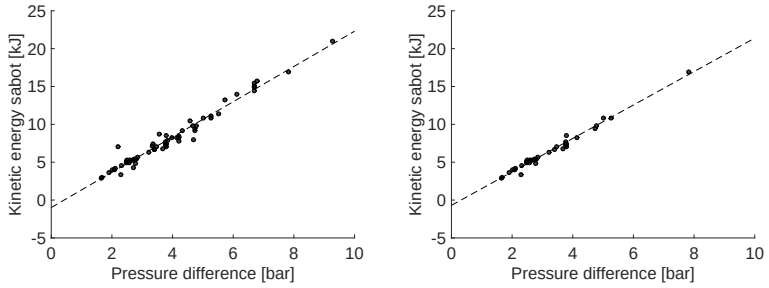

(a) All the tests. **(b)** 0.3 kg tests.

Figure 2.18: Relation pressure - kinetic energy sabot.

The idea is that all the pressure energy is transferred to kinetic energy of the sabot and that the bird maintains the same speed after the stripping process. This would result in a linear relationship, as can be observed in Figure 2.18. The trend for all the tests in function of the pressure respectively corresponds with the following equation:

$$\Delta p = 0.4295 E_{kin,sabot} + 0.4224 \tag{2.6}$$

For the 0.3 kg tests specifically, a more exact fit was obtained:

$$\Delta p = 0.4528 E_{kin,sabot} + 0.3151 \tag{2.7}$$

For higher velocities, these formulations can be extended by assuming adiabatic decompression and including friction. But usually, calibration is still

necessary (Pereira, 2012).

The pressure build-up and release of the trigger mechanism is controlled by a LabVIEW™ program. An analogue NI 9215 DAQ card monitors the pressure inside the vacuum chamber and pressure vessel, while a digital NI 9401 I/O card controls the inlet and outlet valves in the pressure vessel. When the test is initiated, the inlet valve is opened, allowing pressure to build up behind the sabot. When the measured pressure in the pressure vessel exceeds the required pressure by 0.5 bar, all valves are closed. Leak flow along the retaining ring and sabot will slowly lower the measured value. This leak flow has a much lower flow rate than the build-up of pressure in the first stage of the program. This overshoot therefore results in a more precise launch pressure. When the required pressure is reached again, an actuator is switched, dropping the lever and launching the sabot as described in section 2.1.1.

When the signal of the first photo diode drops below 1V, the oscilloscope is triggered, an output trigger is generated by the oscilloscope to the high speed cameras (with a delay of 516 μs, inherent to the oscilloscope) and the data is saved with a certain pretrigger buffer. The triggering and data acquisition is schematically shown in Figure 2.19. This scheme represents a summary of all the measurement devices that are used, but not necessarily simultaneously.

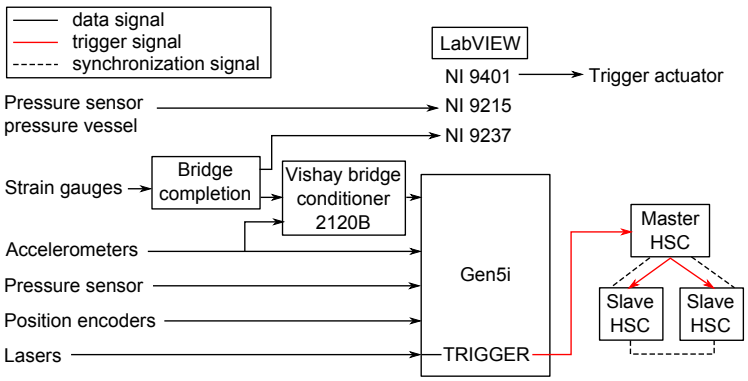

Figure 2.19: Scheme test sequence.

After each test, the weight of the pieces of sabot and bird inside the test and stripper chamber are weighed, photographed and everything is cleaned. Setting up all the DAQ equipment, making a bird and sabot, preparing the target, evacuating the chamber and cleaning can, with up to three people, take up to 10-12 hours.

2.3 Bibliography

ASTM Standard D792-00 (2000), Standard test methods for density and specific gravity (relative density) of plastics by displacement, ASTM International.

Degrieck, J. (2015), 2d line pattern measurement technique. unpublished work.

Diehl, T., Nagaraj, B. and Carroll, D. (1999), 'Using digital processing (DSP) to significantly improve the interpretation of Abaqus/Explicit results', *Abaqus user's conference* .

FTC (2016), 'Gelatine bloom testing', `http://www.foodtechcorp.com/pdf/Gelatine.pdf`. [Online; accessed 14-January-2016].

Guelpa, V., Laurent, G. J., Sandoz, P., Zea, J. G. and Clévy, C. (2014), 'Subpixelic measurement of large 1D displacements: Principle, processing algorithms, performances and software', *Sensors* **14**.

Heimbs, S. (2011), 'Computational methods for bird strike simulations: A review', *Computers & Structures* **89**(23-24), 2093–2112. Munich, Germany.

Kübler LIMES LI50/B2 sensor (2016), `https://www.kuebler.com/english2/prod-sen-linear-LI50.html`. [Online; accessed 16-January-2016].

NI 9237 (2016), `http://www.ni.com/datasheet/pdf/en/ds-58`. [Online; accessed 17-January-2016].

PB Gelatins (2016), 'Gel formation', `http://www.pbgelatins.com/about-gelatin/physical-and-chemical-properties/gel-formation/index.jsp`. [Online; accessed 14-January-2016].

PCB: Basics Sensor Theory (2016), `http://www.pcb.com/techsupport`. [Online; accessed 17-January-2016].

Pereira, J. (2012), An overview of ballistic impact test methods and techniques in aerospace research and development applications, Presented at the ASIDI 2012 conference.

Strain Gage CEA-06-250UN-350 (2016), `http://www.vishaypg.com/docs/11298/250un.pdf`. [Online; accessed 17-January-2016].

CHAPTER 3

Optical measurements for impact testing

Abstract: The very short impact characteristic to bird strike generally results in vibrations and oscillations which proved to impede the use of transducers. Additionally, deriving the kinematics of several set-ups in this work is essential to obtain the necessary information. Therefore, four non-contact optical techniques are used, improved or developed to measure very specific displacements: DIC, 3D shape map measurement and 2D line pattern and 1D line grating techniques. The focus of this chapter lies on the 3D shape map measurement and the 2D line pattern technique developed during this PhD. These optical techniques are used as tool to obtain useful data from target structures during the bird strike tests and can be read almost independently from the following chapters.

3.1 Introduction to optical measurements

An optical measurement technique in this work refers to the acquisition of some measure of displacement and/or strain from subsequent optical images or recordings without coming into contact with the specimen. The advantage above any kind of sensor, especially in ballistic testing, is the fact that it is per definition a non-contact method: no wires that can detach, no triboelectric effect on the wires, no resonance frequencies, electrical current leakage, etc. Also, an image can contain much broader information than a single sensor can.

In this section, first a short introduction to the key parameters in high speed imaging is given. It is not the purpose to give an explanation of the concepts that can also be found in photography (Jacobson et al., 2001), but rather the application of those concepts to high speed imaging, with a nuance on the trade-offs between different settings and a focus on the difficulties seen in bird strike experiments. Secondly, camera calibration will be covered as it is used in the optical techniques described further on. Finally, a short overview of the currently available techniques will be given.

3.1.1 High speed imaging

Similar to photography, in high speed imaging, the goal is to be able to take a series of sharp and bright pictures independent from the situation. This is, as in photography, dependent on several parameters:

Camera (settings) and lens dependent parameters:

- The zoom of the lens
- The focus of the lens
- The diaphragm or aperture of the lens
- The shutter speed of the camera
- The ISO value of the CCD chip
- The frame rate of the camera
- Resolution of the CCD chip and images

Characteristics of the experiment:

- Distance to the object
- Speed of the object
- The amount of illumination
- Characteristics of the surface of the object

The most significant difference with photography, is that the frame rate is much higher. To avoid motion blur, the exposure or shutter time should in general be even several times lower than the time between subsequent frames. As a result of the very short shutter time, the incoming light and therefore contrast is decreased. Because a certain level of contrast is required, multiple measures can be taken:

Add sufficient illumination: Adding more light can only be beneficial to the experiment. Generally diffusive lighting is required instead of specular lighting to avoid reflection and lose contrast. In the experiments, powerful focussed LED-lights are used to illuminate the target. The use of focussed lights is inevitable, because there is a considerable distance between the lighting system and the target in most experiments. Because high deflections of the target can occur during the experiment, the orientation of the surface of the target changes continuously and reflection can become a problem during the experiment.

Open the aperture: Opening the aperture increases the amount of light and decreases the depth of field. Every time the aperture value halves, the light collecting area quadruples. For most experiments, the aperture is only closed a few ticks. As a result, the depth of field is sometimes too small and out-of-focus occurs.

Increase the shutter time: Ideally, a shutter time well beneath 1/50.000 s would be required. For a bird flying at 130 m/s, 1/25.000s corresponds with motion blur over 5.2 mm. Luckily, the velocity of the targets are in general much lower. With the available lighting at the department, a shutter time of 1/50.000s is not possible. For the bird, motion blur therefore is always present.

Use lenses for high speed measurements: Use fast fixed focal length lenses. Lenses are available with a fixed focal length or with a variable focal length. Lenses with a variable focal length provide flexibility, but the amount of light that reaches the CCD chip is reduced significantly.

Increase the ISO value of the CCD chip: The ISO value determines the gain of the CCD sensor. Increasing the ISO value results in an increase of light sensitivity, but also an increase in noise. The ISO values for the available HSCs however, are fixed.

It can be stated that for a given camera and lighting set-up, the aperture together with the shutter speed determines the amount of light captured by the CCD[1]. There is always a trade-off between these two parameters and the achievable contrast. Nevertheless, motion blurring and out-of-focus do occur, which has to be accounted for when choosing or developing an optical measurement technique.

The resolution of the camera determines the spatial resolution and precision of the information that will be extracted from the images. In high speed imaging, the resolution typically reduces with increasing frame rate. This decrease in resolution results in a smaller area of the CCD that is used. With the current high speed cameras, the position of this area can be chosen (the position can be altered in steps of 32 pixels in the horizontal direction for the SA-4 cameras and in both the horizontal and vertical direction for the APX-RS camera, see also section 2.2.1). This means that the centre of the CCD can deviate a lot from the centre of the image, which is a very important fact when calibrating the cameras.

3.1.2 Camera calibration

Calibration of the camera(s) require a camera model. The most basic but well-known model is the thin lens pinhole model (Hecht, 2002). This camera model assumes all light rays to pass linearly through a single point

[1] In photography, ISO is also an important factor. Together with the aperture and the shutter speed it is said to determine the so called exposure triangle.

(infinitesimal aperture). Using this camera model, several transformations can be constructed to relate a point in 3D space defined by the experiment to the 2D image or CCD (Hartley and Zisserman, 2004).

- A coordinate transformation (camera rotation and translation) from the world to the camera coordinate system (6 parameters).
- A central projection on the image plane (1 parameter).
- A 180° rotation of the CCD image.
- A shift of the image to take the location of the reduced resolution image on the CCD into account (1 parameter).
- An iterative process to remove the lens distortions (Lava et al., 2013). For the developed techniques in this work, distortion is not taken into account.

These transformations are also visualized in Figure 3.1.

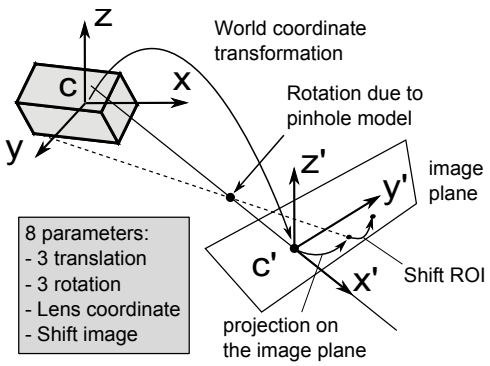

Figure 3.1: Transformations from world to CCD coordinates.

By defining a set of known (calibration) points on the 2D image and in 3D space, the parameters defining these transformations can be found using an iterative optimization method. The sum of the squares of the differences between the world coordinates projected on the image plane, and the corresponding actual image coordinates is used as measure for the quality of a certain set of calibration parameters to guide the optimization procedure.

The entire calibration procedure was solved in Matlab™.

A lot of optimization techniques exist. Essentially, they can be subdivided in local and global techniques. Local optimization starts from an initial guess or also a set of parameters and tries to find the solution starting from this input vector. A global optimization scheme on the other hand tries to examine the entire solution space (in a clever way). In general, local optimization schemes are used for the calibration of the camera. For several reasons explained in future chapters however, global optimization schemes are tested as well.

For the local optimization, a Nelder-Mead algorithm is used. The Nelder-Mead algorithm (Lagarias et al., 1998) is a heuristic algorithm that does not make use of any derivatives. The algorithm starts from an initial simplex[2]. This simplex represents an initial guess of the parameters to be determined. In Matlab™ specifically, the simplex is constructed using the initial guess plus 5 % of each value of the initial guess together with the initial guess itself. During each iterative step, the simplex is modified by means of several operations (*reflection*, *expansion*, *contraction* and *reduction*) in order to move towards the minimum. A Nelder-Mead algorithm was chosen since it proved to be less dependent on the initial guess or simplex than the Levenberg-Marquardt, the conjugate gradiant and the quasi Newton algorithms.

For the global optimization, a genetic algorithm is used. The genetic algorithm (GA) is a global optimization scheme based on the principle of *"survival of the fittest"* (Mitchell, 1996). In a first run (also called *generation*), different sets of random calibration parameters are generated. A parameter set is referred to as an *individual*, and all the individuals together are referred to as the *population*. For each of these parameter sets, the error (referred to as the *fitness*) is calculated. After assigning fitness values to each parameter set in this population, a second generation is created. This is done by picking the best individuals (the individuals with a higher fitness value or lower error have more chance to be chosen) and performing several operations on these individuals (*crossover*, *mutation*, *elitism*, ...). Crossover

[2] A simplex is the n-dimensional equivalent of the triangle in 2D. To construct a simplex in a n-dimensional solution space, n+1 values are therefore needed.

is the most frequently used one where information of two individuals is combined into a new individual (a new set of calibration parameters is created based on the parameters of two well performing sets. It is said that *genetics* are exchanged). Mutation is another operation where for one individual, a certain parameter is randomly changed. Elitism just copies the individual to the next generation. The amount of mutation and elitism is generally low, because mutation often destroys useful genes and elitism tends to let the algorithm converge too fast. After creating the next generation, fitness values are again assigned and everything starts all over again. This generally continues till there is convergence of the best individual, or the mean fitness value is almost the same as the best individual, or a maximum amount of generations have been calculated, or some other criteria.

3.1.3 Available techniques

In the area of non-contact optical displacement and/or strain measurements, a wide range of techniques exists. A very popular set of techniques nowadays calculates full field 3D displacement or rather shape maps (Grédiac, 2013). Except for several methods based on interference or diffraction of coherent or polarized light from a light source or laser (ESPI, holography, etc.), a lot of full field shape map measurement techniques work with a simple projected or applied, structured or randomly distributed pattern of gradients on the specimen. A structured pattern generally consists of one or multiple line gratings, a structured array of dots or other shapes, while a set of randomly shaped speckles is an example of a randomly distributed pattern. A few of the most common full field techniques that use patterns are the following:

- Grid methods (Goldrein et al., 1995; Yang, 1994; Argyriou and Vlachos, 2006; Guelpa et al., 2014): by applying one or multiple line gratings to the specimen, the in-plane deformations, shape and strain maps can be measured, often making use of a local Windowed Fourier Transform, phase stepping or direct phase determination methods. Subpixel accuracy is in general achieved through interpolation or phase correlation.

- Fringe projection or projection moiré (Chen et al., 2005; Gorthi and Rastogi, 2010; Thakur et al., 2007; Zhang et al., 2014; Van Paepegem

et al., 2008): this technique is quite similar to the grid method as it also makes use of a line pattern. The only difference is that the line pattern is projected on the specimen (fringe projection).

- Moiré (Han and Post, 2008; Post and Han, 2008): deflections are measured from the interference of two or more superimposed gratings. Geometric moiré or interferometry moiré can accurately measure in-plane displacements, while shadow moiré can measure out-of-plane displacements.
- Digital Image Correlation or DIC (Sutton et al., 2009; Reu, 2011): this well-known technique makes use of a randomly distributed speckle pattern on the specimen. Multiple subsets of the image are correlated between subsequent images, resulting in displacements. From the change in shape of those subsets, strains can be derived. This technique also makes use of interpolation to achieve subpixel accuracy.

In this work, four techniques are used, from a full field absolute displacement and strain measurement to single point 1-dimensional displacement and strain measurement:

- **DIC**: Digital Image Correlation or DIC is already implemented in many software packages. Therefore, only a brief introduction to the technique will be given.
- **3D shape measurement technique**: a stereo vision technique is developed that is able to calculate 3D shape maps from flat specimens containing a line pattern. The main focus is to enhance the images to some extent, when excessive blurring occurs (see also section 3.1.1). This technique is only able to generate 3D shape maps, no absolute displacement or strain can be derived (Allaeys et al., 2014).
- **2D line pattern measurement**: A new technique developed by (Degrieck, 2015) that is able to do a very accurate local displacement measurement using multiple line gratings. Where most of the current grid methods solely make use of the discrete information obtained from a DFT together with interpolation or correlation techniques to obtain subpixel accuracy, the new approach makes use of a more accurate approach.

- **1D line grating measurement**: Disregarding the fact that also 2D images are used, the processing is done on a 1-dimensional equivalent of each image, which makes it much faster than the 2D line pattern measurement. The displacement (and strain) is calculated in one direction solely from the phase information obtained from a 1-dimensional FFT (Guelpa et al., 2014).

In the following sections, a *line grating* is assumed to be a set of multiple lines or rather sines, with a specific pitch and orientation, while a *line pattern* is the sum of different line gratings present in an image (a sum, to make use of the linearity of the Fourier Transform).

These four techniques will be covered starting from the full-field strain measurement technique (DIC) to the one-directional local displacement measurement (1D measurement technique). The main principles will be covered.

3.2 Digital image correlation

A digital image is essentially a two-dimensional array of intensity values which can be discretized into small subsets. In Digital Image Correlation or DIC, such subsets are matched between an undeformed image and subsequent images as shown in Figure 3.2. A unique signature of each subset is realized by an almost completely random speckle pattern.

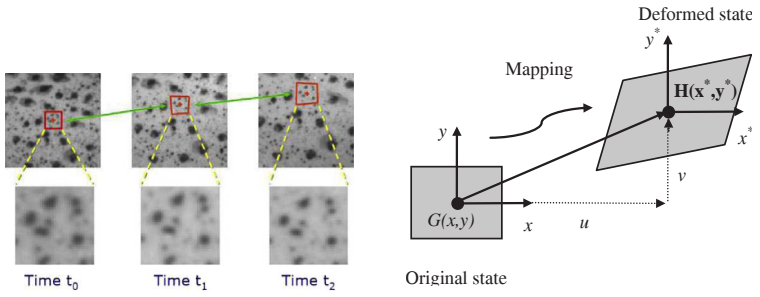

(a) Tracking subsets of the image for DIC (Yates et al., 2010). **(b)** Subset matching (Yates et al., 2010).

Figure 3.2: Concept of digital image correlation.

This is done by means of mathematical mapping and cross correlation functions. For this technique to work well and to achieve a certain level of sub-pixel accuracy, each subset or discrete matrix of grey values is generally fitted with B-splines, bicubic splines or any other interpolation technique (Yates et al., 2010).

The ideal subset size is often a compromise between spatial resolution and accuracy in the case of non-overlapping subsets. As a general rule, larger subset sizes will increase the accuracy whereas a smaller subset will increase the spatial resolution.

In this work, a speckle pattern is applied to a white-painted surface using a technique similar to applying tattoos on paper. The advantage of this technique is that the speckle size can be scaled according to the resolution of the camera (to have an ideal pixels/speckle ratio) and therefore does not require the skill of applying speckles with paint.

The DIC implementation of MatchID™ will be used in chapter 8 as a reference to determine the error of a technique to measure the kinematics of an object.

3.3 3D shape measurement

This technique comprises the calculation of 3D shape maps from specimens during high dynamic events with large displacements, making use of a line grating printed on the specimen. The technique is applied to flat plate experiments. This type of experiment inevitably causes motion blur and out-of-focus to blur parts of the image. An example of motion blur during such an experiment is shown in Figure 3.3. Part of the developed algorithm tries to enhance the images to increase the amount of displacement data retrieved from the calculation.

The line grating is printed on the object. The advantage over shadow moiré and fringe projection techniques is that complete darkness is not required during the experiment. Complete darkness would disturb the other optical recordings and could result in a decrease in contrast.

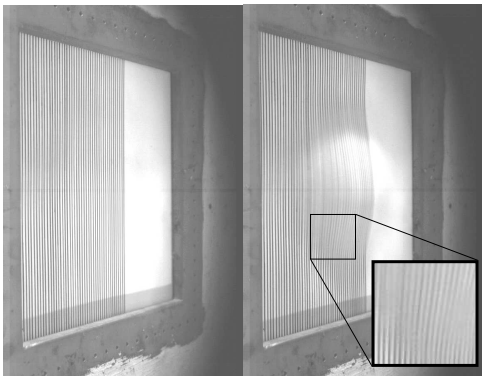

Figure 3.3: Blurring of a line grating on a deforming plate.

In a first step, the cameras are calibrated (briefly covered in section 3.1.2). After that, the images are filtered to finally derive the shape maps. The results of a static verification experiment will be given as well.

3.3.1 Filtering of the line grating

A specific sequence of filters is applied to the images. These filters make it possible to reconstruct lines in blurry regions and ultimately makes it easier to calculate the height maps.

The algorithm to reconstruct the blurry regions is based on the work described in (Hong et al., 1998), who proposed contrast enhancement by means of contextual Gabor filtering for the processing of finger print images. The algorithm determines the orientation and frequency of the lines locally (by dividing the image in blocks) throughout a normalized image after which a pre-stored Gabor filter is applied.

In this study, the algorithm of Hong is modified to facilitate further processing steps. Only in the calculation of the orientation and the frequency of the lines, the image is smoothed by using a Gaussian filter. The Gauss filter eliminates the noise from the image and therefore decreases distortions in the orientation and frequency fields. (Ratha et al., 1995) proposed a method to calculate the orientation map through the gradients, without a singularity at 90 and incorrectly averaged gradients. Therefore the image is first divided

into blocks of w x w pixels after which the orientation is calculated in each block (Equation 3.1).

$$\theta_{block} = \frac{\pi}{2} + \arctan\left(\frac{\sum_{m=-\lceil \frac{w}{2} \rceil}^{\lfloor \frac{w}{2} \rfloor} \sum_{n=-\lceil \frac{w}{2} \rceil}^{\lfloor \frac{w}{2} \rfloor} 2G_x(m,n)G_y(m,n)}{\sum_{m=-\lceil \frac{w}{2} \rceil}^{\lfloor \frac{w}{2} \rfloor} \sum_{n=-\lceil \frac{w}{2} \rceil}^{\lfloor \frac{w}{2} \rfloor} G_x(m,n)^2 - G_y(m,n)^2}\right), \tag{3.1}$$

where G_x and G_y are the gradients which can be calculated using e.g. the Sobel operator. In (Hong et al., 1998), the application of a low-pass Gaussian filter on each block is proposed to eliminate high frequency noise before calculating the orientation. This method did not result in good orientation estimations in the blurry regions (Figure 3.4a). By smoothing the gradient components G_x^2, G_y^2 , and G_xG_y over the entire image, the (pixelwise) orientation calculation (Equation 3.2) proved to be exact in the blurry regions as well, as can be seen in the visualized calculated orientations in Figure 3.4b.

$$\theta(m,n) = \frac{\pi}{2} + \arctan\left(\frac{2G_x(m,n)G_y(m,n)}{G_x(m,n)^2 - G_y(m,n)^2}\right) \tag{3.2}$$

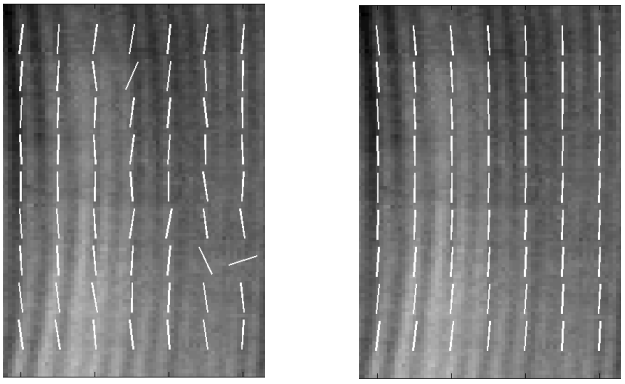

(a) Method from (Hong et al., 1998). **(b)** Proposed pixelwise method.

Figure 3.4: Calculated orientation of a line grating in a blurry region with low contrast.

The method described in (Hong et al., 1998) estimates the line frequency by determining the inverse of the average distance between two consecutive peaks of the x signature (i.e. the summation of the intensities of each

column x of an oriented window). The frequency is assigned to the block corresponding to the rotated window in the image (Figure 3.5).

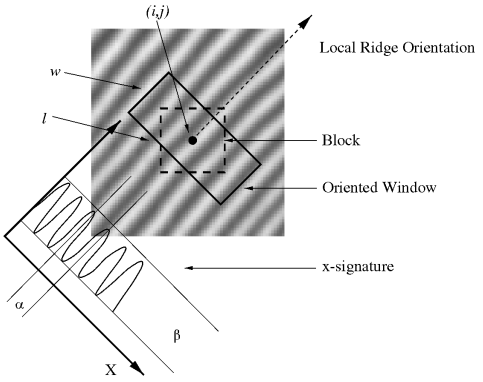

Figure 3.5: Oriented window and x signature.

In order to increase the resolution of the frequency map, the block or region to which the frequency is assigned can optionally be made smaller than the oriented window. In this way the block can be made smaller than the minimum window needed to calculate the frequency. Because the orientation and frequency of the lines is known, an adjusted Gabor filter (without DC component) can be applied. The Fourier transform of a Gabor filter is equal to the sum of two Gaussians centered at $\pm 1/\lambda$, where λ represents the wavelength of the sinusoidal factor. As the standard deviations of these Gaussian functions increase, the tails of the Gaussian functions will start to overlap at the origin, resulting in a non-zero DC component. Subtracting a well-chosen Gaussian function from the Gabor filter in the spatial domain makes it possible to eliminate the DC component and the noise in the image in one single operation. Equation 3.3 shows the adjusted Gabor filter in which the DC component is eliminated in the x direction.

$$n(x,y) = e^{-\pi \frac{x^2+y^2}{\sigma^2}} \cos(2\pi \frac{x}{\lambda}) - be^{-\pi\sigma^2(\frac{1}{\lambda})^2} e^{-\pi \frac{b^2x^2+y^2}{\sigma^2}}, \qquad (3.3)$$

where x and y are the coordinates in a local coordinate system oriented according to the calculated orientation, σ is the standard deviation of the Gaussian envelope and λ is derived from the local line frequency. Figure 3.6 shows the intensities of a pixel line before and after Gabor enhancement, with and without the DC component. At the bottom of the graph a part of

the original image is shown. The pixel line considered in the graph is the one just above the blackened pixel line in the image. The filtered image is an accurate representation of the real grating. At around 80 pixels, severe distortion occurs in the original signal. The Gabor enhancement without DC component completely reconstructs this region and eases further processing of the image.

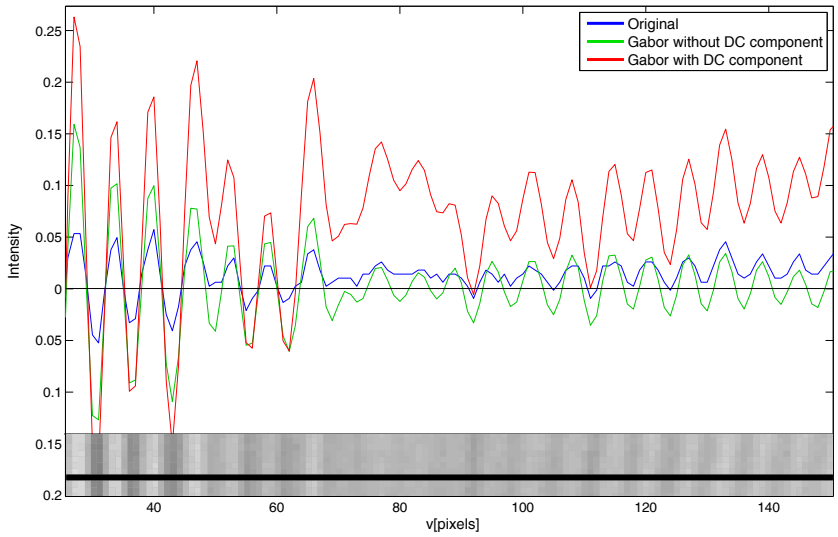

Figure 3.6: Intensities of a pixel line before and after Gabor enhancement.

3.3.2 Wrapped and unwrapped phases

After reducing the noise (high frequency) and background (low frequency) in the original image by means of contextual band-pass filtering, a wrapped phase (between $-\pi$ and π) can be determined. Here, the intensities are transformed to phases. To construct the wrapped phase of the image, all local minima ($-\pi/2$) and maxima ($\pi/2$) are determined. Between these local extrema, the phase in each point is calculated using the intensity of the point and the intensity of the surrounding extrema. In the unreliable regions, where the local amplitude is too small between consecutive extrema, the phase is not determined to make sure no lines are lost when the phases are unwrapped.

Unwrapping the wrapped phase is done by calculating a sum of relative phases to construct an absolute phase. Phase unwrapping is the process of adding correct integral multiples of 2π to each wrapped phase value. Unwrapping makes it possible to uniquely distinguish lines from each other.

The key to reliable phase unwrapping is the ability to accurately detect 2π phase jumps. Noise and discontinuities can result in false phase jumps which necessitates an adequate unwrapping algorithm. For this technique, a quality guided flood fill algorithm was used (Chen et al., 2010). A special buffer guides the algorithm first through the reliable areas. The first value taken from this buffer is the one with the highest local amplitude in the filtered image. Hence, discontinuities in the unwrapped phase map, which are inherent to blurring, only occur in the unreliable areas.

3.3.3 Calculation of the height maps

In case of large deflections, it is necessary to use two cameras for the calculation of the height map. When using only one camera, deflections need to be calculated by estimating the motion of lines. In this case, an assumption has to be made regarding the direction of this motion. When two cameras are available, it is possible to calculate shape maps more accurately by estimating disparities using two images within the same time frame.

3.3.3.1 One camera

When only one camera is used, an assumption has to be made with respect to the direction of the displacements. The most obvious one is to assume that the displacements occur orthogonally to the reference plane (the reference plane is the plane coincident with the plate in its undeformed state or also the direction of impact). Using this assumption, the deflection can be calculated by matching a deformed image with the reference image. Figure 3.7 shows a schematic view of the situation.

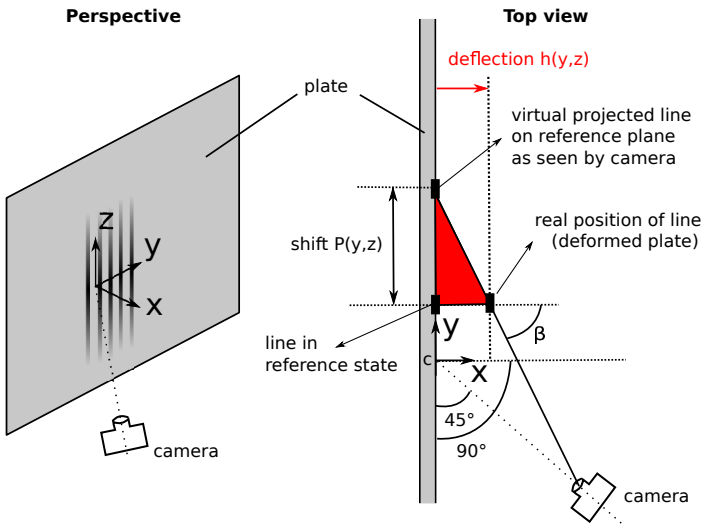

Figure 3.7: Principle shape calculation with one camera.

The relation between the shift of the lines $P(y,z)$, the view angle $\beta(y,z)$ and the deflection $h(y,z)$ is the following:

$$h(y,z) = \frac{P(y,z)}{\tan[\beta(y,z)]} \tag{3.4}$$

3.3.3.2 Stereo vision

Stereo vision allows the construction of deformation maps without using a reference plane. The objective in stereo vision is to match points in one of the images with corresponding points in the other image. Figure 3.8 shows the principle of the stereo vision technique for shape determination based on triangulation, which does not assume epipolar geometry. Consider a point on a line in the first image plane (camera 1). Every point on the corresponding line in the second image plane (camera 2) represents the same point (since nothing is uniquely distinguishable along the line because of the out-of-plane deformation). In order to find the right corresponding point in the second image, for each point on the corresponding line in the second image, a line is constructed from the point to the pinhole (dashed red lines). The point where segment S between the constructed line and the line constructed with the point in the first image (solid red line) is smallest, is assumed to be the corresponding point. The midpoint of the smallest segment is assumed

to hold the correct coordinate of the corresponding points. The line from camera 2 to each pixel in the corresponding picture will mathematically never intersect with the line drawn from camera 1 (none of the dashed lines will ever intersect with the red line).

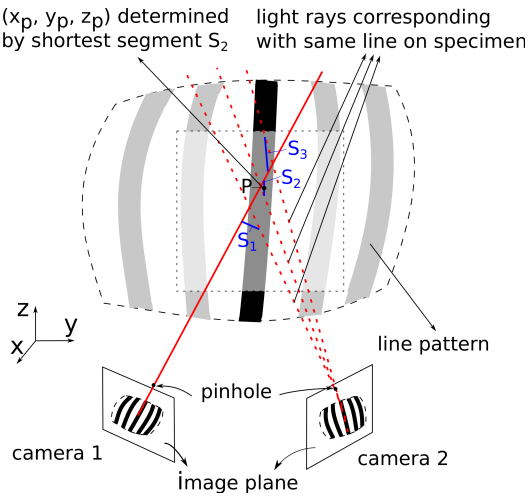

Figure 3.8: Principle shape calculation with two cameras.

To eliminate falsely matched points, the segments should be smaller than 1 mm. In order to minimize the calculation time, the algorithm only calculates the segments in the neighbourhood of the previous matched point instead of calculating the segment of all the possible pixels on the corresponding line.

3.3.4 Static validation experiment

The static calibration set-up shown in Figure 3.9 was used. In this set-up an aluminum strip was bent through a frame and recorded using two cameras, placed at an angle of respectively 32° and 90°. A threaded rod was used to push the aluminium strip through the frame. This rod makes it possible to consider multiple deflections. For each deflection, the shape of the aluminum strip was drawn on graph paper.

Figure 3.10 shows an image of each camera and a top view of the set-up.

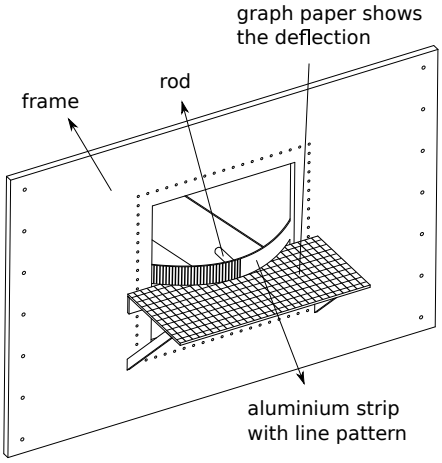

Figure 3.9: Static validation set-up.

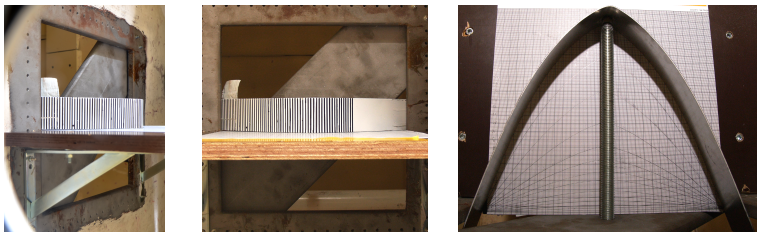

(a) Camera at $32°$. **(b)** Camera at $90°$. **(c)** Top view of the set-up.

Figure 3.10: Image from the camera at $32°$, $90°$ and a top view of the set-up.

3.3.4.1 One camera

In Fig. 11 the deflections calculated by using the images of the 32° camera along the horizon are compared with the curves drawn on graph paper.

When the peak displacement is less than 20 mm, the results are good. Unfortunately, the deflections commonly seen in bird strike tests with supported plates are much larger. Additionally, since the technique makes use of a reference plane in time (the undeformed state of the plate), a shift of the lines in the y-direction (Figure 3.7) due to a real shift or rotation of the plate would add up to $P(y, z)$ and would therefore also be seen as a deflection $h(y, z)$. Since the movement of the lines (in the y-direction) in this experiment at $y = 0$ mm remains close to zero throughout the experiment,

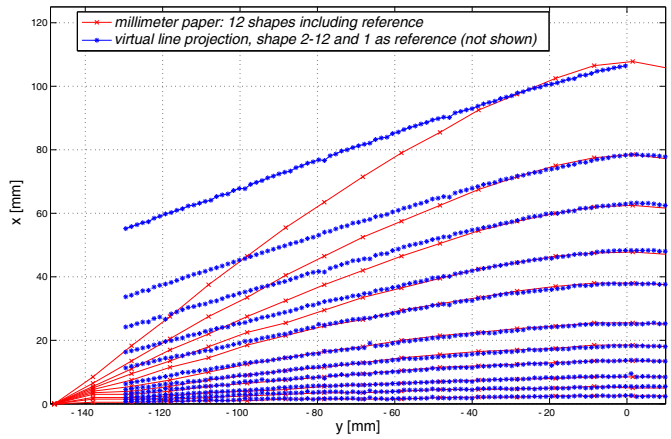

Figure 3.11: Calculated deflection profile using one camera.

the assumption of the orthogonal displacements of the lines is valid and therefore, the calculated deflection is accurate in this point. Close to the edge of the frame, the error is large as a result of the invalid assumption of the orthogonal deflections. It can be concluded that the use of one camera and a line pattern in case of large 3D displacement fields is not recommended.

3.3.4.2 Stereo vision

The calculated shape using the images of 2 cameras agrees well with the experimental evaluation, as can be seen in Figure 3.12. The maximum error is approximately 1 mm, which will be mainly due to the method of recording the actual shape on the graph paper, but also because of the discretization inherent to digital images.

Choosing a large angle between the cameras improves the accuracy of the method, because it reduces the effect of an error in the process. On the contrary, a large angle decreases the range of orientations of the specimen where the deflection can be calculated. At some point, the orientation of the specimen relative to a camera can become so large that there are not enough pixels any longer to differentiate the lines from each other (close to the Nyquist limit). In order to accurately define the maximum intensity of the lines, a minimum resolution is required. Increasing the resolution further minimizes the error due to the discrete representation of the experiment.

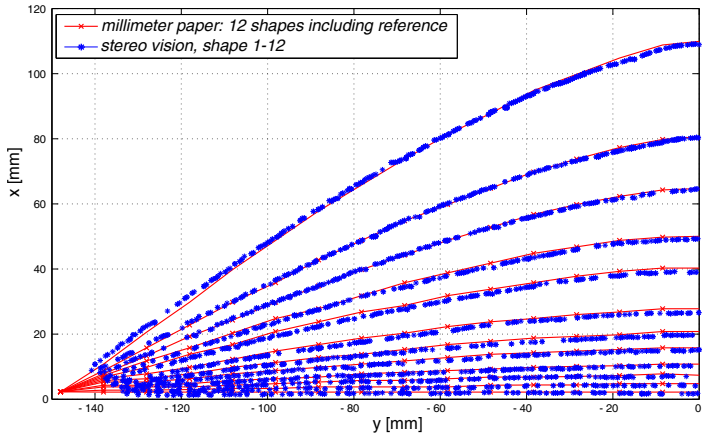

Figure 3.12: Calculated deflection profile using two cameras.

It should be noted that absolute displacements cannot be obtained from multiple shape maps and therefore neither cases of strain nor stress can be calculated. The calculation of absolute displacements is not possible with a line pattern, since it is not uniquely distinguishable in the direction of the lines.

This 3D shape map measurement technique will be used in chapter 7 to calculate the shape of a thin plate during bird impact.

3.4 2D line pattern measurement

3.4.1 The line pattern

Mathematically, the image of a line pattern containing n line gratings, each with a pitch p and an angle relative to the horizontal axis θ_i can be represented by a matrix of intensities G for each pixel position (x, y) by the following equation:

$$G(x,y) = \sum_{i=1}^{n} \cos\left(\frac{2\pi}{p}(x\cos(\theta_i) + y\sin(\theta_i))\right) \tag{3.5}$$

The purpose is to extract information from the movement or deformation of such a line pattern. Depending on the amount of gratings, more information can be extracted:

- **1 line grating:** Only displacement in the direction perpendicular to the lines can be observed. A displacement in the direction of the lines is not visible (as there is no gradient in the direction of the lines).
- **2 line gratings:** To acquire displacements in two directions, at least two non-parallel superimposed line gratings are needed.
- **3 line gratings:** To be able to calculate the two principal strain components, at least three gratings are needed (as well as for other implementations introduced further on).

Therefore, in the remainder of this section, a pattern with three gratings will be considered. Figure 3.13 shows such a (generated) pattern respectively with a $0°$, $+60°$ and $-60°$ orientation. Notice that these angles represent the angle between the gradient direction, i.e. the direction perpendicular to the lines, and the horizontal direction.

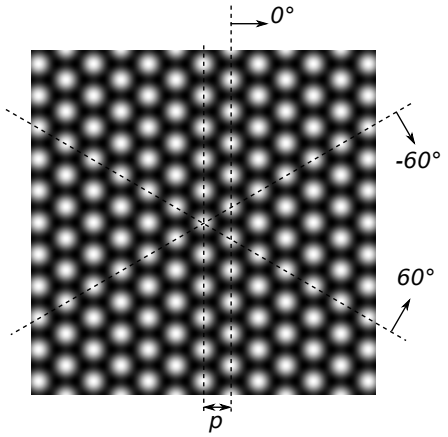

Figure 3.13: Pattern with three line gratings oriented at $0°$, $+60°$ and $-60°$.

3.4.2 Determination of the orientation, pitch and phase

The displacements are derived from the orientation, pitch and phase of the different gratings in the pattern. This information is obtained from

the frequency domain. After applying a circular cosine window, first a two-dimensional Discrete Fourier Transform (DFT) is performed using a Fast Fourier algorithm (FFT). Figure 3.14 shows a zoom of the FFT of the pattern shown in Figure 3.13. Because of the symmetry property of the DFT, each grating is represented as two maxima in the frequency domain. A local maximum search in the frequency domain returns the first six maxima that are of interest (two times three gratings). Each pair of points (located at both sides of the origin) contains the information that is wanted: the orientation of the two dots with respect to the horizontal axis represents the orientation of the lines, the distance to the origin is related to the pitch, and the phase information is directly acquired from the complex amplitude obtained from the FFT. How this discrete information is further refined is omitted in this PhD due to confidentiality.

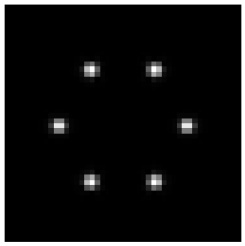

Figure 3.14: Zoom of the two dimensional FFT of the pattern with three line gratings shown in Figure 3.13.

3.4.3 Calculation of the displacements

The phase information is acquired in a wrapped form (between $-\pi/2$ and $\pi/2$) and needs to be unwrapped in order to obtain continuous phase data. Unwrapping adds or subtracts 2π when jumps larger than π are detected between subsequent images. This means that the frame rate should be large enough to keep the phase shift smaller than π between two subsequent images.

After unwrapping, the information of the separate gratings needs to be combined to compute two-dimensional displacement values. A minimum of two non-parallel gratings is needed to calculate these displacements. When

the pattern consists of more than two gratings, redundant information is available. In that case, the displacements can be calculated for each possible pair of gratings and averaged at the end. With n gratings in a pattern, this leads to $(n-1)^2$ displacement values.

For each pair of gratings, the displacement in the direction of the lines is a projection of the actual displacement, as shown in Figure 3.15. For the dark grey and the light grey grating (grating k and l with orientation θ_k and θ_l), the solid lines represent the known displacements of each line set, i.e. the displacement perpendicular to the lines, while the dashed components are unknown (with sizes a and b) because this movement would not result in a change of phase nor orientation of that grating.

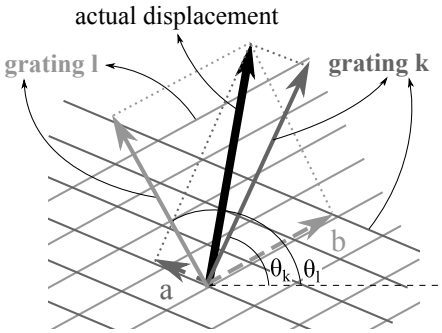

Figure 3.15: The displacement of the line gratings as a projection of the actual displacement.

For each grating, the actual displacement can be written as a sum of the known component (with a known magnitude characterized by the phase φ and the pitch p and a direction characterized by θ) and an unknown component (with an unknown magnitude but a known direction, perpendicular to the known component). Each set of line gratings k and l therefore can be used to write the following complex equilibrium (with $k = 1, .., n$, $l = 1, .., n$ and $k \neq l$):

$$-e^{i\theta_k}\frac{\varphi_k}{2\pi} + a \cdot e^{i(\theta_k+\frac{\pi}{2})} = -e^{i\theta_l}\frac{\varphi_l}{2\pi} + b \cdot e^{i(\theta_l+\frac{\pi}{2})} \tag{3.6}$$

where the unknown magnitude for grating k and l are called a and b respectively. This equilibrium contains two equations: a real and a complex one

and can be used to solve for a and b.

The displacement values are obtained in pixels. When the pattern would be positioned and move perfectly orthogonal to and be intersected in the centre by the optical axis of the camera, the displacement can be converted to physical units by multiplication with the physically measured pitch and dividing by the pitch in pixels. When it is not possible to place the camera in such a way that its optical axis perpendicular to the camera or the displacement is not perpendicular to the optical axis, there are other options to calculate the actual displacement as will be explained in the next section. Because these options can significantly influence the calculated displacements and will be referred to as correction options.

3.4.4 Corrections of the pitch information

Two situations will be covered for which the pitch information is corrected to obtain a more accurate solution. For the first correction option, it is assumed that the pattern moves in-plane or also, parallel to the trajectory (upper case in Figure 3.16). For the second option, the displacement perpendicular to the line of sight is calculated (lower case in Figure 3.16). The line of sight being the ray from the pinhole to the centre of the pattern. Both corrections require the calculation of additional parameters for each image or time step.

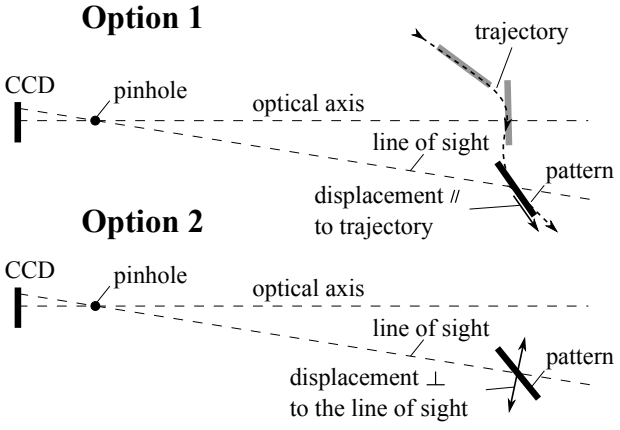

Figure 3.16: Two situations: in-plane displacement (option 1) and displacement perpendicular to the line of sight (option 2).

Both correction options make use of the fact that, for patterns with at least three gratings with the same pitch, the maxima in the frequency domain all coincide on one characteristic ellipse, centred around the origin, with an orientation β of the smallest axis with respect to the horizontal axis and axes sizes f_s for the small axis and f_b for the big axis. The values of these properties depend on the out-of-plane rotation α and movement of the pattern, but not on the in-plane rotation (this is proven in appendix A). For three gratings in the frequency domain, this would look as schematically shown in Figure 3.17. In this figure, the filled dots represent the maxima in the frequency domain for a pattern with three line gratings. As mentioned before, every line grating is represented by two dots and to construct an ellipse, at least three gratings are necessary.

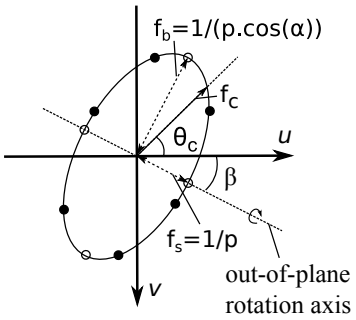

Figure 3.17: Ellipse in the frequency domain.

The smallest axis of the ellipse is oriented along the out-of-plane rotation vector. This is the vector among which the pattern is rotated out-of-plane with respect to the line of sight. The inverse of the magnitude of this axis is equal to the pitch of a (non-existing) line grating that would be perpendicular to the line of sight[3].

The biggest axis of the ellipse is related to the pitch of a (non-existing) line grating that would be aligned with the rotation vector. The orientation of this non-existing line grating therefore has the same out-of-plane rotation α as the pattern itself (schematically shown in Figure A.4).

[3]This is similar to the ellipse obtained from the intersection of a cylinder with a plane, where the smallest axis will always be equal to the diameter of the cylinder.

When the assumption of in-plane displacement can be made (option 1), for each time step, first the direction of the displacement is calculated: θ_c (see Figure 3.17). The fact that the frequency of every line grating with equal pitch should lie on an ellipse can also be used the other way around; the frequency of a pattern in a certain direction θ_c can be acquired from the magnitude of the ellipse at that angle f_c:

$$f_c(\theta_c) = \frac{f_b f_s}{\sqrt{(f_s \cos(\theta_c))^2 + (f_b \sin(\theta_c))^2}} \tag{3.7}$$

As the smallest axis is related to the pitch of a pattern perpendicular to the line of sight, it can be used to correct for the displacement in the direction perpendicular to the line of sight (option 2). The pitch of this axis in pixels is directly related to the actual pitch size of the pattern. It is important to note that the plane perpendicular to the line of sight is not a plane parallel to the CCD, but a plane perpendicular to the line drawn from the tracked pattern to the pinhole of the camera (Figure 3.16).

3.4.5 Further processing of the pitch information

At this point, there are again two options depending on the type of test. As mentioned before, at least three gratings are needed for both options. In the first scenario, the pattern is strained throughout the experiment. Here, the information in the pattern can be used to calculate the three strain components in each time step based on the observed change in pitch for each grating. This will be a mean value over the entire area of the pattern. For this first option, it is very important that the pattern does not rotate out-of-plane as this would mistakenly be recognized as strain because a rotation also influences the observed pitch. In the second scenario, the pattern is assumed to experience only rigid body motion. The information in the grating can then be used to derive the out-of-plane rotation with respect to the line of sight of the camera, the rotation axis as well as the out-of-plane rotation. In the following sections, both options are discussed shortly in more detail.

3.4.5.1 Strain calculation

For each grating n and each time step i, the strain can be calculated directly from the pitch information:

$$\epsilon_{n,i} = \ln(\frac{p_{n,i}}{p_{n,1}}) \tag{3.8}$$

Where $\epsilon_{n,i}$ and $p_{n,i}$ respectively represent the strain and pitch from line grating n at time step i.

When the pattern consists of at least three gratings, enough information is available to calculate (or optimize) the three in-plane strain components ϵ_x, ϵ_y and γ_{xy} using the following relation:

$$\epsilon_x \cos(\theta_{n,i})^2 + \epsilon_y \sin(\theta_{n,i})^2 + \gamma_{xy} \cos(\theta_{n,i}) \sin(\theta_{n,i}) = \epsilon_{n,i} \tag{3.9}$$

x and y being the pixel directions. For a perfect image (generated with Matlab™) with roughly 20 lines and 10 pixels/pitch, the strain resolution for the current implementation is roughly 10 microstrain.

3.4.5.2 Out-of-plane orientation

The second option is the calculation of out-of-plane rotation and can be used in case of rigid body motion. The calculation of the out-of-plane rotation is based on information explained in the corrections section. The rotation axis (around which the pattern is rotated out-of-plane) is equal to orientation of the smallest axis β. The out-of-plane rotation α about the rotation axis can be calculated using both axes of the characteristic ellipse:

$$\alpha = \arccos(\frac{f_s}{f_b}) \tag{3.10}$$

3.4.6 Error quantification

To validate the developed algorithm and to obtain some measure of the accuracy of the method, a known displacement and rotation is applied to a pattern and recorded using two AVT Stingray F201B cameras, with a resolution of 1628x1236 pixels and a pixel size of 4.4 μm. The known displacements and rotations are imposed using a combination of a URB100CC

rotation stage with an absolute accuracy of $0.2° \pm 0.1$ mounted on top of a PM500 translation stage with a resolution of $0.05\,\mu$m. The translation stage is mounted on a vibration isolated table. A picture of the set-up is depicted in Figure 3.18.

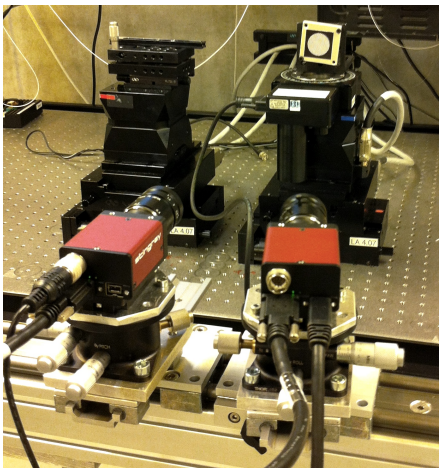

Figure 3.18: Error quantification set-up with translation and rotation stage.

A 1.6 mm pitch pattern with three line gratings at 0°, -60° and 60° is used. The pattern is printed on sticker paper using a professional laser printer. This print process is a first error source. Measuring the absolute value of the pitch of a pattern consisting of a continuously varying grey value is not obvious. Therefore, the relative difference between the three pitches in the pattern is evaluated. This is done by taking a high resolution picture of the pattern (as orthogonal to the pattern as possible) and extracting the pitch information using the developed software.

The laser jet printer from the department can print patterns with an accuracy of 0.1-0.3% (highest relative difference between the three pitches), while the patterns printed by Vanhalst reach 0.02-0.16% (for relatively large patterns). The pattern used to quantify the error on the translation and rotation stage has an error 0.03-0.04%.

In the following sections, first the conclusions of the processing of a series of static images will be discussed (to determine the minimum achievable resolution). After that, the results of 6 experiments will be covered:

- Translation: big step ($100 \times 0.7\,\text{mm}$)
- Translation: small steps ($60 \times 1\,\mu\text{m}$)
- Curved in-plane displacement ($100 \times 0.2°$)
- Rotation in-plane ($30 \times 2°$)
- Rotation out-of-plane ($20 \times 2°$)

Depending on the situation, different combinations of the PM500 translation stage and the URB100CC rotation stage are used. Both stages contain an encoder. Every displacement or rotation is compared to the encoder value in a closed loop. The movement of these stages should therefore be correct within the given accuracy.

3.4.6.1 Displacement and in- and out-of-plane rotation resolution

In Figure 3.19, the noise level of the pitch in pixels and the displacement corresponding with this pitch noise in microns can be observed. These are obtained from 99 static images. There is a relatively large error between the lowest and the largest pitch compared to the one measured before the tests (0.19% compared to 0.03%). This can be the result of perspective. The noise of the displacement is independent of the relative error between the pitches. A peak-to-peak value of roughly $4\,\mu\text{m}$ can be observed.
The noise level in the pitch is roughly 0.005 pixels, which in theory should correspond with $0.005/22.5 \times 1600\,\mu\text{m} = 0.36\,\mu\text{m}$. The worst combination of pitches to derive the displacement however can double this error (see Figure 3.20). Together with a displacement in the other direction, a ptp noise value of $1.08\,\mu\text{m}$ is obtained. This explains most of the noise. It seems however, that there should be another error source as well, because the displacement rises up to $3\,\mu\text{m}$.
In Figure 3.21, the in-plane orientation of the first grating and the out-of-plane rotation is shown for the 99 static images. The in-plane and out-of-plane rotation have a ptp noise floor of respectively 0.005° and 0.2°.

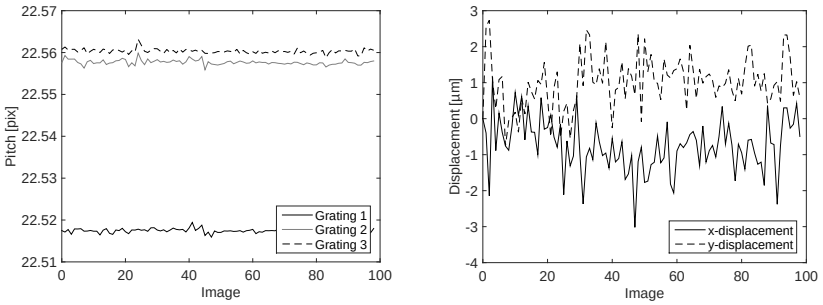

(a) Pitch. **(b)** Displacement.

Figure 3.19: Pitch and displacement for 99 static images.

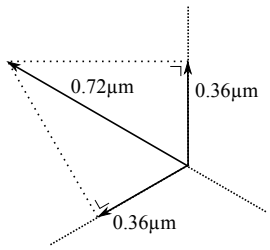

Figure 3.20: Combination of pitch noise increases noise level displacements.

The in-plane rotation is very accurate. The out-of-plane rotation as well, but this likely will be dependent on the absolute out-of-plane angle. The mean value of the out-of-plane rotation is relatively high because the pattern is positioned on the left side of the image (away from the centre).

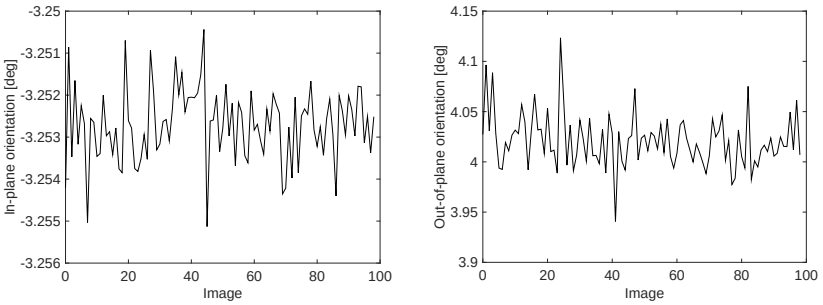

(a) In-plane orientation. **(b)** Out-of-plane rotation.

Figure 3.21: In-plane orientation and out-of-plane rotation for 99 static images.

3.4.6.2 Translation

The translation experiments are processed with and without in-plane correction of the pitch (see also section 3.4.4). Steps just beneath half the pitch are used in the translation experiment with big steps ($100 \times 0.7\,\text{mm}$). Throughout the experiment, the translation stage onto which the pattern is mounted moves from the left to the right of the image. Figure 3.22 shows the start frame, an intermediate frame and the last frame of the experiment.

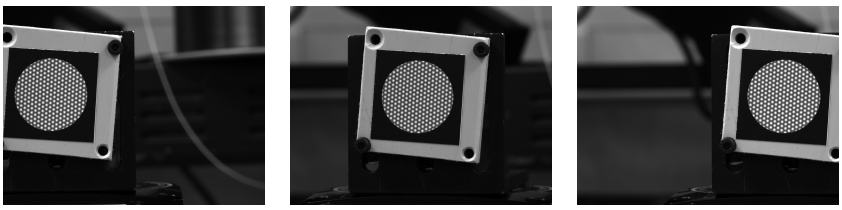

(a) First frame. **(b)** Intermediate frame. **(c)** Last frame.

Figure 3.22: The first, intermediate and last frame of the translation experiment with big steps.

Throughout the experiment, the pattern moves from a perspective to a more or less aligned pattern (perpendicular to the angle of view) and again to a perspective. This effect can be observed in the pitch (Figure 3.23). The pitches are lower at the beginning and the end of the experiment and the relative difference between the pitches is the smallest halfway the experiment.

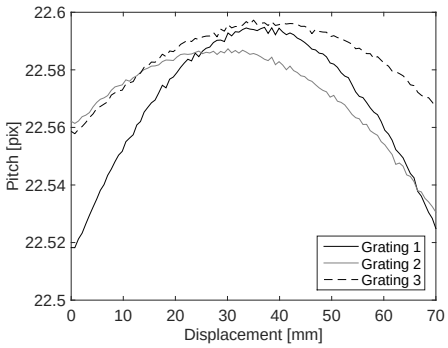

Figure 3.23: The effect of the perspective on the pitch.

The errors on the calculated displacement are shown in Figure 3.24. The noise on the experiment has significantly increased (from 3 to 4 μm in the

static images to 25 μm in the experiment starting, from 30 mm displacement). Disregarding the noise, the calculated displacement is overestimated. The in-plane correction results an error reduction from 0.3% to 0.1%. A smaller pattern compared to the image size would improve the results, because now the perspective is still averaged out over a relatively large area (the pattern diameter is represented in roughly 1/3 of the width of the image).

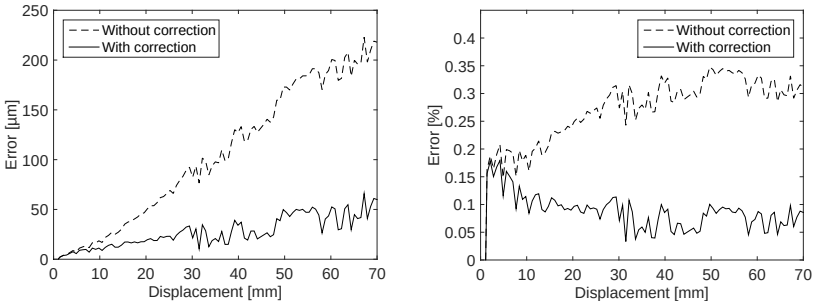

(a) Absolute error. **(b)** Relative error.

Figure 3.24: Absolute and relative error translation experiment with big steps.

The sizes of the frequency axes of the ellipse, the correction of the pitch and the constant pitch from the original implementation without correction are shown for each image in Figure 3.25. Naturally, the big axis is always bigger than the small axis and the correction always lies between the big and the small axis. In the middle of the experiment, the ellipse has changed to a shape closer to a circle (the two axes of the ellipse differ less) in comparison with the beginning and the end. Also, the frequency calculated by the correction option is closer towards the big frequency axis at the beginning and at the end. Some discontinuities can be found at image number 20. This is the result of how the frequency is calculated.

The goal of the translation experiment with small steps ($60 \times 1\,\mu$m) is to evaluate the performance on sub-pixel level. From the 22.6 pixels pitch (Figure 3.23), it can be derived that a pixel in the image corresponds to 71 μm on the pattern. The absolute and relative error is shown in Figure 3.26.

Remarkably, a noise level beneath the one from the static images is obtained. A ptp error value of 3 μm can be observed, which oscillates periodically during translation with a period of approximately $15 - 20\,\mu$m. A sub-pixel

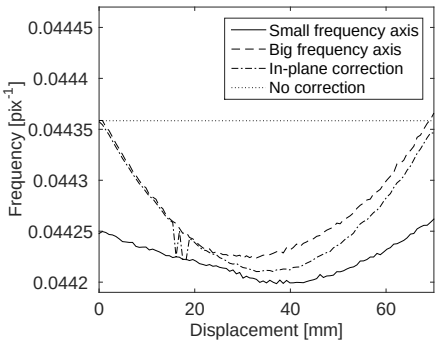

Figure 3.25: The size of the frequency axes, the assumed pitch frequency without correction and the pitch in the direction of displacement (in-plane correction).

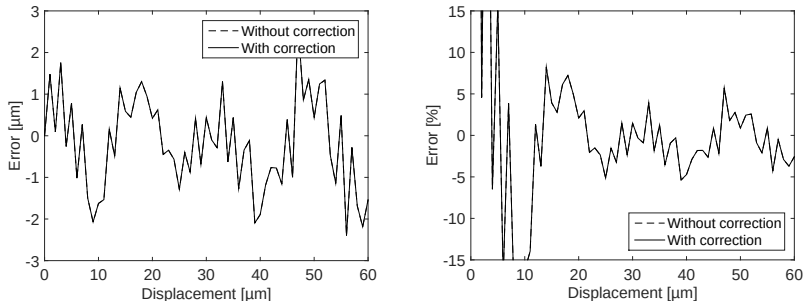

(a) Absolute error. **(b)** Relative error.

Figure 3.26: Absolute and relative error translation experiment with small steps.

displacement accuracy can be achieved within -5% to 5% accuracy with the considered set-up.

The performance of the in-plane correction option can be investigated using a more extreme set-up where the pattern moves tangential to a curved path. A spherical path is created using the rotation stage in combination with an aluminium accessory that holds the pattern 150 mm away from the rotation axis (Figure 3.27). A rotation of $100 \times 0.2°$ is applied, which corresponds to a total angle of 20° and an in-plane displacement of 52.36 mm (in-plane on a circular path).

The errors with and without correction are shown in Figure 3.28.

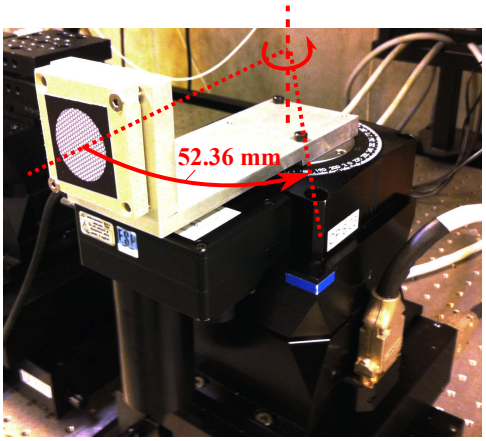

Figure 3.27: The rotation stage with an accessory to move the pattern in a spherical path.

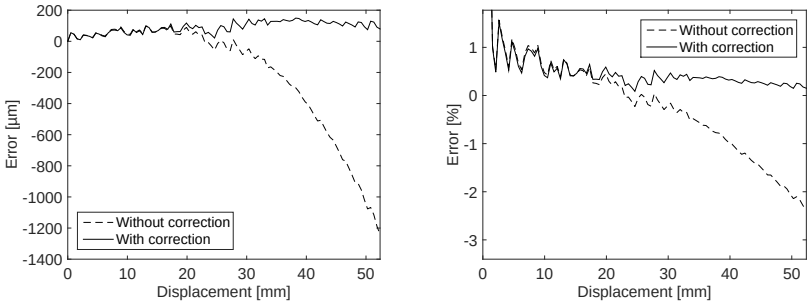

(a) Absolute error. **(b)** Relative error.

Figure 3.28: Absolute and relative error in-plane translation experiment.

The error is still significant even with correction (150 μm). Possibly the error reduces for smaller steps (a better approximation of the spherical path). Compared to the scenario without correction, for the entire displacement, the error is reduced from 2.29% to 0.18%.

The small axis of the ellipse is equal to the frequency of a pattern that is orthogonal to the line of sight. Together with the focal length and the pixel size, the frequency can be translated to an absolute out-of-plane coordinate. The determination of the focal length can be derived from the current calibration algorithms in commercial DIC codes. These algorithms

however are not able to determine the focal length sufficiently accurate. The optimization of the calibration parameters do not provide absolute parameters, but rather a set of parameters that fits the transformations (as in an underdetermined system of equations). The out-of-plane displacement is therefore not further investigated.

3.4.6.3 In-Plane rotation

For the in-plane rotation experiment, the pattern is moved over 60° (the angle between two line gratings) in 30 steps. An advantage in this experiment is that the in-plane rotation should be independent of the accuracy of the pitch. For rotation measurements, a standard laser jet printer therefore can be used. The absolute error in degrees and the error relative to actual rotation is shown in Figure 3.29.

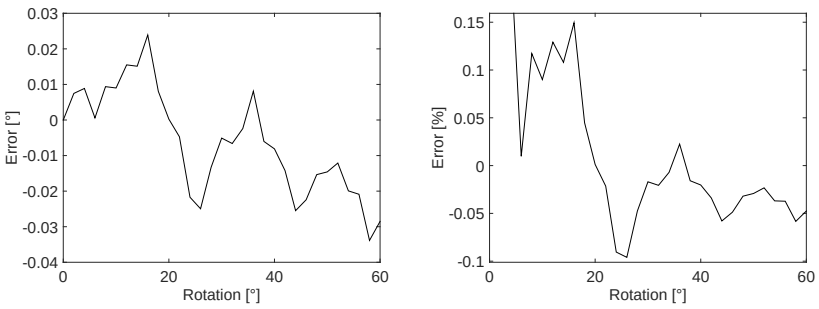

(a) Absolute error. **(b)** Relative error.

Figure 3.29: Absolute and relative error in-plane rotation experiment.

Rotation angles are determined within 0.06°, which is quite accurate. The rotation stage theoretically has an accuracy of 0.1°. So the results might even improve with a more accurate rotation stage.

3.4.6.4 Out-of-plane orientation

For the out-of-plane rotation, the pattern is positioned orthogonal to the line of sight as good as possible. After that, out-of-plane rotation is imposed in 20 steps of 2° (rotation about an axis that initially coincides with the pattern). The absolute and relative error is shown in Figure 3.30.

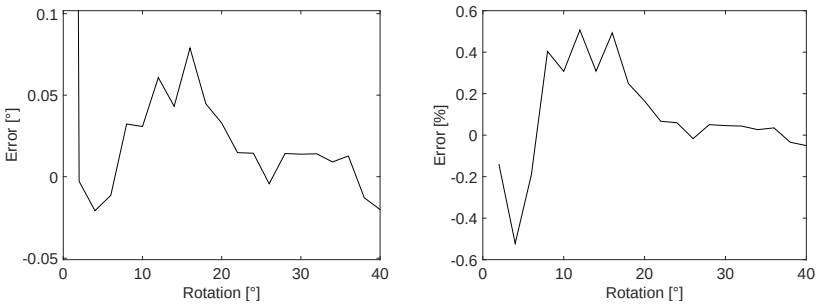

(a) Absolute error. **(b)** Relative error.

Figure 3.30: Absolute and relative error out-of-plane rotation experiment.

It can be seen that the orientation can be determined quite well for the large rotations. For the last step for example (40°), the error is 0.02° or 0.05%.

The error at 0° is 2.2°. After the first step, the error reduces to a maximum of 0.08°. This first error will always be present due to two reasons. First of all, it is not possible to exactly position the camera orthogonal to the pattern. There will always be some misalignment. The influence of this misalignment will be the biggest at 0°. But there is another error source which likely has a bigger influence. A very accurate pattern is required to achieve a more or less correct initial angle as shown in Figure 3.31, where the out-of-plane rotation error in function of the accuracy of the pitch of the pattern is plotted.

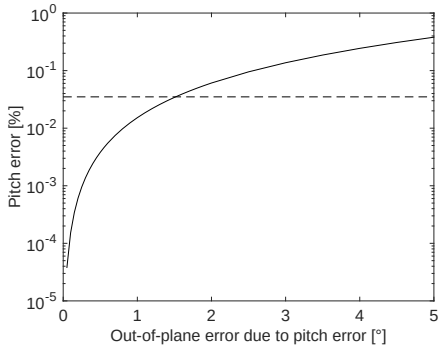

Figure 3.31: Out-of-plane rotation error in function of the accuracy of the (pitch of the) pattern.

The dashed line shows the relative pitch error of the pattern used in this experiment. The solid line represents the out-of-plane angle that would be calculated if the same error would exist on the two axes of the ellipse in the frequency domain. To achieve an out-of-plane angle error of maximum 0.5° in the initial position for example, the error of the pitches should be reduced to approximately 0.004%.

The 2D line pattern measurement technique will be used in chapter 8 to retrieve the kinematics of a certain object.

3.5 1D line grating measurement

The method described in this section is similar to the method described by (Guelpa et al., 2014). In contrast with the 2D line pattern measurement, only one line grating is used (Figure 3.32 shows such a pattern that was used in the experiments).

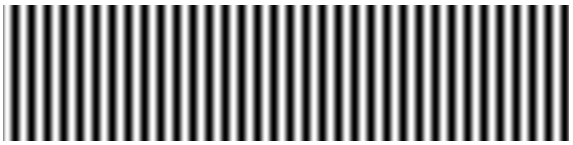

Figure 3.32: 1D line grating used in the experiments.

During processing, each image is first reduced to a 1-dimensional equivalent by averaging the intensity values in the direction of the lines (rather the closest pixel direction). In a second step, a second degree polynomial is fitted to the intensity values. This polynomial is then subtracted from the intensity values. To avoid any high frequencies in the frequency spectrum, the length of the signal is cut to an exact multitude of the pitch of the grating. Next, similar to the previous technique, a squared sine window function is applied on the shortened signal. This prepared signal now undergoes a 1-dimensional FFT routine, from which the phase information is used directly. This makes it much faster than the previous method. Only phases perpendicular to the lines will be measured, a minor misalignment of the pixel direction with respect to the direction of the lines therefore would not cause problems. A single dominant peak is observable in the power

spectrum. At this spatial frequency maximum, the phase is extracted. This process is repeated for every frame recorded by the camera and results in the phase as a function of time. Unwrapping is performed (see also section 3.3). Finally, the phase is converted to displacement by multiplication with $p/2\pi$. This way, a continuous displacement measurement is achieved, which can be differentiated to obtain velocity, and once again to obtain the acceleration.

The 1D line grating measurement technique will be used in chapter 5 to retrieve the translational velocity of the rigid target structures.

3.6 Bibliography

Allaeys, F., Luyckx, G., Sarrazin, C., Van Paepegem, W., Jovanov, L. and Philips, W. (2014), 'A 3D shape measurement technique that makes use of a printed line pattern', *Experimental Mechanics* **54**(6), 999–1009.

Argyriou, V. and Vlachos, T. (2006), 'A study of sub-pixel motion estimation using phase correlation', *British Machine Vision Conference* .

Chen, K., Xi, J., Yu, Y. and Chicharo, J. F. (2010), 'Fast quality-guided flood-fill phase unwrapping algorithm for three-dimensional fringe pattern profilometry', *Optical Metrology and Inspection for Industrial Applications* pp. 1–9.

Chen, L., Quan, C., Tay, C. J. and Fu, Y. (2005), 'Shape measurement using one frame projected sawtooth fringe pattern', *Optics Communications* **246**(46), 275–284.

Degrieck, J. (2015), 2d line pattern measurement technique. unpublished work.

Goldrein, H. T., Palmer, S. J. P. and Huntley, J. M. (1995), 'Automated fine grid technique for measurement of large-strain deformation maps', *Optics and Lasers in Engineering* **23**(5), 305–318.

Gorthi, S. S. and Rastogi, P. (2010), 'Fringe projection techniques: Whither we are?', *Optics and Lasers in Engineering* **48**(2), 133–140.

Grédiac, M. (2013), Identification from full-field measurements: a promising perspective in experimental mechanics, *in* T. Proulx, ed., 'Application of Imaging Techniques to Mechanics of Materials and Structures, Volume 4', Conference Proceedings of the Society for Experimental Mechanics Series, Springer New York, pp. 1–6.

Guelpa, V., Laurent, G. J., Sandoz, P., Zea, J. G. and Clévy, C. (2014), 'Subpixelic measurement of large 1D displacements: Principle, processing algorithms, performances and software', *Sensors* **14**.

Han, B. and Post, D. (2008), *Geometric Moiré*, Springer US, chapter 21, pp. 601–626.

Hartley, R. I. and Zisserman, A. (2004), *Multiple View Geometry in Computer Vision*, second edn, Cambridge University Press.

Hecht, E. (2002), *Optics*, Addison-Wesley.

Hong, L., Wan, Y. and Jain, A. (1998), 'Fingerprint image enhancement: algorithm and performance evaluation', *Pattern Analysis and Machine Intelligence, IEEE Transactions on* **20**(8), 777–789.

Jacobson, R. E., Axford, N., Ray, S. and Attridge, G. G. (2001), *Manual of Photography: Photographic and Digital Imaging*, 9th edn, Butterworth-Heinemann, Newton, MA, USA.

Lagarias, J. C., Reeds, J. A., Wright, M. H. and Wright, P. E. (1998), 'Convergence properties of the Nelder–Mead simplex method in low dimensions', *SIAM Journal on Optimization* **9**(1), 112–147.

Lava, P., Paepegem, W. V., Coppieters, S., Baere, I. D., Wang, Y. and Debruyne, D. (2013), 'Impact of lens distortions on strain measurements obtained with 2D digital image correlation', *Optics and Lasers in Engineering* **51**(5), 576 – 584.

Mitchell, M. (1996), *An Introduction to Genetic Algorithms*, MIT Press, Cambridge, MA, USA.

Post, D. and Han, B. (2008), *Moiré Interferometry*, Springer US, chapter 22, pp. 627–654.

Ratha, N. K., Chen, S. and Jain, A. K. (1995), 'Adaptive flow orientation-based feature extraction in fingerprint images', *Pattern Recognition* **28**(11), 1657 – 1672.

Reu, P. L. (2011), 'Experimental and numerical methods for exact subpixel shifting', *Experimental Mechanics* **51**(4), 443–452.

Sutton, M. A., Orteu, J.-J. and Schreier, H. (2009), *Image Correlation for Shape, Motion and Deformation Measurements: Basic Concepts,Theory and Applications*, Springer Publishing Company, Incorporated.

Thakur, M., Quan, C. and Tay, C. J. (2007), 'Surface profiling using fringe projection technique based on Lau effect', *Optics & Laser Technology* **39**(3), 453–459.

Van Paepegem, W., Shulev, A., Moentjens, A., Harizanova, J., Degrieck, J. and Sainov, V. (2008), 'Use of projection Moiré for measuring the instantaneous out-of-plane deflections of composite plates subject to bird strike', *Optics and Lasers in Engineering* **46**(7), 527–534.

Yang, I. H. (1994), 'Analysis of 3D shape and strain distributions of a deformable object using stereo vision', *KSME Journal* **8**(2), 107–114.

Yates, J., Zanganeh, M. and Tai, Y. (2010), 'Quantifying crack tip displacement fields with DIC', *Engineering Fracture Mechanics* **77**(11), 2063 – 2076.

Zhang, Q., Hou, Z., Wang, X. and Li, X. (2014), Dynamic 3D shape measurement based on grating projection and Fourier fringe analysis, Vol. 9276.

CHAPTER 4

Bird modelling: shock and steady state regimes

Abstract: The impact of a bird on a structure can, in the first place, be characterized by the pressure exerted on that structure. Also in literature, the first step towards bird strike modelling is therefore often the investigation of these impact pressures. This chapter starts with an introduction to bird modelling after which the results of a detailed study on the numerical bird pressures during impact will be presented, including (i) the shock regime with its shock and release waves, (ii) the steady state regime, (iii) the elastic energy during the shock regime and (iv) the influence of target deformability on the shock regime. Analytical models will be introduced and a comparison with the numerical models will be made. Finally, the analytical values and numerical studies are compared to a series of experimental impact pressure measurements.

4.1 Shock propagation in fluids

As introduced in section 1.1.4, the internal stresses of the bird material exceed the material strength to a large extent during bird strike. As a result, the bird shows fluid-like behaviour and several aspects from fluid dynamics can be applied to bird strike.

In this section, first some aspects of shock propagation in fluids relevant to bird strike will be covered. This will be mainly based on the work of Wilbeck (Wilbeck, 1978*a*,*b*; Wilbeck and Rand, 1981) and will remain the basis for the rest of the chapter. In this introduction, the target is assumed rigid.

4.1.1 Shock regime

In bird strike research, the shock regime is generally introduced with an impact of a flat cylinder, which produces a very characteristic shocked state through time. Figure 4.1 shows four stages of the shock regime. Point (a) shows the cylinder before impact, flying at the so-called particle speed v_p. The instantaneous stop of the material at the front of the bird results in a high pressure called the shock or Hugoniot pressure (b). This shocked region starts to propagate through the material in the form of a shock wave, with a speed equal to v_s. Since the edges of the cylinder are not confined, the pressure pushes the material outwards, which results in a decrease in pressure. A pressure release wave is formed that travels inwards (b up to d), with a speed of v_r which is higher than v_s. At (c), when the release wave reaches the centre axis of the projectile, the pressure at the surface of the target is not subjected to the shock pressure any more. The time between the start of the shock (b) and the end of the shock pressure at the target (c) is therefore also termed the shock duration. At point (d), the release wave has caught up with the shock wave. From this point on, a pressure wave continues to travel through the bird and the impact steadily changes to a steady state regime. The pressure in the projectile during the steady state regime is much lower (indicated by the transparent grey color).
To derive the shock pressure at impact, a 1-dimensional equilibrium can be written over the shock front. With a reference system fixed in space (Figure 4.2), the material on the right of the shock wave (region 2) has a speed equal to zero (the material is stopped by the rigid target), and the material on the

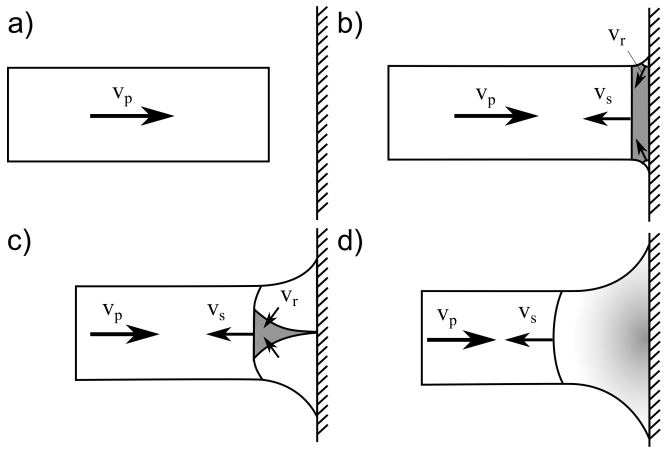

Figure 4.1: The four stages showing the shock propagation in a flat cylinder.

left (region 1), has a speed equal to the undisturbed material and therefore flows at the initial impact or particle velocity v_p.

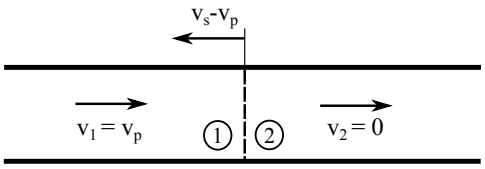

Figure 4.2: 1-dimensional representation of a shock wave, with a reference fixed in space.

A fundamental characteristic is the fact that for materials such as water and gelatine, for low particle velocities such as the ones in this work, a linear relationship exists between the shock velocity and the particle velocity:

$$v_s = c_0 + s \cdot v_p \tag{4.1}$$

In this equation, c_0 represents the adiabatic speed of sound and s the slope of the linear relationship.

The conservation of mass and momentum can be applied over the shock wave, assuming non-viscous adiabatic flow. In order to write the equilibrium, a reference system fixed to the shock wave needs to be defined to acquire a "steady state" scenario (figure 4.3).

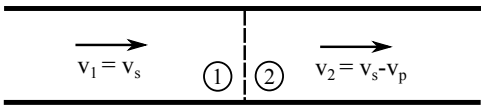

Figure 4.3: 1-dimensional representation of a shock wave, with a reference fixed to the shock wave.

This results in the following equations:

$$\rho_1 v_s = \rho_2 (v_s - v_p) \tag{4.2}$$

$$P_1 + \rho_1 v_s^2 = P_2 + \rho_2 (v_s - v_p)^2 \tag{4.3}$$

Where P and ρ are respectively the pressure and the density in the medium. From the combination of these equations, the pressure rise can be calculated, also referred to as the shock or Hugoniot pressure P_H:

$$P_H = P_2 - P_1 = \rho_1 v_s v_p = \rho_1 (c_0 + s v_p) v_p \tag{4.4}$$

In fluid dynamics, this shock or Hugoniot pressure is also referred to as the water-hammer pressure (Field, 1999).

The release waves travel at the shocked speed of sound v_r, which is higher than the speed of sound because of the non-linearity of the relationship between P and ρ (introduced later on):

$$v_r = \sqrt{\left.\frac{dP}{d\rho}\right|_{P_H}} \tag{4.5}$$

The shock duration T_s where the central axis of the projectile meets the target, for a cylinder with flat ends, can be calculated with the radius r and the shocked speed of sound v_r:

$$T_s = r / v_r \tag{4.6}$$

4.1.2 Steady state regime

After several reflections, the shock wave will disappear as it dissipates energy and converts to kinetic energy. A steady state flow regime forms. The

pressure at the target, at the position of the central axis of the projectile is derived from Bernouilli's equation, assuming negligible shearing forces:

$$\int_{P_0}^{(P_S+P_0)} \frac{dP}{\rho} = \frac{v_0^2}{2} \tag{4.7}$$

with P_S and P_0 respectively the steady state and ambient pressure. For an incompressible flow the steady state pressure can be calculated as follows:

$$P_S = \frac{1}{2}\rho v_p^2 \tag{4.8}$$

Two expressions have been developed that describe the radial pressure distribution on the target, starting from the stagnation pressure in the centre to zero somewhere outside the radius of the cylinder. The first one is represented by equation 4.9 (Banks and Chandrasekhara, 1963) and the second one by equation 4.10 (Leach et al., 1966):

$$P = \frac{1}{2}\rho v_p^2 e^{-\zeta_1(\frac{r}{a})^2} \tag{4.9}$$

$$P = \frac{1}{2}\rho v_p^2 (1 - 3(\frac{r}{\zeta_2 a})^2 + (\frac{r}{\zeta_2 a})^3) \tag{4.10}$$

with r the radial distance from the centre, a the initial radius of the cylinder and $\zeta_1 = 0.5$ and $\zeta_2 = 2.58$ derived from the momentum equilibrium.

A lot of research has been done in the 20th century to acquire pressure signals, including shock and steady state regime (Barber et al., 1975; Wilbeck, 1978*a*,*b*; Wilbeck and Rand, 1981; Challita and Barber, 1979; Challita and West, 1980; Challita, 1980). Performing a pressure measurement along the central axis of the bird gives a very characteristic signal. The typical shape of such a signal is shown in Figure 4.4. It includes a very short but high shock pressure followed by a much lower steady state pressure.

4.1.3 Influence of the shape and tilting

Wilbeck also considered the influence of a tilt angle on the shock wave. He stated that for a flat cylinder, beneath a critical angle ϕ_{crit} between the flat front face and the impact surface (Figure 4.5a), the shock phenomenon

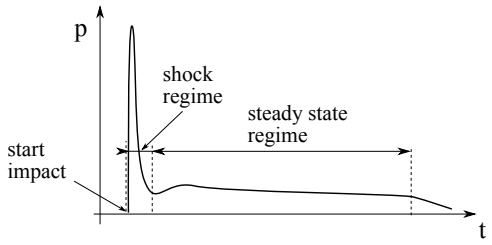

Figure 4.4: A typical pressure signal for bird strike.

would be exactly the same as for the parallel case. And above this angle, no shock would exist at all. For an angle higher than the critical angle, when point a reaches the target, the shock wave initiated at point a would reach b before point b reaches point c and the shock wave would be vented because of the ambient pressure. This critical angle is therefore equal to $\arcsin(v_0/v_s)$. Only a short pressure peak would be created at the first point that touches the target (at the edge of the cylinder).

From this critical angle, the duration of the pressure peak can also be calculated for projectiles with hemispherical ends:

$$t = \frac{r(1 - \cos(\phi_{cr}))}{v_p} + \frac{r \sin(\phi_{cr})}{v_r} \tag{4.11}$$

Where the first part is the time needed for the bird to reach the critical position where the release waves can start to travel inwards, and the second part is the time that the release waves need to travel from the side to the centre of the bird.

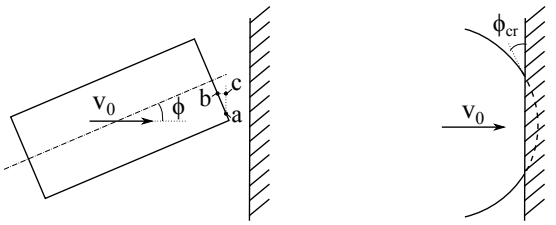

(a) Impact of a tilted flat cylinder. **(b)** Shock waves for hemispherical ends.

Figure 4.5: Impact for non-parallel surfaces.

The analytical models introduced in this chapter and in the next chapters are derived from the continuum equations, making some assumptions or adding some empirical solution. These models have been verified by experiments extensively in previous research. And also in this work, the analytical models are validated with a number of experiments. In the numerical simulations discussed further on, comparisons are made with these analytical models, assuming that they are valid in the considered cases.

4.2 Numerical modelling of bird strike

4.2.1 Finite Element Method (FEM)

The Finite Element Method or FEM is a widely used technique in engineering for solving partial differential equations (PDEs) representing structural, mechanical, heat transfer and fluid dynamics problems, which cannot analytically be solved any more due to their complex geometries, boundary conditions in space and time and/or non-linear material behaviour (Tadmor, 2012). The key principle of the FEM is the discretization of the problem domain in a finite amount of elements (1-dimensional line elements, polygons (2D) or polyhedrons (3D)) that locally approximate the PDE. By creating a combination of such fundamental elements, it is possible to represent very complex geometries. The collection of elements is referred to as the mesh, which has to be dense enough to accurately represent the physics locally but not too dense to keep it computationally feasible. For a transient impact problem such as a bird strike, the PDE to be solved is a dynamic equilibrium containing inertia and internal and external forces which has to be progressively evaluated over time using an explicit time integration scheme. The explicit time integration scheme requires a sufficiently small time increment to achieve a stable solution. In general, the time increment is equal to the element with the smallest characteristic length divided by the dilatational wave speed. Information therefore does not travel faster than one element per time increment. An extensive description of how the explicit FEM works, can be found in literature (Wu and Gu, 2012).

Abaqus/Explicit™ has a quite comprehensive implementation of the explicit FEM combined with the necessary closely related techniques introduced

further on. This software package was therefore used for all the numerical simulations performed in this work. Because Abaqus™ had fundamental updates over the course of this PhD, all the simulations are re-executed with the latest available version, being Abaqus 6.14™. Since the scalability of SPH in Abaqus™ (the use of multiple CPUs) still exhibits some flaws (incorrect recording of the artificial dissipation) and element history output is not supported for multiple CPUs, all the simulations are executed with a single CPU.

4.2.2 Numerical methods for highly deforming matter

As stated in the previous section, the FEM makes use of a discretization of the problem domain in small elements. Several modelling techniques however exist to describe the continuum. Figure 4.6 introduces four techniques: the standard Lagrangian, the Eulerian, the Arbitrary Lagrangian-Eulerian and the Smoothed Particle Hydrodynamics.

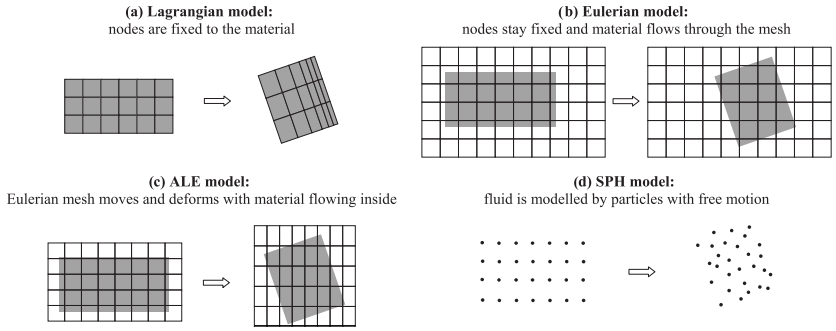

Figure 4.6: Different finite element modelling methods for soft body projectiles (Heimbs, 2011).

Two fundamentally different approaches are the Lagrangian and Eulerian description. In the **Lagrangian** formulation, the mesh moves with the material and there is no mass flow between the elements. In the **Eulerian** formulation on the other hand, the mesh stays fixed in space, and the material flows through the mesh (see Figure 4.6). Contrary to the Lagrangian

method, the time derivative therefore also contains a convective term (the time derivative of the position vector x is not zero):

$$\frac{df(\mathbf{x},t)}{dt} = \frac{\partial f}{\partial \mathbf{x}}\frac{\partial \mathbf{x}}{\partial t} + \frac{\partial f}{\partial t} = \nabla f.\mathbf{v} + \frac{\partial f}{\partial t} \tag{4.12}$$

where d/dt and $\partial/\partial t$ are respectively the total or material and partial derivatives of an arbitrary function f. The boundary of a Lagrangian mesh corresponds with the boundary of the material, while for the Eulerian mesh, only the element volume fractions are known and additional algorithms are required to create the boundary of the object, based on some assumption.

The implementation of the Eulerian formulation in Abaqus™ is essentially an expansion of the Lagrangian method. For each time step, a Lagrangian step is performed first, after which the solution of the distorted mesh is mapped back on the original Eulerian mesh in an advection step, assuming a linear distribution of each variable in each old element (*Abaqus 6.14 documentation*, 2014; Benson, 1992). The implementation of the Eulerian method in Abaqus™ is called **Coupled Eulerean-Lagrangian** or CEL, because it is mostly used in combination with structural parts represented by a Lagrangian mesh to study fluid-structure interaction or FSI problems.

A well known criticism of the standard Lagrangian method is that without the use of special techniques such as rezoning or distortion control, large deformations result in a greatly distorted mesh with therefore an increased computation time due to the decreasing minimum characteristic length and often a breakdown of the simulation. Defragmentation would also require element deletion to be able to separate fragments, which can lead to a decrease in mass while mass determines the force (more about the momentum or force in the next chapter). The Eulerian formulation on the other hand handles large deformations very well but because the mesh is fixed in space, the Eulerian mesh needs to cover the entire domain where mass potentially may flow. This can increase the mesh size and therefore also memory significantly. Additionally, it is difficult to track the time history of field variables.

In theory, every implementation in between the Lagrangian and Eulerian formulation, i.e. movement of the mesh in space and material flow through

the elements, is called an **Arbitrary Eulerean-Lagrangian** or ALE formulation (Benson, 1992; Donea et al., 2004). This can be, as shown in Figure 4.6, a moving mesh that encloses the entire part and adapts for its deformation. But also, the boundary of the mesh that coincides with the material boundary. ALE tries to grasp the advantage of both methods: avoid distorted meshes and reduce mesh sizes.

Smoothed particle hydrodynamics or SPH is a continuum meshfree Lagrangian method that can easily simulate highly deformed matter with defragmentation (Monaghan, 1992; Liu and Liu, 2003). In SPH, the object is represented by a cloud of particles. In contrast to what the word particle might suggest, there is no physical colliding of particles. The material properties of a particle are not discretely defined in each point but rather spatially smoothened in the neighbourhood of the particle by a smoothing kernel, where the influence radius is characterized by the smoothing length. It is a meshfree particle method (MPM) in that sense that there is no fixed connection between the nodes or elements and the set of influencing neighbouring elements therefore typically change throughout the simulation. It is a Lagrangian method because it is based on the Lagrangian equations of motion, each particle has a mass bound to it and therefore the material moves with the mesh of particles (there is no mass flow between elements). Because of its clear advantages above the standard Lagrangian and Eulerian techniques for simulating highly deforming matter, SPH was mainly used to simulate the bird throughout this work. A basic form of its governing equations will be covered briefly in the next section. The purpose however is not to investigate or improve SPH and its shortcomings (consistency, instability, zero energy modes).

4.2.3 Smoothed Particle Hydrodynamics (SPH)

Smoothed particle hydrodynamics is a method developed by Lucy in 1977 (Lucy, 1977). It was initially used for astrophysical problems but later on expanded to continuum solid and fluid mechanics. SPH is generally a spatial discretization of the continuum equations. To derive the spatial discretization, first the particle approximation of the integral representation of an arbitrary function is constructed as explained in the next section. The

integral representation is done using a smoothing kernel, which is further explained in section 4.2.3.2 (Liu and Liu, 2003).

4.2.3.1 Particle approximation of the integral representation of a function

Each particle is characterised by its mass and position in a time-dependent simulation:

$$(m_j(t), \mathbf{x}_j(t))_{j \in P} \tag{4.13}$$

Where P is the set of particles (j=1..N), $m_j(t)$ is the mass of particle j at time t and $\mathbf{x}_j(t)$ is the position of particle j at time t.

The whole concept of SPH is built on the integral representation of a function:

$$f(\mathbf{x}) = \int_\Omega f(\mathbf{x}').\delta(\mathbf{x} - \mathbf{x}', h)d\mathbf{x}' \tag{4.14}$$

Ω being the entire domain where $f(\mathbf{x})$ is defined and continuous. In a first step, the Dirac function is replaced by a smoothing function $W(\mathbf{x} - \mathbf{x}', h)$:

$$f(\mathbf{x}) \approx \int_\Omega f(\mathbf{x}').W(\mathbf{x} - \mathbf{x}', h)d\mathbf{x}' \tag{4.15}$$

where W is the so-called smoothing/kernel function, defined by a smoothing length h. W is zero outside its so-called support domain. Ω is therefore reduced to the support domain. The evaluation of the function f is now dependent on the neighbourhood and therefore not exact any more. This expression is also referred to as the kernel approximation. In figure 4.7, a smoothing function W is shown, centred at particle i. Depending on the amount of spatial dimensions, the kernel used in the integral representation is 1-dimensional, 2-dimensional or 3-dimensional.
The second step is called the particle approximation in which the integral approximation is discretized over the particles in the integration domain. First the infinitely small volume dx' is replaced by the finite volume ΔV_j which is related to the particle mass m_j through the density ρ_j:

$$m_j = \Delta V_j.\rho_j \tag{4.16}$$

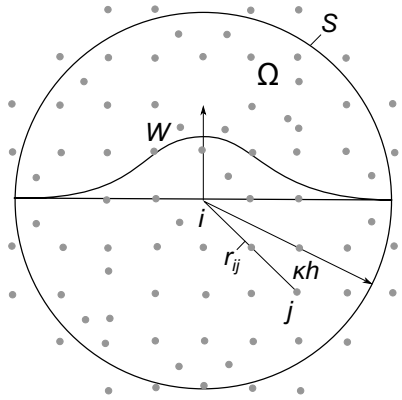

Figure 4.7: The smoothing/kernel function (Liu and Liu, 2003).

The discretization of the integral results in the particle approximation:

$$\begin{aligned} f(\mathbf{x}) &\approx \int_{\Omega} f(\mathbf{x'}).W(\mathbf{x}-\mathbf{x}',h)d\mathbf{x}' \\ &\approx \sum_{j=1}^{N} f(\mathbf{x}_j).W(\mathbf{x}-\mathbf{x}_j,h).\Delta V_j \\ &= \sum_{j=1}^{N} f(\mathbf{x}_j).W(\mathbf{x}-\mathbf{x}_j,h).\frac{\rho_j}{\rho_j}.\Delta V_j \\ &= \sum_{j=1}^{N} .\frac{m_j}{\rho_j}.f(\mathbf{x}_j).W(\mathbf{x}-\mathbf{x}_j,h) \end{aligned} \tag{4.17}$$

For particle i the particle approximation can be written as

$$f(\mathbf{x}_i) \approx \sum_{j=1}^{N} .\frac{m_j}{\rho_j}.f(\mathbf{x}_j).W_{ij} \tag{4.18}$$

Where

$$W_{ij} = W(\mathbf{x}_i - \mathbf{x}_j, h) \tag{4.19}$$

The particle approximation of the integral representation of the derivative of a field function can be constructed similarly and results in the following function:

$$f(\mathbf{x}_i) \approx -\sum_{j=1}^{N} \frac{m_j}{\rho_j} f(\mathbf{x}_j) \bigtriangledown W_{ij} \tag{4.20}$$

Where

$$\bigtriangledown_i W_{ij} = \frac{\mathbf{x}_i - \mathbf{x}_j}{r_{ij}} \frac{\partial W_{ij}}{\partial r_{ij}} = \frac{\mathbf{x}_{ij}}{r_{ij}} \frac{\partial W_{ij}}{\partial r_{ij}} \tag{4.21}$$

4.2.3.2 Smoothing kernel function

The smoothing kernel is defined over a domain called the support domain. The support domain of a field point $\mathbf{x}$=(x,y,z) is the domain around $\mathbf{x}$ that exerts an influence on point $\mathbf{x}$. The smoothing kernel determines the accuracy of the function approximation and the efficiency of the computation. Many kernels can be constructed but all need to posses the following properties:

1. The smoothing function must be normalized over its support domain:

$$\int_{\Omega} W(\mathbf{x} - \mathbf{x}', h) d\mathbf{x}' = 1 \tag{4.22}$$

2. There is a compact support domain for the smoothing function:

$$W(\mathbf{x} - \mathbf{x}', h) = 0, for \mid \mathbf{x} - \mathbf{x}' \mid > \kappa h \tag{4.23}$$

   The dimension of the compact support domain is defined by the smoothing length h and a scaling factor κ, where κ defines the spread of the specified smoothing function.

3. $W(\mathbf{x} - \mathbf{x}', h) \geq 0$ in each point $\mathbf{x}$' within the support domain. This is strictly not a condition for the kernel, but necessary to achieve physically meaningful (stable) results.

4. The smoothing value should be monotonically decreasing with increasing distance from the particle.

5. The kernel function should be approaching the Dirac delta function, when the smoothing length approaches zero:

$$\lim_{h \to 0} W(\mathbf{x} - \mathbf{x}', h) = \delta(\mathbf{x} - \mathbf{x}') \tag{4.24}$$

   This expression shows that convergence in theory should be possible, as the integral representation with the Dirac function is exact. Practically, a smoothing kernel close to 0 is computationally impossible.

6. The smoothing function should be an even function.

7. The smoothing function should be sufficiently smooth.

Many different kinds of smoothing functions can be constructed. Some frequently used functions are: the Gaussian kernel, the cubic, quartic and quintic spline kernels, the quadratic (which is often used for highly dynamic impact analysis) kernel function, etc. Abaqus 6.14™ supports the cubic, quintic and quadratic kernel. By default the cubic spline kernel also known as the B-spline is used, as devised by Monaghan and Lattanzio:

$$W(R,h) = \alpha_d \times \begin{cases} \frac{2}{3} - R^2 + \frac{1}{2}R^3 & 0 \leq R < 1 \\ \frac{1}{6}(2-R)^3 & 1 \leq R < 2 \\ 0 & R \geq 2 \end{cases} \tag{4.25}$$

For a one-, two- and three-dimensional space the factor α_d is respectively $1/h$, $15/7\pi h^2$ and $3/2\pi h^3$. In Abaqus™ however, only 3D kernels are implemented. The initial smoothing length is calculated to have 30 to 50 particles at the start of the analyses and remains constant throughout the analysis (by default). For a structured 3D mesh, this would mean that the support domain has a radius equal to 2 to 2.25 times the mesh size.

The basic equations of fluid dynamics or Navier-Stokes equations are based on the three fundamental physical laws of conservation: conservation of mass, momentum and energy. A complete derivation of the Navier-Stokes equations based on the particle approximation can be found in literature (Liu and Liu, 2003). The total stress tensor σ in these equations is split up in a hydrostatic pressure part p and a deviatoric component τ:

$$\sigma_{ij} = -p\delta_{ij} + \tau_{ij} \tag{4.26}$$

where

$$p = -\frac{1}{3}\sigma_{kk} \tag{4.27}$$

4.2.3.3 Artificial viscosity

Shock waves can take the shape of a discontinuous surface of a shock wave travelling through a medium. Neither the Navier-Stokes equations or a FEM however can represent such a discrete discontinuity. Therefore, in the FEM but also in the closely related techniques such as SPH, an additional artificial term is added to the hydrostatic pressure, termed the artificial or bulk viscosity. Artificial viscosity was first introduced by Neumann and Richtmyer in 1950. They proposed a term proportional to $\nabla.\mathbf{v}$ and $(\nabla.\mathbf{v})^2$ (VonNeumann and Richtmyer, 1950). $\nabla.\mathbf{v}$ represents the divergence of the velocity or also, the volumetric strain rate. Monaghan developed a similar term for SPH, based on the relative velocities between surrounding particles (proportional or squared), dependent on the smoothing length (Monaghan and Gingold, 1983; Monaghan, 1989). Artificial viscosity based on the volumetric strain rate has been proposed as well for SPH (Hernquist and Katz, 1989; Liu and Liu, 2003). In Abaqus™, the linear and quadratic bulk viscosity is also based on the volumetric strain rate (*Abaqus 6.14 documentation*, 2014).

The purpose of the quadratic term is to smear out the shock front over multiple elements and in the meanwhile provide some mechanism of dissipation. Physically, the shock wave dissipates kinetic energy into heat (Liu and Liu, 2003). The linear term damps out further the oscillations that occur close to the shock wave.

The artificial or bulk viscosity is an important parameter to consider, because by default it dissipates too much energy in the SPH simulations (more about the influence of the artificial viscosity in the next chapters).

4.2.3.4 Generating a particle mesh

Because Abaqus 6.14™ does not support the pre-processing of particle meshes, several scripts were written to automatically generate the node and element list of the desired shape to insert into the input file. The scripts are able to

fill a volume representing a flat cylinder or a cylinder with hemispherical ends with a structured mesh.

To simulate the tests, meshes can be generated according to the shape of the moulds as well. To get the exact mass, a small offset can be given to the considered shape. Sometimes however, the shape of the bird in the experiments differs significantly from the mould shape. Therefore, a procedure was also written to create a mesh more conform to the shape in the experiments by generating a mesh based on the contour of the bird drawn in a 2D CAD environment (using the high speed images).

4.2.3.5 Residual momentum and energy of the bird

To obtain the residual momentum and energy of the bird after an impact event, which is needed to verify several analytical models introduced in the next chapters, the speed of the bird after impact $\overrightarrow{v_{b,2}}$ needs to be known. For the simulations, a script is written that calculates the momentum from the velocity vector of each separate particle. Because SPH is a Lagrangian technique, there is no mass diffusion between the elements and the material stays fixed with respect to the particle motion. Structured meshes are used in this work, the particle mass therefore can be calculated directly from the density and the characteristic volume corresponding to the mesh size.

4.2.4 Contact definitions

4.2.4.1 Kinematic versus penalty contact

While the standard Lagrangian FEM is generally used to model structures, several techniques such as the Eulerian method or SPH exist to model fluids. The algorithms of both structure and fluid can differ significantly. To model interaction between those two, some sort of coupling is needed. For the contact of SPH in Abaqus™, particles behave as spheres with radii equal to half of the characteristic length. For a structured mesh, the characteristic length is equal to the mesh size (*Abaqus 6.14 documentation*, 2014). Two approaches can be distinguished: kinematic and penalty contact (Kirtil et al., 2003). The principles are schematically shown in Figure 4.8.
The kinematic contact definition generates a contact force based on the predicted penetration depth, the mass and the time increment. As a result,

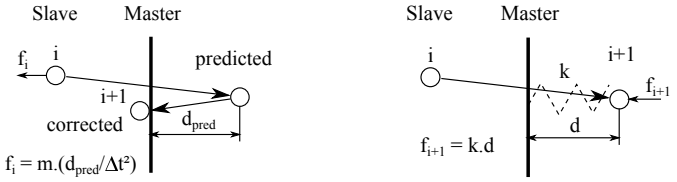

(a) Kinematic contact. **(b)** Penalty contact.

Figure 4.8: Penalty and kinematic contact (Kirtil et al., 2003).

no penetration occurs at the end of each time step. The kinematic contact definition consumes kinetic energy in the form of external work (Kirtil et al., 2003). An iterative approach can be used to account for the movement of the master surface (Attaway et al., 1994). Penalty contact allows small penetrations in order to generate contact forces. A virtual spring creates a contact force linear with the penetration depth. In the Abaqus™ general contact definition which is adopted in this work, penalty contact is used by default. The pressures in the particles of an impacting SPH mesh are therefore not used directly to calculate the contact pressure, but the force increases with the depth of penetration. So the question is rather, does the contact pressure represent the exact pressure in the particles? When the SPH mesh is too coarse for example, discrete contact pressures can be measured after which the pressure in the particle starts to rise with a certain delay.

4.2.4.2 Contact pressures in Abaqus™ for SPH

The impact of particles on the target surface is very discrete in time. Because of the way contact is enforced, a particle does not necessarily stay into contact as would be the case for an actual continuum. Contact therefore can result in several force peaks through time. To have a realistic continuous representation of the contact force on an element level, therefore many particles per element surface are needed ($\sim$ 100 particles per element). For a high amount of particles, a correct, continuous contact pressure is then obtained from the summation of several short pressure peaks.

Important to know is that contact forces in Abaqus™ are stored in the nodes. This means that when a particle hits an element, the induced force is divided

to the surrounding nodes. Simulations showed that the division of the force occurs linearly (Figure 4.9).

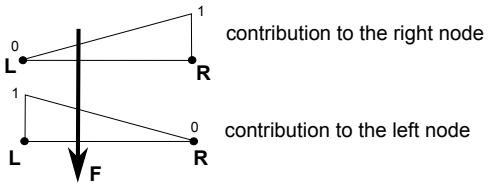

Figure 4.9: Linear contribution of the contact force to the surrounding nodes.

This also means that element contact output is influenced by contact forces of surrounding elements. The best representation of the contact force locally can therefore be achieved via nodal output. This can be achieved by requesting CFN (contact force normal) output of a nodal surface, which is only possible directly via the input file. CFORCE (contact force) does the same but can only be requested for the entire model (which could result in very large output databases or ODBs). CPRESS (contact pressure) is equal to CFORCE divided by the area that the node represents and can also only be requested for the entire model. CAREA (contact area) is a variable that calculates the actual area of the surface that comes into contact (sometimes a fraction of the total area for which the output is requested). CAREA is meant to be used together with CFN, defined over the same surface. Figure 4.10 shows three situations of a structured mesh, where CFN is the sum of all the nodal contact forces (the blue area, including the boundary), while CAREA should be slightly larger to account for the contribution of contact forces of the surrounding elements. CAREA however does not always capture the contact surface well. Internal communication learned that CAREA was not intended to measure a subset of the whole surface that comes into contact, contrary to what is stated in the manual (*Abaqus 6.14 documentation*, 2014; Simulia, n.d.).

4.2.5 Constitutive behaviour

4.2.5.1 Pressure part: The equation of state (EOS)

To be able to solve the conservation of energy equation, a relationship between the pressure, the density and the internal energy needs to be defined. An equation of state (EOS) is such a relationship that relates the

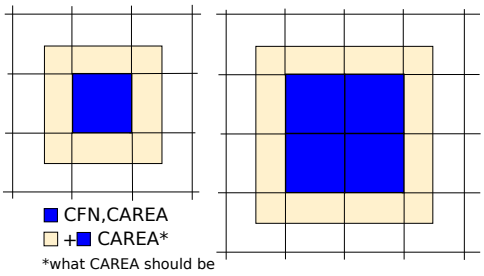

Figure 4.10: CFN and CAREA element contact output in Abaqus 6.14™.

density and internal energy to the pressure, generally based on some physical assumptions. The contribution of internal energy in the EOS is often ignored in bird strike simulations. In that case, the EOS can be seen as the relation between the volumetric strain and the pressure. The volumetric strain can be defined by the logarithmic volumetric strain ϵ_{vol}, but also by nominal volumetric strains η and μ:

$$\epsilon_{vol} = \ln(\frac{\rho_0}{\rho}); \quad \eta = 1 - \frac{\rho_0}{\rho}; \quad \mu = \frac{\rho}{\rho_0} - 1 \tag{4.28}$$

When the volumetric strain is relatively small (which is the case for nearly incompressible fluids), the three definitions η, μ and ϵ_{vol} are equivalent.

The following EOSs were used in bird strike simulations so far:

- **Mie-Grüneisen**: The linear Mie-Grüneisen EOS is partly based on the linear relationship between the shock and post-shock velocity or also, the linear Hugoniot (Equation 4.1) (Ward, 2011). This behaviour has also been observed for water (Wilbeck, 1978*b*). The first order Mie-Grüneisen EOS which is implemented in Abaqus™ is defined by the following equation:

$$p = \frac{\rho_0 c_0^2 \eta}{(1 - s\eta)^2}(1 - \frac{\Gamma_0 \eta}{2}) + \Gamma_0 \rho_0 E_m \tag{4.29}$$

where Γ_0 represents the Grüneisen parameter and s is the slope of the linear shock versus post-shock velocity behaviour. For $\Gamma_0 = 0$, this reduces to the following form:

$$p = \frac{\rho_0 c_0^2 \eta}{(1 - s\eta)^2} \tag{4.30}$$

which is exactly the same equation as Wilbeck derived from the continuity equations (combining 4.1, 4.2 and 4.28) (Wilbeck, 1978*b*).

- **Polynomial**: A popular way to define the EOS is through a polynomial form:

$$p = C_0 + C_1\mu + C_2\mu^2 + C_3\mu^4 \tag{4.31}$$

The constants in the polynomial form are often approximated by a 4-component Taylor expansion of Equation 4.30, evaluated in $\mu = 0$ (Abrate, 2015). This gives the following constants:

$$C_0 = 0; \quad C_1 = \rho_0 c_0^2; \quad C_2 = \rho_0 c_0^2(2s - 1); \quad C_3 = \rho_0 c_0^2(3s^2 - 4s + 1) \tag{4.32}$$

For $C_2 = C_3 = 0$, equation 4.31 reduces to a an integration of the bulk modulus definition, with a pressure independent bulk modulus.

- **Murnaghan or Tait's EOS**: Another EOS with two constants is the Murnaghan EOS (Wilbeck, 1978*b*):

$$p = p_0 + B\left[\left(\frac{\rho}{\rho_0}\right)^{\gamma} - 1\right] \tag{4.33}$$

Coefficients to approximate equation 4.30 have also been derived for this EOS (Wilbeck, 1978*b*):

$$B = \frac{\rho_0 c_0^2}{4s - 1}; \quad \gamma = 4s - 1 \tag{4.34}$$

- **EOS including porosity**: The equation of state including porosity was first introduced by Torvik (Torvik, 1970; Wilbeck, 1978*b*), based

on the observation of Deal that air in a shock regime also behaves according to a linear Hugoniot (Deal, 1957). When a mixture satisfies basic homogeneity and stability conditions, the relation between the density of the mixture in two states can be written as follows:

$$\frac{\rho_{1,avg}}{\rho_{2,avg}} = \sum_{i=1}^{N} f_i \frac{\rho_{1i}}{\rho_{2i}} \tag{4.35}$$

Where f_i is the volume fraction of component i in the mixture, state 1 is the state of the mixture in uncompressed condition and state 2 the stressed state. Using a Murnaghan approximation as the shock EOS of gelatine and a Mie-Grüneisen EOS for the air (the shocked state of air is best represented by the Mie-Grüneisen EOS, with $\Gamma_0 = 0$), the following EOS for a homogeneous medium can be derived:

$$\frac{\rho_{1,avg}}{\rho_{2,avg}} = f_f \left(\frac{P_2}{A} + 1 \right)^{-1/B} + f_a(1 - q) \tag{4.36}$$

Where

$$A = \frac{\rho_{0,f} c_{0,f}}{4s_f - 1}; \quad B = 4s_f - 1 \tag{4.37}$$

$$q = \frac{2\bar{P}s_a + \frac{\rho_{0,a} c_{0,a}^2}{P_0}}{2\bar{P}s_a^2} - \frac{\left\{ (2\bar{P}s_a + \frac{\rho_{0,a} c_{0,a}^2}{P_0})^2 - 4\bar{P}^2 s_a^2 \right\}^{1/2}}{2\bar{P}s_a^2} \tag{4.38}$$

With $\bar{P} = P_2/P_1$, f_f and f_a being the volume fraction of the fluid and the air respectively, $\rho_{0,f}$ and $\rho_{0,a}$ the density of the fluid and the air in reference state and $c_{0,f}$, s_f, $c_{0,a}$ and s_a the parameters defining the linear Hugoniot for the fluid and the air. The air will first compress resulting in an initially low slope of the pressure-density curve. After the air is compressed, a steep slope follows describing the compression of the fluid.

- **The tabulated EOS**: Tabulated forms exist as well, in general these are just evaluations of one of the previously mentioned EOSs.

- **Other**: Elastic-Plastic models are also used (Wang and Yue, 2010; Mol and Salem, 2012; Kirtil et al., 2003). Visco-hyperelastic laws to describe the behaviour of gelatine have been investigated as well (Salisbury and Cronin, 2009; Cronin, 2011; Liu et al., 2013; Liu, Fan and Li, 2014; Ravikumar et al., 2015).

A considerable amount of research uses only the bulk modulus to construct the EOS. The bulk modulus definition can be implemented using only the C_1 coefficient in the polynomial (for example $C_1 = 2250\,\text{MPa}$ (Langrand et al., 2002), used in (Blair, 2008; Chuan, 2006; Hanssen et al., 2006; Sun et al., 2014; Yulong et al., 2008), or $C_1 = 2200\,\text{MPa}$ used in (Guida et al., 2013; Azevedo and Alves, 2009)). As a reference, the C_1 component in the polynomial approximation of the Mie-Grüneisen EOS for water is equal to 2199 MPa, based on the linear Hugoniot found in (Wilbeck, 1978*b*). The bulk modulus definition can also be implemented using the Mie-Grüneisen EOS, with $s = 0$ (Mav, 2013; Smojver and Ivančević, 2010*a*,*b*, 2011, 2012; Ivančević and Smojver, 2016).

Implementations of the Mie-Grünisen for water have been found in literature with $\Gamma_0 = 0$ (Hedayati and Ziaei-Rad, 2013; Nishikawa et al., 2011; McCallum and Constantinou, 2005) and with $\Gamma_0 \neq 0$ (Dar et al., 2013; Hedayati and Ziaei-Rad, 2013; Hedayati, Sadighi and Mohammadi-Aghdam, 2014; Hedayati, Ziaei-Rad, Eyvazian and Hamouda, 2014; Hedayati and Ziaei-Rad, 2014). The polynomial approximation of the Mie Grüneisen is also used (Kumar et al., 2014; Ensan et al., 2008; Azevedo and Alves, 2007; Tho and Smith, 2008; Lavoie et al., 2007*b*). A popular 3-term polynomial for water is the one introduced by Brockman (Brockman and Held, 1991). This EOS has been used in (Siddens et al., 2012; Siddens and Bayandor, 2013; Meguid et al., 2008; Mao et al., 2008; Jain and Shivayogi, 2006; Airoldi and Cacchione, 2006, 2005; Chuan et al., 2015; Simulia, n.d.). 3-term polynomials similar to this definition can be found as well (Selezneva et al., 2012; Lavoie et al., 2008; Jenq et al., 2007). However, the comparison of the Mie-Grüneisen EOS with $s = 0$ and $s \neq 0$ and its two approximations for water, using the linear Hugoniot data from Wilbeck (with $c_0 = 1482.9\,\text{m/s}$, $s = 2.0$ and $\rho_0 = 1000\,kg/m^3$) depicted in Figure 4.11, shows that the polynomial approximation is a less good approximation. Even worse is the linear approximation using the

bulk modulus ($s = 0$). The Murnaghan EOS is almost identical to the Mie-Grüneisen EOS.

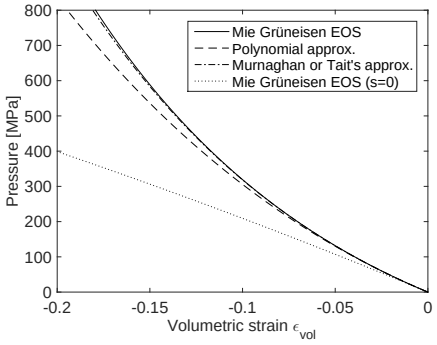

Figure 4.11: The Mie-Grüneisen EOS with $s = 0$ and $s \neq= 0$ and the two approximations.

The linear Hugoniot has been studied for gelatine as well using the plate impact technique. This has been done for 20% porcine gelatine (Wilgeroth et al., 2010; Shepherd et al., 2009). In (Shepherd et al., 2009) for example, a sound speed of 1570 m/s with a slope of $s = 1.77$ was obtained.

In another approach, the EOS is derived from an optimization procedure based on experimental data. The downside of such a technique is that it might perform well for the used training data, but cannot be extended to other applications. A very popular EOS obtained after optimization is the Murnaghan EOS obtained in (McCarthy et al., 2004). In their work, the polynomial and Murnaghan EOS was fitted on the signals of 12 pressure transducers obtained from bird strikes with real and substitute birds on a plate mounted at 90° and 45° with respect to the bird's trajectory. The polynomial EOS did not give good results, but consistent parameters were found for the Murnaghan EOS: $B = 128$ MPa and $\gamma = 7.98$ (compared to water: $B = 314.1$ MPa and $\gamma = 7$). This EOS was used in (Vignjevic et al., 2013; Georgiadis et al., 2008; Guida, 2008; Liu and Li, 2013; Orlowski, 2015). Another attempt was taken in (Liu, Li and Gao, 2014), where a 1-coefficient polynomial ($C_1 = 2800MPa$) and a Murnaghan EOS ($B = 9300$ MPa and $\gamma = 7.14$) was optimized using strain, displacement and force data from bird strike experiments on flat plates. This EOS was used in (Kou and Xu, 2015;

Liu, Li, Gao and Yu, 2014).

A comparison between the most frequently used EOSs is shown in Figure 4.12a, including the bulk modulus EOS of Lagrand, the polynomial EOS of Brockman, the EOS optimized by McCarthy and the Mie-Grüneisen EOS for water and gelatine assuming a linear Hugoniot relationship, based on the results of Wilbeck and Shepherd. Some significant difference can be observed between these EOSs.

A final approach is to use a porous EOS. In literature, tabular forms can be found, stating that it is derived from Wilbeck's equations (the 10% EOS used in (Guida et al., 2011; Guida, 2011; Marulo and Guida, 2014; Grimaldi et al., 2013)), but also polynomial approximations (Simulia, n.d.; Selezneva et al., 2012). A comparison in Figure 4.12b however shows that a polynomial EOS is not capable of capturing the almost bilinear behaviour of the porous EOS defined by Wilbeck. The Wilbeck EOS in Figure 4.12b is based on equations (4.36) to (4.38) and makes use of the linear Hugoniot of gelatine derived in (Shepherd et al., 2009) with a density of $1040\,kg/m^3$ and the characteristics of air stated in (Wilbeck, 1978*b*).

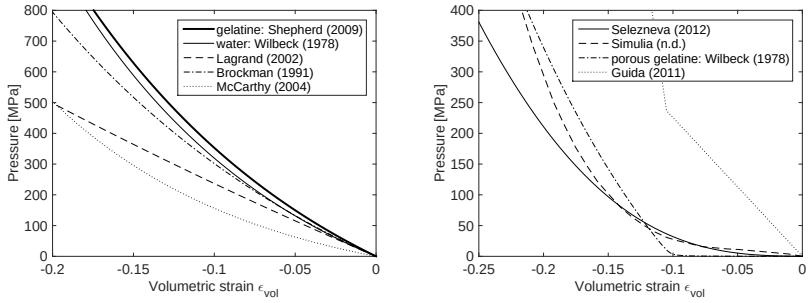

(a) Several frequently used EOSs found in literature. **(b)** Porous EOSs found in literature.

Figure 4.12: Equations of state.

There is a big difference between the EOSs for porosity found in literature. For a homogeneous distribution using micro-balloons, Wilbeck's bilinear EOS is definitely closer to reality. But the question remains if it also captures

the behaviour of more local porosities as in real birds.

A tensile failure or hydrostatic pressure cut-off criterion can be added to the EOS to limit the hydrostatic tension stress to a specific value. In (Simulia, n.d.), 2.75 MPa was used and 10 MPa in (Kirtil et al., 2003; Strnad and Doubrava, 2009).

4.2.5.2 Deviatoric part: shear moduli or viscosity

Although the constitutive behaviour of water is mainly dominated by the hydrostatic part, the deviatoric part is sometimes modelled as well in literature. This can be in the form of elastic-plastic behaviour including shear modulus, yield stress and hardening modulus as in (Brockman and Held, 1991; Lavoie-Perrier, 2008; Lavoie et al., 2008, 2009; Selezneva et al., 2012; Anghileri and Sala, 1996; Jenq et al., 2007; Airoldi and Cacchione, 2005; Liu, Li and Gao, 2014; Vignjevic et al., 2013), or in the form of a very low dynamic shear viscosity, to stabilize the calculation ($0.001\,Ns/m^2$ in (Hanssen et al., 2006; Nagaraj and Velmurugan, n.d.)). In Abaqus™ however, it is not possible to have shear stiffness and viscosity simultaneously when using an EOS.

Several papers use a shear modulus of 2000 MPa, a yield stress of 0.02 MPa and a hardening modulus of 0.001 MPa (Lavoie-Perrier, 2008; Lavoie et al., 2007*b*, 2008, 2009; Selezneva et al., 2012; Jenq et al., 2007; Vignjevic et al., 2013; Orlowski, 2015), likely introduced by (Anghileri and Sala, 1996).

A much lower gelatine shear stiffness in the order of $5 - 20$ kPa has been observed in blunt impact, vibro-acoustography and elastography experiments (Liu, Fan and Li, 2014; Urban, Nenadic, Chen and Greenleaf, 2010; Urban, Fatemi and Greenleaf, 2010; Chen et al., 2002; Engel and Bashford, 2015).

Non-Newtonian shear-thickening behaviour has been observed for gelatine in literature using polymer Hopkinson bar experiments. Power law coefficients are derived for a 1:9 MR in (Subhash et al., 2012) ($\mu = \alpha\dot{\gamma}^{n-1}$ with $\alpha = 0.0045$ and $n = 2.22$).

In the next two sections, the results of a numerical study on the impact pressures during bird strike will be presented. The impact can be roughly subdivided in a shock regime (section 4.3), followed by a steady state regime (section 4.4). The goal in these sections is to give a first insight into the performance of the SPH model in terms of impact pressure and the correlation with and questioning of the analytical models introduced in the first section.

4.2.5.3 The used bird model

In the previous sections, an extensive review of the material models used in literature and a brief introduction of the most important numerical aspects are given. The used parameters in this work can be summarized and justified as follows:

- **The EOS**: A Mie-Grüneisen EOS is chosen because it accounts for the linear relationship between shock and particle velocity, most other EOS are an approximation of this EOS (see also Figure 4.11) and Wilbeck obtained this EOS directly from the continuity equations. The linear Hugoniot for 20% porcine gelatine from (Shepherd et al., 2009) is used ($c_0 = 1570\,\mathrm{m/s}, s = 1.77, \Gamma_0 = 0$).
- **A tensile failure criterion**: A 1 MPa tensile cut-off pressure is set. To omit the tensile failure criterion is not an option because otherwise, high unrealistic tensile stresses occur where the mesh is split, resulting in a serious overestimation of the momentum transfer (the influence of these unrealistic tensile stresses might diminish for very fine meshes, this has not been investigated). Setting a tensile cut-off pressure also improves the stability. Reducing the cut-off pressure on the other hand makes particles more easily detach from the bulk material. Setting the cut-off pressure is therefore a trade-off.
- **The kernel**: The default cubic kernel is used because the other kernels available in Abaqus (the quadratic and quintic) resulted in erroneous shock and steady state pressures and durations. The other kernels therefore have not been investigated further.
- **The bulk viscosity**: The default setting for the bulk viscosity dissipates too much energy or momentum. For denser meshes between

$1 - 2\,\text{mm}$, setting the linear and quadratic bulk viscosity scale factor at 20% gave correct momentum transfer results (see also chapter 5).

- **The contact definition**: Default general (node-to-surface) penalty contact is used as it gives good results and does not dissipate energy.

4.3 Simulation of the shock regime

The results presented in this section focus on the shock pressure and several important influences on its creation and propagation. In this study, a majority of the cases will use flat cylinders as impacting geometry because of the following reasons:

- The shock energy at impact is much higher for a flat cylinder than for a cylinder with hemispherical ends, because the flat cylinder has a large area that is instantaneously stopped at impact. It can be seen as the most conservative case in terms of shock energy.
- The amplitude of the shock pressure is in theory independent of the shape of the bird. The flat cylinder therefore suffices to get an idea of the shock pressure amplitude.
- For a flat cylinder, there is only a discrete step in time (the time before impact and the time after impact). For a hemispherical end, the first impact theoretically is also discrete in space, the first area that contacts is only a point. This makes it more difficult to study the impact phenomenon using a cylinder with hemispherical ends. The very local high pressure also results in high speed water jets that are initiated from the first point of impact, when the edge velocity drops below the shock velocity (Haller et al., 2002). This jetting is more violently compared to the impact of a flat front.
- The flow of the shock and release waves are more characteristic and much easier to distinguish and follow for flat cylinders.

To introduce the results of the numerical simulations of the shock regime, first an overall picture of the impact event is shown. Figure 4.13 shows several subsequent frames of one central layer of particles of a flat cylinder impacting a rigid plate at $100\,\text{m/s}$. The linear Hugoniot for gelatine from (Shepherd

et al., 2009) is used. According to equation 4.4, the amplitude of the shock pressure should be $P_H = 1040\,\mathrm{kg/m^3}(1570\,\mathrm{m/s} + 1.77 \cdot 120\,\mathrm{m/s})100\,\mathrm{m/s} = 181.7\,\mathrm{MPa}$. The colors indicate a pressure ranging from $-1\,\mathrm{MPa}$ to $181.7\,\mathrm{MPa}$ (a tensile failure criterion of $1\,\mathrm{MPa}$ is set). The discontinuities in the shock pressure field can be caused by contact ringing. 0 μs is the time increment just before impact. At 3.1 μs, the shock wave starts to develop and travel through the cylinder. At 9.4 μs, the release waves can be observed that start to travel inwards. The release waves represent a pressure drop, which results in an increase of kinetic energy, or also, the start of flow in the radial direction. At 23.9 μs, the release waves are catching up with the shock front and the shock wave starts to decrease in amplitude. At 38.9 μs, the pressure is reduced to roughly half the initial shock pressure. Throughout this entire time frame, the material above the shock front is not experiencing any change of state.

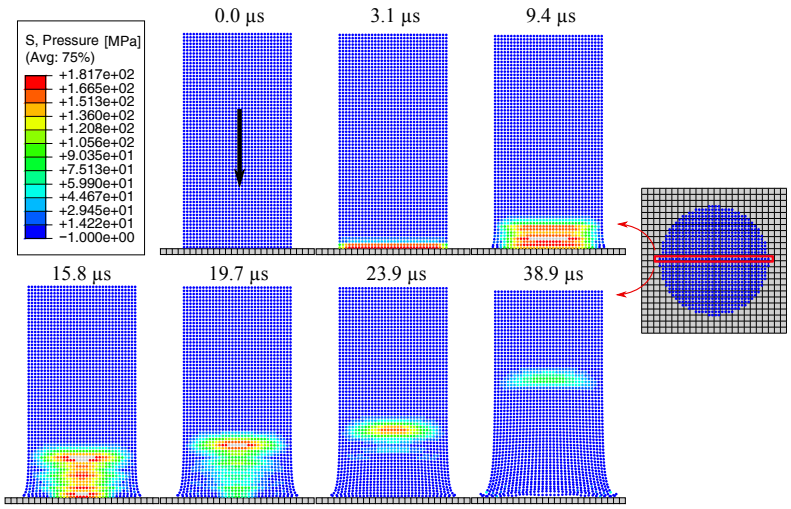

Figure 4.13: Pressure distribution of the shock regime for a 100 m/s impact of a gelatine flat cylinder.

Differentiating the Mie-Grüneisen EOS (equation 4.30) to the density and taking the square root (equation 4.5) results in the following formula for the speed of the release waves:

$$v_r = \sqrt{\frac{-\rho_0^2 c_0^2 (s\rho - s\rho_0 + \rho)}{(s\rho - s\rho_0 - \rho)^3}} \tag{4.39}$$

From the Mie-Grüneisen EOS, the density at shock pressure can be calculated ($1103.1\,\mathrm{kg/m^3}$), which gives a release wave speed of $1823.3\,\mathrm{m/s}$. Theoretically, the shock duration at the centre of impact should take $13.7\,\mu\mathrm{s}$ (with the mesh radius of $25\,\mathrm{mm}$ in equation 4.6). In the simulation, the shock pressure in the central axis decreases between $15.8\,\mu\mathrm{s}$ and $19.7\,\mu\mathrm{s}$. Even at $19.7\,\mu\mathrm{s}$, the release waves are not completely vented yet. This shows that the release waves initiate a decrease in pressure and not a sudden drop to zero pressure. A more detailed look into the release waves will be given in section 4.3.4.

The initial velocity of the centre node of the cylinder decreases from $100\,\mathrm{m/s}$ to $91\,\mathrm{m/s}$ when the shock wave travels through the bird, which gives a good indication of the limited amount of momentum that is transferred by the shock regime.

In the following subsection, first it will be shown that the numerical shock pressure pulse can be obtained very accurately and is quite close to the analytical results. This is done under very specific circumstances. Based on these results, an expression for the energy in the shock region is developed and compared with the simulations. This expression introduces a new way of looking at the shock regime. The frontal shape of the projectile (parallel or inclined flat surface or hemisphere) is an important parameter in the shock regime. In this section, its influence on the shock pressure amplitude and duration and on the shock energy is investigated thoroughly.

4.3.1 Shock pressure amplitude

A lot of research has already been done on contact pressures in simulations. To compare the simulations with the theory, the typical approach is to request contact pressure output over a certain small area and probe the maximum value contained in the peak. The results of the encountered literature can be summarized as follows:

- A shock peak pressure is obtained close to the analytical value in (Lavoie et al., 2007*b*; Lavoie-Perrier, 2008; Smojver and Ivančević, 2012; Langrand et al., 2002; Hedayati, Ziaei-Rad, Eyvazian and Hamouda, 2014; Iannucci and Donadon, 2006; Dar et al., 2013; Nishikawa et al., 2011; Jain and Shivayogi, 2006; Orlowski, 2015; Airoldi and Cacchione,

2006; Simulia, n.d.). From these works, only in (Smojver and Ivančević, 2012; Nishikawa et al., 2011; Jain and Shivayogi, 2006; Airoldi and Cacchione, 2006; Simulia, n.d.), the obtained peaks are clearly not obtained by sampling a discrete peak.

- An underestimation of the peak pressure is observed in (Airoldi and Cacchione, 2006; Jain and Shivayogi, 2006; Nizampatnam, 2007; Ugrčić, 2012; Hedayati, Ziaei-Rad, Eyvazian and Hamouda, 2014; Ivančević and Smojver, 2011; Smojver and Ivančević, 2010*b*; Chuan et al., 2015; Anghileri et al., 2012; Jenq et al., 2007; Meguid et al., 2008; Mao et al., 2008; Tho and Smith, 2008; Johnson and Holzapfel, 2003). Only in (Anghileri et al., 2012; Ivančević and Smojver, 2011; Johnson and Holzapfel, 2003), the peak pressure is clearly not obtained from discrete points in the pressure signal.
- In (Airoldi and Cacchione, 2006; Jain and Shivayogi, 2006; Nizampatnam, 2007; Blair, 2008; Hedayati and Ziaei-Rad, 2013; Hedayati, Sadighi and Mohammadi-Aghdam, 2014), a trend can be observed of decreasing peak pressure for smaller initial contact areas.
- Occasionally the acquired pressure signals are filtered first to remove numerical noise (Airoldi and Cacchione, 2006; Anghileri et al., 2012; Simulia, n.d.). In (Airoldi and Cacchione, 2006), it is shown that the cut-off frequency has a big influence on the obtained shock pressure.

Other work on peak pressure measurements with less information can be found as well (Lavoie et al., 2007*a*; McCallum and Constantinou, 2005; Siddens and Bayandor, 2013; Siddens et al., 2014; Chalipat and Shankapal, 2002; Kim et al., 2011; Ensan et al., 2008).

In this work, an attempt is made to zoom in on the pressure peak by combining the use of dense meshes and forcing more output in time. This way, a pressure pulse is obtained that can be compared to the analytical models directly without filtering or sampling discrete peaks.

The impact object is also scaled down, which can be done because the shock wave pressure amplitude is independent of the size. Additionally, the simulation is deliberately forced to use very small time increments, to

achieve a smooth solution in time. Apart from using dense SPH meshes which already leads to small increments, this can be further reduced via three options:

- Force field output with a much higher output frequency.
- Add a very small deformable dummy element to the simulation (the decrease in minimum characteristic length decreases the stable time increment).
- Force the simulation to use a constant small time increment throughout the simulation (direct user control).

Decreasing the time increment using a small element or enforcing a small time increment results in too high oscillations in the contact pressure curve and will not be covered. It is still a question how Abaqus™ calculates the penalty stiffness, but the time increment (the stable or effectively used increment) definitely plays a significant role. Reducing the time increment by forcing field output on the other hand provides good results.

4.3.1.1 Non-porous gelatine

The considered model for the target consists of a 16 mm × 16 mm × 1 mm thick steel plate with a rigid boundary condition. The plate is meshed with cubic elements with an edge size of 1 mm and is attached to a reference node with an additional 1 kg able to move in the impact direction. Freeing this boundary condition improves stability and has no influence on the results for the performed simulations. The mesh of the impactor is a 12 mm × 12 mm × 20 mm prism. Mesh sizes of 1 mm, 0.5 mm, 0.25 mm and 0.2 mm are considered (Figure 4.14), respectively corresponding to 1, 4, 16 and 25 particle(s)/element. Note that contrary to the study of the steady state regime, a high particle/element ratio is not required for the initial impact (the shock regime) because all the elements do impact simultaneously and stay into contact with the plate during the shock pulse. The EOS for gelatine from (Shepherd et al., 2009) is used, together with a density of 1040 kg/m^3.
The simulation is executed for 10 μs, with 500 enforced pressure field outputs. Figure 4.15 shows the pressure in the centre particle at the front layer of SPH particles and Figure 4.16 the contact pressure measured at the centre

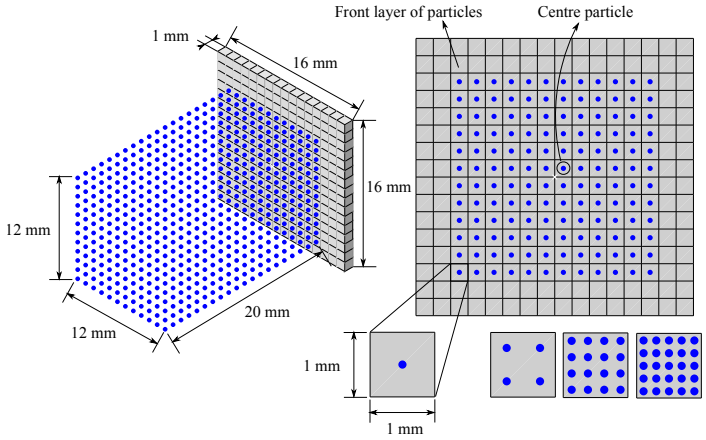

Figure 4.14: Considered meshes to study the shock regime.

node of the plate for the four considered meshes, together with the analytical solution ($P_H = 181.69\,\text{MPa}$). A very stable shock pressure plateau can be observed for the particle pressure of the denser SPH meshes. The pressure matches the analytical result very well. The contact pressure curves do look worse (large oscillations superimposed on the pressure plateau). But apart from the oscillations, the pressure pulse is estimated quite good for the 0.5 mm, 0.25 mm and 0.2 mm meshes. The smoothing inherent to the SPH algorithm is probably responsible for the smoother curves of the particle pressure.

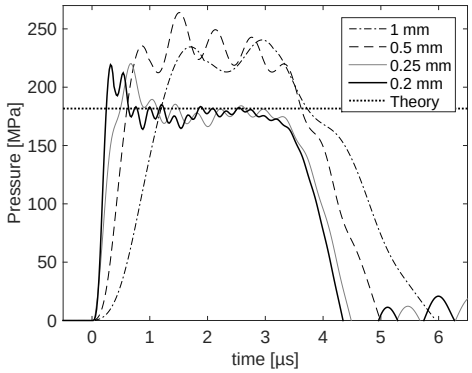

Figure 4.15: Particle pressure for four mesh sizes (theory according to Eq 4.4).

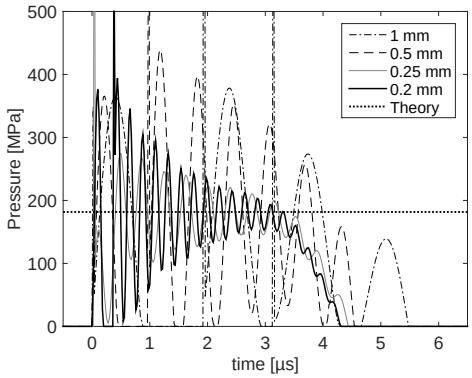

Figure 4.16: Contact pressure for four mesh sizes (theory according to Eq 4.4).

A release wave speed of 1823.3 m/s can be calculated, which corresponds with a shock duration of 3.29 μs for the shortest edge (6 mm) up to 4.26 μs for the diagonal (8.49 mm), because of the cubic shape of the cross section. The figures indeed show that the pressure starts dropping approximately at 3.5 μs after impact.

At initial contact, there is a small overshoot in the particle pressure curves for the denser meshes. SPH is a continuum technique, but there is still a certain discrete mass fixed to the particles, opposed to an infinitesimal boundary of mass that is initially stopped. The inertia of the first row of particles that needs to be stopped however is not the cause, as the velocity of the particles starts oscillating around zero already during the rise of the pressure.

The 0.25 mm mesh can be used to check the influence of the impact velocity. Figure 4.17 shows the pressure pulse measured at the centre particle for 75, 100, 150, 200 and 250 m/s.

Up to 200 m/s, the shock pressure is estimated very well, but the pressure pulse of 250 m/s is slightly overestimated. This might again be a mesh convergence issue. An overestimation of the pressure pulse was also seen for the coarser meshes in Figure 4.15. For higher pressures, the shock duration decreases slightly because of an increase of the speed of sound at higher pressures (see also Equation 4.5).

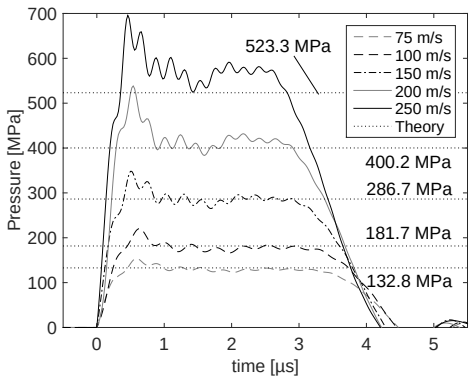

Figure 4.17: Particle pressure pulse for the $0.25\,\mathrm{mm}$ mesh at 75, 100, 150, 200 and $250\,\mathrm{m/s}$ (theory according to Eq 4.4).

4.3.1.2 Porous gelatine

Introducing porosity significantly reduces the shock speed and therefore also the Hugoniot pressure. A porous gelatine mixture with 10% porosity is considered, bringing the mean density up to $936\,\mathrm{kg/m^3}$. From equation 4.2,4.3 and 4.36, a shock speed of $822.6\,\mathrm{m/s}$ can be calculated for an impact speed of 100 m/s (compared to $1747\,\mathrm{m/s}$ without porosity), which results in a Hugoniot pressure of theoretically 77 MPa. Figure 4.18 shows the pressure in the centre of the plate impacted by the $0.25\,\mathrm{mm}$ and $0.2\,\mathrm{mm}$ mesh for a 10% porous gelatine mixture together with the polynomial approximation from (Selezneva et al., 2012). Much higher spatial pressure oscillations occur in the SPH mesh, possibly due to the bilinearity of the EOS. Therefore only the contact pressure is shown. High oscillations can be observed in the contact pressure pulse as well. The much more pronounced bilinear behaviour of Wilbeck's equations compared to the solution using Selezneva's EOS is likely responsible for the higher oscillations (see also Figure 4.12b). The shock pressure amplitude is better approximated by the EOS of Selezneva. But, because the derivative of the polynomial describing Selezneva's EOS for the shock pressure is slightly lower at the considered shock pressure (see also Figure 4.12b), the release speed is therefore also lower and the shock duration larger. For higher shock pressures, the opposite will occur, because the derivative for higher pressures is higher than Wilbeck's EOS.

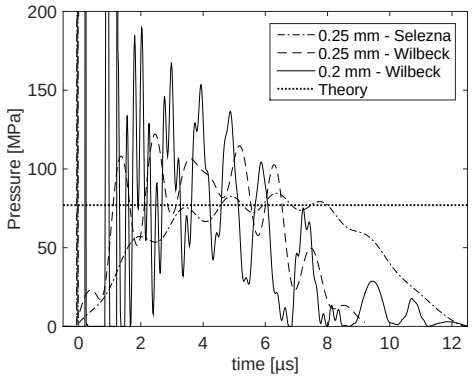

Figure 4.18: Contact pressure for a 10% porous mixture for the $0.25\,\mathrm{mm}$ and $0.2\,\mathrm{mm}$ mesh at $100\,\mathrm{m/s}$ (theory according to Eq 4.4).

The EOS from Selezneva is an approximation of the EOS developed by Wilbeck. In that sense, it would be advisable to use the one from Wilbeck. However, the EOS from Wilbeck seems to result in quite large oscillations. Choosing a porous EOS therefore could be trade-off.

4.3.2 The influence of tilting

In section 4.1.3, the influence of tilting the projectile according to Wilbeck was covered. The behaviour described in that section is investigated using the 0.25 mm mesh. Because the particles do not impact at the same time, the contact pressure curves are worse. To maintain the same spatial resolution and to show the clear trend at increasing tilt angle, the signals are filtered with a cut-off frequency of 1 MHz. The results covered in this section are not necessarily converged. Figure 4.19 shows the contact pressure on the centre node of the plate after impact of the mesh at 100 m/s, with an angle of 0 °, 2 °, 3 °, 4 °, 6 °, 8 ° and 15 ° with respect to the surface of the plate. According to Wilbeck, no shock wave should be observed any more at the centre of the plate above the critical angle of 3.28 °. But this is not the case. At 2 °, the amplitude starts to rise. At $3 - 4\,°$, the shock pressure rises up to rougly 190 % of the theoretical value. Further increasing the tilt angle reduces the contact pressure again, ultimately creating a flow more similar to a steady state regime as for example for the 15 ° impact.

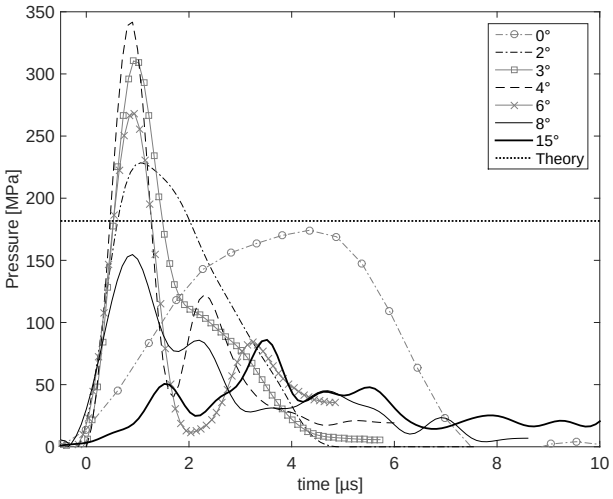

Figure 4.19: Contact pressure of a flat projectile tilted $0\,^\circ$, $2\,^\circ$, $3\,^\circ$, $4\,^\circ$, $6\,^\circ$, $8\,^\circ$ and $15\,^\circ$ (theory according to Eq 4.4).

As seen in the contact pressure graph, the pressure can increase for certain impact angles. This is because of an additional material flow that originates and accumulates with the original impact speed, as shown in the speed vector plot of Figure 4.20a, showing the speeds of a central vertical layer of particles at the moment where the additional flow reaches the centre of the target for the $3\,^\circ$ tilted mesh.

For angles beneath the critical angle, release waves still travel from the side that impacts first. The contact pressure is therefore a running pulse, as shown in Figure 4.20b. This running pulse can also be observed in the pressure field of the simulations. The spatially small pulse is also the cause of the shock duration that is much smaller for tilted impacts. The angle would have to be much smaller than the critical angle for the release waves to have a negligible influence on the pressure distribution compared to a perpendicular impact.

These simulations indicate that there is no critical angle that determines whether a shock wave is created or not (as introduced by Wilbeck, see also section 4.1.3). There is a rather smooth transition of pressure amplitude and duration when altering the tilt angle, resulting in a variety of pressure

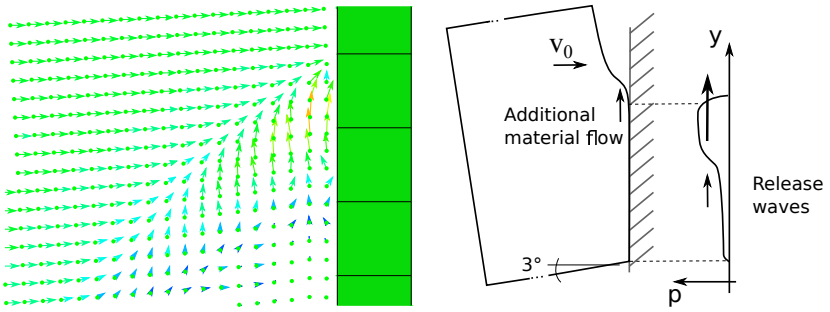

(a) Speed vector plot for a 3° tilted impact. **(b)** Additional flow and a running pressure pulse.

Figure 4.20: Material flow at a tilted impact.

amplitudes (that can increase above the theoretical shock pressure because of the additional flow) and a variety of pressure pulse durations (because the release waves can vent the shock pressure from the side that impacts first). This is important to keep in mind when performing impact pressure measurements.

After investigating the shock amplitude and duration with prismatic impactors, a switch to axisymmetric shapes is made (cylinders with flat or hemispherical ends).

4.3.3 Hemispherical ends

Infinitesimally, the impact point of a hemispherical surface is also represented by a flat surface. Very locally, the creation of the shock wave is therefore similar to the impact of a flat cylinder. The numerical representation of a hemisphere with a structured mesh inevitably consists of a flat surface at the front. This is shown on the left side of Figure 4.21, where the effect of a mesh refinement on the front layer of particles is shown (mesh 2 being denser than mesh 1). When a structured mesh is generated, starting from the tip of the hemisphere (the $\times$ in Figure 4.21), there is no particle that fits the volume at $z = 0$. The first layer therefore lies at a distance equal to the mesh size away from the origin. Figure 4.21 also shows the first particle layer of a projectile with hemispherical ends for the 0.5 mm, 0.25 mm and 0.2 mm mesh impacting the same plate as shown in Figure 4.14. The projectile

consists of a cylindrical shape with hemispherical ends, with a diameter of 12 mm and a length of 24 mm.

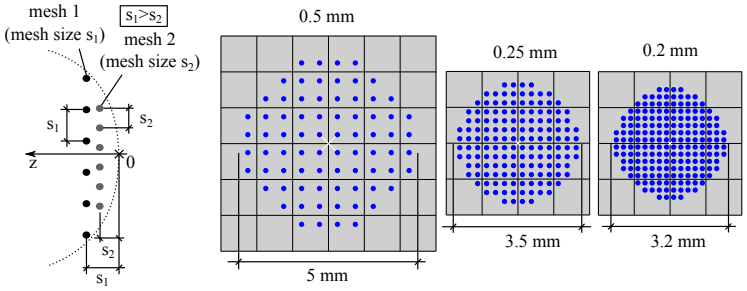

Figure 4.21: Discrete representation of a hemisphere by a structured mesh.

Compared to the diameter of the projectile, the size of the front layer is relatively large. The hemisphere however is represented quite well, as can be observed in Figure 4.22, which shows the hemisphere for the three mesh sizes.

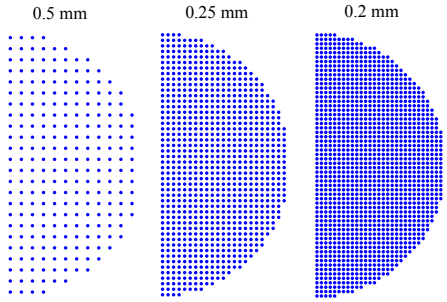

Figure 4.22: Discrete representation of a hemisphere by a structured mesh (side view).

In Figure 4.23, the pressure in a centre particle of the front layer of particles is shown. The peak pressure is slightly larger than the theoretical one (181 MPa), which might be because of the overshoot also seen in the simulations with the flat surfaces. From the 0.5 mm to the 0.2 mm mesh, the shock duration almost halved.

The reduction of the shock duration will be partly the result of the decreased radius of the front layer of particles. But it will also partly be the result of convergence. It is computationally impossible however to obtain a much smaller radius of the front layer of particles.

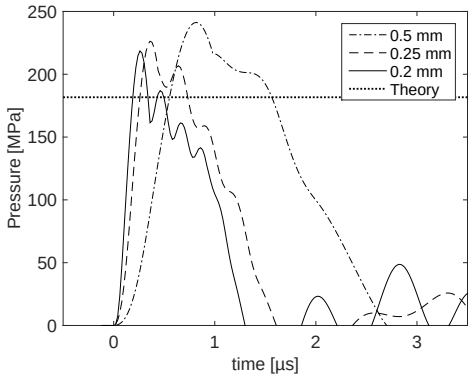

Figure 4.23: The pressure in a centre particle of the front layer of particles of the hemispherical $0.5\,\mathrm{mm}$, $0.25\,\mathrm{mm}$ and $0.2\,\mathrm{mm}$ mesh (theory according to Eq 4.4).

4.3.4 The elastic energy in the shocked region

Local measurements on element level often result in highly oscillating signals not representative for the behaviour on a larger scale. A more global approach can therefore learn more about the influence of certain input parameters. The elastic energy inside the shock wave could be such a global parameter, which can help to study convergence issues, the influence of the shape, numerical parameters, etc. In this section, first an analytical expression is developed that calculates the energy inside the shocked volume. Before this is addressed, it is verified if the speed of the shock and release waves are more or less as predicted by the theory. Both the determination of the elastic energy and the verification of the release and shock wave speed is done using a cylinder with flat ends.

First, the speed of the release waves is investigated with a 0.25 mm flat cylinder mesh with a radius of 6 mm. The pressure distribution along a central array of 24 particles in the front layer is tracked over time (an array starting from the centre up to the edge of the mesh). Six pressure distributions are depicted in Figure 4.24a. For 100 subsequent time frames, the particle closest to the pressure drop beneath 95% of the maximum pressure in each distribution is tracked. During the very short period represented by these frames ($2\,\mu$s), it is assumed that the particles do not move considerably. The location of the drop for the six release waves is

indicated by an $\times$ in Figure 4.24a. The location of the drop for the 100 subsequent time frames is depicted in Figure 4.24b.

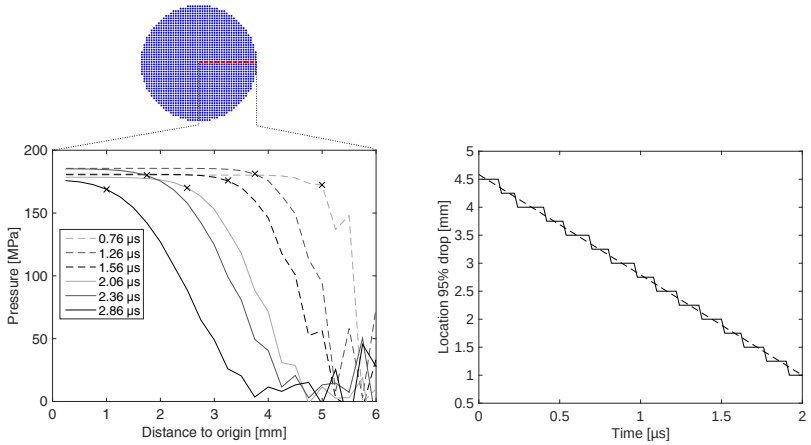

(a) Six pressure distributions of a centre array of particles in the front layer.

(b) Location of the pressure drop in function of time.

Figure 4.24: Drop of the pressure beneath 95% of the maximum pressure in the pressure distribution for 100 subsequent time frames.

Because the centre array contains only 24 particles, discrete steps can be observed in the location curve, a step for each 0.25 mm. Despite that there are only 24 particles, a line fit seems to give a good indication of the release wave speed. For the data presented in Figure 4.24b, 1784 m/s is obtained. However, depending on the chosen threshold (95%) and the considered time period (2 μs), different release speeds can be obtained ranging from 1600 m/s to 1800 m/s. Theoretically, the release wave speed should be 1823.3 m/s. From Figure 4.24a it can also be observed that the release wave does not drop immediately to zero. There is a steady decrease towards the edge of the projectile as the elastic energy is converted to kinetic energy.

A similar procedure can be applied to the shock front. Figure 4.25 shows the pressure distribution of a centre array of 80 particles along the impact axis of the projectile for six subsequent time frames. The release of the shock pressure can already be observed in the curve at 3.42 μs after impact. At 5.42 μs, the pressure starts to rise again close to the origin. This is the start of the transition towards the steady state regime. Considering the front of

the shock wave at the location where the pressure drops below 95 % of the maximum pressure gives a velocity of 1672 m/s. Adding the impact speed gives a shock velocity of 1772 m/s (shock equilibrium in Figure 4.2), opposed to 1747 m/s according to the linear Hugoniot. The better correlation of the shock wave speed will be partly the result of the larger distance over which the line is fitted, but also the steeper shock front which makes the result less dependent on the threshold.

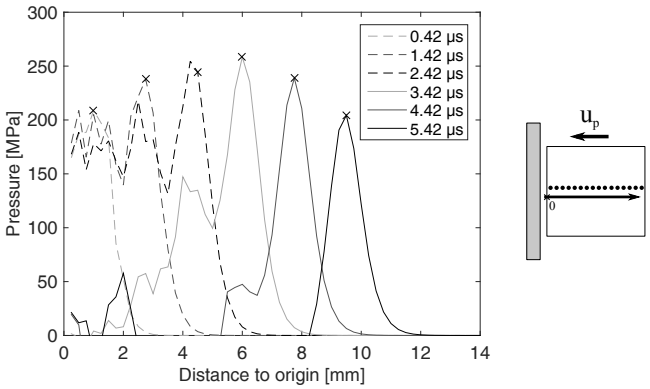

Figure 4.25: Six pressure distributions of a centre array of particles along the axis of the projectile.

The energy inside the shocked region can be calculated assuming adiabatic compression (using a derivative of equation 4.28: $\mathrm{d}V = -V_0 \mathrm{d}\eta$):

$$\begin{aligned} E_{shock} &= -\int p\mathrm{d}V = -\int -V_0 \frac{\rho_0 c_0^2 \eta}{(1-s\eta)^2}\mathrm{d}\eta \\ &= -\left[\frac{\rho_0 c_0^2 V_0}{s^2}\left(\frac{1}{s\eta - 1} - \ln(|s\eta - 1|)\right)\right]_{\eta_0}^{\eta_1} \end{aligned} \tag{4.40}$$

Where $\eta_0 = 0$, η_1 can be calculated from the Mie-Grüneisen EOS and $V_0 = V/(1-\eta_1)$. This last substitution introduces the compressed volume in the equation, which can be determined based on the shock and release wave speed. Notice the minus sign to make the calculated elastic energy positive. In this derivation, the following assumptions are made:

- The release and shock wave speed are equal to the ones derived from the theory.

- The speed of the release and shock wave is constant. Just after impact this assumption is valid. But as the shock wave loses energy while it travels through the material, the speed of the material behind the shock wave is not zero any more.
- The pressure in the shocked region is constant.
- Both the release and shock wave are discrete surfaces travelling through the projectile.
- The release wave vents the shock pressure immediately when the two fronts collide.

The last two assumptions for the release wave are likely the biggest error source in the obtained solution.

The volume in function of time can be derived from a revolution about the axis of the projectile, of the area enclosed by the release wave, the shock front and the axis of the projectile. As shown in Figure 4.26, the front of the initial release wave is always further propagated than any other point along the edge of the projectile because the release wave is faster than the shock wave.

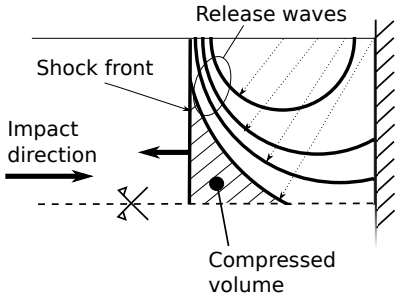

Figure 4.26: Shocked region: the shock and release waves.

The radius of the release wave and the position of the shock front in function of time (Figure 4.27) can be written as follows:

$$r_r = v_r t; \quad x_s = v_s t \tag{4.41}$$

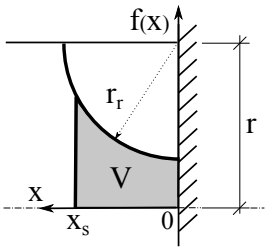

Figure 4.27: Derivation of the shocked volume in function of time.

The distance between the radial release wave and the x-axis can be integrated up to the location of the shock:

$$\begin{aligned} V &= \pi \int_{x_0}^{x_s} f(x)^2 \mathrm{d}x = \pi \int_{x_0}^{x_s} (r - \sqrt{r_r^2 - x^2})^2 \mathrm{d}x \\ &= \pi \left[r^2 x - 2r \left(\frac{x\sqrt{r_r^2 - x^2}}{2} + \frac{r_r^2}{2} \arcsin\left(\frac{x}{r_r}\right) \right) + r_r^2 x - \frac{x^3}{3} \right]_{x_0}^{x_s} \end{aligned} \tag{4.42}$$

with

$$x_0 = \begin{cases} 0 & \text{if } t \leq r/v_r \\ \sqrt{r_r^2 - r^2} & \text{if } r > r/v_r \end{cases} \tag{4.43}$$

and

$$x_s \leq \sqrt{\frac{r}{\frac{v_r^2}{v_s^2} - 1}} \tag{4.44}$$

Figure 4.28 compares the analytical result with the elastic energy in the simulation for a flat cylinder with a radius of 6 mm and a length of 24 mm. The analytical result is calculated for both the theoretical release wave speed of 1823 m/s and a 175 m/s slower release wave speed using Eq 4.40 and 4.42. The elastic energy is shown for a mesh size of 0.5 mm, 0.25 mm and 0.2 mm. The influence of 1 MPa tensile failure criterion is also shown for the 0.25 mm mesh. The theoretical end of the shock pressure on the target for the theoretical case is indicated with an asterisk.
The analytical result underestimates the elastic energy quite a lot, which could be expected from the slow drop in pressure by the release waves

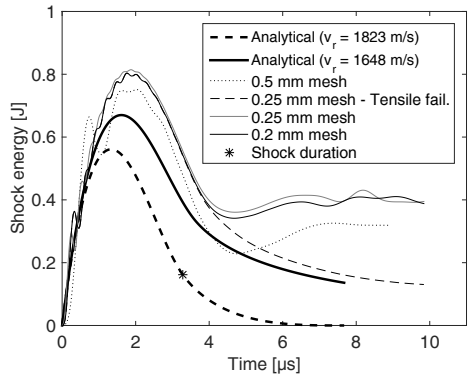

Figure 4.28: Shock energy: analytically (using Eq 4.40 and 4.42) and numerically.

(Figure 4.24a). The influence of this slow pressure drop is shown by reducing the release wave speed, which clearly makes the analytical result better correspond with the simulations. Nevertheless, the shape of the curve is very well represented. The deviation of the simulations without tensile failure from the shape of the analytical result at approximately 4 μs is because of a tensile wave that starts to form right after the pressure drops to zero. The influence of this tensile wave will be further investigated in a next section.

Compared to the initial kinetic energy of 7.1 J, up to 10% approximately is temporarily converted to elastic energy at impact. According to the peak pressure in the centre, the 0.25 mm mesh is converged. This can be concluded from the elastic energy curve as well, both the 0.25 mm and 0.2 mm mesh give a very similar elastic energy curve over time.

The influence of the impact velocity for the 0.25 mm mesh is shown in Figure 4.29a. The shock energy seems to have a more or less quadratic relationship with the speed (a similar trend can be found with the analytical expression). This is partly because the shock pressure increases slightly higher than linear with the speed, but also because the relative difference between the shock and release wave speed increases at higher impact speeds.

The elastic energy for a larger projectile with a 25 mm radius and 50 mm long bird with a 2 mm, 1.5 mm and 1 mm mesh is shown in Figure 4.29b.

The shock energy increases when the mesh is refined. The peak of the 2 mm mesh for example is only 88 % of the peak of the densest mesh.

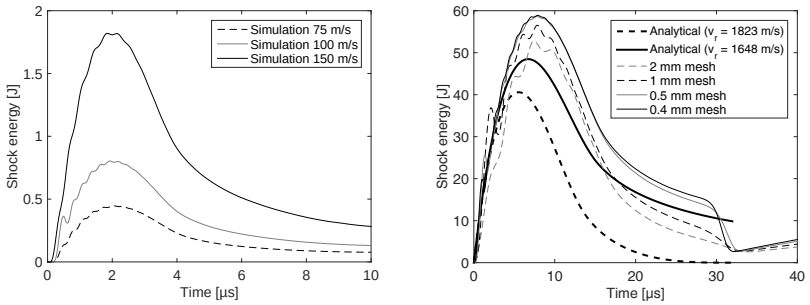

(a) Shock energy in function of speed.

(b) Shock energy for a larger projectile ($r = 25\,\mathrm{mm}$ and $l = 50\,\mathrm{mm}$), analytically (using Eq 4.40 and 4.42) and numerically.

Figure 4.29: Influence speed and projectile size on shock energy.

Because of the smaller l/d ratio (1 opposed to 2), reflection at the back of the projectile should occur at approximately $l/v_s = 28.6\,\mu$s. In the simulations, a drop can be observed in the shock energy curves around $30\,\mu$s after impact. This drop is the result of the tensile failure criterion which makes the existence of a (tension) reflective wave impossible. For a normal $l/d = 2$ ratio however, the drop is much less because the shock wave has much more time to dissipate.

The elastic energy can serve as an indicator for the presence of the shock regime. Comparing the shock energy between flat cylinders and cylinders with hemispherical ends for example clearly shows the negligible shock regime in case of the hemispherical ends. This is illustrated in Figure 4.30a, showing the elastic energy for the three hemispherical meshes considered in section 4.3.3 compared to the shock energy of the similar 0.25 mm flat cylinder plotted in Figure 4.28. This gives a much better impression of the shock regime for a cylinder with hemispherical ends compared to the shock pressure measurement at the centre, which exists only very locally at the impact point (Figure 4.23). When the speed is increased, the front surface impacts the plate quicker, but still, even for an impact at 250 m/s, the elastic energy

reaches only half of the energy of the flat end at 100 m/s, while the impact kinetic energy is 6.25 times higher (Figure 4.30b).

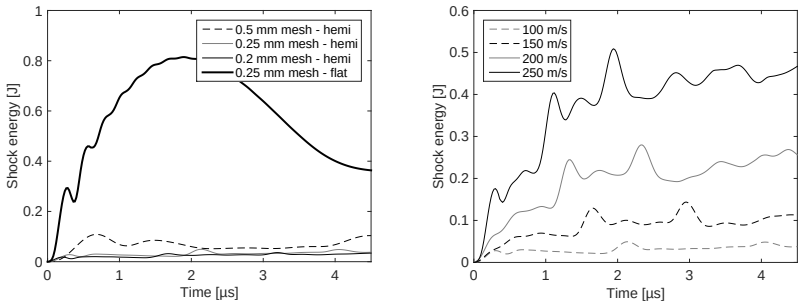

(a) The much lower shock energy for a hemispherical end.

(b) Influence of the speed on the shock energy.

Figure 4.30: Shock energy for a hemispherical end.

The exact same conclusion can be made for the larger $r = 25\,\text{mm}$ and $l = 50\,\text{mm}$ projectile using a 0.8 mm mesh (25 J for a 250 m/s impact of the cylinder with hemispherical ends compared to the 60 J for the 100 m/s impact of the cylinder with flat ends shown in Figure 4.29b).

In a bird strike experiment, the shape is never strictly flat or hemispherical but often something in between as a result of the launching process. The shock energy therefore lies somewhere between the negligible shock pressure of a hemispherical end and the amplitude of the shock energy in case of the flat end. A continuously decreasing energy amplitude could be observed when changing the hemisphere gradually to a flat end (creating intermediate scenarios using ellipsoïd shaped ends).

4.3.5 The influence of the deformability of the target structure

The shock regime is defined by a very short, very high pressure pulse. In the simulations, this regime is typically tested on (or assuming) rigid target surfaces. Also for experimental research, a good approximation of a rigid surface is a requirement to obtain precise pressure measurements. How this regime is influenced by a deformable target however and how it affects the pressure measurement, can be questioned. Therefore, several simulations

are performed to give an idea of how much the shock regime is influenced by deformability. The larger $r = 25\,\text{mm}$ and $l = 50\,\text{mm}$ projectile with a $0.8\,\text{mm}$ mesh is used in these simulations to obtain a practical scale of target parameters.

In an extreme case, the influence of the deformation of a bulk block of material can be considered. More specifically, a steel cube with a size of $100 \times 100 \times 100\,\text{mm}^3$ is used as target structure. According to Wilbeck, the pressure is reduced when impacting a deformable bulk target. The pressure is reduced with a factor equal to the weighed sum of the density times the shock velocity of the target (Wilbeck, 1978*b*). For a steel bulk material, the pressure would be reduced by 4%. Figure 4.31 shows a comparison of the developed particle pressure together with the theoretical shock pressure and a 4% lower shock pressure. The particle pressure indeed is slightly reduced, except for the overshoot at the end. From the start of impact up to $10\,\mu\text{s}$, the centre of the steel contact surface is pushed in linearly up to $38\,\mu\text{m}$, after which the surface returns to its original position over another $10\,\mu\text{s}$. The influence of the deformation therefore diminishes around $10\,\mu\text{s}$, after which the opposite effect occurs when the surface returns to its original position, resulting in a shock pressure that slightly increases above the pressure signal of the rigid plate. Nevertheless, it can be said that apart from the 4%, the deformation of the bulk material does not have a significant influence on the shock regime.

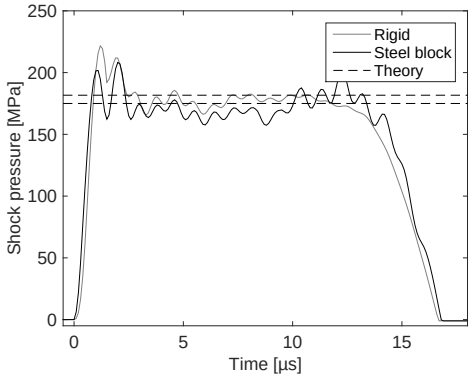

Figure 4.31: Shock pressure for an impact on a deformable steel $100 \times 100 \times 100\,\text{mm}^3$ cube (theory according to Eq 4.4 together with a 4% reduced value).

Also the mass will have an influence on the shock regime. The influence of this parameter can be investigated by reducing the inertia of a rigid target. Figure 4.32 shows the shock pressure in a centre front particle as well as the elastic energy for several inertia values. These inertia values correspond respectively with 97000% up to 5% of the impacting mass (divided by two for a normal length conform the $l/d = 2$ ratio). Only below 100 g (target mass $\approx$ projectile mass), the shock pressure starts to reduce. At 5% of the impacting mass, the shock energy is roughly 10% of the shock energy in case of a rigid target.

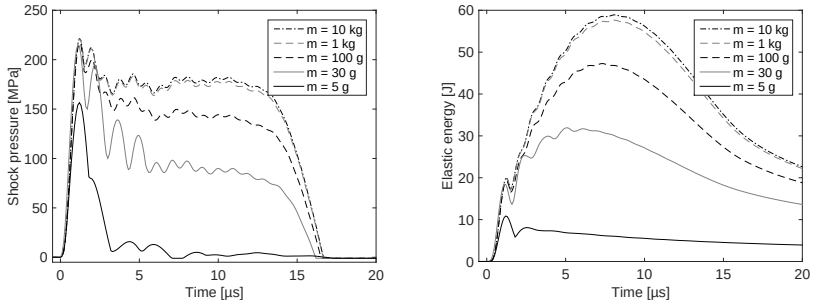

(a) Influence of the target inertia on the shock pressure.

(b) Influence of the target inertia on the elastic energy.

Figure 4.32: Influence of the target inertia.

Combining the decreased mass and deformability into one target can be done by considering a thin deformable flat plate, more conform a booster vane for example. According to Wilbeck, reflection waves travel between both surfaces of the plate which cause an increase in particle velocity and therefore a decrease in pressure (Wilbeck, 1978*b*). To get an idea of the shock regime that is formed, the shock energy is monitored and compared for an impact on a 1 mm, 2 mm and 4 mm thick 100×50 mm plate clamped at the two shortest edges by the larger $r = 25$ mm and $l = 50$ mm projectile with a 0.8 mm mesh. The elastic energy for the projectile in function of time and the deflection of the plate roughly 20 μs after impact are shown in Figure 4.33a. Figure 4.33a includes the shock pressure from the steel block described before.

There is a steady decrease, but even for a 2 mm plate, still 50% of the shock energy is present compared to a rigid plate impact (see also Figure

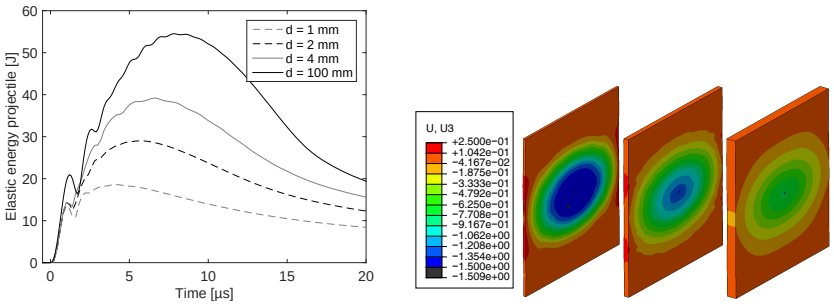

(a) Influence of the plate thickness on the elastic energy.

(b) Displacement in the impact direction for a 1 mm, 2 mm and 4 mm thick plate.

Figure 4.33: Displacement in the impact direction $20\,\mu$s after impact.

4.29b). Figure 4.33b shows the local deformation. For the three plates a circular shaped displacement can be observed, which is higher for decreasing thickness. Away from the impact location, no displacement can be observed yet. These results indicate that failure during the shock regime therefore can occur very locally.

4.4 Simulation of the steady state regime

After the shock wave is dissipated, with or without reflections, a steady state regime starts to form, characterized by a continuous radial flow which lasts until all of the mass has lost its momentum in the impact direction. According to Wilbeck, the steady state pressure at the centre of impact should be 5.2 MPa for a 100 m/s impact of a 1040 kg/m^3 gelatine mixture (Equation 4.8). Figure 4.34 shows a section cut of a coarser version of the cylinder impact scenario introduced in section 4.3 for a range of pressures between -1 MPa and 5.2 MPa. The pink particles indicate a pressure higher than 5.2 MPa. A lot of noise can be observed in the pressure distribution.

The contact pressure at the plate cannot be monitored any more in a particle, because the set of particles at a certain point in space changes continuously (there is a considerable flow in contrast to the shock regime). The contact pressure in this regime is rather an impact of particles than the contact of a

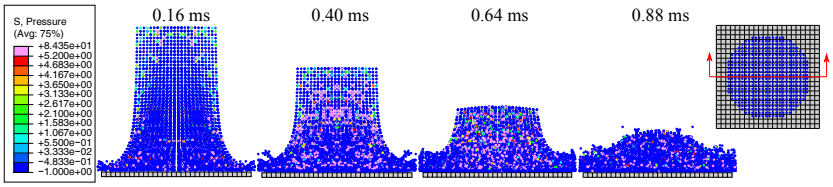

Figure 4.34: Pressure distribution of the steady state regime for a $100\,\mathrm{m/s}$ impact of a gelatine flat cylinder.

continuum body. Therefore a lot of particles per plate element are needed to get a continuous pressure signal on plate element level.

4.4.1 Rebounce effect

Before considering the steady state pressures, a closer look is taken into the transition between shock and steady state regime for a flat cylinder. Figure 4.35 shows four centre layers of particles for the $100\,\mathrm{m/s}$ impact also shown in Figure 4.34. The big pink area in the first subfigure is the shocked region, with a considerably higher pressure than the steady state pressure.

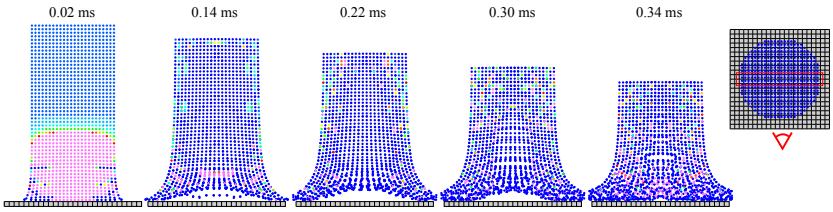

Figure 4.35: Rebounce effect between the shock and steady state regime for a $100\,\mathrm{m/s}$ flat gelatine cylinder impact.

The material bounces back right after the shock pressure at the target is vented. The rebounce of the material is the result of the tensile wave that starts to form after the drop of the shock pressure. Because there is no vacuum pressure that would prevent the impacting surface from bulging out, and cavitation is not supported by the material model, the material starts to move in the other direction. Cavitation has been observed in impacting drops and jets as well (Field et al., 2012), proving the existence of a tensile wave during impact.

This phenomenon is translated in a zero pressure period just after the shock regime. This behaviour has been observed in several numerical pressure measurements found in literature as well, but not explicitly mentioned (Blair, 2008; Simulia, n.d.; Ugrčić, 2012; Chalipat and Shankapal, 2002; Jain and Shivayogi, 2006; Airoldi and Cacchione, 2006; Smojver and Ivančević, 2010*b*; Mol and Salem, 2012). Also for hemispherical ends, a short drop to zero pressure was already observed (Lavoie et al., 2007*a*,*b*, 2009). The observation of this effect for hemispherical ends depends on the mesh size of the projectile because, as mentioned before, the initial contact is always a flat surface. It also depends a lot on the target element size, because the contacting surface and therefore also the surface over which material is bounced back is much smaller.

4.4.2 Steady state pressure

The hemispherical 0.8 mm mesh with a radius of 25 mm and a length of 100 mm is used to investigate the steady state pressures. The element size of the target plate is increased to a width of $8 \times 8\,\text{mm}^2$ to have 100 particles/element and assure a continuous pressure signal. From the centre to the edge of the plate, the single node surface forces are tracked and divided by $64\,\text{mm}^2$ to obtain an average pressure over the represented area. As mentioned in section 4.2.4.2, the force on element level is transferred to the surrounding nodes so the pressure distribution will only be an approximation. Averaging out can capture linear gradients. Especially in the centre, the pressure therefore can be slightly lower.

Including the shock pressure at the start of impact or the decay near the end of impact would not be correct. In literature, it has been suggested to use the average of the pressure between $1/3T$ and $2/3T$, where T stands for the impact duration (Simulia, n.d.; Airoldi and Cacchione, 2006). Figure 4.36a shows the pressure signal at the centre node for a 100 m/s impact, including the two boundaries between which the pressure will be averaged out (0.33 ms and 0.67 ms) and the theoretical steady state pressure. The steady state pressure corresponds very well with the theory. An average pressure of 5.1 MPa is obtained, compared to the theoretical pressure of

5.2 MPa (determined in the previous section with Equation 4.8).

Figure 4.36b shows the pressure distribution along the radius for 100 m/s, 150 m/s and 200 m/s, together with the two analytical expressions introduced in section 4.1.2. The shape is represented quite well. There is a only a slight overestimation at a radial position of 20 mm. Similar pressure distributions have also been observed by (Airoldi and Cacchione, 2006) for a Lagrangian mesh or slightly off in (Lavoie et al., 2009) for a SPH bird.

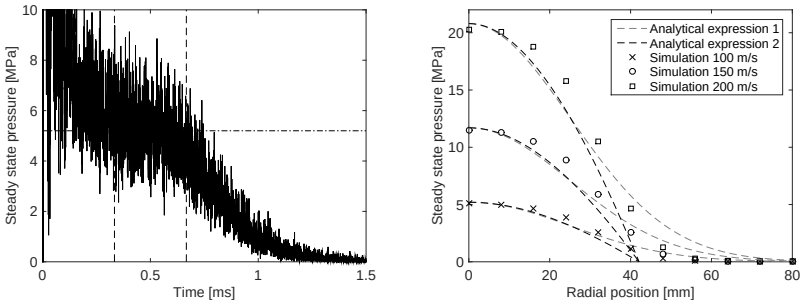

(a) Pressure signal at the centre node with the $1/3T$ and $2/3T$ interval and the theoretical steady state pressure (Eq 4.8).

(b) Steady state pressure distribution along the radius for $100\,\mathrm{m/s}$, $150\,\mathrm{m/s}$ and $200\,\mathrm{m/s}$ (compared to the analytical expressions from Eq 4.9 and Eq 4.10).

Figure 4.36: Steady state pressures.

4.5 Experimental pressure measurements

In this section, the results of several experimental pressure measurements will be covered, to investigate and validate several analytical models and numerical observations. The impact target used in this study is briefly introduced in section 4.5.1, the input conditions are covered in section 4.5.2, after which the results are discussed in section 4.5.3.

4.5.1 Pressure measurement set-up

To make an infinitely rigid experimental set-up is impossible. A rigid set-up however can be approximated by making a very stiff structure. This can be

done by creating a high confined inertia, which should have a minor effect on the pressure measurement (see also section 4.3.5). In this experimental study, the high confined inertia is achieved with a solid steel bar. Figure 4.37 shows the different parts of the set-up. The sensor (1) is mounted in an insert (2) which on its turn is screwed into the so-called sensor head (4). A 20 mm thick steel plate (3) enlarges the impact surface. Three bolts mount the steel plate (3) together with the sensor head (4) to the inertia in the shape of a solid steel bar (5). The entire assembly weighs approximately 100 kg and is positioned at the correct height. A drill-hole in the sensor head allows the data acquisition cable to reach the sensor.

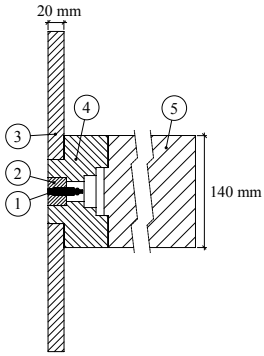

(a) Section cut.

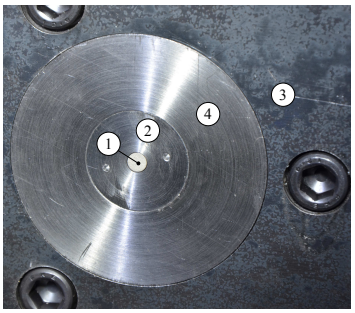

(b) Front of the set-up.

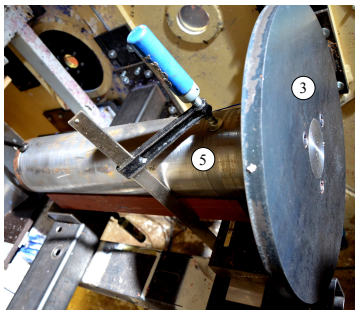

(c) Side of the set-up.

Figure 4.37: The impact pressure measurement set-up.

The three cameras are used to get a good overview of the impact conditions. Two cameras record an overview from the top and the side at 10.000 fps, while a third camera records the impact of the front surface at 125.000 fps (with a shutter time of 1/125.000 s). The goal of this third camera is to get

a better overview of the shock regime: where the high pressures occur and in which direction jets are initiated.

4.5.2 Test matrix

In total, ten experiments are performed: three experiments with 1:6 MR gelatine birds, three with porous 1:6 MR gelatine birds and four experiments with pigeons. Three out of the ten tests are not completely successful, as a result of the threaded connection with the data acquisition cable at the back of the sensor. Vibrations of the set-up occasional causes disconnections at this location, causing a zero shift in the pressure signal. The best solution for this is to retighten the connection before each test. Table 4.1 contains the impact conditions, the obtained peak and steady state pressures and zero shift of the pressure signal. Important to note is that the resolution of the signal is 0.13 MPa (very high shock pressures need to be measured as well as relatively low steady state pressures, resulting in a relatively low pressure resolution for the lower pressures). Most shifts are in the order of magnitude of the noise level, but for PM-2, PM-3 and PM-5, disconnections occurred and a relatively high zero shift is obtained.

Table 4.1: Test matrix impact pressure measurements (P_H: Hugoniot pressure, P_S: steady state pressure).

Test	**Bird**	**v [m/s]**	**P_H [MPa]**	**P_S [MPa]**	**Shift [MPa]**
PM-1	1:6 MR	113.6	44.4	7.43	-0.79
PM-2	1:6 MR	121.3	189.3	×	-1.42
PM-3	1:6 MR	132.1	439.6	×	-5.55
PM-4	Porous	109.2	38.8	7.52	-0.01
PM-5	Porous	122.2	117.0	×	-4.88
PM-6	Porous	131.7	30.5	9.18	-0.65
PM-7	Pigeon	108.5	×	7.99	-0.03
PM-8	Pigeon	116.5	×	9.50	0.03
PM-9	Pigeon	128.0	×	9.54	0.26
PM-10	Pigeon	139.3	108.1	10.66	-0.84

Note: The porous birds are composed from a 1:6 gelatine MR, mixed with microballoons.

The peak pressures are obtained by averaging the pressures in a stable high pressure region. A pressure significantly higher than the steady state

pressure however, is not always observed (indicated by an $\times$ in Table 4.1).

The steady state pressures are obtained by averaging the pressure between $1/3T$ and $2/3T$. This interval however depends to a great extent on the assumed start and end of impact. For each experiment, the start of the signal is assumed to be the time at which the pressure starts to rise. The end of impact on the other hand, which defines T, is quite a subjective parameter. Here, the impact duration is obtained by (i) dividing the length of the bird by the impact speed or (ii) by estimating the time at which the pressure drops back to zero. The length of the bird however is not always the same as the one measured before launch. For the gelatine birds, the first method is used (the length can be estimated quite well), and for the real birds the second method is used (the neck of the bird does not always impact first and the length of the bird is also quite different).

Because the shock regime for hemispherical substitute birds occurs only very locally and the shock duration is significantly shorter, the choice is made to cut off the hemispherical front of the gelatine birds, to have a flat front impacting the sensor and therefore increase the possibility to measure a shock amplitude.

In the following section, the results of the pressure measurements will be discussed.

4.5.3 Results

In this section, first a general overview of the steady state pressure will be given. Afterwards, for each type of bird, the pressure signals including the shock regime will be further investigated in the corresponding subsections. Figure 4.38 shows the steady state pressure together with some analytically determined steady state pressure curves.
In this figure, for the three types of bird, three analytical steady state pressures are included:

- **Gelatine birds:** The analytical curve assuming incompressibility is obtained directly from the gelatine density (assuming $1040\,\mathrm{kg/m^3}$) and impact velocity (Equation 4.8).

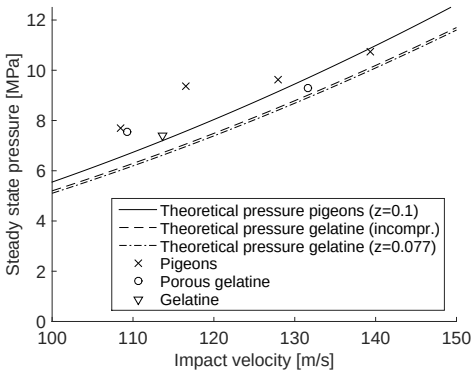

Figure 4.38: Overview experimentally measured steady state pressures.

- **Porous birds:** Compressibility is taken into account (obtained by numerically integrating the left term in Equation 4.7). The porosity factor for the porous gelatine mixtures ($z = 0.077$) is obtained assuming a gelatine and mixture density of respectively $1040\,\mathrm{kg/m^3}$ and $960\,\mathrm{kg/m^3}$.
- **Real birds:** Also here, compressibility is taken into account. The densities of the real birds are obtained from Equation 1.1 (approximately $1020\,\mathrm{kg/m^3}$). For the porosity factor of 0.1 proposed in Wilbeck's work (Wilbeck, 1978*a*), a solid density of $1133\,\mathrm{kg/m^3}$ is assumed to obtain a mixture density of $1020\,\mathrm{kg/m^3}$.

The analytically calculated steady state pressure curves are quite similar. The one for the real birds is only slightly higher.

Despite the influence of the assumed impact duration T, the measured steady state pressures correspond quite well with the analytical results. In general, the steady state pressure seems to be slightly higher. For the scarce amount of tests, no clear distinction can be observed between the different bird types.

4.5.3.1 1:6 MR gelatine birds

Only for PM-1, a reliable steady state pressure is obtained. In Figure 4.39, a zoom on the steady state regime is shown. The red part of the pressure curve indicates the area over which the steady state pressure is averaged (the

horizontal grey line represents this average) and the solid and dashed black horizontal line respectively indicate the analytical steady state pressure for non-porous and porous gelatine.

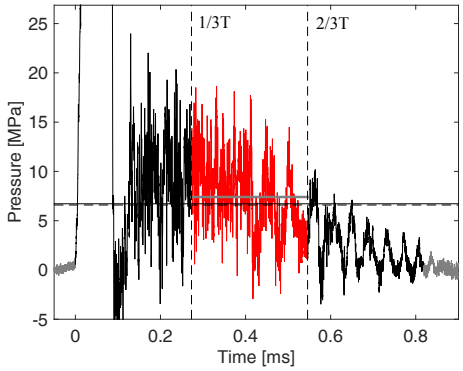

Figure 4.39: Shock and steady state pressure PM-1.

Two things can be observed. First of all, around 0.1 ms, the pressure drops back to zero, as was also observed in the numerical simulations (section 4.4.1). Disregarding the zero shift in PM-2, a drop to zero was also observed in this pressure signal right after the shock regime. Secondly, the analytical pressure approximates very well the pressure in the steady state regime, although it is rather a steadily decreasing than a constant (steady state) pressure. Because of the decreasing steady state pressure, the influence of T will be significant. Likely, a more constant steady state pressure will be obtained when shooting with bigger (rather longer) projectiles.

The shock pressures for the three tests with gelatine are shown in Figure 4.40. The solid and dashed black line respectively indicate the theoretical non-porous and porous shock pressure.
The shock pressure is twice much lower and once significantly higher than the theoretical pressure indicated by the black horizontal lines. If anything can be concluded, it is the fact that the front shape has a high influence on the obtained shock pressures and that most likely, dependent on the location where the pressure is measured, very different shock pressures can be obtained. Figure 4.41 shows a sequence of images from test PM-3 (the red indication shows a high speed jet that is formed), taken with the third

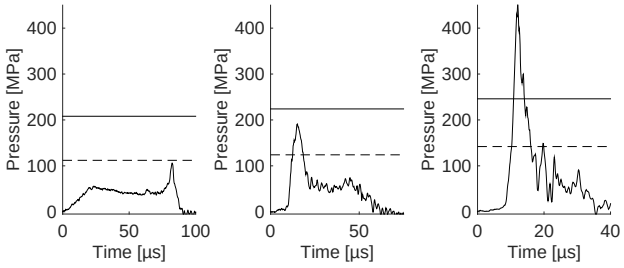

Figure 4.40: Shock pressure for test PM-1, PM-2 and PM-3.

camera. Light flashes can be observed during impact, which could be the result of adiabatic compression of air entrapped between solid and liquid (Brunton, 1966) or a mechanoluminescence property of gelatine at high pressures. Possibly a slightly non-parallel impact surface resulted in an increase of the shock pressure up to almost double the theoretical value, as was also observed in section 4.3.2.

Theoretically, the shock duration should be around 32 μs for the three tests. For the third test, the shock duration is shorter (and the shock pressure higher), which is a trend that was also observed in section 4.3.2 (as a result of release waves that can vent the shock pressure sooner).

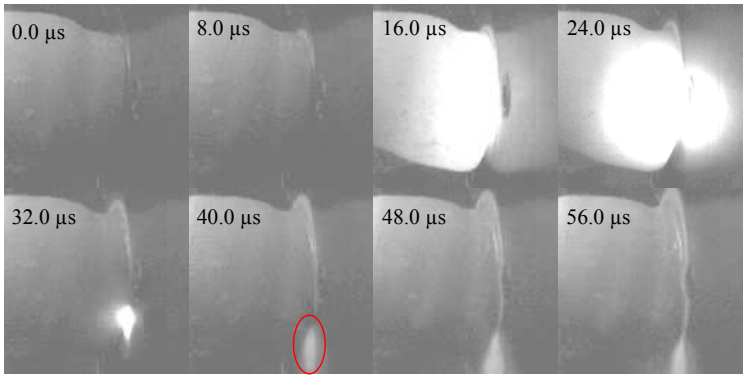

Figure 4.41: First impact of experiment PM-3.

4.5.3.2 Porous 1:6 MR gelatine birds

Figure 4.42 shows the steady state pressures for PM-4 and PM-6. Again, the steady state pressure is steadily decreasing, which results in a measured average steady state pressure that depends highly on the assumed impact time T. Especially for PM-6, the analytical value represents the steady state regime quite well. For PM-6, a drop to zero pressure is again observed right after the pressure peak.

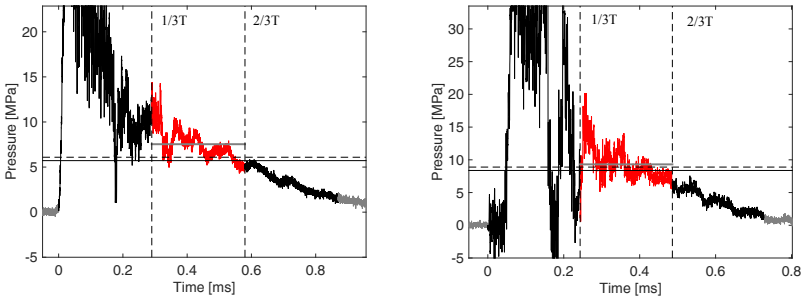

(a) Test PM-4. **(b)** Test PM-6.

Figure 4.42: Steady state pressures porous 1:6 MR gelatine birds.

The pressure in the steady state regime oscillates less than the non-porous gelatine birds, which can also be observed in the pressure signals of Wilbeck (Wilbeck, 1978*b*).

Figure 4.43 shows the shock peaks observed in the three tests with porous birds. Only in PM-5, the front surface is well aligned with the target surface and the shock pressure amplitude corresponds well with the analytical result. The shape of the pulse and the large oscillations however make the measurement less trustworthy. Possibly, the first disconnection occurred already around 10 μs.

Wilbeck obtained a very good correlation between the measured shock pressure and the analytical curves (Figure 41, Wilbeck 1978*b*), for flat cylinder porous birds with a porosity factor of 0.4. This would have required projectiles which maintained their shape well during stripping and with a very good alignment with the target surface.

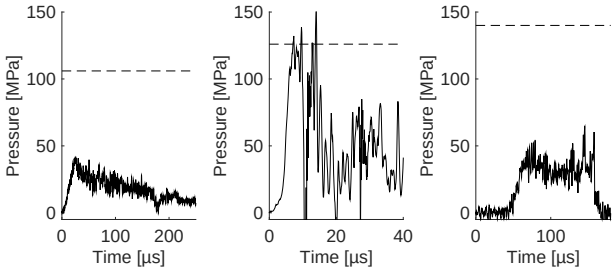

Figure 4.43: Shock regime test PM-4, PM-5 and PM-6.

4.5.3.3 Pigeons

In Figure 4.44, the steady state pressures for the four experiments with pigeons are shown. Compared to the experiments with gelatine, relatively large fluctuation of the pressures occur in the steady state regime, which might be an indication of the bird not being as homogeneous as expected at these impact speeds. Disregarding these heterogeneities, the steady state pressure corresponds well with the analytical results.

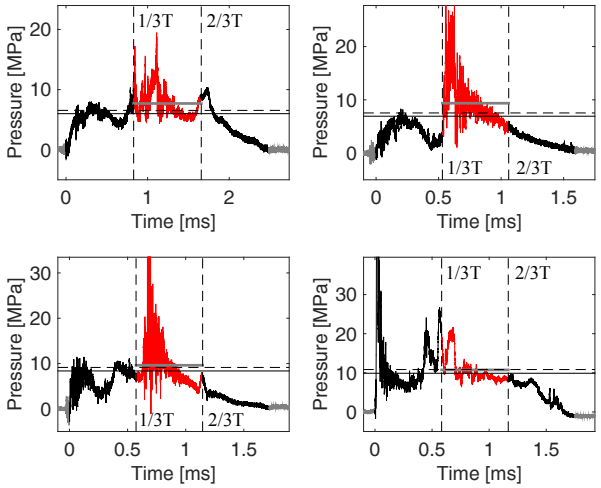

Figure 4.44: Steady state pressures for the four experiments with pigeons.

The birds are shot with the head first. The high speed images show that for the first three tests, the head impacts roughly 10 mm away from the sensor.

Only for PM-10, the head impacted the sensor directly and a shock pressure is measured (Figure 4.45).

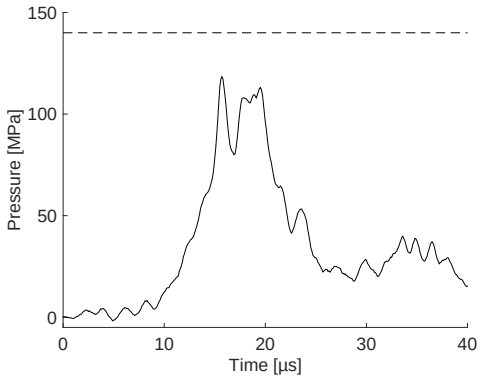

Figure 4.45: Shock pressure PM-10.

The peak pressure is slightly lower than the theoretical value. The analytical value however is based on many assumptions and it can be questioned to what extent these are always valid. The assumptions are the following:

- The average density is used to calculate the theoretical shock pressure, based on the logarithmic function introduced in chapter 2. The logarithmic function however is fitted on data with a lot of scatter. It can also be questioned if the local density in the head (combination bone, brain, beak, etc.) resembles well with the average density.
- The equation of state (speed of sound and k-factor) is assumed to be equal to water. The equation of state might also vary between the different parts of the bird.
- A porosity factor of 0.1 is used. Contrary to the gelatine, the porosities in a real bird are likely much more heterogeneous. The porosity in the head therefore can be much lower.

In fact, the analytical shock pressure is entirely defined by these parameters. In Wilbeck's results, a high deviation is therefore also obtained in the obtained shock pressures. But, the measured shock pressures are always beneath the theoretical shock pressure of this reference mixture (Wilbeck, 1978*b*). In terms of shock pressure, porous gelatine therefore might indeed

be a conservative mixture with shock pressures still significantly less than pure gelatine.

4.6 Conclusion

In this chapter, an introduction to bird modelling is given. The analytical models describing the shock and steady state regime are introduced, the numerical techniques with a focus on SPH are covered and the bird material models, focussing on the equation of state are defined and compared.

The remainder of the chapter summarizes a study on the shock and steady state regime. The following conclusions can be made for the shock regime:

- The shock pressure pulse (amplitude, shape and duration) is investigated with a flat ended projectile. Using relatively fine mesh sizes with deliberately decreased time increments results in very accurate shock pressure pulses that correspond with the analytical models from literature.
- In contrast with the prediction of Wilbeck, simulations show that slightly tilting the projectile can increase the shock pressure up to 190% of the analytical value.
- The impact of hemispherical ended projectiles results in shock pressures equal to the flat ended projectiles as can be predicted by the theory.
- An analytical model is developed for the elastic energy in the shock region. The shape of this curve resembles well with the simulation, but the amplitude is underestimated due to a simplified representation of the release waves. The elastic energy shows to be a good measure for the presence of the shock regime. This shows that the shock regime for hemispherical ends is relatively negligible.
- The influence of mass and deformability of the target is investigated. It can be concluded that only for very low masses or thin plates, the shock energy starts to decrease significantly and that local failure indeed can occur during the shock regime.

For the steady state regime, the following conclusions can be made:

- When the shock regime transitions to the steady state regime, the material or mesh bounces back from the target as a result of a tensile wave that starts to form after the shock regime. This phenomenon can also be observed in literature.
- The steady state pressure profiles correspond well with the expressions developed in literature.

Finally, several experimental impact pressure measurements are performed and investigated, showing a good correlation with the analytical models and the simulations. Also in the experiments, peak pressures above the analytical value are detected as was also observed in simulations. The rebounce effect observed in the simulations can also be observed in several experiments.

4.7 Bibliography

Abaqus 6.14 documentation (2014).

Abrate, S. (2015), 'Soft impacts on aerospace structures', *Progress in Aerospace Sciences* .

Airoldi, A. and Cacchione, B. (2005), 'Numerical analyses of bird impact on aircraft structures undergoing large deformations and localised failures', *International conference on impact loading of lightweight structures* **49**, 1–18.

Airoldi, A. and Cacchione, B. (2006), 'Modelling of impact forces and pressures in Lagrangian bird strike analyses', *International Journal of Impact Engineering* **32**(10), 1651 – 1677.

Anghileri, M., Milanese, A., Moretti, G. and Castelletti, L. (2012), Preliminary investigation on the feasibility of a bird surrogate for full-scale bird impact test, *in* 'Proceedings of the 28th ICAS congress', pp. 1–8.

Anghileri, M. and Sala, G. (1996), Theoretical assessment, numerical simulation and comparison with tests of birdstrike on deformable structures, *in* 'Proceedings of the 20th ICAS congress', pp. 665–674.

Attaway, S., Heinstein, M. and Swegle, J. (1994), 'Coupling of smooth particle hydrodynamics with the finite element method', *Nuclear Engineering and Design* **150**(23), 199 – 205.

Azevedo, R. and Alves, M. (2007), Numerical simulation of bird strike impact against balanced fiberglass/epoxy composite plates, *in* '19th International Congress of Mechanical Engineering'.

Azevedo, R. L. and Alves, M. (2009), 'Numerical simulation of soft-body impact on GFRP laminate composites: mixed SPH-FE and pure SPH approaches', *Mechanics of Solids in Brazil* pp. 15 – 30.

Banks, R. B. and Chandrasekhara, D. V. (1963), 'Experimental investigation of the penetration of a high-velocity gas jet through a liquid surface', *Journal of Fluid Mechanics* **15**, 13–34.

Barber, J. P., Taylor, H. R. and Wilbeck, J. S. (1975), Characterization of bird impacts on a rigid plate: Part 1, Technical Report AFFDL-TR-75-5, Dayton University.

Benson, D. J. (1992), 'Computational methods in lagrangian and eulerian hydrocodes', *Computer Methods in Applied Mechanics and Engineering* **99**(23), 235 – 394.

Blair, A. (2008), Aeroengine fan blade design accounting for bird strike, Master's thesis, University of Toronto.

Brockman, R. A. and Held, T. W. (1991), Explicit finite element method for transparency impact analysis, Technical Report WL-TR-91-3006, University of Dayton Research institute.

Brunton, J. H. (1966), 'High speed liquid impact', *Philosophical Transactions of the Royal Society of London. Series A, Mathematical and Physical Sciences* **260**(1110), 79–85.

Chalipat, S. and Shankapal, S. (2002), 'Characterization of bird impact properties using finite element code', pp. 56–62.

Challita, A. (1980), Validation of a bird substitute for development and qualification of aircraft transparenciles, Technical Report AFWAL-TR-80-3098, University of Dayton Research Institute.

Challita, A. and Barber, J. P. (1979), The scaling of bird impact loads, Technical Report AFFDL-TR-3042, University of Dayton Research Institute.

Challita, A. and West, B. S. (1980), Effects of bird orientation at impact on load profile and damage level, Technical Report AFWAL-TR-3009, University of Dayton Research Institute.

Chen, S., Fatemi, M. and Greenleaf, J. F. (2002), 'Remote measurement of material properties from radiation force induced vibration of an embedded sphere', *The Journal of the Acoustical Society of America* **112**(3), 884–889.

Chuan, K. C. (2006), Finite element analysis of bird strikes on composite and glass pannels, Master's thesis, National University of Singapore.

Chuan, Z., Xiang-hua, J., Xiang-hai, C. and Tong-cheng, S. (2015), 'TC4 hollow fan blade structural optimization based on bird-strike analysis', *Procedia Engineering* **99**, 1385 – 1394.

Cronin, D. (2011), 'Ballistic gelatin characterization and constitutive modeling'.

Dar, U. A., Zhang, W. and Xu, Y. (2013), 'FE analysis of dynamic response of aircraft windshield against bird impact', *International Journal of Aerospace Engineering* p. 12.

Deal, W. E. (1957), 'Shock hugoniot of air', *Journal of Applied Physics* **28**(7), 782–784.

Donea, J., Huerta, A., Ponthot, J.-P. and Rodrguez-Ferran, A. (2004), Arbitrary LagrangianEulerian methods, *in* 'Encyclopedia of Computational Mechanics', John Wiley & Sons, Inc., chapter 14, pp. 1–15.

Engel, A. and Bashford, G. (2015), 'A new method for shear wave speed estimation in shear wave elastography', *IEEE Transactions on Ultrasonics, Ferroelectrics, and Frequency Control* **62**(12), 2106–2114.

Ensan, M. N., Zimcik, D., Lahoubi, M. and Andrieu, D. (2008), 'Soft body impact simulation on composite structures', *Transactions ofthe CSME /de la SCGM* **32**, 283–296.

Field, J. (1999), 'ELSI conference: invited lecture: Liquid impact: theory, experiment, applications', *Wear* **233235**, 1 – 12.

Field, J., Camus, J.-J., Tinguely, M., Obreschkow, D. and Farhat, M. (2012), 'Cavitation in impacted drops and jets and the effect on erosion damage thresholds', *Wear* **290291**, 154 – 160.

Georgiadis, S., Gunnion, A. J., Thomson, R. S. and Cartwright, B. K. (2008), 'Bird-strike simulation for certification of the Boeing 787 composite moveable trailing edge', *Composite Structures* **86**(13), 258–268.

Grimaldi, A., Sollo, A., Guida, M. and Marulo, F. (2013), 'Parametric study of a SPH high velocity impact analysis a birdstrike windshield application', *Composite Structures* **96**, 616 – 630.

Guida, M. (2008), Study, design and testing of structural configurations for the bird-strike compliance of aeronautical components, PhD thesis, University of Naples "Federico II".

Guida, M. (2011), SPH High Velocity Impact Analysis - A Birdstrike Windshield Application, PhD thesis, University of Naples "Federico II".

Guida, M., Marulo, F., Meo, M., Grimaldi, A. and Olivares, G. (2011), 'SPH lagrangian study of bird impact on leading edge wing', *Composite Structures* **93**(3), 1060 – 1071.

Guida, M., Marulo, F., Meo, M. and Russo, S. (2013), 'Certification by birdstrike analysis on C27J fullscale ribless composite leading edge', *International Journal of Impact Engineering* **54**, 105–113.

Haller, K. K., Ventikos, Y., Poulikakos, D. and Monkewitz, P. (2002), 'Computational study of high-speed liquid droplet impact', *Journal of Applied Physics* **92**(5), 2821–2828.

Hanssen, A., Girard, Y., Olovsson, L., Berstad, T. and Langseth, M. (2006), 'A numerical model for bird strike of aluminium foam-based sandwich panels', *International Journal of Impact Engineering* **32**(7), 1127 – 1144.

Hedayati, R., Sadighi, M. and Mohammadi-Aghdam, M. (2014), 'On the difference of pressure readings from the numerical, experimental and

theoretical results in different bird strike studies', *Aerospace Science and Technology* **32**(1), 260–266.

Hedayati, R. and Ziaei-Rad, S. (2013), 'A new bird model and the effect of bird geometry in impacts from various orientations', *Aerospace Science and Technology* **28**(1), 9 – 20.

Hedayati, R. and Ziaei-Rad, S. (2014), 'New bird model for simulation of bird strike on various layups used in transparent components of rotorcrafts', *Journal of Aerospace Engineering* **27**(1), 76–85.

Hedayati, R., Ziaei-Rad, S., Eyvazian, A. and Hamouda, A. M. (2014), 'Bird strike analysis on a typical helicopter windshield with different lay-ups', *Journal of Mechanical Science and Technology* **28**(4), 1381–1392.

Heimbs, S. (2011), 'Computational methods for bird strike simulations: A review', *Computers & Structures* **89**(23-24), 2093–2112. Munich, Germany.

Hernquist, L. and Katz, N. (1989), 'TREESPH - a unification of SPH with the hierarchical tree method', *Astrophysical Journal Supplement Series* **70**, 419–446.

Iannucci, L. and Donadon, M. (2006), 'Bird strike modeling using a new woven glass failure model', *9th International LS-DYNA Users Conference* .

Ivančević, D. and Smojver, I. (2011), 'Hybrid approach in bird strike damage prediction on aeronautical composite structures', *Composite Structures* **94**(1), 15–23.

Ivančević, D. and Smojver, I. (2016), 'Explicit multiscale modelling of impact damage on laminated composites part ii: Multiscale analyses', *Composite Structures* **145**, 259 – 268.

Jain, R. and Shivayogi (2006), Effect of bird material and projectile shape on temporal pressure during bird impact, *in* 'Proceedings of the Altair's user conference', pp. 1–14.

Jenq, S., Hsiao, F., Lin, I., Zimcik, D. and Ensan, M. N. (2007), 'Simulation of a rigid plate hit by a cylindrical hemi-spherical tip-ended soft impactor', *Computational Materials Science* **39**(3), 518 – 526.

Johnson, A. F. and Holzapfel, M. (2003), 'Modelling soft body impact on composite structures', *Composite Structures* **61**(12), 103 – 113.

Kim, M., Zammit, A., Siddens, A. and Bayandor, J. (2011), 'An extensive crashworthiness methodology for advanced propulsion systems, part I: Soft impact damage assessment of composite fan stage assemblies', *49th*

AIAA Aerospace Sciences Meeting including the New Horizons Forum and Aerospace Exposition .

Kirtil, E., Pestal, D., Kolofrath, A., Gänsicke, N. and Mendler, J. (2003), 'Simulating the impact behaviour of composite aircraft structures', *Abaqus user's conference* .

Kou, J. and Xu, F. (2015), 'The influence of bird's shape and attitude on bird-strike analysis of structure', *Advances in Computer Science Research* .

Kumar, P. A., Kalam, S. A. and Kumar, R. V. (2014), 'Soft body impact on aircraft structures', *International Journal of Engineering Research & Technology* **3**(10).

Langrand, B., Bayart, A.-S., Chauveau, Y. and Deletombe, E. (2002), 'Assessment of multi-physics FE methods for bird strike modelling-application to a metallic riveted airframe', *International Journal of Crashworthiness* **7**(4), 415–428.

Lavoie, M., Gakwaya, A. and Ensan, M. N. (2008), 'Application of the SPH method for simulation of aerospace structures under impact loading', *10th European LS-DYNA Users Conference* .

Lavoie, M., Gakwaya, A., Ensan, M. N. and Zimcik, D. (2007*a*), 'Review of existing numerical methods and validuation procedure available for bird strike modelling', *International Conference on Computational & Experimental Engineering and Sciences* **2**, 111–118.

Lavoie, M., Gakwaya, A., Ensan, M. N. and Zimcik, D. (2007*b*), 'Validation of available approaches for numerical bird strike modeling tools', *International Review of Mechanical Engineering* .

Lavoie, M., Gakwaya, A., Ensan, M. N., Zimcik, D. and Nandall, D. (2009), 'Bird's substitute tests results and evaluation of available numerical methods', *International Journal of Impact Engineering* **36**(1011), 1276 – 1287.

Lavoie-Perrier, M.-A. (2008), Soft body impact modelling and development of a suitable meshless approach, PhD thesis, Université Laval.

Leach, S. J., Walker, G. L., Smith, A. V., Farmer, I. W. and Taylor, G. (1966), 'Some aspects of rock cutting by high speed water jets [and discussion]', *Philosophical Transactions of the Royal Society of London. Series A, Mathematical and Physical Sciences* **260**(1110), 295–310.

Liu, G. R. and Liu, M. B. (2003), *Smoothed particle hydrodynamics : a meshfree particle method*, World Scientific, New Jersey.

Liu, J. and Li, Y. (2013), 'Numerical simulation of a rotary engine primary compressor impacted by bird', *Chinese Journal of Aeronautics* **26**(4), 926 – 934.

Liu, J., Li, Y., Gao, X. and Yu, X. (2014), 'A numerical model for bird strike on sidewall structure of an aircraft nose', *Chinese Journal of Aeronautics* **27**(3), 542 – 549.

Liu, J., Li, Y. L. and Gao, X. S. (2014), 'Bird strike on a flat plate: Experiments and numerical simulations', *International Journal of Impact Engineering* **70**, 21–37.

Liu, L., Fan, Y. and Li, W. (2014), 'Viscoelastic shock wave in ballistic gelatin behind soft body armor', *Journal of the Mechanical Behavior of Biomedical Materials* **34**, 199 – 207.

Liu, L., Jia, Z., Ma, X. L. and Fan, Y. R. (2013), 'Analytical and experimental studies on the strain rate effects in penetration of 10wt % ballistic gelatin', *Journal of Physics: Conference Series* **451**(1).

Lucy, L. (1977), 'A numerical approach to the testing of the fission hypothesis', *Astronomical Journal* **82**, 1013–1024.

Mao, R. H., Meguid, S. A. and Ng, T. Y. (2008), 'Transient three dimensional finite element analysis of a bird striking a fan blade', *International Journal of Mechanics and Materials in Design* **4**(1), 79–96.

Marulo, F. and Guida, M. (2014), 'Design criteria for birdstrike damage on windshield', *Advances in Aircraft and Spacecraft Science* **1**(2), 233–251.

Mav, R. K. (2013), Numerical analysis of bird strike damage on composite sandwich structure using Abaqus Explicit, Master's thesis, San José State University.

McCallum, S. and Constantinou, S. (2005), 'The influence of bird-shape in bird-strike analysis', *5th European LS-DYNA Users Conference* .

McCarthy, M. A., Xiao, J. R., McCarthy, C. T., Kamoulakos, A., Ramos, J., Gallard, J. P. and Melito, V. (2004), 'Modelling of bird strike on an aircraft wing leading edge made from fibre metal laminates part 2: Modelling of impact with SPH bird model', *Applied Composite Materials* **11**(5), 317–340.

Meguid, S., Mao, R. and Ng, T. (2008), 'FE analysis of geometry effects of an artificial bird striking an aeroengine fan blade', *International Journal of Impact Engineering* **35**(6), 487 – 498.

Mol, K. S. and Salem, S. C. (2012), 'Projectile parametric studies on bird impact behaviour of aircraft leading edges', *International Journal of Emerging Technology and Advanced Engineering* **2**(11), 240–246.

Monaghan, J. (1989), 'On the problem of penetration in particle methods', *Journal of Computational Physics* **82**(1), 1 – 15.

Monaghan, J. and Gingold, R. (1983), 'Shock simulation by the particle method SPH', *Journal of Computational Physics* **52**(2), 374 – 389.

Monaghan, J. J. (1992), 'Smoothed particle hydrodynamics', *Annual review of astronomy and astrophysics* **30**, 543–574.

Nagaraj, V. and Velmurugan, T. (n.d.), 'Numerical bird strike impact simulation of aircraft composite structure', *Journal of Mechanical and Civil Engineering* pp. 1–10.

Nishikawa, M., Hemmi, K. and Takeda, N. (2011), 'Finite-element simulation for modeling composite plates subjected to soft-body, high-velocity impact for application to bird-strike problem of composite fan blades', *Composite Structures* **93**(5), 1416 – 1423.

Nizampatnam, L. S. (2007), Models and methods for bird strike load predictions, PhD thesis, Wichita State University.

Orlowski, M. (2015), Experimental and Numerical Investigation on the Bird Impact Resistance of Novel Composite Sandwich Panels, PhD thesis, Cranfield University.

Ravikumar, N., Noble, C., Cramphorn, E. and Taylor, Z. A. (2015), 'A constitutive model for ballistic gelatin at surgical strain rates', *Journal of the Mechanical Behavior of Biomedical Materials* **47**, 87 – 94.

Salisbury, C. P. and Cronin, D. S. (2009), 'Mechanical properties of ballistic gelatin at high deformation rates', *Experimental Mechanics* **49**(6), 829–840.

Selezneva, M., Stone, P., Moffat, T., Behdinan, K. and Poon, C. (2012), 'Modeling bird impact on a rotating fan: The influence of bird parameters', *11th European LS-DYNA Users Conference* .

Shepherd, C. J., Appleby-Thomas, G. J., Hazell, P. J. and Allsop, D. F. (2009), 'The dynamic behaviour of ballistic gelatin', *AIP Conference Proceedings* **1195**(1), 1399–1402.

Siddens, A. and Bayandor, J. (2013), 'Multidisciplinary impact damage prognosis methodology for hybrid structural propulsion systems', *Computers & Structures* **122**, 178 – 191. Computational Fluid and Solid Mechanics

2013, Proceedings Seventh MIT Conference on Computational Fluid and Solid Mechanics.

Siddens, A., Bayandor, J. and Celestina, M. L. (2014), Detailed post-soft impact progressive damage assessment for hybrid structure jet engines, Technical Report NASA/TM-2014-218397, NASA Glenn Research Cente.

Siddens, A. J., Bayandor, J. and Abdi, F. (2012), Coupled micromechanics-finite element progressive failure dynamic analysis approach F-16 canopy case study, *in* 'Proceedings of the 28th ICAS congress', pp. 1–10.

Simulia (n.d.), 'A strategy for bird strike simulations using Abaqus/Explicit'.

Smojver, I. and Ivančević, D. (2010*a*), 'Coupled Euler Lagrangian approach using Abaqus/Explicit in the bird strike aircraft damage analysis', *2010 SIMULIA Customer Conference* .

Smojver, I. and Ivančević, D. (2010*b*), 'Numerical simulation of bird strike damage prediction in airplane flap structure', *Composite Structures* **92**(9), 2016 – 2026. Fifteenth International Conference on Composite Structures.

Smojver, I. and Ivančević, D. (2011), 'Bird strike damage analysis in aircraft structures using Abaqus/Explicit and coupled Eulerian Lagrangian approach', *Composites Science and Technology* **71**(4), 489 – 498.

Smojver, I. and Ivančević, D. (2012), 'Advanced modelling of bird strike on high lift devices using hybrid EulerianLagrangian formulation', *Aerospace Science and Technology* **23**(1), 224 – 232. 35th ERF: Progress in Rotorcraft Research.

Strnad, V. and Doubrava, R. (2009), 'Utilization of air gun and methods of structural test by flying object strike for test method simulation development', *Czec Aerospace Proceedings* pp. 11–13.

Subhash, G., Kwon, J., Mei, R. and Moore, D. F. (2012), 'Non-Newtonian behavior of ballistic gelatin at high shear rates', *Experimental Mechanics* **52**(6), 551–560.

Sun, Q., Liu, Y. and Jin, R. (2014), Numerical simulation of bird strike in aircraft leading edge structure using a new dynamic failure model, *in* 'Proceedings of the 29th ICAS congress', pp. 1–10.

Tadmor, E. (2012), 'A review of numerical methods for nonlinear partial differential equations', *Bulletin of the american mathematical society* **49**(4), 507 – 554.

Tho, C.-H. and Smith, M. R. (2008), 'Accurate bird strike simulation methodology for BA609 tiltrotor', *American Helicopter Society 64th Annual Forum* .

Torvik, P. J. (1970), A simple theory for shock propagation in homogeneous mixtures, Technical Report AFIT TR 70-3, Air Force Institute of Technology, Wright-Patterson Air Force Base.

Ugrčić, M. (2012), 'Application of the hydrodynamic theory and the finite element method in the analysis of bird strike in a flat barrier', *Scientific Technical Review* **62**, 28–37.

Urban, M. W., Fatemi, M. and Greenleaf, J. F. (2010), 'Modulation of ultrasound to produce multifrequency radiation forcea)', *The Journal of the Acoustical Society of America* **127**(3), 1228–1238.

Urban, M. W., Nenadic, I., Chen, S. and Greenleaf, J. F. (2010), 'Generalized response of a sphere embedded in a viscoelastic medium excited by ultrasound radiation force.', *The Journal of the Acoustical Society of America* **128**(4), 2337–2337.

Vignjevic, R., Orlowski, M., De Vuyst, T. and Campbell, J. C. (2013), 'A parametric study of bird strike on engine blades', *International Journal of Impact Engineering* **60**, 44–57.

VonNeumann, J. and Richtmyer, R. D. (1950), 'A method for the numerical calculation of hydrodynamic shocks', *Journal of Applied Physics* **21**(3), 232–237.

Wang, F. and Yue, Z. (2010), 'Numerical simulation of damage and failure in aircraft windshield structure against bird strike', *Materials & Design* **31**(2), 687 – 695.

Ward, G. M. (2011), The simulation of shock- and impact-driven flows with Mie-Grüneisen equations of state, PhD thesis, California Institute of Technology.

Wilbeck, J. S. (1978*a*), 'Bird impact loading', *The shock and vibration bulletin* **48**, 115–120.

Wilbeck, J. S. (1978*b*), Impact behavior of low strenght projectiles, Technical Report AFML-TR-77-134, Air Force Materials Laboratory, Wright-Patterson Air Force Base.

Wilbeck, J. S. and Rand, J. L. (1981), 'The development of a substitute bird model', *Transactions of ASME Journal of Engineering for Gas Turbine and Power* **103**(4), 725–730.

Wilgeroth, J. M., Hazell, P. J. and Appleby-Thomas, G. J. (2010), 'The shock response of a rendered porcine fat', *Journal of Applied Physics* **108**(9).

Wu, S. R. and Gu, L. (2012), *Introduction to the Explicit Finite Element Method for Nonlinear Transient Dynamics*, John Wiley & Sons, Inc.

Yulong, L., Yongkang, Z. and Pu, X. (2008), 'Study of similarity law for bird impact on structure', *Chinese Journal of Aeronautics* **21**(6), 512 – 517.

CHAPTER 5

Rigid target calibration tests: experiments

Abstract: Initial (calibration) tests are a necessity prior to full scale testing. Bird strike calibration tests on rigid targets specifically, give a valuable insight in the complex behaviour of a bird. This chapter presents the results of a series of bird strike tests on three rigid targets (a plate, a wedge and a splitter) to quantify the forces originating from the change of momentum and splitting of the bird. In this study, momentum transfer is the key parameter to compare birds with different masses, materials, speeds, etc., as proposed in the reference works from the 20th century. The main purpose of this chapter is fourfold: (i) to introduce another way to measure momentum transfer on these kinds of targets and therefore get more consistent results, (ii) to show that gelatine generates similar impact forces as real birds, (iii) to point out that apart from the change of direction of the momentum, the deviatoric and/or dissipating constitutive behaviour of the bird also plays an important role and (iv) to show that a simple plate target can be used to measure the residual energy of the bird remainders after an impact event.

5.1 Rigid target impact

5.1.1 Previous research

The first bird strike tests on simplified targets date back to reference works from the 20^{th} century. There has always been a big focus on flat plate target, rigid as well as deformable, since this kind of target represents the most dangerous scenario for a bird strike and generates the highest impact forces. In this research, the influence of different impact speeds, masses and substitute materials can be investigated by comparing impact forces, strains, substitute bird behaviour, etc. Initial research on a rigid plate (orthogonally or rotated with respect to the impact direction) can be found in the well documented reports of Willbeck (Wilbeck, 1978; Wilbeck and Rand, 1981), Barber et al. (Barber et al., 1975, 1977) and Challita (Challita and Barber, 1979; Challita and West, 1980; Challita, 1980), where the effect of different porosities and substitute materials for the bird on the impact pressure and force was tested thoroughly. Allcock (Allcock and Collin, 1969) already measured the impact force on different kinds of targets, such as a knife-like structure and a rigid nose. The reference works from the 20^{th} century showed that momentum transfer is the key parameter for comparison. Their results gave an idea of the main impact forces.

More recent work on rigid plates exists as well (Lavoie et al., 2008; Lavoie-Perrier, 2008; Lavoie et al., 2009; Karthikeyan et al., 2011; Anghileri et al., 2012; McCarthy et al., 2004; Johnson and Holzapfel, 2006; Prato et al., 2015). The improvement of high speed imaging equipment in the 21^{th} century introduced the possibility to make qualitative comparisons. In (Lavoie et al., 2008; Lavoie-Perrier, 2008; Lavoie et al., 2009), the deformation of gelatine birds is tracked using such images and several pressure measurements were performed. In (Anghileri et al., 2012; Prato et al., 2015; Johnson and Holzapfel, 2006), the peak forces and/or force signals of multiple gelatine projectiles impacting a rigid plate were investigated. A Murnaghan EOS was fitted on 12 pressure signals obtained from rigid plate experiments in (McCarthy et al., 2004) (see also chapter 4).

5.1.2 Considered targets

The purpose of this study is to get an idea of the average impact forces and bird behaviour, which will subsequently give an idea of the overall performance of the numerical techniques and material models in the next chapter. Rigid targets specifically, provide the opportunity to focus on the bird behaviour during impact.

In most impact events (on a leading edge, fan, nacelle, etc.) three main forces can be distinguished:

- The force as a result of the change of momentum
- The splitting force (the force as a result of the splitting of the bird)
- The friction force

In order to characterize these forces, three rigid targets were considered:

- A splitter: to characterize the splitting force
- A wedge (an angle shaped structure): a considerable change of impulse is present. The unique aspect of this shape is that the constitutive behaviour of the bird and friction between the target and the bird can have a large influence on the force.
- A plate: theoretically one of the worst scenarios for a bird strike

The three rigid targets are shown in Figure 5.1.

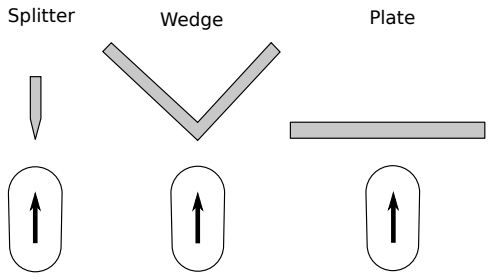

Figure 5.1: The rigid splitter, wedge and plate target.

The idea is that a combination of the effects seen during the defined calibration tests will occur in the experiments on the booster vanes (Figure

5.2). Matching the numerical models with these calibration experiments is therefore an essential step towards the modelling of bird strike on booster vanes.

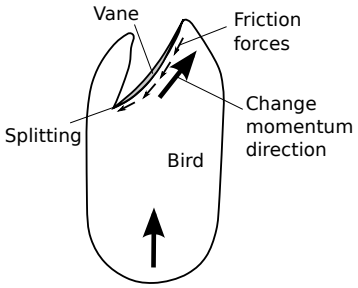

Figure 5.2: Possible forces during bird strike on a booster vane.

In this chapter, the results of multiple tests with different gelatine to water ratios (1:4, 1:6 and 1:9) as well as real birds with different masses and range of velocities will be discussed to gain a better understanding of the main differences between gelatine and real birds. New insights will be revealed that make it possible to evaluate the performance of substitute birds, focus on the differences between real and substitute bird behaviour and evaluate the state-of-the-art numerical simulations. In this study, the momentum transfer shows to be the measure for the average impact force while being, in general, independent of the impact mass, velocity and shape. The consistency of these results is assured by using a new way to measure the transferred momentum in bird strike experiments. Additionally, a new concept to measure the residual energy of a bird after an impact event with a plate target will be introduced and a method to visualize the bird trajectory is shown.

In the next section, the measurement principle for impact force and momentum transfer will be introduced. In section 5.3, the rigid target set-ups will covered. The development of several analytical models is explained in section 5.4. After that, in section 5.5, the results of the different rigid target experiments are discussed and finally, the principle to measure residual energy and the method to visualize the bird impact are elaborated respectively in section 5.6 and 5.7, to end with a conclusion.

5.2 Force/momentum measurement

5.2.1 Available techniques

The validation of the numerical models for bird strike requires quantitative measurements. Strain gauges on one hand can tell something about local deformations at discrete points on a structure. The measurement of residual energy after impact and reaction forces on the other hand are valuable parameters that give an idea of the global performance. Optical measurements can also provide full field displacement and strain data (see also chapter 3). The optical view however is often disturbed in bird strike experiments, and a stereo set-up of high-speed cameras dedicated to the measurement would be required. The measurement of reaction forces therefore remains one of the primary parameters for characterizing the impact event. Several techniques were already successfully used, from ballistic pendulums to Hopkinson bars and load cells and methods in between.

The oldest technique is the ballistic pendulum. The original idea dates back from the reference work of Robins in 1742 (Robins, 1742), where it was used to measure the momentum of a bullet. An application of the pendulum in bird strike research can be found in (Bertke and Barber, 1979), where a 5 wire pendulum was used to measure the total transferred momentum of a bird strike on titanium blades. They calculated the transferred momentum from the chord length and the oscillation period after impact.

Hopkinson introduced a first version of the Hopkinson bar in 1914 (Hopkinson, 1914), which was basically an advanced version of the ballistic pendulum. Hopkinson proposed a co-axial system of two bars, where the second bar is suspended and able to trap a part of the momentum depending on its length. The strain waves in the first bar however can, in the ideal case, be directly related to the impact force, as was tried in the reference works on bird strike (Barber et al., 1977; Wilbeck, 1978), in which forces were measured during bird strike on flat and inclined surfaces using a Hopkinson bar set-up. But, they had to integrate the force signals. Because of the high frequencies that were dispersed due to the large diameters of the bars, exact force-time signals could not be obtained. A more recent attempt was taken

as well in (Seidt et al., 2012).

In (Allcock and Collin, 1969), the targets were attached to a set of calibrated beams. The deflection of the target was measured, from which the impact force was derived.

To test bigger and more complex full scale structures such as leading edge wings, flaps or windshields and to acquire force-time signals, a set of load cells or instrumented links are often used to measure the reaction force at discrete points (McCarthy et al., 2004; Guida, 2008; Guida et al., 2008, 2013; Georgiadis et al., 2008; Zhu et al., 2014; Liu et al., 2014; Anghileri and Sala, 1996; Kermanidis et al., 2005). The problem with load cells is that the force signal is often influenced by vibrations of the supporting structure. Numerical simulations are capable of incorporating a part of the boundary conditions, but the interpretation of the signals is nevertheless not straightforward.

In (Edge and Degrieck, 1999), the displacement of a splitter target with one DOF in the direction of impact was measured using a Moiré Fringe grating. By deriving the acceleration from the obtained displacement signal and multiplication with the mass of the target structure, the force was obtained.

Reaction forces were already measured in multiple directions by (Premont and Stubenrauch, 1974; Steinhagen and Salemme, 1973). A rigid object able to pivot around one point gave the transferred rotational momentum which is a measure for the force. The kinematics around the three axes which are necessary to calculate the momentum were determined using accelerometers.

5.2.2 Measurement principle for impact force and momentum transfer

For the principle to measure the force or rather momentum transfer, the three targets are mounted with one translational degree of freedom in the bird impact direction, as was also done in (Edge and Degrieck, 1999). By

rewriting Newton's law and averaging the force integral, the average force can be obtained from the target velocity after impact:

$$F = m_t.a_t \tag{5.1}$$

$$\int m_t.dv_t = \int F.dt \tag{5.2}$$

$$m_t.v_{t,2} = F_{avg}\Delta t \tag{5.3}$$

$$F_{avg} = \frac{m_t.v_{t,2}}{\Delta t} = \frac{J_{t,2}}{\Delta t} \tag{5.4}$$

Where t stands for target, Δt is the total impact time, which can be approximated by the time that the bird needs to travel through its own length, or, be obtained directly from the high speed images if the shape deviates a lot from its original shape. m_t and $v_{t,2}$ respectively represent the mass and the final velocity of the target (the initial speed of the target $v_{t,1}$ is 0) and $J_{t,2}$ represents the final target momentum $m_t.v_{t,2}$. This last equation shows that the average force F_{avg} during impact is proportional to the momentum of the target after impact ($m_t.v_{t,2}$). The momentum of the target is therefore a measure for the force. Equation 5.1 also implies that the force at a certain point in time is proportional to the derivative of the momentum of the target.

In this work, the momentum of the target is normalized by dividing it by the impact momentum of the bird. The normalized momentum of the target can be seen as the amount of momentum that is transferred from the bird to the target structure or also, the momentum transfer (MT):

$$MT = \frac{m_t.v_t}{m_b.v_{b,1}}.100\ [\%] \tag{5.5}$$

Where m_b and $v_{b,1}$ respectively represent the mass and the initial velocity of the bird. The momentum transfer can be considered at the end of the impact event ($v_t = v_{t,2}$) or in function of time ($v_t = v_t(t)$). This expression is valid for each target and can be used to obtain the actual momentum transfer in the experiments and simulations.

In addition, for each target, a momentum equilibrium can be made of the entire system, including the target and bird momentum and knowing that the target is at rest before impact. Because the direction of $v_{b,2}$ does not necessarily coincide with the impact direction (e.g. for the rigid wedge), a switch to vector notation is made:

$$m_b.\overrightarrow{v_{b,1}} = m_t.\overrightarrow{v_{t,2}} + m_b.\overrightarrow{v_{b,2}} \tag{5.6}$$

This equilibrium is the basis for the analytical models discussed in section 5.4. In combination with Equation 5.5, the momentum equilibrium is further elaborated in that section into an analytical expression for the momentum transfer.

Summarized, instead of determining forces directly via force transducers or a Hopkinson bar, the forces are derived from the measured velocities during impact. The weight of each set-up is chosen in such a way that the inertia limits the movement over which the target is accelerated during impact to a couple of millimetres. This first part of the velocity signal of each rigid target therefore consists of a very fast increase in velocity that lasts up to $1 - 2$ ms (the actual impact). After the collision with the bird has finished, the rigid target continues to move over a distance of approximately 100 mm which results in a relatively constant velocity plateau. At the end, the rigid target is decelerated in a controlled way. Figure 5.3a and 5.3b respectively show an example of a rigid plate velocity signal for a 300 gram and 1.8 kg gelatine bird impact. Figure 5.3b represents one of the worst velocity signals (experiments with such velocity signals do not occur that often).

Inevitably, oscillations are present in the velocity signal and an estimate of the obtained velocity of the target just after the collision needs to be made. For each experiment, a line is therefore fitted to the velocity plateau and evaluated at the first intersection with the velocity signal (the circles in Figure 5.3). This has the advantage of (theoretically) eliminating the influence of any friction in the bearings (a decreasing trend in the theoretically constant velocity plateau) and/or influence of the pressure wave behind the bird (which would increase the velocity).

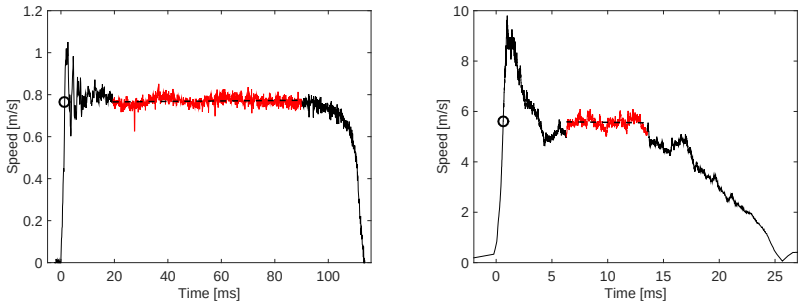

(a) Rigid plate signal from a 300 gram bird impact on the Al plate.

(b) Rigid plate signal from a $1.8\,\mathrm{kg}$ bird impact on the sandwich structure.

Figure 5.3: Velocity signals from two rigid plate experiments.

By limiting the displacement during collision to a couple of millimetres, the impact of the bird is comparable to the impact onto a fixed target, but the experiment is decoupled from the test chamber, minimizing the influence of the surroundings or boundary conditions on the experiment and guaranteeing safety. The set-ups are also quite compact when compared to a Hopkinson bar or pendulum and can therefore easily be used inside the vacuum chamber.

The concept to measure the force will be validated numerically in the next chapter.

5.3 Set-ups

5.3.1 Plate

The rigid plate set-up consists of a stiff $400 \times 600\,\mathrm{mm}^2$ steel plate reinforced sandwich panel bolted to a stiffened steel frame and attached to a linearly movable box (Figure 5.4a). Figure 5.4b shows the steel reinforcing structure which consists of a steel cross welded to a frame. This reinforcing structure on its turn is bolted to the wooden box. The linear movement of the box is realised by four needle bearings. The friction induced by these bearings is negligible compared to the high inertia forces acting in this type of experiment.

The sandwich panel is an assembly of an Acrosoma® panel (*Acrosoma*, 2016) covered by two steel plates. The Acrosoma® panel panel consists of a foam core covered by glass fibre laminates with stitches through the thickness. Some crushing could be observed throughout the test series. For the latter tests with the 0.3 kg birds, the sandwich panel is therefore replaced by a 12 mm Al plate (Figure 5.4c). The weight of the set-up with the Al plate is 39.50 kg.

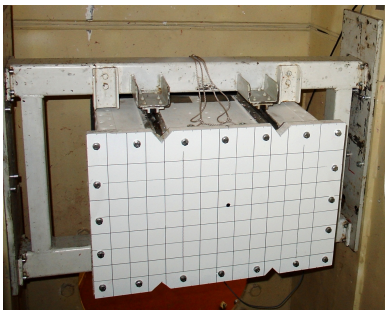

(a) First version of the rigid plate set-up mounted in the test chamber.

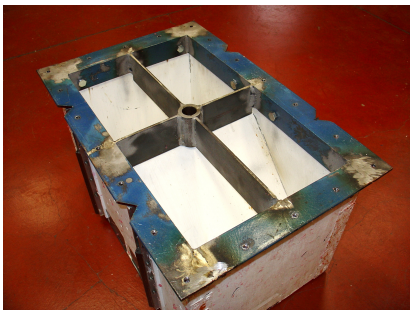

(b) Reinforcements behind plate.

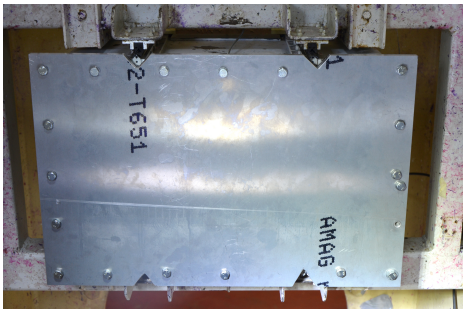

(c) 12 mm aluminium plate.

Figure 5.4: The rigid plate set-up.

After the bird impact, the heavy box moves at a considerable speed and needs to be slowed down in a controlled manner. Initially, steel crushing tubes with a diameter of 60 mm and a thickness of 3.5 mm were used. A pressure test and simulations showed that these are capable of absorbing roughly 8.1 J/mm (per millimetre crushed tube length) over a displacement of 50 mm. Depending on the test (weight bird and impact speed), crushing tubes were manufactured according to the expected transferred energy. At the end, these tubes were replaced by honeycomb cardboard which exhibit a

force plateau of roughly 0.25 N/mm^2 during crushing (per mm^2 cardboard surface).

5.3.2 Wedge

The wedge consists of a reinforced steel L-profile that fixes two aluminium plates orthogonally with respect to each other (Figure 5.5). The plates have a height of 300 mm and a length of 350 mm. It is designed in such a way that the inertia (and stiffness) is located at the centre of impact to minimize oscillations. The initial idea was to use a rotated plate. But, a wedge has the advantage to have, in theory, no reaction force in the direction perpendicular to the impact direction. The linear translation is again guaranteed by four linear needle bearings. The weight of the wedge is 21.7 kg.

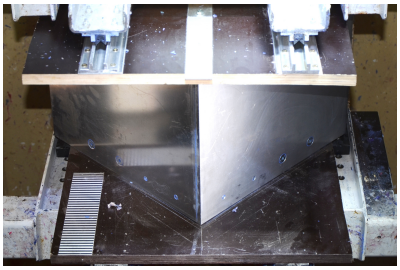

(a) The front of the wedge.

(b) The back of the wedge.

Figure 5.5: The wedge set-up.

5.3.3 Splitter

The splitter is a thin knife-like structure (Figure 5.6). The aim of this target is to get an idea of the acting forces during the splitting of the bird. The splitter consists of a foam core with steel plates at each side. The actual tip of the splitter is a machined, almost entirely solid piece. The linear movement is ensured by needle bearings in V shape (one at the bottom and one on the top). The final weight of the splitter including sensors is 1.73 kg.

5.3.4 Instrumentation

For the splitter and the plate, the Kübler Limes LI50/B2 linear displacement transducer and at least one PCB 350B24 accelerometer are used. These

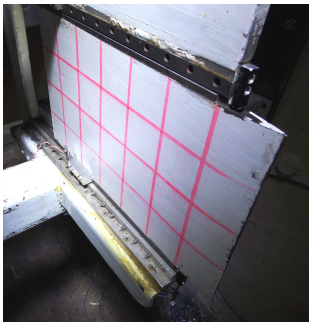

Figure 5.6: The splitter set-up.

sensors are sampled with the HBM Gen5i oscilloscope (1 MHz for the accelerometer and 10 MHz for the displacement transducer).

The high speed cameras are used to record the experiments from different angles. For some experiments, optical tracking of the displacement of the target is also done using the 1D line grating technique introduced in chapter 3. For the Kübler Limes and optical tracking measurements, numerical differentiation of the displacement signals is performed to obtain the corresponding velocity signals and for the accelerometer measurements, the accelerations are integrated.

5.4 Analytical models

5.4.1 Plate

For the plate, the experiments show that the velocity of the bird in the impact direction is zero after impact and that the bird moves only in the radial direction (Figure 5.7). Considering the conservation of momentum (Equation 5.6) in the impact direction (the y-direction) and equating $v_{b,2}$ to 0, it can be deduced that the momentum of the plate is equal to the impact momentum of the bird. As a result, the momentum transfer after impact is 100% (Equation 5.5) or also, the momentum of the bird is entirely transferred to the plate.
According to the analytical model, the momentum transfer is always 100%, independent of the shape, the material, mass or velocity of the impactor.

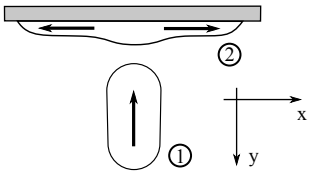

Figure 5.7: Mass flow plate impact.

This reveals the advantage of momentum transfer over average force. Equation 5.4 contains Δt, which depends on the velocity and the length of the bird. The length of a real bird is in general slightly larger and for the substitute birds, the volume does not scale linearly with the length of the bird (the volume does not have a linear relationship with the length because of the fixed length to diameter ratio). Thus, the mass has a non-linear influence on the force too. To compare the different impactors, with different masses and velocities, using the momentum transfer therefore has a considerable advantage over the force.

In the plate experiments, large oscillations are present in the plate velocity curves after impact, indicating that the target structure is not rigid enough. The force at each time step therefore is not represented by the current change in velocity of the plate target (Equation 5.1). However, simulations show that elastic deformation of the target structure has a minor influence on the final momentum transfer.

5.4.2 Wedge and splitter

Figure 5.8 gives several schematic overviews that will clarify the momentum equilibrium for the wedge (the same principle can be applied to the splitter). Because there is a fundamental difference with a rotated plate, this will be covered first (first picture in Figure 5.8). It can be assumed that after impact, there is no momentum of the bird perpendicular to the plate (the y-direction). To avoid introducing the speed of the bird after impact $v_{b,2}$ in the momentum equilibrium, Equation 5.6 is first considered in the y-direction. The initial momentum of the bird in the y-direction is indicated by the green vector. This green vector is equal to the initial momentum times the sinus of

the angle α in which the bird is deflected. From the momentum equilibrium in the y-direction, the target momentum is directly obtained:

$$J_{t,2} = m_b.v_{b,1}\sin(\alpha) \tag{5.7}$$

When the target momentum is measured in the impact direction however, only a projection of $J_{t,2}$ is measured, indicated by the upper triangle. The target momentum in Equation 5.7 therefore has to be projected again on the impact direction (by multiplying it again with $\sin(\alpha)$). To obtain the momentum transfer, it is also divided by the bird impact momentum:

$$MT_{impact\ direction} = \sin(\alpha)^2.100\ [\%] \tag{5.8}$$

It can be said that the momentum transfer is defined by $\sin(\alpha)^2$. For an angle of 45°, the momentum transfer would be 50% of the initial momentum. Experiments on rotated rigid plates with porous gelatine and real birds, for angles of 90°, 45° and 25° have been investigated by Wilbeck and Barber (Wilbeck, 1978; Barber et al., 1977). If friction forces would have been present, the momentum transfer would have increased by a certain amount above the theoretical momentum (because a high normal force would be generated, which would result in a friction force that has a considerable component in the measurement direction). The momentum transfer however was as predicted by the analytical model without friction (within the obtained scatter). Allcock and Collin used a similar reasoning to obtain the momentum transfer for wedge like structures (Allcock and Collin, 1969). They obtained the momentum transfer by mistakenly considering two times the impact of half a bird on a rotated plate to obtain the same momentum transfer, as shown in the centre of Figure 5.8. This is not correct. Considering the two halves of a bird separately requires the use of a symmetry force, as indicated in the third figure. If only one half of the bird would impact the wedge and there would be another plate in the symmetry plane, a pressure would be exerted on that plate which proves the necessity of a symmetry force. Symmetry implies that shear forces cannot be present at the symmetry plane, which is why the symmetry force can only be horizontal.

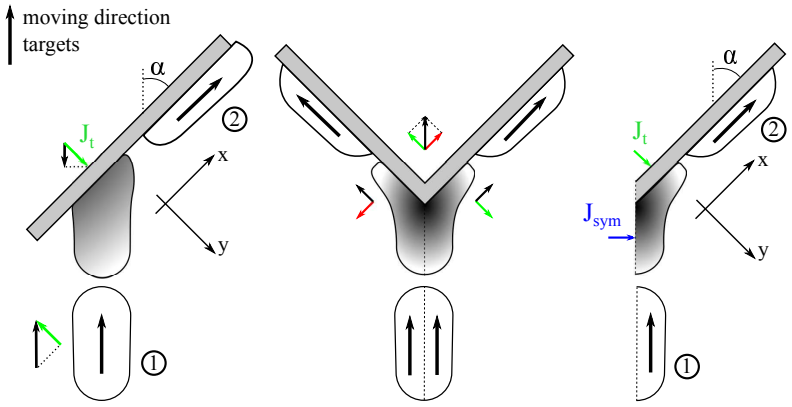

Figure 5.8: Mass flow rotated plate and wedge impact.

The momentum equilibrium in both the x- and y-direction are now necessary to obtain the momentum transfer:

$$x: \; J_{sym}\sin(\alpha) + \frac{m_b.v_{b,1}}{2}\cos(\alpha) = \frac{m_b.v_{b,2}}{2} \tag{5.9}$$

$$y: \; J_{t,2} + J_{sym}\cos(\alpha) = \frac{m_b.v_{b,1}}{2}\sin(\alpha) \tag{5.10}$$

Where J_{sym} is the momentum equivalent to the symmetry force defined earlier, $J_{t,2}$ is the target momentum equivalent to the reaction force of the plate, $v_{b,1}$ and $v_{b,2}$ are respectively the absolute velocity of the bird before and after impact and α is the angle over which the bird deviates from its initial direction. It would be more correct to write a force balance instead of a momentum balance (since there is no movement and therefore no momentum at the symmetry plane). Dividing Equation 5.9 and 5.10 by Δt would result in a symmetry force (Equation 5.4). To keep the discussion in this section about momentum however, an equivalent momentum is considered.

Combining these two equations by eliminating J_{sym}, equating for J_t, projecting the momentum on the impact direction, doubling the result to account for the other half and dividing by the initial momentum, results in the following expression for the transferred momentum:

$$MT = \left(1 - \frac{v_{b,2}\cos(\alpha)}{v_{b,1}}\right).100\ [\%] \tag{5.11}$$

This expression can be used for the wedge and also for the splitter. Obtaining the analytical solution in the experiments for the wedge requires the speed of the bird after impact $v_{b,2}$, which cannot be determined accurately from the experimental data. In the simulations on the other hand, $v_{b,2}$ can be determined (as was introduced in chapter 4). Since Equation 5.5 (which can be derived from experimental measurements and simulations) and Equation 5.11 (derived from simulations) both calculate the same momentum transfer, they can be used interchangeably and can validate one another. Further, if the bird in the experiments remains quite intact after impact and its velocity $v_{b,2}$ can be estimated from high speed images, the momentum transfer can be measured in two independent ways (through target velocity and bird velocity).

For the splitter, the assumption can be made that a negligible amount of kinetic energy is dissipated in the bird ($v_{b,2} = v_{b,1}$), which results in a theoretical momentum transfer of 1.23% for a deviation angle α of 9° (the tip angle of the stripper is 18°).

For each target, the analytical expressions derived in this section will be compared to the actual transferred momentum in the experiments derived from the momentum of the target (Equation 5.5).

5.5 Results

Figure 5.9 shows the momentum transfer for the three rigid targets in function of impact speed (impact speed instead of impact momentum to get a better overview of the results). All data points are derived from the measurement of the target velocity after bird collision and calculation of Equation 5.5. All the birds are shot at a velocity between $60 - 150\,\mathrm{m/s}$. The relatively larger range in initial momentum is solely the result of the different masses. To get an idea of the absolute values of the average impact forces, a force graph is given as well (Figure 5.10). To obtain the force, the ΔT is derived from the high speed images if the bird is deformed severely, or from the shape of the mould when the shape is well maintained (which is generally the case for the 300 gram birds). How representative the average

force is for the instantaneous force over time will be covered further on in this section.

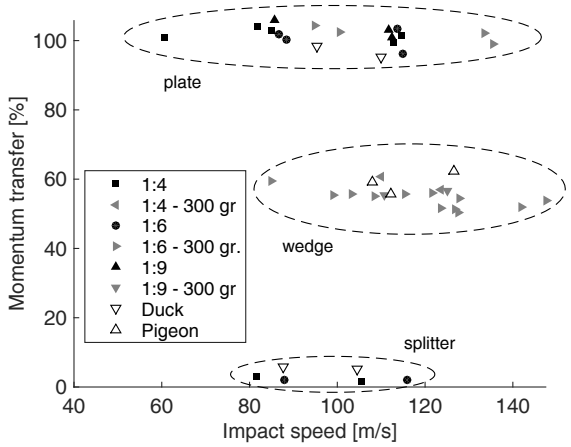

Figure 5.9: Momentum transfer in the plate, wedge and splitter experiments.

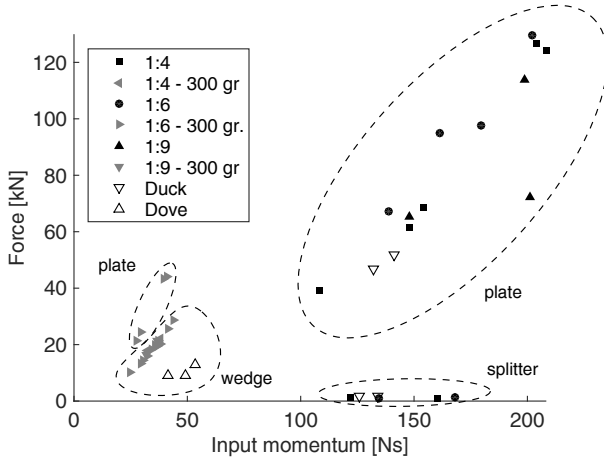

Figure 5.10: Average impact force in the plate, wedge and splitter experiments.

To give a better perspective on the consistency of the results, a graph relating the output momentum with the input momentum for the rigid plate experiments is shown in Figure 5.11, as was also done in the reference work of Wilbeck (Wilbeck, 1978). The 100% momentum transfer expected from

the analytical model translates to a one-to-one relation between input and output momentum, which can be observed in the graph.

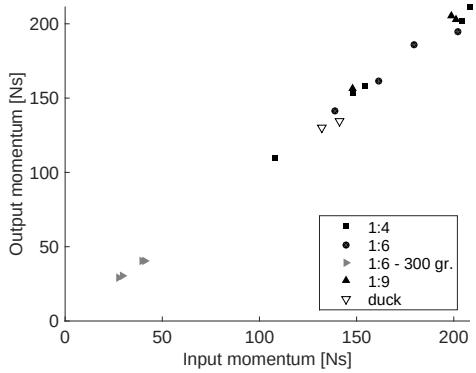

Figure 5.11: Output versus input momentum for the plate target.

Still, some scatter can be observed in the rigid plate and wedge experiments. Multiple error sources can be identified:

- The measurement of the bird velocity (see also section 2.2.2.1).
- The measurement of the target velocity (see also section 5.2.2). Some error will be introduced by the way the velocity is derived from the velocity signal. Ideally, the pressure waves accompanying the bird and the friction in the linear bearings of the target have a negligible effect on the determination of the target velocity just after impact.
- Debris that enters the test chamber (foam, pieces of sabot cap and sabot tube).

Especially the last item can have a significant influence on the average momentum transfer. During the stripping process, the bird is stripped from the sabot through the supporting foam. Inevitably, some foam enters the chamber. For a 300 gram bird for example, up to 50 gram of foam, dust and pieces of sabot can be found in the test chamber after impact. This is equal to 16.7% of the total weight of the bird and can therefore have a big influence on the mean force. Luckily, this mass does not necessarily contribute fully to the transferred momentum for two reasons. Firstly, the pressure wave blows debris inside the chamber just after impact. All the debris therefore

does not necessarily enter the chamber at the speed of the bird. Secondly, the dust and foam exhibit a very high drag to weight ratio, which makes them decelerate quickly (limited because of the very low ambient pressure). An investigation of several lumps of foam indicates that the amount of foam can increase the momentum transfer up to 1-2%. On the other hand, a small misalignment due to the crushing of the supporting foam in the sabot might cut off a slice of the bird during impact.

In the following subsections, the results for the three rigid targets will be examined separately.

5.5.1 Plate

In total, 18 experiments are performed on the rigid plate. The different input characteristics can be found in the appendix (Table B.1), respectively showing the type of bird (gelatine mixing ratio or decapitated duck), the bird mass and impact speed, the calculated momentum transfer and average force and the type of target plate. The ducks do have a lower weight than the big gelatine birds (roughly 1.3-1.4 kg opposed to 1.5-1.8 kg). The procedure for creating the birds, the launching procedure and the velocity measurement of the plate is optimized for the last tests with the 300 gram birds. Together with the fact that the forces are smaller, this results in less scatter in the momentum transfer and force of the 300 gram birds. An overview of the birds before impact together with the momentum transfer is shown in Figure 5.12, the majority of the collection showing a side view.
The momentum transfer for the plate target is close to 100%, as predicted by the analytical model. There is no clear influence of the bird material on the order of magnitude of the observed scatter seen in the results. A mean value of 101.2% momentum transfer is obtained from the experiments. The slightly higher momentum transfer can be the result of lightweight foam that encloses the bird.

The highest observed momentum transfer is the one from test RP-2. In this specific case however, a large part of the end cap of the sabot continued its trajectory together with the bird after the stripper chamber. A sabot cap weighs 160 gram, which corresponds with almost 10 % of the bird's

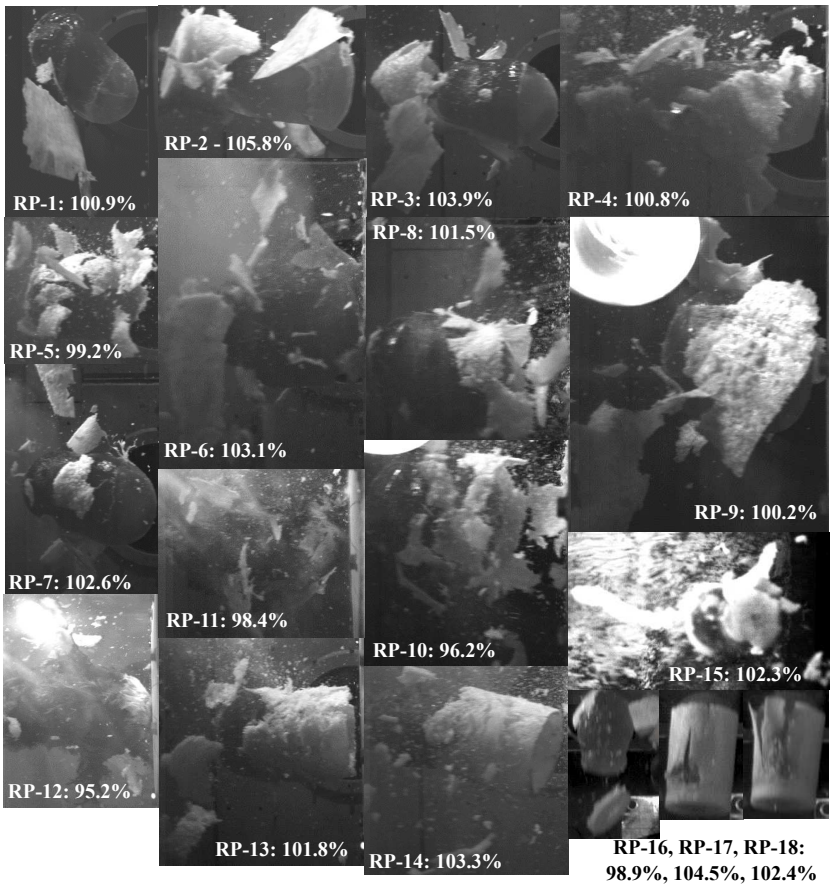

Figure 5.12: Overview of the birds before impact on the rigid plate set-up.

weight. From the high speed images (the side views shown in Figure 5.12 but also perspectives from the top), it can be concluded that test RP-4, RP-8, RP-10, RP-11, RP-12, RP-15 and RP-16 experienced few or little chunks of foam while test RP-3, RP-13, RP-17 and RP-18 experienced large chunks of foam. These tests correspond respectively with 100.8%, 101.5%, 96.2%, 98.4%, 95.2% and 103.9%, 101.8%, 104.5%, 102.4% momentum transfer, clearly showing the influence of foam. It can be stated that some further optimization is necessary to further reduce the foam accompanying the bird.

The consistent momentum transfer around 100% is an interesting observation. To get a momentum transfer similar to a real bird, the substitute material

should be able to disintegrate in the radial direction at the observed velocities, with zero momentum in the impact direction after impact. Gelatine clearly behaves according to this assumption.

Linear trends can be observed in the force plot (Figure 5.10). For the 300 gram birds, the force increases faster than for the bigger birds. As mentioned before, this is because the impact time (related to the length of the bird) does not decrease as fast as the mass for smaller birds (when using a fixed l/d ratio, see also Equation 5.4). Some outliers can be found. In test RP-4 at approximately 200 Ns and 70 kN, a 1:9 gelatine mixture is used. Because of the low strength of the 1:9 mixture birds, it is more difficult to keep the bird in its original shape throughout the launching process. In this specific case, the bird is stretched out quite a lot, resulting in a significantly lower average force. The momentum transfer and force for the ducks are slightly lower. Compared to the experiments with gelatine birds, no foam is present which could be an indication that some mass is cut off during the stripping process. The lower force is also partly the result of the fact that the ducks are roughly 150% longer than the gelatine birds.

Decreasing the gelatine MR (decreasing the amount of gelatine) increases the fluid-like behaviour of the bird. This can be observed when comparing a 1:9 with a 1:4 gelatine MR. Figure 5.13 shows four subsequent frames from test RP-2 (1:9 MR gel) and RP-3 (1:4 MR gel), both at a similar impact velocity. A higher "splashing" velocity can be observed for the 1:9 MR.

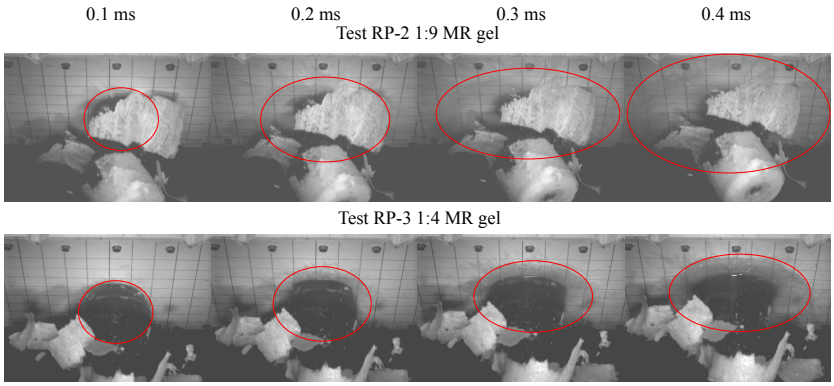

Figure 5.13: Four subsequent frames from test RP-2 and RP-3.

Also after impact, the 1:9 MR generally disintegrates completely into small pieces of gelatine, which is not comparable to the duck (Figure 5.14). The shape is also very hard to maintain during acceleration and stripping of the bird, which is why a 1:9 MR bird is not ideal as substitute bird in a booster vane experiment. The 1:4 and 1:6 MR birds resulted in big lumps after impact. A 1:6 MR naturally resulted in smaller lumps, more comparable to the ducks. The big lumps after impact are a first indication that gelatine is capable of storing a high amount of elastic energy.

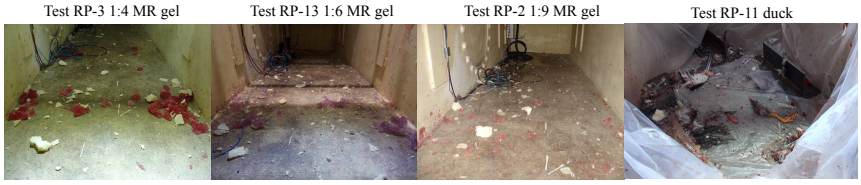

Figure 5.14: Size of the gelatine lumps after impact for different birds, compared to a real bird.

It is difficult to compare different types of birds due to the different shapes (the speed of the jets that are formed depend highly on the front shape of the bird) and obstruction of foam material. An attempt is made by comparing four subsequent frames of the impact event of test RP-14, RP-5 and RP-12 (Figures 5.15, 5.16 and 5.17), which are three tests with different types of birds (a 1:6 and a 1:4 gelatine MR and a duck) with an impact speed close to 110 m/s. The first frame in this comparison is the point in time where a visible radial mass flow starts to form. For the duck, this starts significantly later. This is partly because of the much smaller cross section at the front but could also be because of the feathers and other organic material that are compressed first. The gelatine birds have a smaller length than the ducks, which takes this effect into account.

For these three tests, with the limited visibility that is achieved (due to the foam, but also the shape of the duck that is hard to distinguish), the overall behaviour is comparable.

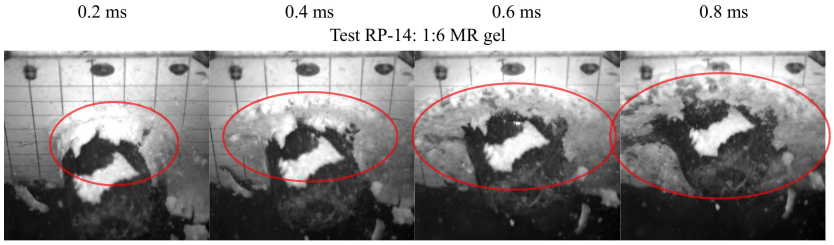

Figure 5.15: A sequence of four frames from test RP-14.

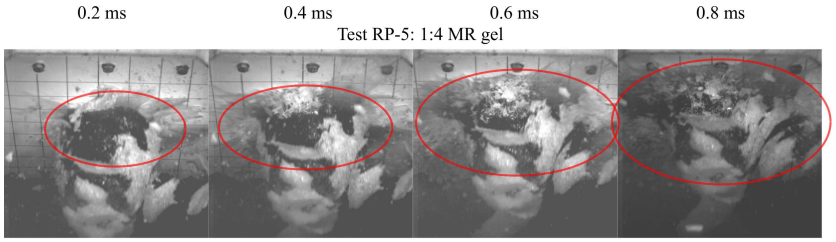

Figure 5.16: A sequence of four frames from test RP-5.

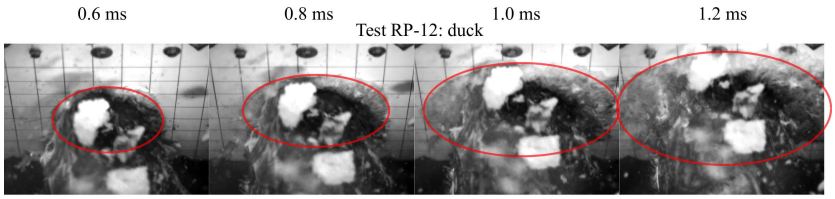

Figure 5.17: A sequence of four frames from test RP-12.

5.5.2 Wedge

The 19 wedge experiments are summarized in the appendix (Table B.2). In total, 12 birds with a 1:6 gelatine MR, 2 with a 1:4 gelatine MR, 2 with a 1:9 gelatine MR and three pigeons are tested. Contrary to the previous section, the real birds are not decapitated before launch.

For the three considered mixing ratios, as well as for the pigeons, a momentum transfer between 50-60% is obtained. According to the analytical model, this would mean that the velocity after impact is always lower than the impact velocity and that the velocity after impact relative to the impact speed is comparable for all the impactors.

Figure 5.18 shows three frames of test WE-2, with a 0.3 kg 1:6 MR gelatine bird at 100 m/s.

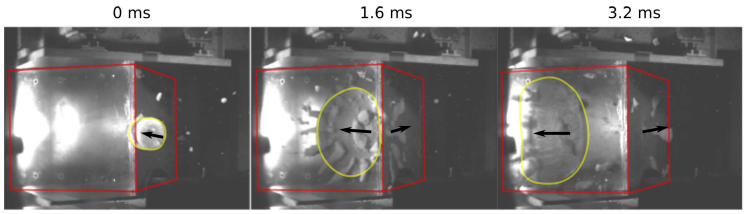

Figure 5.18: Wedge test WE-2.

What is striking, is the amount of elastic deformation of the gelatine, even at these high impact velocities. This can also be observed in the momentum transfer graphs. Figure 5.19a shows the momentum transfer over time for three experiments with different gelatine mixing ratios and two experiments with pigeons. A 300 gram gelatine bird travels its own length in approximately 1 ms, the momentum however is transferred over a time span which is rather in the order of magnitude of 2 ms (i.e. the momentum transfer keeps increasing up to 2 ms after the start of impact), which can only be the result of kinetic energy that is temporally transferred to elastic energy during impact. The momentum transfer of the real birds takes even longer. This is partly the result of the length of the bird. In the experiments with the pigeons, the neck is stretched out in the impact direction. The head and neck therefore impact approximately 1 ms earlier than the body. As a result, the average impact force for the pigeons in Figure 10 is also considerably lower than for the gelatine birds. Shifting the curves 1 ms to the left (Figure 5.19b) shows that the slope of the curves, which is a measure for the force, is quite similar for the pigeons and the gelatine birds. Also, the momentum transfer graphs of the gelatine birds and the pigeons are all between 50 and 60%. Regardless of the head and the neck, gelatine is therefore able to capture the average force and momentum transfer of a pigeon quite well.
A qualitative comparison between a gelatine bird and a pigeon impacting at 110 m/s is made in Figure 5.20 (with the same shift in time as in Figure 5.19b). The gelatine impactor is completely split at 1.5 ms, contrary to the pigeon. Disregarding the length of the neck, the higher length of the pigeon does not increase the time over which the momentum is transferred (Figure 5.19b).

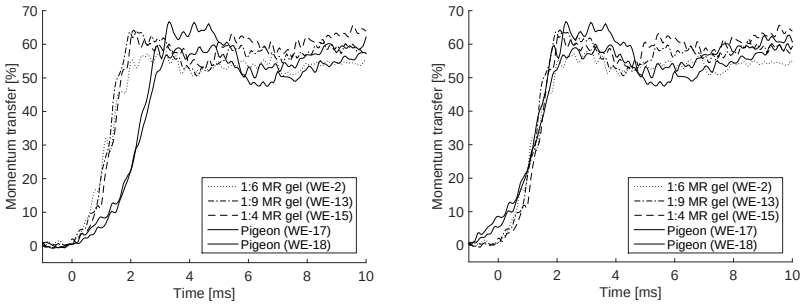

(a) Synchronized at the start of impact. **(b)** Shifted the pigeon momentum curves over the impact time of the head and neck of the pigeons.

Figure 5.19: Momentum transfer curves for wedge experiments with different impactors (three different gelatine mixing ratios and two pigeons).

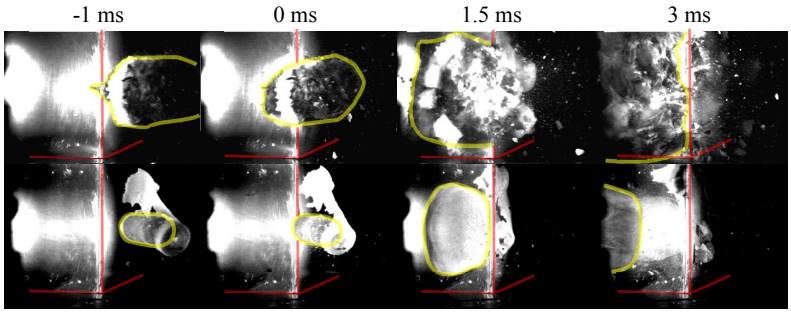

Figure 5.20: Comparison between a gelatine impactor and a pigeon impacting the wedge at roughly $110\,\mathrm{m/s}$ (test WE-5 and WE-17).

5.5.3 Splitter

Six experiments on the splitter are performed: two experiments with a 1:4 and two with a 1:6 gelatine MR and two with a duck. Table B.3 in the appendix contains the type of bird (gelatine mixing ratio or duck), the bird mass and impact speed, the calculated momentum transfer and force for each experiment and the deviation angle α of the bird after impact, estimated from the high speed images. As for the rigid plate, the ducks were decapitated before launch.

A zoom on the momentum transfer and force results for the splitter is shown in Figure 5.21.

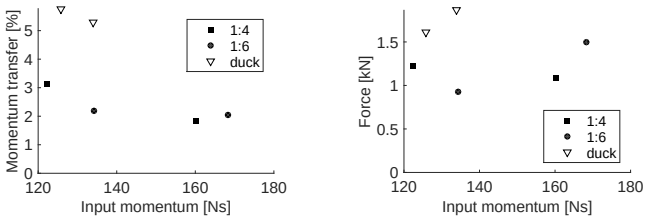

(a) Momentum transfer. **(b)** Force.

Figure 5.21: Momentum transfer and force splitter.

The momentum transfer for the gelatine birds is between 1.8-3.1% for both mixing ratios. A theoretical momentum transfer of 1.23% was calculated in section 5.4.2 for a deviation angle α of 9°. The images from the experiments however show that the gelatine birds do not deviate over an angle of 9°, but rather 5-6°, which corresponds to approximately 0.46% momentum transfer (the deviation of the birds after impact is shown in Figure 5.22). Because the actual tip of the splitter is much shorter compared to the plates of the wedge (see also Figure 5.5 and 5.6), it is possible that the deviation angle is lower than the one defined by the splitter tip. There are two possible explanations for the higher momentum transfer in the experiments : (i) the assumption $v_{b,2} = v_{b,1}$ is not correct or (ii) some friction might be at play. The first assumption for sure has a large influence on the results. Because of the small deviation angle, the cosine in Equation 5.11 is very close to 1. For the 5-6° for example, this is around 0.9954. Even for a relatively small dissipation in the bird (a small decrease of the bird velocity), a relatively large increase in momentum transfer can be obtained.

The ducks deviate even less (3-4°), which corresponds to a negligible momentum transfer as a result of a change in momentum direction, while the momentum transfer is almost double as the one from gelatine. The fact that the ducks deviate considerably less than the gelatine birds is an interesting observation. This again indicates that gelatine is capable of storing (much more) elastic energy.

The higher momentum transfer of the real birds compared to the gelatine can also be observed in the momentum transfer over time curves shown in Figure 5.23. Contrary to the wedge, these curves are derived from integrated

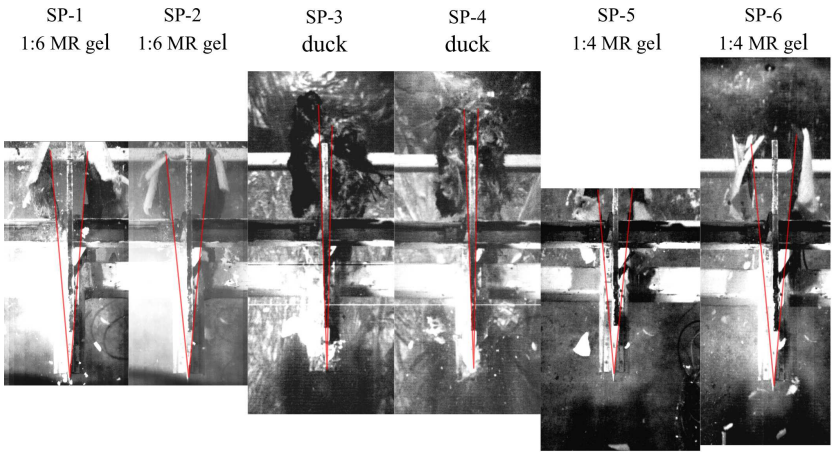

Figure 5.22: Bird deviation after impact.

accelerometer signals. From the three considered targets in this chapter, the splitter is the most rigid. The accelerometer is attached firmly to the target and can therefore be used to obtain very accurate momentum over time signals. The connection failed for one of the 1:6 MR experiments (SP-2). For the two 1:4 MR birds (SP-5 and SP-6), drift is present on the acceleration signal. This drift is subtracted from the original signal, which results in quite comparable graphs for the first slope. The distortion between 5-6 ms after impact for SP-1 is due to a piece of sabot cap that hits the splitter after impact. For SP-5 and likely for SP-6 as well, a small piece of sabot cap also hit the splitter just after impact (between 3-4 ms).
For the three experiments with gelatine birds, the slope and therefore force is quite similar. For the two experiments with ducks, the slope or force is also consistent, but considerably higher. The final momentum transfer is almost three times higher for the real birds. The substitute birds clearly underestimate the force and momentum transfer of the real birds, contrary to the plate and wedge experiments.

The energy equilibrium is very important in this type of experiment. For the gelatine birds for example, the kinetic energy of a 3 gram piece of bird is so large that it would double the final speed of the splitter when that piece of bird is decelerated from the initial bird velocity to the velocity of the splitter. Figure 5.24 shows several high speed images taken from the

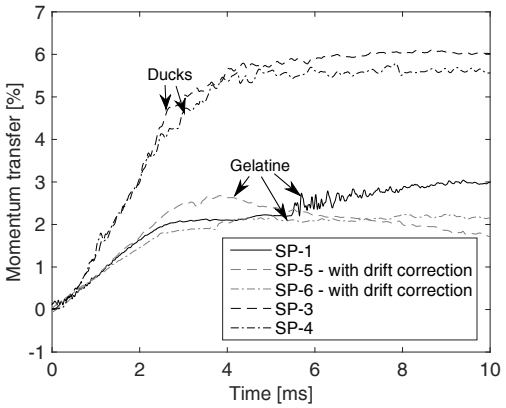

Figure 5.23: Momentum transfer curves for several splitter experiments.

left side of the splitter (see also Figure 5.6), where the bird impacts from the right side of the image and one half of the bird can be observed after impact. It can be observed that pieces of duck stick to the splitter, because of tendon, feathers and so on. These pieces can increase the energy transfer by a large extent. For the gelatine experiments, this is not observed. The mass that sticks to the splitter could be the reason for the higher force, but the question remains if this is the only mechanism that generates force.

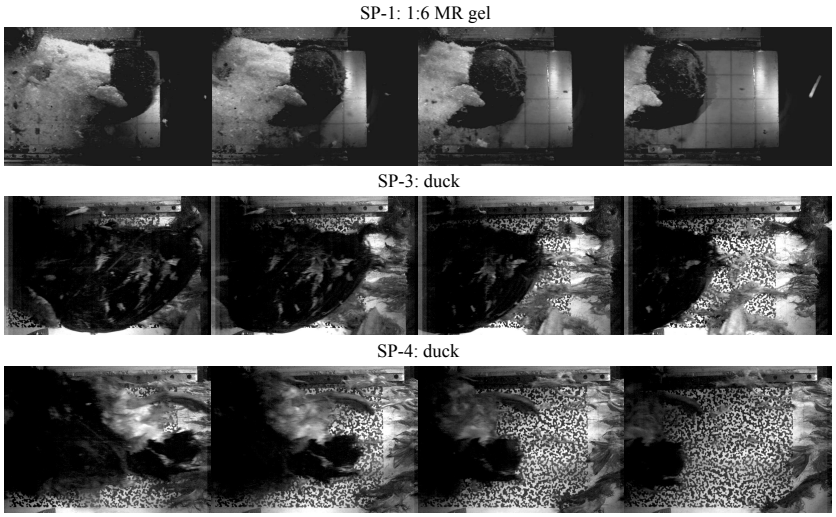

Figure 5.24: Bird pieces stuck to splitter after impact.

The bird mass that sticks to the splitter falls off after the experiment, which makes it impossible to get an idea of the kinetic energy that is transferred.

Another cause for the higher momentum transfer of the ducks could be the fact that the ducks are longer than the gelatine birds. The "splitting" force therefore acts longer. The difference between the ducks and the gelatine is relatively smaller for the momentum transfer (Figure 5.21a) compared to the force (Figure 5.21b), because the ducks are longer and therefore the impact time is a bit higher compared to the gelatine birds.

Disregarding the sticking of tendon and feathers, the slopes are quite constant for the real birds, which gives an indication that the bird, including bones, feathers, flesh and so on, interacts quite homogeneously in splitter tests at these impact speeds.

In general, the forces induced on the splitter are much lower compared to the wedge and the plate. For each of the six experiments, the force is lower than 2 kN. Compared to the 50-100 kN seen in the plate experiments (for the same range of initial momentum), splitting forces (as far as it is actually about splitting), should have a minor effect in an impact event with a considerable change of momentum direction.

Figure 5.25 shows three frames from experiment SP-6, where a 1.5 kg 1:6 MR gelatine bird impacts at 106 m/s on the splitter target. The red and yellow shapes respectively indicate the tip of the stripper and the contour of the bird. During splitting, the bird maintains its original shape quite well. The figure shows that the gelatine bird remains in two pieces after impact. There are no pieces of gelatine that stick to the splitter.

5.6 Residual energy measurement

Within the context of the project, a set-up to measure the residual energy of the bird remainders after impact is of high importance. Several attempts were made to make a "catcher box" which can catch the bird and therefore measure its kinetic energy. Simulations are not useful in this development because it requires a very accurate material model for the bird including all

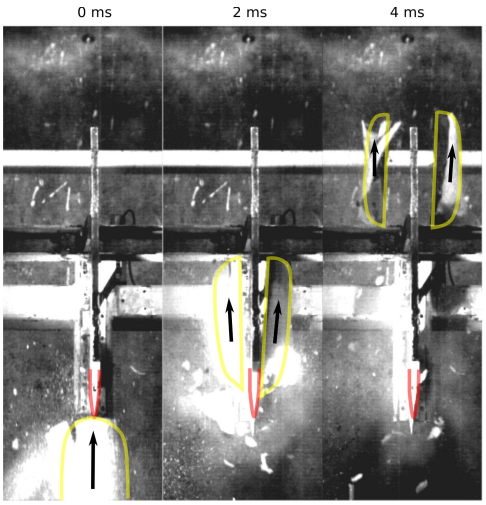

Figure 5.25: Test SP-6: impact of a 1.5 kg 1:4 MR gelatine bird (yellow contour) on the splitter (red contour).

its energy dissipating mechanisms.

The original catcher box and a new concept are shown in Figure 5.26. The original catcher box consists of a wooden box with a wedge-like structure at the centre. The new concept consists of a wooden box stiffened by a metal framework at the end (not visible on the picture), filled with metal grids with different offsets with respect to each other. The idea is that bird is stopped purely by friction forces. Both catcher boxes are tested behind the splitter set-up. According to the results from the splitter, only a small part of the initial kinetic energy of the bird is transferred to the splitter and most of the initial impact energy should be measured by the catcher boxes.
For the original catcher box, the high speed images however show that the energy is not absorbed, as a majority of the mass bounces back again after impact and flies out (Figure 5.27). Several frames later, the bird flies at a similar speed in the other direction. These images reveal that any concept where the energy of the bird is captured by deviating or "catching" the bird will not work. Barely one tenth of the initial energy is captured by the box.
The new concept performs even worse. Figure 5.28 shows several frames from the impact on the new concept with metal grids in test SP-5 and the catcher box after impact for test SP-3 to SP-6. The gelatine bird flies into

(a) Original catcher box set-up. **(b)** New catcher box with metal grids.

Figure 5.26: Two catcher box set-ups.

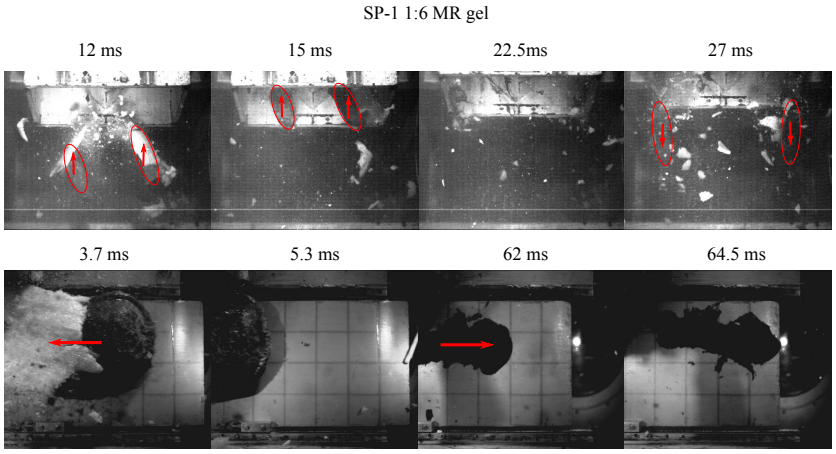

Figure 5.27: Impact original catcher box in test SP-1.

the grid seemingly without much resistance. For the ducks however, a large part of the bird including wings, feathers and legs are obstructed by the first grid. These experiments show that gelatine can perform very different opposed to real birds when the target consists of confined spaces (this also raises the question if gelatine is a good substitute for experiments on vane structures). For the real birds as well as for the gelatine birds, less than 5% of the initial kinetic energy is captured.

The final solution to the residual energy measurement problem is found to be the rigid plate set-up. The plate analytical model and experiments learned that 100% (101.2% in the experiments) of the impact momentum is transferred to the plate, independent of the shape, mass or velocity of the

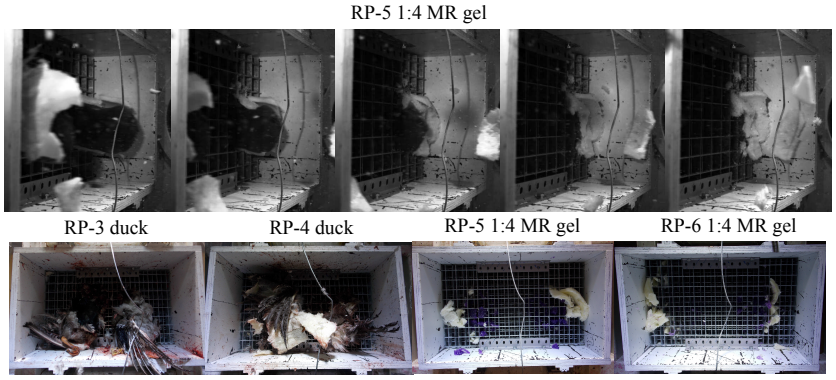

Figure 5.28: Results new concept with metal grids in test SP-3 to SP-6.

bird. This fact can be used the other way around, instead of determining the momentum transfer from the impact momentum of the bird and the momentum after impact of the target, the momentum of the bird can be determined from the momentum of the target and the assumption that 100% of the momentum is transferred. The obtained momentum of the bird in the direction orthogonal to the plate can be used to obtain the velocity of the bird, from which the residual energy in the direction of impact can be calculated.

For an experiment where the residual energy of the bird after primary impact on some target needs to be measured, the rigid plate set-up with one degree of freedom can be positioned behind the target. Only for the bird mass that hits the plate, the momentum is measured, so the rigid plate should be positioned as close as possible behind the target. Furthermore, only the bird momentum component orthogonal to the plate is measured. This projection of the momentum and therefore residual energy can in extremis be used to approximate the total residual energy from an estimation of the angle between the bird velocity vector and the direction orthogonal to the plate derived from the high speed images.

The next chapter will give an additional (numerical) verification for a more extreme example, considering an impact of a deformed bird.

Taking the square of the momentum transfer for the plate (which can be done because it is theoretically 100%), multiplying it with the bird mass and dividing by the mass of the rigid plate gives the energy transfer:

$$1 = \frac{m_t v_{t,2}}{m_b v_{b,1}} \tag{5.12}$$

$$1^2 \frac{m_b}{m_t} = \frac{m_b}{m_t} \frac{m_t^2 v_{t,2}^2}{m_b^2 v_{b,1}^2} = ET \tag{5.13}$$

$$ET = \frac{m_b}{m_t}.100 \ [\%] \tag{5.14}$$

The energy transfer depends solely on the ratio of the impactor mass to the rigid plate mass. For the rigid plate set-up for example, the energy transfer is 4.5% and therefore much less than the momentum transfer. The energy transferred to the rigid plate decreases for an increasing mass of the set-up. This can be very useful when designing set-ups. This reasoning was used in the development of the pressure measurement set-up discussed in the previous chapter. By choosing a high inertia, the energy that is transferred to the target should be limited.

5.7 Extra visualization of the bird impact

During the experiments on the booster vanes, the three HSCs are needed to obtain necessary information such as the impact position, but also to track the line pattern to obtain the residual energy. Any additional information can be helpful. An attempt is therefore made to visualize the area where the bird impacts. Different substances are tested in the plate experiments before the actual experiments on the booster. To be useful, some requirements need to be fulfilled:

- The substance should not be blown away by the air pressure wave before and after the bird. Any bird material sliding over the surface on the other hand, should remove the substance.
- It should have a negligible influence on the experiment.
- Sufficient contrast with the plate should be obtained.
- The substance needs to cover the entire surface uniformly.

- It should be easy to apply and remove (without removing the plate).

Several substances are tested: shoe polish, tooth paste, choco, Nivea creme, chalk powder and chalk powder mixed with water. The shoe polish and tooth paste have a good contrast but dry out while evacuating the test chamber. As a result, the substance cannot be removed during the bird impact. The choco and Nivea creme are too sticky and are not completely removed by the bird during impact. The dry chalk powder provides a poor surface covering. The best option proves to be the wetted chalk powder. It is relatively easy to apply, it has a very good surface covering and contrast, and the bird path is visualized very well. Figure 5.29 shows the rigid plate covered with wetted chalk powder from test RP-17, before and after impact.

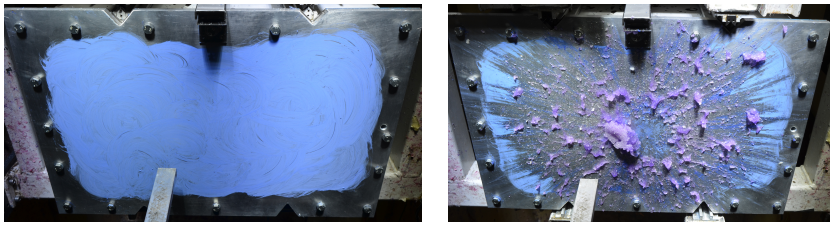

(a) Chalk powder cover before impact. **(b)** Chalk powder cover after impact.

Figure 5.29: Performance wetted chalk powder to visualize bird impact.

5.8 Conclusion

Bird impact experiments on a rigid plate, wedge and splitter target with gelatine and real birds have been performed and investigated. In this study, the momentum transfer proved to be a good measure to compare birds with different materials, masses, lengths and speeds with each other. To study the impact on these rigid targets, a new principle to acquire the momentum transfer in bird strike experiments has been introduced and validated. The results of the different experiments can be summarized as follows:

- Gelatine versus real birds: Especially for the plate and the wedge, fluid-like impactors have comparable mass flows and therefore comparable average impact forces and momentum transfer. As a result, the impactor material (gelatine or real bird) has a negligible influence in

this kind of experiment. Different gelatine mixing ratios (MRs) were tested as well as real birds. A 1:9 MR bird proved to perform too liquid, while a 1:4 and 1:6 MR bird often disintegrated into several big lumps. The main difference between gelatine and real birds can be found for the splitter, where the real bird material is more likely to get stuck on the splitter and increases the momentum transfer (and therefore also force) by a large extent, because of its high kinetic energy. The gelatine is also capable of storing much more elastic energy, which results in a higher deviation angle in case of the splitter experiments and a relatively long increase of the momentum transfer for the wedge.

- The momentum transfer: The impact force is mainly driven by the change of momentum direction, as predicted by the analytical models. The momentum transfer for the plate, wedge and splitter experiments is respectively 100%, 50-60% and 2-6%. The results show that the wedge target can be a very valuable set-up to test bird material models in the future because the momentum transfer depends highly on the velocity of the bird after impact and therefore depends greatly on the constitutive behaviour of the bird material. The average splitter forces are quite low compared to the plate and wedge.
- Residual energy measurement: The rigid plate can be used to measure the residual energy of a bird after an impact event because the momentum transfer for fluid-like impactors is 100%, independent from the type of bird, shape, mass and impact velocity. This can be deduced from the performed experiments and the analytical model.
- Several substances are applied to the smooth surface of the rigid plate in order to visualize the bird impact. Wetted chalk powder proved to be the best option because it has a very good surface covering, high contrast and the bird path is visualized very well.

5.9 Bibliography

Acrosoma (2016), `http://www.vdlfibertechindustries.com/?page/5791502/Acrosoma.aspx`. [Online; accessed 27-july-2016].

Allcock, A. and Collin, D. (1969), The development of a dummy bird for use in bird strike research, Technical Report R.303-A.R.C.30697, National Gas Turbine Establishment.

Anghileri, M., Milanese, A., Moretti, G. and Castelletti, L. (2012), Preliminary investigation on the feasibility of a bird surrogate for full-scale bird impact test, *in* 'Proceedings of the 28th ICAS congress', pp. 1–8.

Anghileri, M. and Sala, G. (1996), Theoretical assessment, numerical simulation and comparison with tests of birdstrike on deformable structures, *in* 'Proceedings of the 20th ICAS congress', pp. 665–674.

Barber, J. P., Taylor, H. R. and Wilbeck, J. S. (1975), Characterization of bird impacts on a rigid plate: Part 1, Technical Report AFFDL-TR-75-5, Dayton University.

Barber, J. P., Taylor, H. R. and Wilbeck, J. S. (1977), Bird impact forces and pressures on rigid and compliant targets, Technical Report AFFDL-TR-77-29, Air Force Flight Dynamics Laboratory, Wright-Patterson Air Force Base.

Bertke, R. S. and Barber, J. P. (1979), Impact damage on titanium leading edges from small soft body impacts, Technical Report AFML-TR-79-4019, University of Dayton Research institute.

Challita, A. (1980), Validation of a bird substitute for development and qualification of aircraft transparenciles, Technical Report AFWAL-TR-80-3098, University of Dayton Research Institute.

Challita, A. and Barber, J. P. (1979), The scaling of bird impact loads, Technical Report AFFDL-TR-3042, University of Dayton Research Institute.

Challita, A. and West, B. S. (1980), Effects of bird orientation at impact on load profile and damage level, Technical Report AFWAL-TR-3009, University of Dayton Research Institute.

Edge, C. H. and Degrieck, J. (1999), 'Derivation of a dummy bird for analysis and test of airframe', *Bird Strike Committee-USA/Canada, First Joint Annual Meeting, Vancouver, BC* .

Georgiadis, S., Gunnion, A. J., Thomson, R. S. and Cartwright, B. K. (2008), 'Bird-strike simulation for certification of the Boeing 787 composite moveable trailing edge', *Composite Structures* **86**(13), 258–268.

Guida, M. (2008), Study, design and testing of structural configurations for the bird-strike compliance of aeronautical components, PhD thesis, University of Naples "Federico II".

Guida, M., Marulo, F., Meo, M. and Riccio, M. (2008), 'Analysis of bird impact on a composite tailplane leading edge', *Applied Composite Materials* **15**(4-6), 241–257.

Guida, M., Marulo, F., Meo, M. and Russo, S. (2013), 'Certification by birdstrike analysis on C27J fullscale ribless composite leading edge', *International Journal of Impact Engineering* **54**, 105–113.

Hopkinson, B. (1914), 'A method of measuring the pressure produced in the detonation of high explosives or by the impact of bullets', *Philosophical Transactions of the Royal Society of London A: Mathematical, Physical and Engineering Sciences* **213**(497-508), 437–456.

Johnson, A. F. and Holzapfel, M. (2006), 'Numerical prediction of damage in composite structures from soft body impacts', *Journal of Materials Science* **41**(20), 6622–6630.

Karthikeyan, K., Ramachandra, S., Vizhian, S. and Chandra, S. (2011), 'Signal processing, wavelets and high-speed image interpretation of bird impact', *Defence Science Journal* **61**(1), 62–71.

Kermanidis, T., Labeas, G., Sunaric, M. and Ubels, L. (2005), 'Development and validation of a novel bird strike resistant composite leading edge structure', *Applied Composite Materials* **12**(6), 327–353.

Lavoie, M., Gakwaya, A. and Ensan, M. N. (2008), 'Application of the SPH method for simulation of aerospace structures under impact loading', *10th European LS-DYNA Users Conference* .

Lavoie, M., Gakwaya, A., Ensan, M. N., Zimcik, D. and Nandall, D. (2009), 'Bird's substitute tests results and evaluation of available numerical methods', *International Journal of Impact Engineering* **36**(1011), 1276 – 1287.

Lavoie-Perrier, M.-A. (2008), Soft body impact modelling and development of a suitable meshless approach, PhD thesis, Université Laval.

Liu, J., Li, Y. L. and Gao, X. S. (2014), 'Bird strike on a flat plate: Experiments and numerical simulations', *International Journal of Impact Engineering* **70**, 21–37.

McCarthy, M. A., Xiao, J. R., McCarthy, C. T., Kamoulakos, A., Ramos, J., Gallard, J. P. and Melito, V. (2004), 'Modelling of bird strike on an aircraft wing leading edge made from fibre metal laminates part 2: Modelling of impact with SPH bird model', *Applied Composite Materials* **11**(5), 317–340.

Prato, A., Anghileri, M., Milanese, A. and Castelletti, L. M. (2015), 'Soft body impact against aeronautical structures', *Journal of Structural Mechanics* **48**(1), 34–48.

Premont, E. and Stubenrauch, K. (1974), Impact resistance of composite fan blades, Technical Report NASA CR-134707, Aircraft Engine Group, General Electric Co.

Robins, B. (1742), *New principles of gunnery: containing the determination of the force of gun-powder and an investigation of the difference in resisting power of the air to swift and slow motions.*

Seidt, J. D., Pereira, M. J., Hammer, J. T., Gilat, A. and Ruggeri, C. (2012), Dynamic load measurement of ballistic gelatin impact using an instrumented tube, *in* V. Chalivendra, B. Song and D. Casem, eds, 'Dynamic Behavior of Materials, Volume 1', Conference Proceedings of the Society for Experimental Mechanics Series, Springer New York, pp. 243–250.

Steinhagen, C. and Salemme, C. (1973), The impact resistance of current design composite fan blades tested under short haul operating conditions, Technical report, General Electric Company.

Wilbeck, J. S. (1978), Impact behavior of low strenght projectiles, Technical Report AFML-TR-77-134, Air Force Materials Laboratory, Wright-Patterson Air Force Base.

Wilbeck, J. S. and Rand, J. L. (1981), 'The development of a substitute bird model', *Transactions of ASME Journal of Engineering for Gas Turbine and Power* **103**(4), 725–730.

Zhu, S., Wang, Y., Tong, M. and Xiong, P. (2014), 'Numerical simulation of bird impact on fibre metal laminates', *Polymers & Polymer Composites* **22**(2), 147–156.

CHAPTER 6

Rigid target calibration tests: simulations

Abstract: The rigid target experiments introduced in the previous chapter gave consistent momentum transfer for the rigid plate, wedge and splitter. Matching the numerical models with these calibration experiments and understanding in which situations these models do not suffice, are an essential step towards the modelling of bird strike on booster vanes. In this chapter, the performance of the numerical material model is investigated for the three rigid targets, mainly using SPH, but also using the CEL method.

6.1 Previous research

Initial numerical research was performed on rigid flat plates to calculate pressure profiles, momentum and force using dedicated codes in (Rosenblatt et al., 1976) or by applying analytical bird loading models on the structure as in (McCarty, 1980; Boehman and Challita, 1982; Hirschbein, 1982).

As introduced in chapter 4, a majority of the more recent research on rigid flat plates focuses on the validation of the pressure at the centre of impact. But several papers also compare the deformation of the bird or the transferred momentum for different shapes, impact speeds and/or modelling techniques such as the standard Lagrangian, ALE, SPH or CEL method (Lavoie et al., 2007*b*,*a*; Lavoie-Perrier, 2008; Langrand et al., 2002; Jain and Shivayogi, 2006; Meguid et al., 2008; Nishikawa et al., 2011; Mao et al., 2008).

Qualitative comparisons between experiment and simulation for bird impact on an orthogonal and rotated plate using SPH and ALE can be found in (Lavoie et al., 2008, 2009; Lavoie-Perrier, 2008). The overall behaviour is approximated well by both techniques. In (Anghileri et al., 2012), a qualitative comparison is also made between experiments and SPH simulations. The peak force is compared as well, which showed to be very dependent on the l/d ratio (which ranged between 2 and 3).

Non-dimensional momentum and peak force have been investigated in (Walvekar, 2007; Simulia, n.d.; Airoldi and Cacchione, 2006). (Walvekar, 2007) obtained a momentum transfer very close to 100% for relatively dense SPH birds at high impact velocities (200-300 m/s) in LS-Dyna. A momentum transfer between 90% and 100% was obtained for Abaqus™ in (Simulia, n.d.) for Lagrangian and CEL birds with and without porosity, where CEL performed slightly better. The peak force was underestimated when compared to the numerical results of (Airoldi and Cacchione, 2006). In (Airoldi and Cacchione, 2006) the non-dimensional momentum for a Lagrangian bird with different shapes (l/d ratio and flat or hemispherical ends) was investigated with ESI/Pam-Crash. They showed that not all the momentum is transferred at the end of the impact duration defined by T (the time during which the bird travels its own length). Increasing the yield limit of

the elastic deviatoric behaviour proved to increase the momentum transfer and increase the tendency to rebound from the target.

Force-time signals have been reported for bird models with similar shape of a duck as well in (Hedayati et al., 2014).

Momentum transfer for rigid knife-like structures such as the wedge and the splitter were not found in literature even though these are an important intermediate step towards booster vane simulations. This chapter will reveal the importance of the artificial viscosity in rigid target simulations. A validation of the concept to measure the residual energy after impact will be given, the wedge as a tool to assess the performance of a bird material model will be further addressed and the influence of the mesh size on very thin knife-like structures will be shown. The results presented in this chapter will be of utmost importance to understand the observations in the booster vane simulations.

In the next section, the principle to measure the force and momentum by releasing one translational DOF is validated numerically. After that, the results of the simulations on the plate, rotated plate, wedge and splitter target are covered respectively in section 6.3, 6.4, 6.5 and 6.6.

6.2 Numerical validation of the force and momentum measurement

In this chapter, the targets are modelled as rigid objects (using analytical surfaces or solids with rigid constraints). Each target is fixed to a reference node able to move in the direction of impact. Extra inertia is added to achieve a similar mass as the experimental set-ups. To verify that the translational DOF has a negligible influence on the impact, a comparison with a fixed boundary condition is made for the plate target. The reaction force of the plate with complete fixation in the direction of impact is integrated over time, giving the momentum of the fixed boundary condition (Equation 5.2). The momentum of the plate with the translational DOF is obtained by multiplying the mass of the target with the velocity of the target ($m_t.v_t(t)$).

This is done for a 300 gram bird with a mesh size of 2 mm. The result is depicted in Figure 6.1. The momentum curves lie on top of each other, validating the concept to measure the momentum or force.

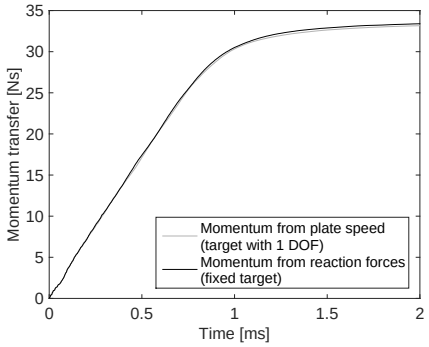

Figure 6.1: Momentum over time obtained from the speed of a free plate and from the reaction force of a fixed plate for the same impact conditions.

The same validation simulation is performed for the splitter and the wedge. A final check is also done by altering the mass of the target set-up (for sake of conciseness this is not included).

6.3 Rigid plate simulations

Very consistent results are obtained from the rigid target experiments in terms of momentum transfer, independent of the shape (l/d ratio, frontal shape of the bird), mass and impact velocity. Therefore, to further investigate this phenomenon, a 300 gram SPH bird model in the shape of a cylinder with hemispherical ends will first be used instead of exact replicas of the performed tests. After that, a comparison will be made with the actual tests.

To introduce this section, the impact on the plate target of a bird with a 2 mm mesh at 110 m/s is discussed. A reference density of 1040 kg/m^3 is assumed and the EOS from (Shepherd et al., 2009) is used, together with a tensile failure criterion of 1 MPa. A bulk viscosity scaling factor of 0.2 is used for both the linear and the quadratic term. Several frames during impact are shown in Figure 6.2.

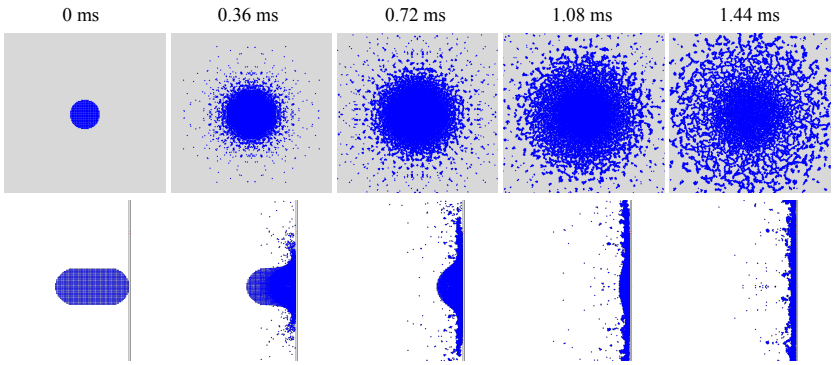

Figure 6.2: Overview of a 300 gram SPH bird impacting a rigid plate at $110\,\mathrm{m/s}$.

The bird runs through its own length in 1.09 ms, which can also be observed in Figure 6.2. The momentum however, as was also observed in (Airoldi and Cacchione, 2006), is transferred over a considerably longer period. Figure 6.3 shows the momentum transfer over time. At T and $1.2T$, respectively 94.1% and 97.2% is transferred to the plate. At the end of the simulation (at 2 ms), 100.1% is transferred to the plate.

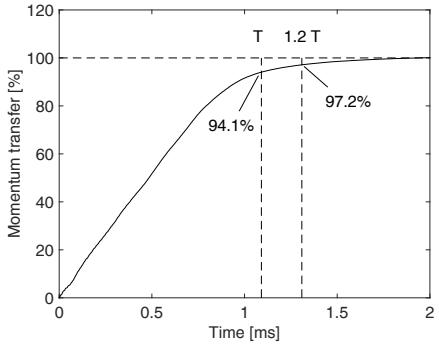

Figure 6.3: Momentum transfer over time for the 2 mm mesh with bulk viscosity scale factors equal to 0.2.

In the following subsections, first the influence of the artificial dissipation and the mesh density is covered, because it has a major influence on the results. After that the influence of shape will be investigated by changing the l/d ratio, the tilt angle and altering the mass and the concept to measure the residual energy of the bird after an impact event will be validated. In

section 6.3.4, some results of the CEL method are discussed. Finally, a comparison with a test is made.

6.3.1 Artificial dissipation and mesh density

In the simulation introduced above, the default linear and quadratic bulk viscosity factors are reduced to 20%. The influence of this scale factor and the mesh density can be quite large. Figure 6.4 shows the momentum transfer for a 1 mm, 2 mm, 4 mm and 8 mm bird mesh (respectively corresponding with 288368, 36192, 4504 and 556 elements) for bulk viscosity scale factors equal to 0.1, 0.2, 0.4, 0.6 and 1.0. Decreasing the mesh size decreases the momentum transfer, which is too high for coarser meshes. For the two finest meshes, the default bulk viscosity factor (scale factor 1.0) underestimates the momentum transfer by 10%. Decreasing the bulk viscosity factor improves the momentum transfer for the finer meshes.

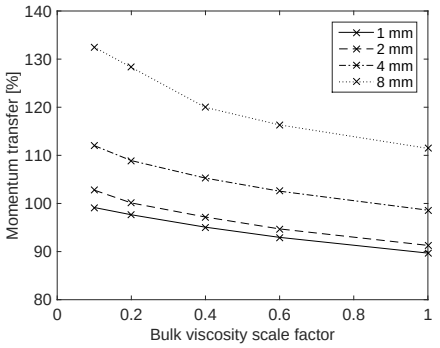

Figure 6.4: Momentum transfer in function of the bulk viscosity scale factor for different mesh sizes.

Disregarding the fact that artificial dissipation has a high influence on the momentum transfer and therefore force, this factor has not yet been discussed in the examined literature.

The momentum transfer dictates the force that is applied to a structure and should, according to the analytical solution and the experiments, be 100%. However, because the coarser meshes seem to behave rather as a cloud of particles than a continuum, the momentum transfer is increased above the theoretical value. The particles rather bounce back than represent

a continuous flow. The momentum after impact adds up to the momentum equilibrium (Equation 5.6) and will increase the momentum above 100%. An overview from the top is shown in Figure 6.5 for the four meshes at the end of the simulation (with a bulk viscosity scale factor of 0.2).

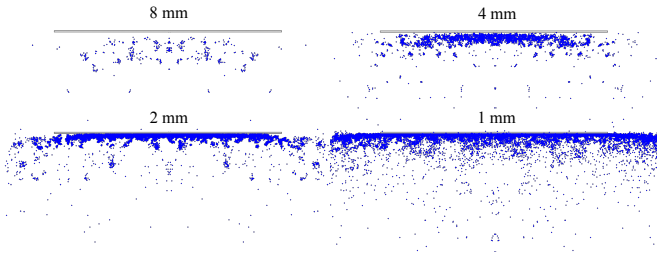

Figure 6.5: Bounce back versus flow for different mesh sizes.

These images show that, especially for the coarser meshes, a relatively large part of the mass is bounced back from the plate. To get an idea of the momentum that corresponds with this mass, the script mentioned in section 4.2.3.5 is used to calculate the momentum in the direction orthogonal to the plate (from the velocity vector of each separate particle). With this script, the momentum values in Table 6.1 are obtained. $J_{b,1}$ stands for the initial momentum of the bird for the different mesh sizes. These are not always the same because it is impossible to get an exact match in shape and mass for different mesh sizes. $J_{b,2}$ stands for the momentum of the bird in the direction orthogonal to the plate at the end of the simulation. The last column contains $J_{b,2}$ relative to the initial momentum $J_{b,1}$ in percent. The obtained momentum after impact indeed corresponds well with the overestimation of the momentum in Figure 6.4 for the bulk viscosity scale factor equal to 0.2. The overestimation is therefore clearly a result of the inability of the coarser meshes to flow (possibly also related to high contact forces).

The large influence of the bulk viscosity scale factor and mesh density can also be observed in the energy levels. The artificial bulk viscosity dissipates energy (Figure 6.6a), which is used partly to smear out the shock front over a band of elements (see also chapter 4). The smaller the mesh size, the shorter the shock front can be and therefore the less energy that needs to be dissipated. Decreasing the scale factor also decreases the amount of dissipated energy. A substantial amount of energy is dissipated, which can

Table 6.1: Momentum after impact for the bulk viscosity factor of 0.2

Mesh size [mm]	$J_{b,1}$ **[Ns]**	$J_{b,2}$ **[Ns]**	$J_{b,2}/J_{b,1}$ **[%]**
8	32.566	-9.674	29.7
4	32.976	-3.705	11.2
2	33.123	-0.983	3.0
1	32.989	-0.069	0.2

also be observed in the final kinetic energy (Figure 6.6b). For the 2 mm mesh for example, the residual kinetic energy can vary over 20% depending on the scale factors. For simulations where secondary impacts can occur, the residual energy is of great importance. Any physical dissipation mechanism so far is not modelled, so only the bulk viscosity scale factors can alter the amount of energy dissipation in the bird during impact.

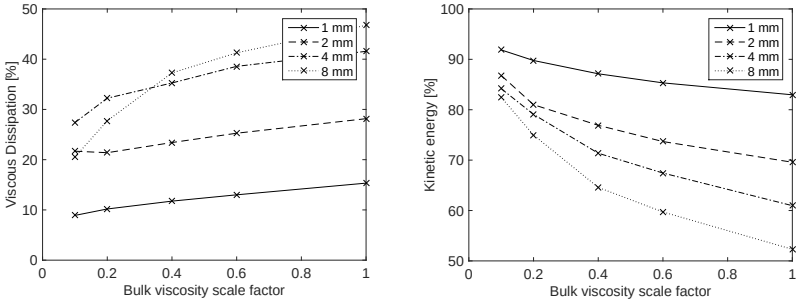

(a) Influence on the artificial dissipation. **(b)** Influence on the kinetic energy.

Figure 6.6: Influence of the bulk viscosity on the artificial dissipation and the kinetic energy for the rigid plate (relative to the impact energy).

It must be noted that orthogonal impact on a rigid plate is the most violent scenario. For targets that are deformable or for targets which makes the bird deviate considerably less from the original trajectory, the induced pressures and shock waves might be lower, resulting in a lower amount of dissipation. So the 20% mentioned previously might be a conservative value for the more practical cases.

6.3.2 Influence of the shape

Inherent to bird strike experiments, small deviations can be found in the impact conditions (due to the launching and stripping process). The bird can deviate slightly from the original shape, the bird might rotate during flight, resulting in a certain impact tilt angle, etc. Several simulations with a range of aspect ratios (l/d=1, 1.5, 2, 3 and 4), tilt angles (0°, 10°, 15°, 30° and 45°) and bird masses (m=0.11 kg, 0.17 kg, 0.30 kg, 0.42 kg and 0.79 kg) are performed to further investigate the influence of such deviations (Figure 6.7 to 6.9). Figure 6.7 shows the momentum transfer in function of time for the considered aspect ratios with an approximately constant mass (the shapes are shown on the right). The final momentum is each time 100%, but is transferred over a time period relative to its length (the time it takes to reach 100%). As a result, the slope and therefore the force scales relative to its length.

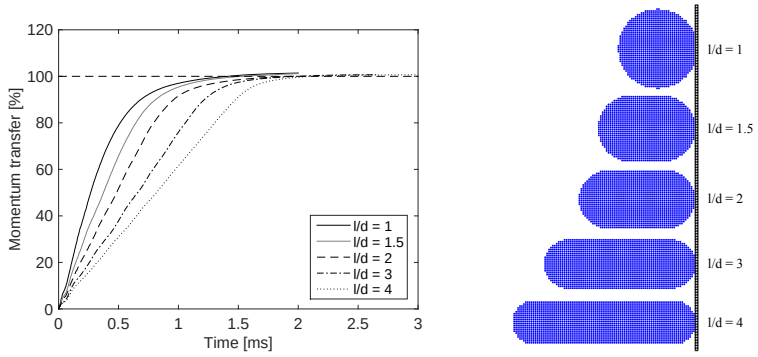

(a) Momentum transfer for different aspect ratios.

(b) Considered aspect ratios.

Figure 6.7: Influence of the aspect ratio.

In (Airoldi and Cacchione, 2006), it was also concluded that the momentum transfer is approximately the same for different aspect ratios. The small differences that can be observed are likely the result of the energy dissipation mechanism, which depends on how violent the steady state regime is.

Figure 6.8 shows the influence of the projectile's tilt angle (the initial impact momentum vector is still orthogonal to the plate, but the bird is rotated in the vertical plane as displayed in Figure 6.8b). Again the momentum

transfer is 100% for all the considered impact angles. There is only a small influence on the impact force. Beneath 30°, the influence is almost negligible. As can be observed in Figure 6.8b, the length of the projectile orthogonal to the plate indeed does not change that much for angles beneath 30°.

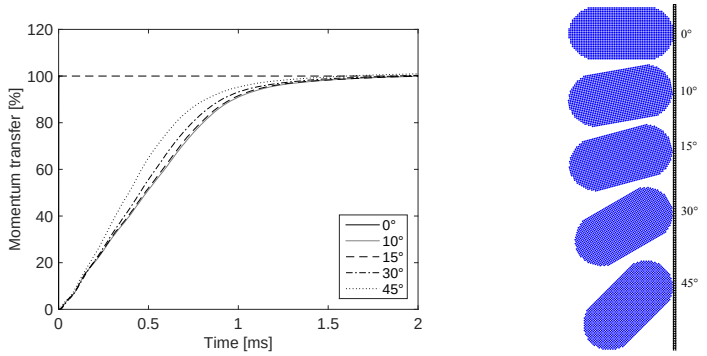

(a) Momentum transfer for different tilt angles.

(b) Considered tilt angles.

Figure 6.8: Influence of the tilt angle.

In Figure 6.9, the momentum transfer for different impact masses is considered. A slightly higher momentum transfer is obtained for the lower masses. This effect however can be the result of the mesh density per volume that decreases. The change in relative artificial dissipation also fluctuates much more for the simulations with a variable mass. The force increases slightly with increasing mass, which is also observed in the previous chapter.
These simulations give an indication that the momentum transfer is independent of the shape. This can be concluded from the experiments (see Figure 5.9), the simulations (Figure 6.7 to 6.9) and the analytical model, which led to the final concept for the set-up to measure the residual energy of the bird after an impact event, as derived in the previous chapter.

6.3.3 Validation of the bird residual energy measurement concept

A final validation of the concept is done by considering a secondary impact where a 300 gram 2 mm mesh SPH bird first hits a rigid rotated plate, after which the deformed bird hits a second rigid plate. The second plate is restricted to move in the direction orthogonal to the plate and the velocity

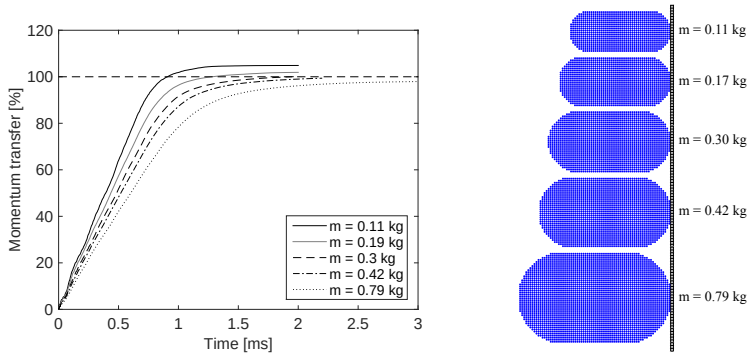

(a) Momentum transfer for different projectile masses.

(b) Considered projectile masses.

Figure 6.9: Influence of the projectile mass.

of the reference node is tracked.

In this simulation, a variable smoothing length is needed to maintain stability throughout the analysis. In fact, it is very difficult to maintain stability when simulating secondary impact in one simulation, even with increased bulk viscosity scale factors, averaging out the velocity field using XSPH (Monaghan, 2005) and a variable smoothing length.

Figure 6.10 shows several frames of a simulation with and without the second plate. The absence of tensile strength makes the particles easily detach from the continuum. This effect is even increased in secondary impact.

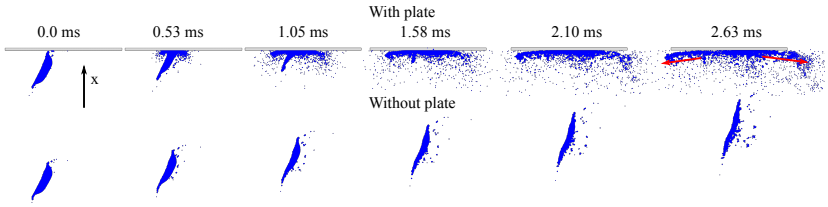

Figure 6.10: Secondary impact with and without a second plate.

The bottom row shows the simulation without a second plate, which is used to derive the reference impact momentum of the bird. A momentum of 26.56 Ns in the direction orthogonal to the second plate (the x-direction) is obtained from this simulation. The momentum transfer over time of the

second plate (in the upper row)) relative to this value is shown in Figure 6.11.

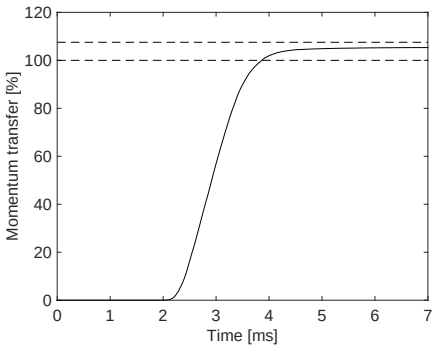

Figure 6.11: Momentum transfer second plate for a highly deformed bird.

As can be observed in Figure 6.10, after the impact on the second plate, the deflected mass does not exactly move orthogonal to the x-direction (the velocity vectors are represented by red arrows), there is some momentum in the negative x-direction. The momentum of the bird after impact in the x-direction is equal to approximately 2 Ns (the red vectors in Figure 6.10 projected on the x-direction). Adding this residual bird momentum to the one of the plate and dividing by the initial bird momentum results in a momentum tranfser of 107.5 % instead of 100 %, which is also added to Figure 6.11. The momentum of the plate is indeed higher than 100 % and quite close to the 107.5 %. In the experiments however returning mass is never observed so for the mass that hits the plate, a momentum transfer of 100 % can be assumed.

6.3.4 Comparison to the CEL method

For the same characteristic mesh lengths as the SPH meshes (1 mm, 2 mm, 4 mm and 8 mm), CEL simulations are performed. The Euler domain is chosen as tight as possible around the path where the material flows in a full-scale model or one fourth with appropriate symmetry boundary conditions for the denser meshes (Figure 6.12a). For the simulations with symmetry boundary conditions, the final momentum is multiplied by four to account for the force of the other four parts. The momentum transfer over time for the four meshes is shown in Figure 6.12b.

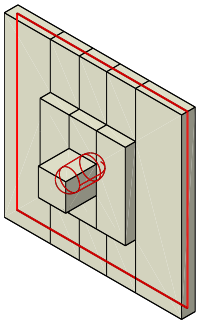

(a) Euler domain rigid plate impact.

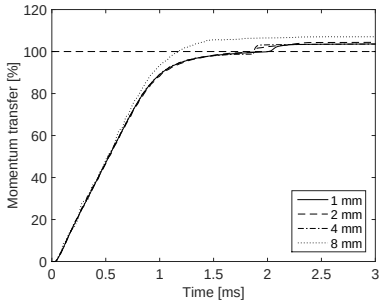

(b) Momentum transfer.

Figure 6.12: CEL simulation rigid plate: model and momentum transfer.

An unrealistic jump in the momentum transfer occurs around 1.9 ms, which increases the momentum transfer above the theoretical 100%. This occurs at approximately the same time where the bird layer is only one element thick (or less) any more and this will likely be a numerical artefact. The momentum transfer however has reached a constant value before this point. In the energy levels, several artefacts can be found as well. Figure 6.13 shows the viscous dissipation and total energy over time for the different meshes.

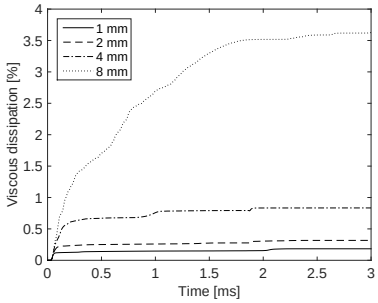

(a) Viscous dissipation.

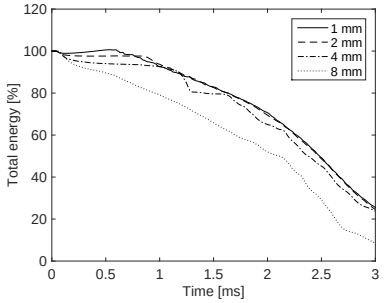

(b) Total energy.

Figure 6.13: Viscous dissipation and total energy for a CEL impact on the rigid plate.

The dissipation is more than 10 times less than for SPH (see Figure 6.6a). This is a considerable difference with SPH. For the same impact scenario, more energy needs to be dissipated to obtain a stable solution with SPH. The much lower dissipation cannot be observed in the residual kinetic energy, because mass flows out of the Eulerean domain at approximately 1 ms.

This is also shown in the total energy graph (Figure 6.13b). A drop in the total energy already occurs just after impact at 0.05 ms. This drop is also observable in the kinetic energy. The mass in the Eulerean domain starts dropping after 1 ms, which means that the drop of the kinetic energy will be the result of a drop in speed. The drop decreases with decreasing mesh size, so it can be a convergence issue.

It can be concluded that CEL leads to the same results as SPH in terms of momentum transfer and that the solution is obtained with much less artificial dissipation. On the other hand, to keep track of the energy levels is less straightforward due to the fact that for an adequate Eulerian domain, mass flows out very soon after impact. Some numerical artefacts are also observed in the solution and the development of the model is much more time consuming.

6.3.5 Comparison with a test

High contrast images with a low amount of foam are obtained in experiment RP-16 (0.3028 kg at 135.4 m/s). A 2 mm SPH bird mesh is generated conform the mould and a mass close to the one in the experiment. A visual comparison between experiment and simulation, from a similar point of view, is shown in Figure 6.14. To increase the contrast in the simulation, the field output *COOR3* is shown, which stands for the coordinate in the impact direction.

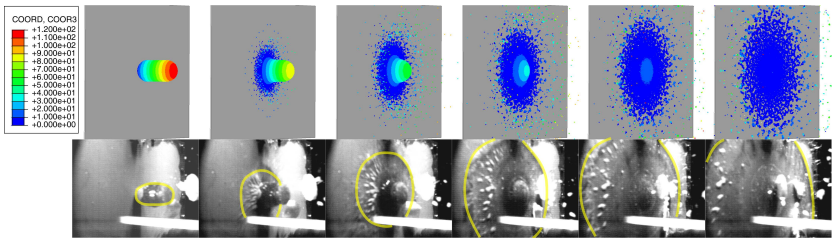

Figure 6.14: Visual comparison between experiment RP-16 and an SPH simulation.

The shape of the bird before the radial flow is comparable. The speed at which the bird is deviated outwards seems to be slightly higher in the experiment. This however is very dependent on the mesh size. Lighter particles are more easily accelerated outwards. The denser meshes can also give the impression to have a higher radial speed because the same mass is

represented by more particles. A comparison between the three densest SPH meshes with bulk viscosity factor scale factor 0.2 is shown in Figure 6.15.

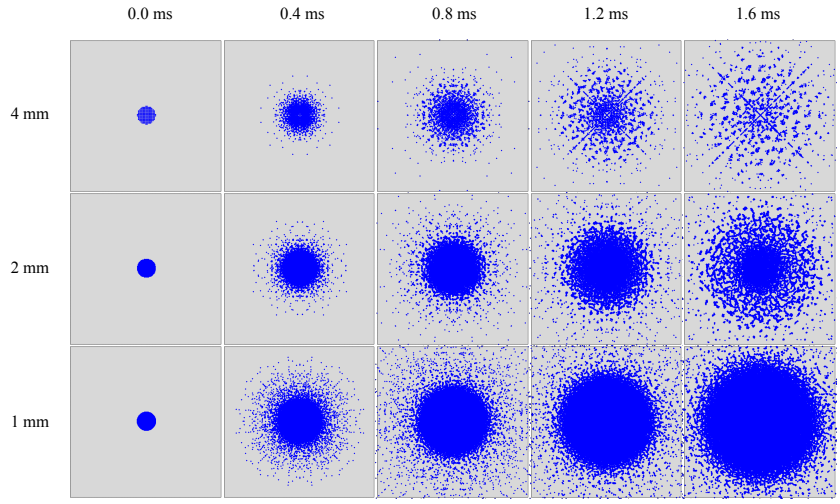

Figure 6.15: Radial particle flow for SPH mesh sizes 1 mm, 2 mm and 4 mm.

This very high change of momentum direction and jetting is much less pronounced in the experiments and simulations on the vane.

6.4 Rotated plate simulations

The analytical models introduced in section 5.4 showed that contrary to the wedge, the momentum transfer of a rotated plate is defined by $\sin(\alpha)^2$, independent of the speed of the bird after impact. To validate this and consequently reveal the significant difference between the rotated plate and the wedge, simulations are performed both on a rotated plate and on a wedge structure.

Figure 6.16 shows an overview of a 2 mm bird mesh impacting the rotated plate with an angle of 45° with respect to the impact direction, at 110 m/s (a view perpendicular to the plate and a view from the top).
As with the plate orthogonal to the impact direction, the bird expands radially in a plane parallel to the plate. But in this case, there is a more pronounced mass flow to the right end of the plate, because there is an initial impact momentum in that direction.

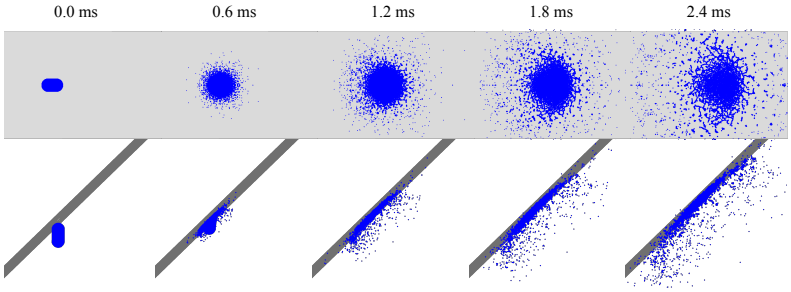

Figure 6.16: Impact of a 2 mm mesh bird on the rotated plate at 110 m/s: a view perpendicular to the plate (top row) and a view from the top (bottom row).

6.4.1 Comparison to the analytical model

The analytical model assumes that there is no momentum perpendicular to the plate after impact. In the simulation, it can be observed that there is again some momentum perpendicular to the plate after impact. The obtained momentum perpendicular to the plate, relative to the initial momentum perpendicular to the plate however is only 1.8%. From the final speed of the rotated plate, a momentum transfer of 50.0% is obtained, which corresponds well with the analytical model.

Figure 6.17 shows the final momentum transfer of the rotated plate for a set of angles ($\alpha = 30°$, 40°, 45°, 60° and 70°), for the default bulk viscosity and 20% reduced bulk viscosity, compared to the analytical solution (Equation 5.8). Again, the momentum transfer correlates well with the analytical solution for the reduced bulk viscosity.

6.4.2 Comparison to the CEL method

Also for the CEL method, a good correlation with the analytical solution is obtained. This is investigated for the plate rotated at 45°. Figure 6.18a shows the deformation of a 2 mm Eulerian mesh, 1.2 ms after impact. Figure 6.18b shows the obtained momentum transfer for three mesh sizes (2 mm, 4 mm and 8 mm). Even for the coarser meshes, the momentum transfer is quite close to the analytical result.
For the rigid plate, perpendicular or rotated with respect to the impact direction, the requirements to obtain a correct momentum transfer are easily

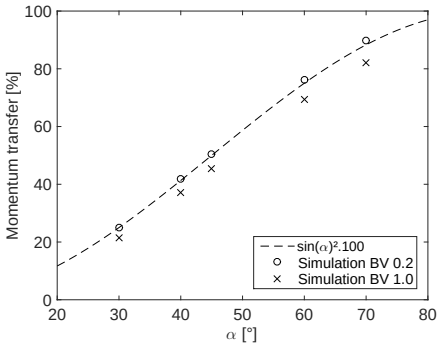

Figure 6.17: Final momentum transfer for the rotated plate, in function of the angle with the impact direction.

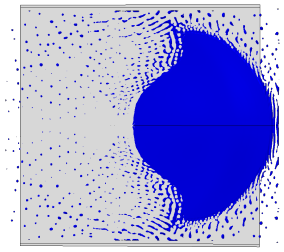

(a) 2 mm Eulerian mesh, 1.2 ms after impact.

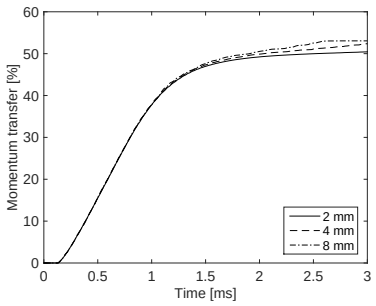

(b) Momentum transfer.

Figure 6.18: CEL simulation rigid plate: global deformation and momentum transfer.

fulfilled (the independence of the bird velocity after impact), contrary to the wedge.

6.5 Wedge simulations

Figure 6.19 shows an overview of a 2 mm bird mesh impacting the wedge at 110 m/s (a view perpendicular to the right plate and a view from the top). The bird mass is splitted and deviated in two directions. Also in the vertical direction, the bird is deformed. When comparing the shape of the bird at 1.2 ms with the rotated plate simulation, it can be observed that they resemble quite well (Figure 6.16).

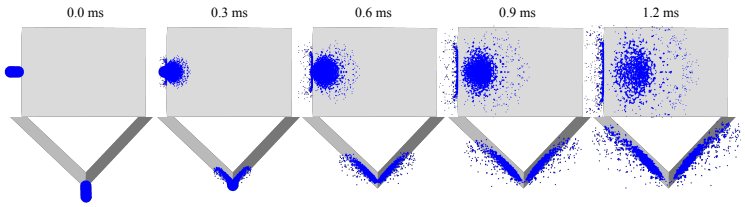

Figure 6.19: Impact of a 2 mm mesh bird on the wedge at 110 m/s: a view perpendicular to the right plate (top row) and a view from the top (bottom row).

6.5.1 Comparison to the analytical model

Figure 6.20a shows the momentum transfer over time of the wedge ($\alpha = 45°$) for simulations with different bird mesh sizes (8, 4, 2 and 1 mm). The momentum transfer for the wedge converges to a value of about 37%. To validate the analytical expression of the momentum transfer for the wedge (Equation 5.11), the speed of the bird after impact $v_{b,2}$ can be derived using the script introduced in section 4.2.3.5. For the 2 mm bird mesh in Figure 6.20a, with an initial bird impact speed $v_{b,1} = 110$ m/s, a speed after impact $v_{b,2}$ of 96.6 m/s is obtained, which translates to a momentum transfer of 37.9% (Equation 5.11). This is very close to the momentum transfer obtained from the velocity of the plate in Figure 6.20a. This proves that the momentum balance is valid.

Despite the fact that the momentum balance is correct (both analytically and in the simulation), the momentum transfer in Figure 6.20a is much lower than the 50-60% seen in the experiments (see also Figure 5.9). The fact that the momentum transfer in the experiments is much higher can only be because of a lower $v_{b,2}$ (since Equation 5.11 has been proved to be valid). The momentum is also transferred over a much shorter period in the simulations. The momentum transfer keeps rising up to roughly 1 ms, opposed to the 2 ms in the experiments. This is also shown in Figure 6.20b, where the momentum transfer over time of the bird with the 2 mm mesh and a bulk viscosity scale factor of 0.2 is compared with the experimental momentum curves shown in the previous chapter.
These two observations give an indication that the material model is not capable to simulate this event (the momentum transfer is underestimated by 20%). Some deviatoric and/or dissipating constitutive behaviour could decrease the speed of the bird after impact $v_{b,2}$ and therefore increase the

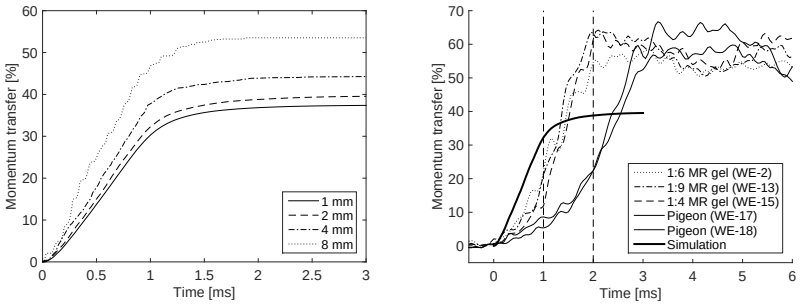

(a) Wedge momentum over time for different bird mesh sizes.

(b) Comparison momentum transfer over time from experiments with the 2 mm mesh simulation.

Figure 6.20: Momentum transfer wedge.

momentum transfer. Deviatoric stiffness for sure is missing to increase the impact time and obtain a more elastic behaviour. Several unsuccessful attempts were made to improve the material model. All the attempts systematically deteriorated the performance in other situations.

This type of target hereby proves to be very valuable for testing the performance of bird material models as the momentum transfer depends greatly on the constitutive behaviour of the impactor material. The wedge target can be used to test new material models in the future.

6.5.2 Comparison with the CEL method and a test

Several simulations with the CEL method are performed. For a 2 mm, 4 mm and 8 mm mesh, a momentum transfer of respectively 41.9%, 39.1% and 38.2% is obtained. A comparison with test WE-5 is shown in Figure 6.21 (a perspective slightly looking downwards, the bird is quite well aligned with the impact direction), where the bird is modelled once with a 2 mm SPH bird mesh (centre row) and once with the 2 mm CEL bird mesh (bottom row). Red contours are drawn around the initial bird shape to compare with the final deformation of the bird.
Up till 2 ms after impact, the deformation of the bird is similar. After 2 ms, the flat shape of the bird starts contracting again because of the stored elastic energy, contrary to the bird in the simulations which just keeps expanding.

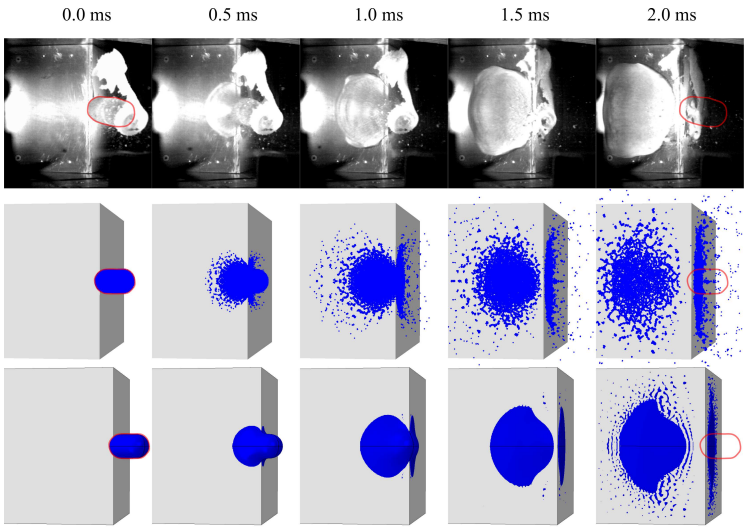

Figure 6.21: Impact of a $2\,\mathrm{mm}$ CEL (bottom row) and SPH (centre row) bird on the wedge at $110\,\mathrm{m/s}$, compared to test WE-5 (top row).

6.6 Splitter simulations

Running the splitter simulations with reduced bulk viscosity scale factors often results in instabilities during simulation (explosions of particles followed by a decrease of the stable time increment). Figure 6.22 shows such an instability for a $1.262\,\mathrm{mm}$ bird mesh. These instabilities also distort the mesh greatly further on in time.

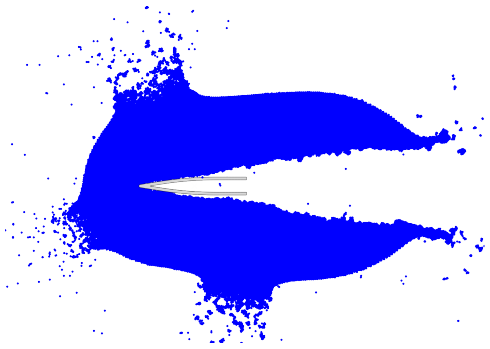

Figure 6.22: Impact of a $1.262\,\mathrm{mm}$ mesh bird on the splitter at $88\,\mathrm{m/s}$ (SP-1).

Therefore splitter simulations are performed with a reduced bulk viscosity scale factor and a variable smoothing length as well as without reducing the bulk viscosity.

Several splitter simulations are performed with the same input parameters as experiment SP-1 (the 1:6 MR gelatine bird with an impact momentum of 135 Ns in Figure 5.21). Figure 6.23a shows the final momentum transfer for different mesh sizes (the finest mesh size is 1.002 mm, corresponding with 1.5 million elements), for SPH with the default and reduced bulk viscosity and the CEL method. The dashed lines represent the minimum and maximum experimentally obtained momentum transfer for gelatine (1.83% and 3.11%). The influence of the mesh size is relatively higher for the splitter simulations compared to the wedge and the plate. The momentum transfer seems to decrease linearly with decreasing mesh size. For a decreasing mesh size, the elastic energy keeps decreasing. As a result, the bird deviates less from the impact direction (dashed line) for a decreasing mesh size, as shown on the right in Figure 6.23b for two mesh sizes. The upper part only shows the contour of the 2.52 mm mesh in green which deviates more from the impact direction (the dashed line) than the 1.59 mm mesh in blue.

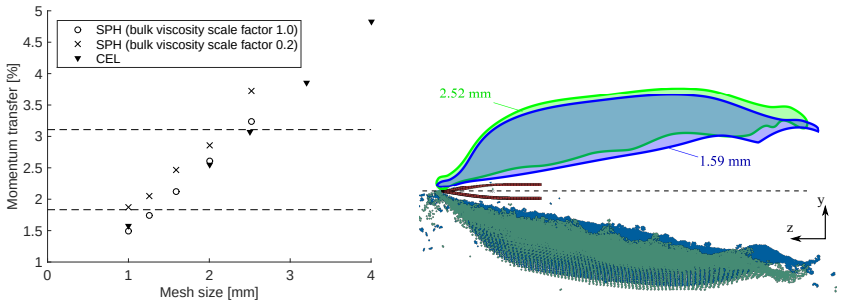

(a) Momentum transfer in function of the mesh size.

(b) Deviation of the bird for different mesh sizes.

Figure 6.23: Final splitter momentum transfer in function of the mesh size and a comparison of the deviation of two different mesh sizes.

It is also important to note that for the large ratio of bird mesh size to splitter tip radius, the particle distribution has a large influence on the result. Small offsets can lead to large deviations of the bird from the impact direction. Figure 6.24 shows a zoom of the 1.59 mm mesh 0.67 ms after impact, with

no offset (in the splitter simulations so far, one layer of particles was initially always aligned with the splitter), an offset of 0.495 mm and an offset of 0.795 mm and a comparison with the 1.002 mm mesh. The red angle is the reference situation with an offset of 0.795 mm.

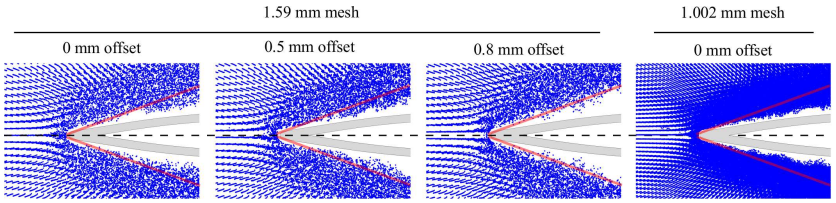

Figure 6.24: Deviation of the 1.59 mm bird mesh for different offsets compared to the 1.002 mm mesh (the red angle is the reference situation with an offset of 0.795 mm).

For the mesh offset of 0.795 mm, the two central layers of particles are much more deviated outwards after contact, preventing the mesh to slide over the angled surfaces, increasing the deviation of the bird after impact and therefore increasing the momentum transfer. This effect decreases at decreasing mesh size, which can be observed when comparing the deviation of the 1.59 mm mesh with the 1.002 mm mesh.

Because the distance over which the bird can be deviated in case of the splitter is much shorter than for the wedge, the elasticity of the gelatine bird stops to contribute to the momentum transfer much sooner. As a result, the impact duration is better approximated by the simulation in case of the splitter. Figure 6.25 shows the momentum transfer over time of the 1.002 mm SPH bird mesh with default bulk viscosity scale factors (input conditions of SP-1), compared to the experiments with gelatine birds. Compared to the experiment, the slope in the simulation is also constant but slightly lower. The impact duration is slightly lower, but not that extreme as in the wedge simulations.

Also in the booster vane simulations, the distance over which the bird can be deviated will be significantly shorter than the wedge. The underestimation of the impact duration in the simulation will therefore also be much smaller than the one seen in the wedge simulations.

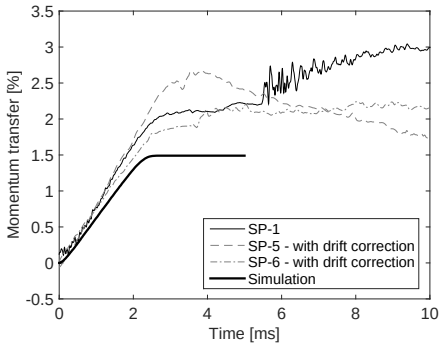

Figure 6.25: Momentum transfer over time of the $1.002\,\mathrm{mm}$ SPH bird mesh compared to the experiments with gelatine.

In the previous chapter, it was already shown that the speed of the bird after impact has a relatively large influence on the momentum transfer for small deviation angles. To obtain the theoretical momentum transfer in the simulation, the deviation angle and the speed of the bird after impact needs to be determined. Therefore, the velocity vectors of each particle in the bird are summed up separately for each half of the bird (the upper and lower half). To obtain the deviation angle, the angle between these two vectors and the y-direction (defined in Figure 6.23b) is calculated, subtracted from $\pi/2$ and averaged. The speed of the bird after impact is obtained by summing up the absolute y and z-components of the lower and upper part velocity vector, calculating the magnitude of this vector in the y-z plane and dividing it by the amount of particles.

For the finest SPH mesh of 1.002 mm, with the default bulk viscosity scale factor and a variable smoothing length, a deviation angle of 6.7° and a bird speed of 85.51 m/s after impact is obtained, for an impact speed of 87.60 m/s. This corresponds with a momentum transfer of 2.38%, opposed to the 1.49% obtained directly from the speed of the splitter after impact. The momentum transfer is overestimated, which can be the result of the speed of the bird after impact that is underestimated. Possibly, this is the result of the artificial dissipation, which consumes momentum of the bird and results in a lower momentum after impact than should be the case. For the 2.0 mm mesh for example the momentum transfer is approximated better

by the simulation with reduced artificial dissipation. Table 6.2 gives, for the two simulations (only differing in bulk viscosity scale factor and the use of a variable smoothing length), the calculated speed and deviation angle of the bird after impact, the theoretical momentum transfer MT_{th} determined from the analytical expression (Equation 5.11) and the actual momentum transfer MT_{act} determined from the speed of the splitter after impact (Equation 5.5). For the reduced bulk viscosity scale factor, the bird speed after impact is larger, which makes the momentum transfer decrease and therefore better correlates with the actual momentum transfer.

Table 6.2: Actual and theoretical momentum transfer for the 2.0 mm splitter simulation with the default and reduced bulk viscosity scale factor.

BV factor	**Variable h**	$\mathbf{v_{b,2}}$ **[m/s]**	$\boldsymbol{\alpha}$ [°]	$\mathbf{MT_{th}}$ [%]	$\mathbf{MT_{act}}$ [%]
1.0	no	84.99	9.29	4.25	2.61
0.2	yes	85.30	8.23	3.65	2.86

The absence of deviatoric and/or dissipating constitutive behaviour might again be the reason that the momentum transfer is slightly underestimated for the finer meshes, although the momentum transfer is still very well in line with that of the gelatine birds in Figure 5.21a and Figure 5.23.

A comparison between the overall behaviour of the SPH and CEL bird with the 2.0 mm mesh, impacting the splitter, is shown in Figure 6.26. The shape of the bird before, during and after the event is quite similar.
Again, the CEL method is very close to the solution obtained with SPH. Also for the wedge and the plate (orthogonal or rotated with respect to the impact direction), the overall behaviour and the momentum transfer in case of the CEL method is very close to SPH. The high mesh dependency for the splitter simulation is almost identical to SPH. This shows that both methods are equivalent in terms of general behaviour. For the splitter, the mesh dependency hereby is proven to be a mesh convergence issue instead of a numerical artefact of SPH. Computation time however is higher for the CEL method. The CPU time for the simulation with a single processor, with the 2.0 mm mesh for the bird and the wedge as target for example, is 13 minutes

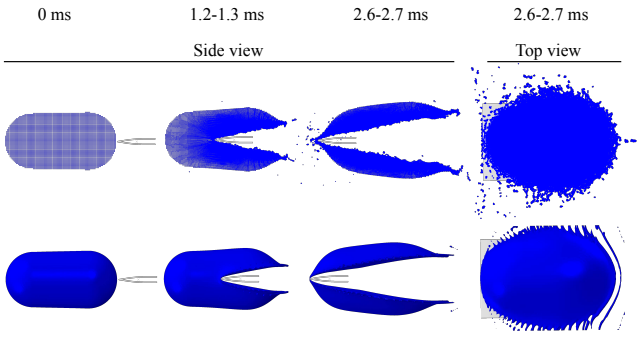

Figure 6.26: Comparison of the SPH and CEL bird with a 2.0 mm mesh, impacting the splitter (not exactly at the same time frame).

for SPH, while the CEL method takes up to 9 hours (for simulating only one quarter of the bird). Because of the much higher domain that needs to be covered by the CEL method, much more elements are needed (322320 opposed to 36072 for SPH).

6.7 Conclusion

This chapter summarizes the results of the rigid target simulations. In general, it is shown that the change of momentum of the bird is the main driving force during impact, but that deviatoric and/or dissipating constitutive behaviour is missing to get the momentum transfer right for the wedge and splitter simulations. For the different targets, the following conclusions can be made:

- **Plate:** The artificial viscosity has a large influence on the momentum transfer. By default, it dissipates too much momentum, leading to an underestimated momentum transfer. As predicted by the analytical model, the momentum transfer is independent of the shape, mass and impact velocity. This has been proven by considering different aspect ratios, tilt angles and masses of the bird. This lead to the concept to measure the residual energy in the previous chapter, which is now also validated numerically.
- **Wedge:** The momentum transfer for the rotated plate corresponds well with the analytical model. So does the wedge, but the momentum

transfer is much lower than in the experiments. The momentum is also transferred over a much shorter time. Most likely, deviatoric and/or dissipating constitutive behaviour is missing to increase the elasticity of the bird and decrease the velocity of the bird after impact. Several unsuccessful attempts were made to improve the material model. All the attempts systematically deteriorated the performance in other situations.

- **Splitter:** A very high dependency of the mesh size is observed in the momentum transfer of the splitter. Mesh convergence is not yet reached as a result of the instabilities occurring and the computational effort that is required (in the order of millions of elements) when further decreasing the mesh size. Again deviatoric and/or dissipating constitutive behaviour possibly is needed to improve the correlation with the experiments for the finer meshes.

The CEL method performs very similar to SPH, in terms of momentum transfer and general behaviour. This is an indication that both methods are worthy of simulating bird strike and is another proof that some observations throughout this chapter are not the result of some numerically related artefact.

The performed experiments and simulations prove that rigid targets can still be valuable in bird strike research because it allows to focus on the bird behaviour contrary to the otherwise highly coupled impact event.

6.8 Bibliography

Airoldi, A. and Cacchione, B. (2006), 'Modelling of impact forces and pressures in Lagrangian bird strike analyses', *International Journal of Impact Engineering* **32**(10), 1651 – 1677.

Anghileri, M., Milanese, A., Moretti, G. and Castelletti, L. (2012), Preliminary investigation on the feasibility of a bird surrogate for full-scale bird impact test, *in* 'Proceedings of the 28th ICAS congress', pp. 1–8.

Boehman, L. and Challita, A. (1982), A model for predicting bird and ice impact loads, Technical Report AFWAL-TR-82-2046, University of Dayton Research Institute.

Hedayati, R., Sadighi, M. and Mohammadi-Aghdam, M. (2014), 'On the difference of pressure readings from the numerical, experimental and theoretical results in different bird strike studies', *Aerospace Science and Technology* **32**(1), 260–266.

Hirschbein, M. S. (1982), Bird impact analysis package for turbine engine fan blades, Technical Report Nasa-TM-82831, NASA, Lewis Research Center.

Jain, R. and Shivayogi (2006), Effect of bird material and projectile shape on temporal pressure during bird impact, *in* 'Proceedings of the Altair's user conference', pp. 1–14.

Langrand, B., Bayart, A.-S., Chauveau, Y. and Deletombe, E. (2002), 'Assessment of multi-physics FE methods for bird strike modelling-application to a metallic riveted airframe', *International Journal of Crashworthiness* **7**(4), 415–428.

Lavoie, M., Gakwaya, A. and Ensan, M. N. (2008), 'Application of the SPH method for simulation of aerospace structures under impact loading', *10th European LS-DYNA Users Conference* .

Lavoie, M., Gakwaya, A., Ensan, M. N. and Zimcik, D. (2007*a*), 'Review of existing numerical methods and validuation procedure available for bird strike modelling', *International Conference on Computational & Experimental Engineering and Sciences* **2**, 111–118.

Lavoie, M., Gakwaya, A., Ensan, M. N. and Zimcik, D. (2007*b*), 'Validation of available approaches for numerical bird strike modeling tools', *International Review of Mechanical Engineering* .

Lavoie, M., Gakwaya, A., Ensan, M. N., Zimcik, D. and Nandall, D. (2009), 'Bird's substitute tests results and evaluation of available numerical methods', *International Journal of Impact Engineering* **36**(1011), 1276 – 1287.

Lavoie-Perrier, M.-A. (2008), Soft body impact modelling and development of a suitable meshless approach, PhD thesis, Université Laval.

Mao, R. H., Meguid, S. A. and Ng, T. Y. (2008), 'Transient three dimensional finite element analysis of a bird striking a fan blade', *International Journal of Mechanics and Materials in Design* **4**(1), 79–96.

McCarty, R. E. (1980), Evaluation of the impact computer program as a linear design tool for bird-resistant aircraft transparencies, Technical Report AFFDL-TR-79-3103, Air Force Flight Dynamics Laboratory, Wright-Patterson Air Force Base.

Meguid, S., Mao, R. and Ng, T. (2008), 'FE analysis of geometry effects of an artificial bird striking an aeroengine fan blade', *International Journal of Impact Engineering* **35**(6), 487 – 498.

Monaghan, J. J. (2005), 'Smoothed particle hydrodynamics', *Reports on Progress in Physics* **68**(8), 1703.

Nishikawa, M., Hemmi, K. and Takeda, N. (2011), 'Finite-element simulation for modeling composite plates subjected to soft-body, high-velocity impact for application to bird-strike problem of composite fan blades', *Composite Structures* **93**(5), 1416 – 1423.

Rosenblatt, M., Eggum, G., DeAngelo, L. and Kreyenhagen, K. (1976), Numerical analyses of soft body impacts on rigid and deformable targets, Technical Report AFML-TR-76-202, California Research and Technology, Inc.

Shepherd, C. J., Appleby-Thomas, G. J., Hazell, P. J. and Allsop, D. F. (2009), 'The dynamic behaviour of ballistic gelatin', *AIP Conference Proceedings* **1195**(1), 1399–1402.

Simulia (n.d.), 'A strategy for bird strike simulations using Abaqus/Explicit'.

Walvekar, V. (2007), Bird strike analysis on leading edge of an aircraft wing using a smooth particle hydrodynamics bird model, Master's thesis, Wichita State University.

CHAPTER 7

Deformable plates: experiments and simulations

Abstract: In this chapter, a step towards targets with relatively large deformations is taken by considering the impact of a bird on a thin flat aluminium plate, simply supported onto a thick steel frame with a square opening. In this type of test, there is a large deformation of the bird and the target structure. The overall behaviour of the numerical model is investigated by comparing the shape of the bird and the target over time. The influence of certain input parameters such as bird density, l/d ratio and centre of impact of the bird is investigated as well. The static springback analysis is introduced, which is needed to obtain the final shape of the plate after the dynamic simulation.

7.1 Literature review

In deformable plate experiments or simulations, the purpose is to obtain and measure a certain amount of deformation with some well-chosen boundary conditions. This is in contrast with the rigid plates covered in chapter 5, where the purpose was to minimize the deformation, to obtain a target as rigid as possible.

Initial research of orthogonal and inclined bird impact on flat polycarbonate plates has been done by Challita (Challita and West, 1980; Challita, 1980), describing the amount of damage that occurred based on the impact location and orientation. In (Welsh and Centonze, 1986), bird impact on aluminium plates was investigated with chickens and porous gelatine birds. They found that the maximum permanent deformation was about 35% larger for the chickens and therefore discourage the use of gelatine as substitute material. Numerical work on this type of experiments can be found in (Ericsson, 2012; Mav, 2013; Smojver and Ivančević, 2010, 2011).

More recent, deformable flat plate experiments were performed on clamped aluminium and triaxial braided carbon/epoxy composite square plates in (Roberts et al., 2005), observing the damage and determining the penetration limit or also, the velocity at which penetration occurs. They stated that it is difficult to extrapolate the results to a more practical example because of the large influence of the boundary conditions. A comparison of these experiments with Lagrangian and CEL simulations for the centre deflection and global deformation was made in (Smojver and Ivančević, 2011). In (Hou and Ruiz, 2007), multiple unidirectional and woven carbon epoxy plates, clamped on one side, were tested. Damage patterns were compared for different layups, using visual inspections and ultrasonic C-scans to reveal which resin and fibre characteristics influence the impact resistance. They achieved local failure, independent from the boundary conditions, by using smaller masses at higher impact velocities. Results from Lagrangian and CEL simulations of these experiments can be found in (Ivančević and Smojver, 2011; Smojver and Ivančević, 2011; Ivančević and Smojver, 2016), comparing the damage contours from the simulations with the visual inspections after impact from the experiments. Also in (Iannucci and Donadon,

2006), where clamped woven glass composites were subjected to bird strike, it was observed that for a higher impact velocity, failure occurred more locally.

Bird strike on square carbon/epoxy composite plates, prestressed in tension and compression, clamped on two sides and simply supported on the other sides has been investigated with experiments and Lagrangian and CEL simulations in (Heimbs, 2011; Heimbs and Bergmann, 2012), comparing interlaminar and matrix damage with ultrasonic C-scans.

The influence of an impactor with a geometry close to a real bird on the damage pattern of different transparent layups (acrylic and glass) was investigated in (Hedayati and Ziaei-Rad, 2014). The influence of the bird's orientation (tail side, head side and wing side) was also compared to a traditional bird model, resulting in very different damage patterns. The damage induced by the "head side" model matched quite closely to the traditional bird model and the "wing side" was the most severe. Using the results of bird impact simulations on aluminium plates, in (McCallum and Constantinou, 2005), it was also shown that the neck of the bird can pre-stress the plate prior to impact of the torso, which can have an influence on the damage initiation and failure of the target.

More brief discussions on deformable aluminium plates (Nizampatnam, 2007; Ugrčić, 2012; Wang et al., 2014), circular fiberglass/epoxy composite plates clamped over their entire edge (Azevedo and Alves, 2007, 2009) and steel and fibre metal laminates (Zhu et al., 2014) can be found as well. The influence of the Lagrangian bird mesh size, porosity and yield strength on the maximum contact force and plastic strain for an impact on a polycarbonate plate was investigated in (Airoldi and Cacchione, 2006). In (Liu et al., 2014), bird material parameters were optimized using displacement, strain and force data from bird impact tests on clamped square aluminium plates.

7.2 The deformable plate set-up

The target in the deformable plate test consists of a square $400 \times 400\,\mathrm{mm}^2$, 2 mm thick 2024-T3 aluminium plate, simply supported onto a thick 16 mm steel frame with a square $300 \times 300\,\mathrm{mm}^2$ opening. The edge of the square

opening at the side of the aluminium plate is rounded to a radius of approximately $1 - 2\,\text{mm}$. The thick steel frame is mounted to the walls of the test chamber using rigid support parts. Figure 7.1 shows the front and the back of the deformable plate set-up, ready for an experiment.

(a) Front. **(b)** Right.

Figure 7.1: Deformable plate set-up.

At the back of the plate, a line pattern can be observed. When two high speed cameras are available, a stereo vision set-up can be created to record this line pattern and obtain the 3D shape map using the technique described in chapter 3.3. In every experiment, one high speed camera is placed on the ceiling of the chamber to capture the deforming plate and behaviour of the bird from a top view. In some experiments, this overview camera is pointed straight downwards to record a set of mirrors: one mirror to capture the perspective of the experiment and two other mirrors to capture two side views of the bird to retrieve an estimate of the impact location (Figure 7.2. These mirrors however were not rigid enough and vibrations typically occurred as a result of the pressure waves and vibrations in the test chamber.

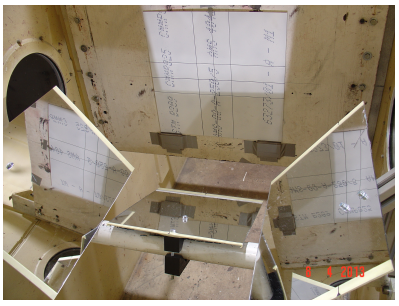

Figure 7.2: Mirrors to estimate the impact position of the bird in two directions with one camera.

In following section, the numerical model will be discussed (the combination of the aluminium plate and the steel frame and the springback analysis). After that the performed experiments and results are discussed briefly. Finally, the correlation with the numerical simulations will be shown and the influence of several numerical parameters will be discussed.

7.3 Numerical model

7.3.1 Aluminium plate

Because of the highly dynamic event, hardening and strain rate effects have a significant influence on the material behaviour of the plate. A Johnson Cook model is therefore adopted, for the hardening and strain rate effect as well as for the damage model. The stress in the Johnson Cook model is determined by the following equation:

$$\sigma = (A + B(\bar{\epsilon}^{pl})^n)\left(1 + C\ln\frac{\dot{\bar{\epsilon}}^{pl}}{\dot{\bar{\epsilon}}_0^{pl}}\right)(1 - (T^*)^m) \tag{7.1}$$

With $\bar{\epsilon}^{pl}$ the equivalent plastic strain (a scalar representative for the plastic strain tensor), A, B and n material dependent parameters describing the hardening behaviour, C and $\dot{\bar{\epsilon}}_0^{pl}$ describing the plastic strain rate effect and T^* and m being factors to include temperature dependency. In the results shown in this work, T^* is set zero.

The Johnson Cook damage law determines the strain at failure in the material model. The failure criterion is met once the following damage initiation criterion condition is satisfied:

$$\omega_D = \int \frac{d\bar{\epsilon}^{pl}}{\bar{\epsilon}_D^{pl}(\eta, \dot{\bar{\epsilon}}^{pl})} = 1 \tag{7.2}$$

With $\bar{\epsilon}^{pl}$ again the equivalent plastic strain and $\bar{\epsilon}_D^{pl}$ the value of the equivalent plastic strain at the onset of damage. This parameter depends on the plastic strain rate $\dot{\bar{\epsilon}}^{pl}$ and the stress triaxiality η, defined as $-p/q$, with p the pressure part of the Cauchy stress and q the Von Mises equivalent stress.

Johnson Cook has a damage model that empirically characterizes $\bar{\epsilon}_D^{pl}$ with parameters $d_1 - d_5$:

$$\bar{\epsilon}_D^{pl} = (d_1 + d_2 e^{-d_3 \eta}) \left(1 + d_4 \ln \frac{\dot{\bar{\epsilon}}^{pl}}{\dot{\bar{\epsilon}}_0^{pl}}\right) (1 + d_5 T^*) \tag{7.3}$$

in which the term T^* is again zero.

Parameters for the Johnson Cook material and damage model for 2024-T3 aluminium are found in literature (Lesuer, 2000) and shown in 7.1.

Table 7.1: Parameters for the Johnson Cook material and damage initiation model for 2024-T3 aluminium (Lesuer, 2000).

A [MPa]	**B** [MPa]	**n** [-]	**C** [-]
369	684	0.73	0.0083
$\mathbf{d_1}$ [-]	$\mathbf{d_2}$ [-]	$\mathbf{d_3}$ [-]	$\mathbf{d_4}$ [-]
0.13	0.13	-1.5	0.011

Once the damage initiation criterion is met, material failing occurs. This can be modelled using a damage evolution law, representing a progressive degradation of the stiffness until the material cannot sustain any loads any more. The damage evolution after initiation is based on the effective plastic displacement ($\dot{\bar{u}}^{pl} = L\dot{\bar{\epsilon}}^{pl}$), with L the characteristic length of the element, to obtain a plastic dissipation which is less dependent on the mesh size (it reduces strain localization). Damage evolution is divided into two different mechanisms, a decrease of the Young's modulus and a decrease of the yield stress (in this case a linear degradation with respect to the plastic displacement). A damage variable d is introduced, once this damage variable reaches unity, the corresponding integration point fails. When all the integration points inside an element fail, the element is deleted. In case of a linear evolution, the increase of the damage variable is calculated using Equation 7.4.

$$\dot{d} = \frac{\dot{\bar{u}}^{pl}}{\bar{u}_f^{pl}} \tag{7.4}$$

With $\bar{u}_f^{pl}$ the effective plastic displacement at the point of failure.

For the mesh of the plate, $2 \times 2\,\text{mm}^2$ quadrilateral shell elements with full integration are used, which is the minimum to maintain an appropriate in-plane to thickness mesh size ratio. The internal energy during the simulation deviates not more than 5% when refining the mesh, so the mesh is assumed to be converged.

7.3.2 Steel frame

In this section, the influence of the fillet on the square opening (the amount of elements representing the fillet) is shown using a small scale model as well as the results of a mesh convergence study. The amount of detail that is necessary to realistically simulate a specific experiment is an important question when constructing a model. Straight edges at the square opening of the frame e.g. are not realistic and introduce stress concentrations in the plate. An investigation of the high speed images also indicates that the frame which is initially assumed to be rigid is in fact oscillating because of the high forces induced by the deforming plate.

7.3.2.1 Fillet edge of the frame

Filleting the edges of the square opening requires locally a very fine mesh in order to accurately represent the curvature. In order to study the effect of the mesh size of the fillet, a simple model is constructed where an aluminium strip is drawn over a rounded discrete rigid edge under a uniform pressure of 0.5 MPa during 10 ms, as schematically shown in Figure 7.3. 0.5 MPa is just enough to keep the plate in contact throughout the entire explicit simulation. An explicit simulation was opted to acquire the exact same contact formulations as in the bird strike simulations.

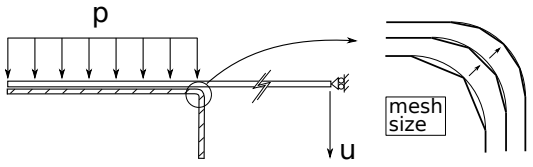

Figure 7.3: Concept to test mesh and radius dependency of the edge fillet.

A static friction penalty of 0.1 is chosen between the aluminium strip and the rigid frame. The effect of the mesh size is tested by comparing a straight edge with a 2 mm radius fillet meshed with 2, 3, 4, 5, 6, 8 and 10 elements. The frictional and plastic energy dissipation and required external work converges within 3% of the finest mesh for 3 elements and within 1.5% for 5 elements. In the model of the frame, the 5 elements will be used. The plastic energy dissipation fluctuated over 14.3% of the converged value before stagnation, showing the necessity of multiple elements among the fillet. In this type of simulation, the influence of the fillet radius and mesh on the plastic energy dissipation is relatively larger compared to the actual experiments. This convergence study is therefore more stringent and conservative.

For the friction between the plate and the frame, an exponential decay friction model is used ($\mu_1 = 0.61$ and $\mu_2 = 0.47$ at 1/s) (Serway et al., 2010). This friction law can have a big influence, because together with the stiffness of the plate, it determines how much the plate tends to be pulled through the frame.

7.3.2.2 Deformable frame

As shown in the previous section, an accurate representation of the fillet requires relatively small elements (in respect to the outer dimensions of the frame). To maintain decent aspect ratios throughout the plate, a large amount of elements is needed. For the mesh convergence of the frame, one quarter of the plate with appropriate boundary conditions is modelled in a static elastic simulation and a pressure of 0.6 MPa is applied on the surface where the plate will be mounted (the amount of pressure arbitrary because it does not influence the result in an elastic simulation). The mesh convergence of the frame is done without the necessary fine mesh at the fillet. After the mesh of the frame converges, the fillet mesh is refined to its necessary size while making sure that the results do not change. The final frame consists of 250973 linear 8-node continuum elements and deflects 1.917 mm at the central node just above the square opening. The undeformed and (scaled) deformed configuration of the frame are shown in Figure 7.4, where the red surface indicates the area that will be covered by the plate.

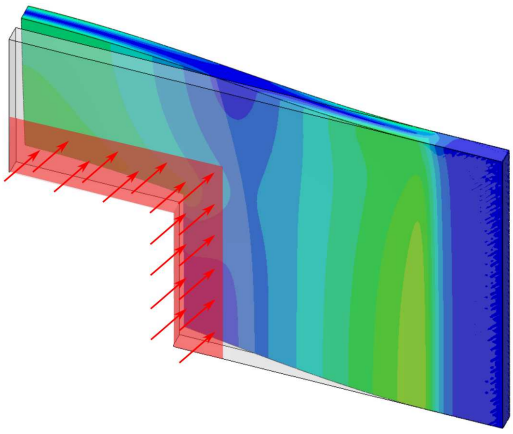

Figure 7.4: Undeformed and deformed model of on quarter of the frame (scaled).

7.3.3 Springback analysis

Bird strike is a highly dynamic event, resulting in large oscillations of the plate after impact. Computation time would be very large if the oscillations would have to damp out in the explicit analysis (if they even damp out), because of the very small stable time increment. Therefore, it can be interesting to switch to a simple static analysis, when the impact is finished. The stresses that occur in the last frame of the explicit analysis can be defined as the initial stress in a plate with an elastic model and the same deformation in a static analysis. The step from dynamic to static is only valid because the strain rate at the end of the experiment is on average roughly 15 times smaller than the strain rate at the beginning of the experiment. Also, the strain rate effects in aluminium are rather small.

In the explicit analysis, when only a part of the element fails, the stresses in the corresponding integration points are set to zero throughout the rest of the analysis. In this case, the element is not deleted. As no information about the failed integration points is interchanged between the explicit and standard analysis, all integration points of the non-deleted elements are again active in the springback analysis. At the beginning of the springback analysis, the stress in the failed integration points is zero, but further on in the analysis stress build up is possible. Luckily, since damage occurs only very locally, the overall effect of this artefact is assumed to be negligible.

7.4 Performed experiments

In total, four experiments are performed. Table 7.2 summarizes the input conditions (mass and impact velocity) and indicates in which experiment, the plate was shot through the steel frame.

Table 7.2: Test matrix deformable plate experiments.

Test	Bird	m [kg]	v [m/s]	Shot through
DP-1	1:4 MR	0.653	77.3	no
DP-2	1:4 MR	0.504	143.0	yes
DP-3	1:4 MR	1.782	79.7	yes
DP-4	1:4 MR	1.816	85.0	yes

The plates after impact are shown in Figure 7.5, from the bird side (top row) and the opposite side (bottom row). The plates in this overview are oriented in the same way as the experiments (the top side up).

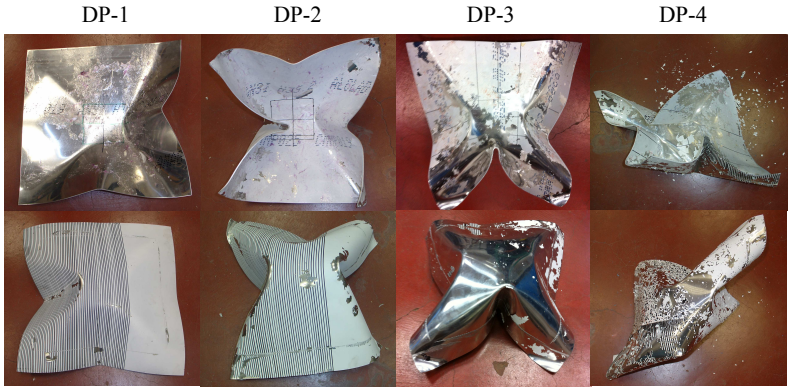

Figure 7.5: Deformed plates from the front (top row) and from the back (bottom row).

The deformation for the plates that were shot through the frame are naturally larger. For these three tests, the plate also hits the back of the test chamber. Although foam panels were attached to the back of the test chamber, some deformation can still be the result of this secondary impact. Especially for DP-4, where the plate slammed against the back wall of the chamber, bounced back and slammed again onto the frame. But also for the corners

of the plate in DP-2 for example, the high speed images showed that the deformation of the right bottom corner (looking from the front in Figure 7.5) was not caused by the bird or the frame.

7.5 Numerical results

In this section, the results of the numerical simulations are covered. For each experiment, first the input conditions are determined. The input conditions include the mass, velocity and shape of the bird, as well as the impact location. The bird never strikes at the exact centre of the plate. As the impact location proved to be very important, it is estimated as accurately as possible from the high speed images.

Numerical models are created conform the input conditions and explicit simulations are performed, simulating the event for 10 ms. After that, springback analyses are performed to acquire the final shape. For each plate, a qualitative comparison is made between the deformation of the bird and the plate in the experiments and the simulations. The influence of several main input parameters is investigated for experiment DP-2.

In order to get some measure of validation, the distances between the four corners of the plate are compared between experiment and simulation (the plate obtained after the springback simulation), indicated by the red arrows in Figure 7.6. The error is calculated with Equation 7.5.

$$\Delta = \frac{\sum_{i=1}^{4}(|s_{i,exp} - s_{i,sim}|)}{\sum_{i=1}^{4}(|400 - s_{i,exp}|)} \tag{7.5}$$

Where $s_{i,exp}$ and $s_{i,sim}$ respectively corresponds to experimentally and numerically measured distance i for the four edges of the plate. The error is normalized to the actual deformation in the experiment ($|400 - s_{i,exp}|$).

A comparison between the maximum height of the plate in its static equilibrium (the three circles in Figure 7.6 for DP-2) is made as well. The height is expressed as the error between the simulation and the experiment, relative to the actual value measured from the experiment.

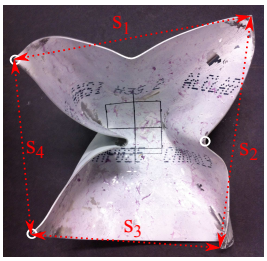

Figure 7.6: Quantitative measures to compare simulation with experiment.

7.5.1 DP-1: 0.65 kg at 77.3 m/s

In the experiment, the bird is deformed severely during the launching process. To improve the correlation, a bird mesh is generated based on the contour observed in the high speed images (see also section 4.2.3.4). In this experiment with a relatively low mass and impact speed, the elastic energy of the bird proves to be very important. This can be concluded from the comparison between high speed images from the experiment and simulation. Figure 7.7 compares several time frames of the simulation from the same angle of view as the experiment. Up till 5.3 ms after impact, the deformation of the bird corresponds well with the experiments. But at this point, the bird in the experiment exhibits a lot of elastic deformation. This can be concluded from the images at 9.3 ms, where the bird in the experiment does not expand any more, contrary to the simulation, where a lot of kinetic energy is deviated away from the plate.

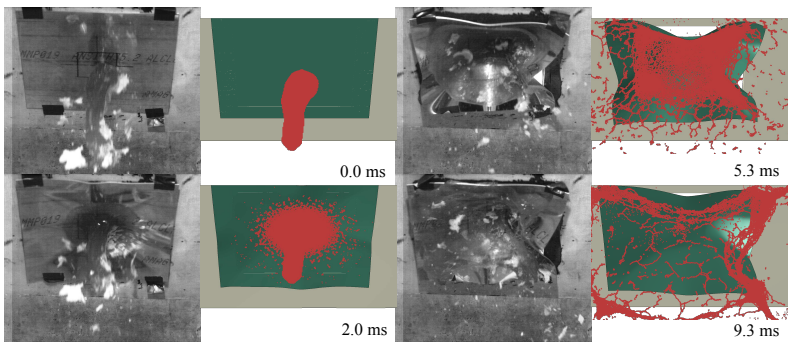

Figure 7.7: Comparison experiment DP-1 with simulation.

Disregarding the elastic deformation that is not modelled in the simulation, the final deformation of the plate corresponds quite well with the experiment (Figure 7.8).

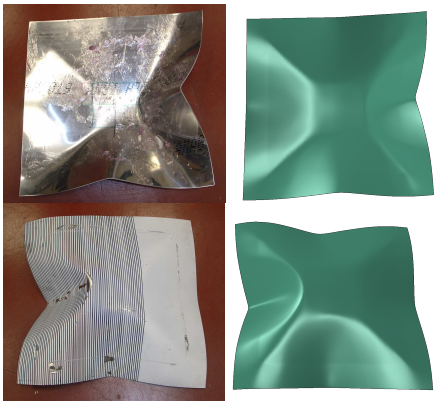

Figure 7.8: Comparison experimental and numerical deformed plate of experiment DP-1.

An error of 57.6% is obtained, which is mainly the result of an underestimation of the deformation. The error is quite large because the deformation is relatively small (the denominator in Equation 7.5). A height of 77.1 mm is derived from the simulation, opposed to 105 mm in the experiments (which corresponds with an error of 26.6%).

7.5.2 DP-2: 0.50 kg at 143.0 m/s

At the higher speed in this experiment, the elastic regime plays a relatively smaller role. Figure 7.9 shows a comparison between experiment and simulation. Contrary to the previous experiment, the bird is deviated away from the plate several milliseconds after impact. The white markings highlight the areas where the deformation of the bird and the plate in the simulation corresponds well with the experiment. The areas where the light can pass through are in the same order of size and shape in time.

The way the plate deforms through the frame as well as the splashing of the bird in different regions is quite similar in the simulation. The final deformation of the plate for the experiment and simulation is shown in Figure 7.10. The shape corresponds well, especially the left wrinkle (when

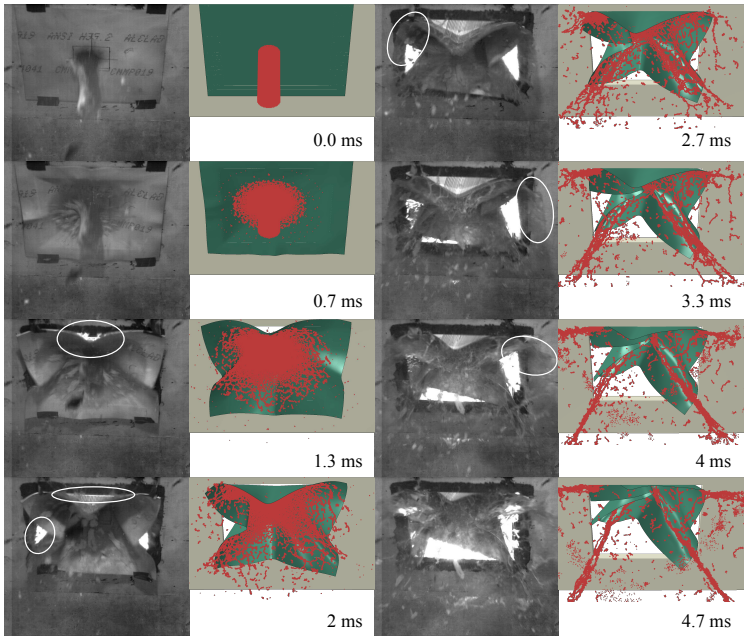

Figure 7.9: Comparison high speed images experiment DP-2 with simulation.

looking from the front). The wrinkle at the bottom of the plate on the other hand is overestimated in the simulation.

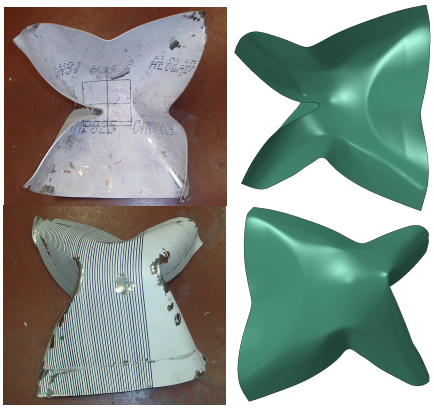

Figure 7.10: Comparison experimental and numerical deformed plate of experiment DP-2.

The error calculated from the distances between the corners is 11.4%. The maximum height of the plate in the simulation is 169.8 mm in the simulation, opposed to 176 mm in the experiment (an error of 3.5%).

Figure 7.11a shows the damage initiation criterion (ω_D in Equation 7.2) in the integration points at the back of the plate. From blue to red, the damage initiation criterion ranges from 0 and 1. There is damage present in the origin of the left wrinkle of the plate in the experiment. In the simulation, the damage initiation criterion at this place reaches one in most of the integration points through the thickness, but elements are never deleted. A mesh refinement should be done in this region, but since a minimum element size to thickness ratio needs to be respected, this has not been done.

At the location where the bird hits the plate, some damage can be observed as well (encircled with a dashed line in Figure 7.11a). A closer look on the local damage variable over time and the elastic energy with a clearly distinguishable shock peak (the shock duration theoretically is 16.5 μs) is shown in Figure 7.11b. These curves show that the local damage is not the result of the shock regime, because the damage criterion starts to rise significantly later than the peak in the elastic energy. The local damage therefore occurs during the steady state regime. This proves that also the steady state regime can cause local damage or failure.

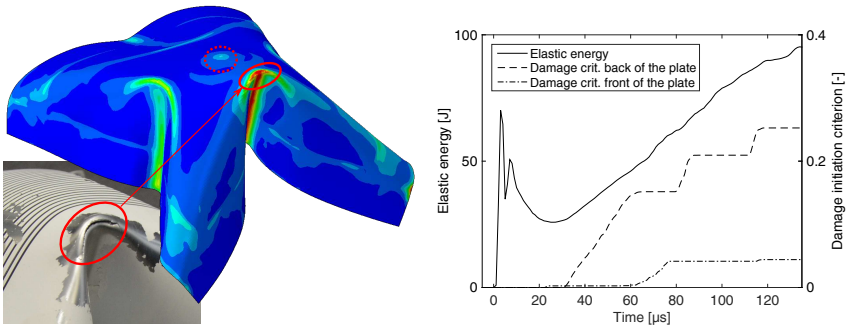

(a) In the wrinkles. **(b)** At the location where the bird impacts.

Figure 7.11: Local damage on the plate.

In the following subsections, the influence of several important input parameters on the final shape of the plate from experiment DP-2 is investigated. Slightly decreasing or increasing the density (from the measured 1021.3 kg/m^3 to 997.7 kg/m^3 and 1045.4 kg/m^3), the l/d ratio (from 2.83 to 2.18 and 3.41), the centre of impact (from the estimated horizontal and vertical offset of respectively -20 mm and -5 mm to -10 mm and -2.5 mm and -30 mm and -7.5 mm) and the thickness of the plate (from the measured 2.05 mm to 2.0 mm and 2.1 mm) is considered as well as the influence of assuming that the frame is rigid. The parameters are increased and decreased with a difference that could be the result of a wrong measurement or estimation. For each input parameter, the final shapes are compared qualitatively, looking from the same angle of view. Each comparison contains the final shape obtained after the experiment together with the final shape after springback from the simulation with the decreased parameter, the reference shape from the original simulation and finally the simulation with an increased input parameter. Also quantitatively, the influence of the different input parameters are compared, using the mean distance between the corners and the height. Table 7.3 summarizes these results.

Table 7.3: The mean difference of the distances between the four corners of the plate after springback analysis and the experiment DP-2 for several influencing parameters as well as the difference between the top height of the plate in its natural position.

	Dist. corners [%]		**Height [%]**	
Original	11.4		3.5	
	Decrease	**Increase**	**Decrease**	**Increase**
Infl. density	25.9	17.1	6.2	3.3
Infl. l/d ratio	39.6	31.0	21.9	10.5
Infl. centre of impact	24.1	40.6	6.1	8.8
Infl. thickness plate	25.4	16.4	4.2	1.1
Infl. rigid frame	34.6		1.1	

This table shows that the input parameters have a large influence on the final shape. For each parameter, the error calculated from the distance between the corners (Equation 7.5) get worse. Also for the height of the plate, the correlation in general gets worse. Only increasing the thickness of the plate

yields better results. The errors in Table 7.3 also show that especially the l/d ratio and the location of impact have a big influence on the final shape of the plate.

7.5.2.1 Influence of the bird density

The 2.4% change (decrease or increase) in bird density corresponds to a same change (increase or decrease) in volume. The same change in amount of elements is obtained in a way the l/d ratio is changed as little as possible. The density has a considerable effect on the shape, especially for the decreased density. For an increased density, the change in errors and shape is limited. This shows that using the EOS of water as an approximation for gelatine can lead to significantly different results. This error source is reduced by measuring the bird density just before each experiment.

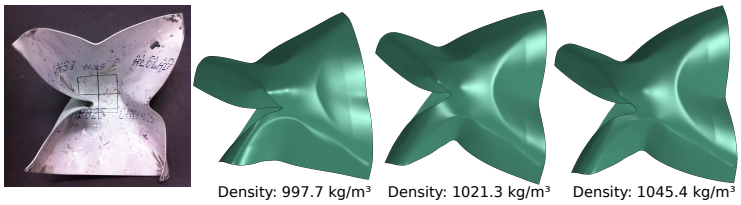

Figure 7.12: Influence of the density on the final shape of the plate (DP-2).

7.5.2.2 Influence of the l/d ratio

For the smaller 300 gram birds, the shape is generally well maintained throughout the launching process. This is not always the case for the larger birds. In case the bird is deformed significantly and foam disturbs the view, the estimation of the actual l/d ratio can be inaccurate. In this subsection, the l/d ratio is changed while maintaining a constant mass (shortening the length while increasing the diameter and vice versa). The momentum therefore has to be transferred over a period which is 15-16 % shorter or longer. The results are shown in Figure 7.13.
For both the reduced as the increased l/d ratio, the wrinkle at the left side is considerably less pronounced, making the obtained shape more symmetric. For the higher l/d ratio, it could be the result of the longer period over which the momentum is transferred. For a longer period, the mass has

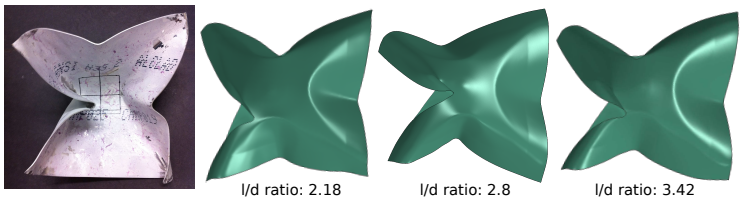

Figure 7.13: Influence of the l/d ratio on the final shape of the plate (DP-2).

more time to distribute towards the centre. For both cases, the distance between the corners and the height differ a lot from the shape obtained from the experiment (Table 7.3). It can be stated that the l/d ratio has a large influence on the result.

7.5.2.3 Influence of the centre of impact

The centre of impact is not easy to measure in the order of millimetres. The foam and debris in the experiment often disturb the view and the shape often deviates substantially from a perfect cylinder. In this next series of simulations, the roughly estimated centre of impact (horizontally $-20\,\text{mm}$ and vertically $-5\,\text{mm}$) is moved towards ($-10\,\text{mm}$ and $-2.5\,\text{mm}$) and away ($-30\,\text{mm}$ and $-7.5\,\text{mm}$) from the centre.

The final shapes are shown in figure 7.14. There is a clear trend visible in this set of experiments. A smaller offset results in a more symmetric shape. This is not conform the experiment, which can also be observed from values in Table 7.3. The bigger offset results in a large crack from the left side towards the centre of the plate. A lot of attention should go to the correct estimation of the centre of impact in the experiment.

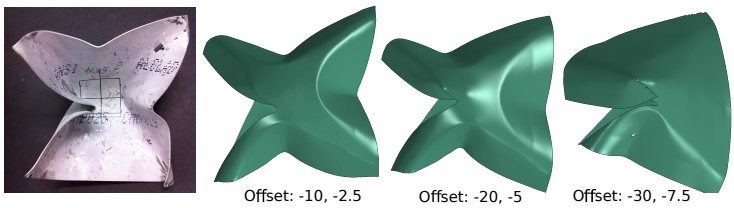

Figure 7.14: Influence of the impact centre on the final shape of the plate (DP-2).

7.5.2.4 Influence of the thickness of the plate

Measurements showed that the thickness of the plate can deviate over more than 10 μm. The result of altering the thickness of the plate (2.1 mm and 2.0 mm instead of 2.05 mm) is therefore investigated. This change in thickness of the plate results in a more pronounced change in bending stiffness (7-8%), which can also be observed in the results (Figure 7.15).

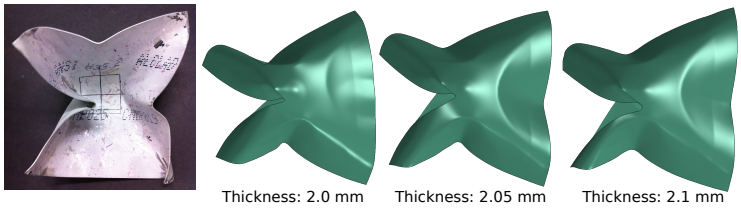

Figure 7.15: Influence of the plate thickness on the final shape of the plate (DP-2).

Decreasing the plate thickness results in a height that corresponds better with the experiment, but the overall shape is not better, the wrinkle on the right g.e. disappears completely. A thicker plate deviates more from the actual shape (the error of the distance between the corners increases).

7.5.2.5 Influence of the frame

Modelling the frame as a deformable part is computationally quite demanding. But assuming the frame is rigid is definitely not an option as shown in the Figure 7.16. In the simulation, the plate fractured from the left side to the middle, which is not at all in accordance to the experiment.

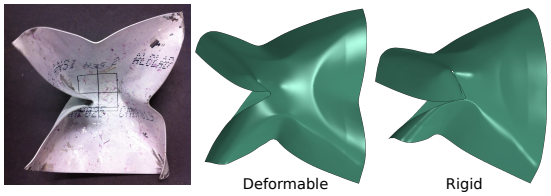

Figure 7.16: Influence of the rigid frame constraint on the final shape of the plate (DP-2).

All the investigated input parameters have a considerable impact on the result. The centre of impact showed to be the most critical. After that the

l/d ratio. These simulations show the necessity of high speed cameras, as both parameters can be estimated from the obtained images.

7.5.3 DP-3: 1.78 kg at 79.7 m/s

A comparison between the high speed images and the simulation is shown in Figure 7.17. The perspective recorded from the front is not captured very well, which is why a comparison is made with a camera from the back. The overall movement of the plate during impact and the point in time where the plate flies through the frame is captured very well, both for the bottom as the top of the plate).

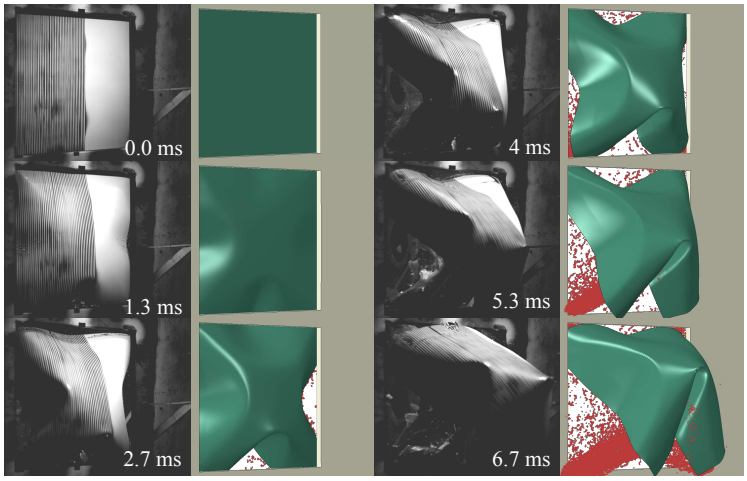

Figure 7.17: Comparison high speed images experiment DP-3 with simulation.

In this experiment, two high speed cameras are dedicated to a stereo view from the back and 3D shape maps are obtained (see chapter 3). For three pairs of high speed camera frames, shape maps are constructed and section cuts are made in the horizontal symmetry plane and 50 mm and 100 mm beneath this plane at 0.5 ms, 1.17 ms and 1.83 ms after impact. For the simulation, the field output is written at the same time (as good as possible, with a maximum error of 0.17 ms). Exact section cuts are calculated from the deformed plate mesh through time. Figure 7.18 shows the section cuts for the three camera frames. After the last frame, a large part of the plate turns black due to insufficient lighting, as shown in the Figure 7.17. The discontinuities in the experimental section cuts (the dashed indications)

prove that there is room for improvement in the developed algorithm as likely some lines are skipped in the unwrapping algorithm.

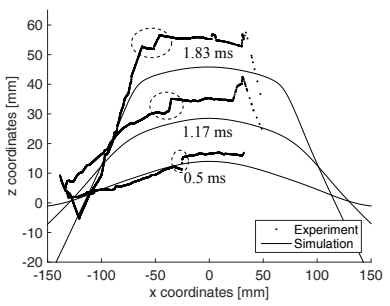

(a) Horizontal symmetry plane.

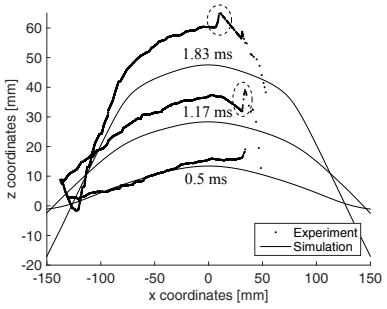

(b) 50 mm below the horizontal symmetry plane.

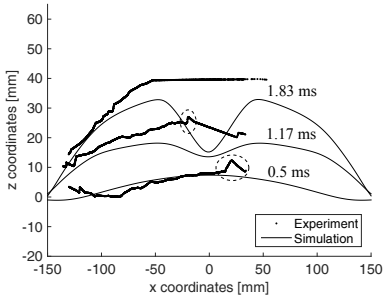

(c) 100 mm below the horizontal symmetry plane.

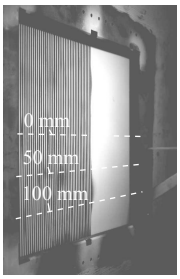

(d) Locations of the section cuts.

Figure 7.18: Comparison of experimental and numerical section cuts at the horizontal symmetry plane and 50 mm and 100 mm beneath this plane. The dashed indications show erroneous jumps in the shape map.

In general, the deformations are underestimated in the simulations. The first time frame at 0.5 ms is approximated quite well, but after that the correlation gets worse. This can again be caused by the lack of elasticity in the bird model. But it is also important to note that small deviations of the impact location change these graphs significantly.

The plate after springback is compared with the experiment in Figure 7.19. The shape resembles very well. Again there is a crack in the most pronounced wrinkle at the bottom of the plate from the experiment. In the simulation, there is one integration point through the thickness that does not fail. Some

elements are deleted at the centre of the bottom edge of the plate in the simulation.

The overall shape is very similar. The error from the distances between the corners is 14.7%. The height is 5.9% lower than the experimentally measured 154.9 mm.

Figure 7.19: Comparison experimental and numerical deformed plate of experiment DP-3.

Although this experiment has a similar speed as DP-1, the correlation seems to be better. A possible explanation is that because the mass and therefore impact momentum is much higher, the plate is deformed a lot and shot through the frame before the elastic deformation can start to play an important role.

7.5.4 DP-4: 1.82 kg at 85.0 m/s

Figure 7.20 compares three frames through time of test DP-4 from the back of the plate. The wrinkle at the right side of the plate is overestimated quite a lot. The scenario is comparable to test DP-2, where the wrinkles at one pair of opposite sides are more pronounced than at the other one. In the section discussing the results of DP-2, none of the investigated input parameters affected this kind of behaviour. A possible cause might be local areas with a higher friction force (up to adhesion) between the plate and the frame. This can for example be observed in Figure 7.20. The red indication

in the frame at 5 ms shows an area where the plate is scratched severely by the frame.

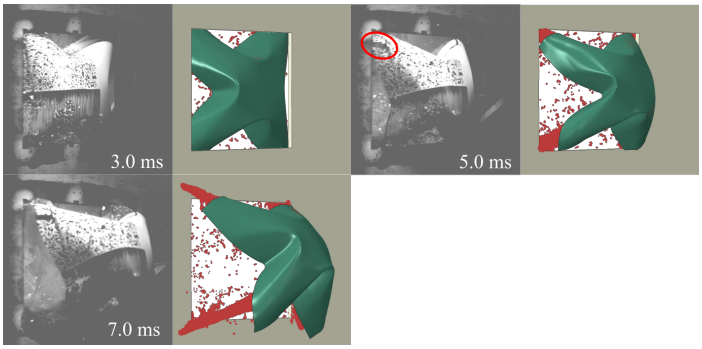

Figure 7.20: Comparison experimental and numerical deformed plate of experiment DP-4.

In the experiment, the plate slammed against the back wall of the chamber, bounced back and slammed again onto the frame. The plate therefore suffered a lot of post-impact deformation. A springback analysis of the explicit simulation is not useful, since it cannot be compared to the plate obtained from the experiment.

7.6 Conclusion

In this chapter, a test is introduced where the bird hits a thin flat aluminium plate in front of a thick steel frame with a square opening. Characteristic for this kind of test is the high deformation of the target and the bird. The results of four experiments and several simulations are covered. The shape of the plate over time and the final shape at the end of the test correlate well between the experiment and simulation. The influence of the bird l/d ratio, impact position, density of the bird, thickness of the plate and boundary condition (rigid or deformable frame) on the final shape has been investigated. It is shown that mainly the impact position and the l/d ratio have a considerable influence on the results. This shows that the input conditions should be measured as accurately as possible and therefore at least one high speed camera (ideally two) is necessary to obtain a good estimation of these parameters.

7.7 Bibliography

Airoldi, A. and Cacchione, B. (2006), 'Modelling of impact forces and pressures in Lagrangian bird strike analyses', *International Journal of Impact Engineering* **32**(10), 1651 – 1677.

Azevedo, R. and Alves, M. (2007), Numerical simulation of bird strike impact against balanced fiberglass/epoxy composite plates, *in* '19th International Congress of Mechanical Engineering'.

Azevedo, R. L. and Alves, M. (2009), 'Numerical simulation of soft-body impact on GFRP laminate composites: mixed SPH-FE and pure SPH approaches', *Mechanics of Solids in Brazil* pp. 15 – 30.

Challita, A. (1980), Validation of a bird substitute for development and qualification of aircraft transparenciles, Technical Report AFWAL-TR-80-3098, University of Dayton Research Institute.

Challita, A. and West, B. S. (1980), Effects of bird orientation at impact on load profile and damage level, Technical Report AFWAL-TR-3009, University of Dayton Research Institute.

Ericsson, M. (2012), Simulating bird strike on aircraft composite wing leading edge, Master's thesis, KTH Engineering Sciences.

Hedayati, R. and Ziaei-Rad, S. (2014), 'New bird model for simulation of bird strike on various layups used in transparent components of rotorcrafts', *Journal of Aerospace Engineering* **27**(1), 76–85.

Heimbs, S. (2011), 'Bird strike simulations on composite aircraft structures', *2011 SIMULIA Customer Conference* .

Heimbs, S. and Bergmann, T. (2012), 'High-velocity impact behaviour of prestressed composite plates under bird strike loading', *International Journal of Aerospace Engineering* .

Hou, J. P. and Ruiz, C. (2007), 'Soft body impact on laminated composite materials', *Composites Part a-Applied Science and Manufacturing* **38**(2), 505–515.

Iannucci, L. and Donadon, M. (2006), 'Bird strike modeling using a new woven glass failure model', *9th International LS-DYNA Users Conference* .

Ivančević, D. and Smojver, I. (2011), 'Hybrid approach in bird strike damage prediction on aeronautical composite structures', *Composite Structures* **94**(1), 15–23.

Ivančević, D. and Smojver, I. (2016), 'Explicit multiscale modelling of impact damage on laminated composites part ii: Multiscale analyses', *Composite Structures* **145**, 259 – 268.

Lesuer, D. R. (2000), Experimental investigations of material models for Ti-6Al-4V titanium and 2024-T3 aluminium, Technical Report DOT/FAA/AR-00/25, Federal Aviation Administration.

Liu, J., Li, Y. L. and Gao, X. S. (2014), 'Bird strike on a flat plate: Experiments and numerical simulations', *International Journal of Impact Engineering* **70**, 21–37.

Mav, R. K. (2013), Numerical analysis of bird strike damage on composite sandwich structure using Abaqus Explicit, Master's thesis, San José State University.

McCallum, S. and Constantinou, S. (2005), 'The influence of bird-shape in bird-strike analysis', *5th European LS-DYNA Users Conference* .

Nizampatnam, L. S. (2007), Models and methods for bird strike load predictions, PhD thesis, Wichita State University.

Roberts, G. D., Pereira, J. M., Revilock, D. M., Binienda, W. K., Xie, M. and Braley, M. (2005), 'Ballistic impact of braided composites with a soft projectile', *Journal of Aerospace Engineering* **18**(1), 3–7.

Serway, R. A., Jewett, J. W. and Peroomian, V. (2010), *Physics for scientists and engineers*, 8 edn, Brooks/Cole, Cengage Learning, Belmont, CA.

Smojver, I. and Ivančević, D. (2010), 'Coupled Euler Lagrangian approach using Abaqus/Explicit in the bird strike aircraft damage analysis', *2010 SIMULIA Customer Conference* .

Smojver, I. and Ivančević, D. (2011), 'Bird strike damage analysis in aircraft structures using Abaqus/Explicit and coupled Eulerian Lagrangian approach', *Composites Science and Technology* **71**(4), 489 – 498.

Ugrčić, M. (2012), 'Application of the hydrodynamic theory and the finite element method in the analysis of bird strike in a flat barrier', *Scientific Technical Review* **62**, 28–37.

Wang, J., Xu, Y. and Zhang, W. (2014), 'Finite element simulation of PMMA aircraft windshield against bird strike by using a rate and temperature dependent nonlinear viscoelastic constitutive model', *Composite Structures* **108**, 21 – 30.

Welsh, C. and Centonze, V. (1986), Aircraft transparency testing - artificial birds, Technical Report AEDC-TR-86-2, Arnold Engineering Development Center.

Zhu, S., Wang, Y., Tong, M. and Xiong, P. (2014), 'Numerical simulation of bird impact on fibre metal laminates', *Polymers & Polymer Composites* **22**(2), 147–156.

CHAPTER 8

Booster vane experiments and simulations

Abstract: In this chapter, the results of the booster vane experiments will be discussed. The goal of these experiments is threefold: (*i*) to determine the main influencing parameters, (*ii*) to reveal the weakest link in the assembly together with its failure mechanism and (*iii*) to generate experimental data to validate our numerical model. To obtain valuable data, a good set-up is needed. This will be covered in the first part of this chapter and will focus on the development of a method to measure the multi-axial impact momentum. This tool is tested with a simplified vane, to validate the set-up and to serve as an intermediate step towards the booster vane experiments. After the results from the booster vane experiments, the correlation with the simulations will be discussed. Some results are omitted due to confidentiality.

8.1 Literature review

Initial experimental research about foreign object debris or FOD impact on composite or titanium vanes and blades was performed on whirligig set-ups in (Graff et al., 1973; Steinhagen and Salemme, 1973; Johns, 1974; Premont and Stubenrauch, 1974; Graff et al., 1976), including impact of artificial and real birds, ice balls, gravel, bolts, etcetera (see also section 1.1.4). Several of these initial works investigated possibilities to improve the impact resistance by changing the build-up of the vane or blade or by using multiple materials (Friedrich, 1974; Graff et al., 1973; Johns, 1974; Premont and Stubenrauch, 1974; Graff et al., 1976). In (Bertke and Barber, 1979), the influence of the specimen geometry and size, impact angle, etc. on the impact damage was also considered.

As already mentioned in chapter 6, the first simulations started with analytical bird loading models, coupled to FEM models. In (Boehman and Challita, 1982; Hirschbein, 1982), the bird loading model for example could account for slicing of a projectile by rotating blades. An analytical model to determine the force during bird strike on a rotating blade is developed in more recent work as a tool to validate or steer the numerical simulation (Sinha and Turner, 2011). Current numerical research incorporates fully coupled FSI models including pre-stress analyses to obtain the initial stress state as a result of centrifugal forces, the transient bird strike event and even long-term response of a full assembly due to defragmentation of the blades (Vasko, 2000; Chevrolet et al., 2002; Jain and Ramachandra, 2003; Ryabov et al., 2007; Castelletti and Anghileri, 2008; Meguid et al., 2008; Mao et al., 2008; Shmotin et al., 2009; Zammit et al., 2010; Selezneva et al., 2012; Kim et al., 2011; Sinha and Turner, 2011; Liu and Li, 2013; Siddens and Bayandor, 2013; Siddens et al., 2014; Vignjevic et al., 2013; Orlowski, 2015; Chuan et al., 2015). All the work found in literature is on fan blade assemblies. Fan blades have a lot of similarities with booster vanes (large in-plane to thickness dimensions, curvature, splitting and deviation of the bird). Research on booster vanes specifically was not found. The main difference between the IGVs investigated in this work and the fan blades are (*i*) the fan blades are rotating while the IGVs are stationary, (*ii*) the booster vanes have much lower in-plane dimensions compared to the fan blades and (*iii*) the fan

blades do not have an outer casing or shroud to which the blades are attached.

Models go from one to three blades with or without disk or hub (Vasko, 2000; Chevrolet et al., 2002; Meguid et al., 2008; Mao et al., 2008; Zammit et al., 2010; Kim et al., 2011; Sinha and Turner, 2011; Vignjevic et al., 2013; Orlowski, 2015; Chuan et al., 2015) up to a half or full assembly of vanes (Jain and Ramachandra, 2003; Ryabov et al., 2007; Castelletti and Anghileri, 2008; Shmotin et al., 2009; Zammit et al., 2010; Selezneva et al., 2012; Kim et al., 2011; Siddens and Bayandor, 2013; Siddens et al., 2014), the most detailed include the axle with appropriate boundary conditions at the bearings, casing and spinner (Siddens and Bayandor, 2013; Siddens et al., 2014). Because of the high surface to thickness ratio, the fan is generally modelled with shell elements (linear hexahedral elements were used in (Vignjevic et al., 2013; Orlowski, 2015; Chuan et al., 2015)). In some work, aerodynamic forces are included in the model (Kim et al., 2011; Zammit et al., 2010), although they likely have a minor effect on the stress state compared to centrifugal forces.

In (Jain and Ramachandra, 2003), forming limit diagrams are used to prove that tearing will not occur in the considered case. They also check whether the deflection of the blades is small enough to avoid impact with stator vanes or cause unacceptable forces due to unbalance.

The influence of friction forces for a Lagrangian bird model is investigated in (Shmotin et al., 2009). Based on the experimental strain data on 16 locations, they concluded that zero friction gives the best results.

In the work of Siddens (Siddens and Bayandor, 2013; Siddens et al., 2014), a full fan blade assembly including axle, casing and spinner was considered. Their model shows that the defragmentation of the blades creates an unbalance which can cause more severe damage, because of the small tip clearance between the blades and the casing. A similar damage pattern was found in the experiments.

(Vignjevic et al., 2013; Orlowski, 2015) shows that the impact location of the bird is a very important parameter, because it determines the slice and

accompanying mass that hits the blades. The final deflection of the vane obtained from experiments correlates well with the simulations for a series of considered impact locations.

8.2 The stator vane: a combination of previous tests

In the previous chapters, bird impact has been examined from different angles to be able to understand the bird impact phenomenon and the performance of the numerical model in different situations. In chapter 4, the impact of a bird is characterized by the impact pressure exerted on the structure. Both the shock and steady state regime are studied. It was concluded that with the birds with hemispherical ends at the range of impact speeds considered in this work, the shock regime has a negligible influence. The rigid target experiments and simulations (chapter 5 and 6) on the other hand focused on the main impact forces during impact (Figure 5.2). These chapters showed that the force by pure deviation (rotated plate) is predicted quite well by the numerical model. In case of wedge and splitter like situations, the underestimation of the dissipating and deviatoric behaviour of the bird might lead to an underestimation of the impact force. In the previous chapter, a first look into highly deforming targets was taken. It could be concluded that the overall deformation of the target is estimated quite well and that the impact location plays a crucial role on the final shape. The booster vane ultimately will be subjected to the mechanisms and influences investigated in the previous chapters.

8.2.1 The simplified steel vane

As an intermediate step towards the booster vane experiments and to validate the set-up to test the booster vanes, a simplified steel vane will be used (Figure 8.1a). The vane consists of a V-shaped steel bar welded to a plate. Making a (construction steel) vane which behaves similar and has a comparable geometry as the titanium vanes (in terms of elastic energy, deformation and thickness) is almost impossible because of the difference in

yield strength and stiffness.

The holes in the plate will be used to mount the vane to the set-up. Two strain gauges are mounted on the vane, one at the left side and one at the back of the vane (Figure 8.1b). The strain gauge at the left side and at the back respectively measure the bending deformation along the weak axis and strong axis of the vane.

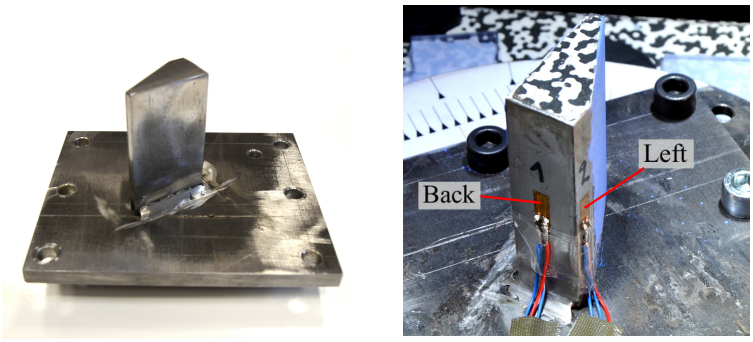

(a) The steel vane.

(b) Strain gauges at the left side and at the back of the vane.

Figure 8.1: Simplified steel vane.

The steel vane will serve as an intermediate step between the calibration experiments covered in the previous chapters and the experiments on the booster vanes because it will combine a significant amount of change of momentum with the splitting of the bird and the surface over which mass is deflected is significantly shorter compared to the wedge.

8.2.2 The booster vane

Testing a complete booster would be very expensive and inefficient. Therefore, only a part of the booster will be tested, or more specifically, one set of two vanes. Figure 8.2 shows the first stage of a booster in the picture on the left, with its inner and outer shroud (IS and OS). The vanes are welded to the outer shroud and pass through sleeves in the inner shroud.

The main part of the fixture developed in E-Break is shown in the CAD image on the right of Figure 8.2 (note that the outer shroud is downwards

and the inner shroud upwards. This is the orientation in which the vanes will be tested). The outer shroud is connected to a stiff rectangular frame or chassis which will be bolted to the set-up. The black part in the CAD image of Figure 8.2 is a rubber-like material called the abradable (positioned at the inner side of the inner shroud). The abradable serves as a sealing between the static and rotating parts, see also section 1.2. The vanes, outer and inner shroud and the chassis shown in Figure 8.2 are made of the alloy Ti6Al4V.

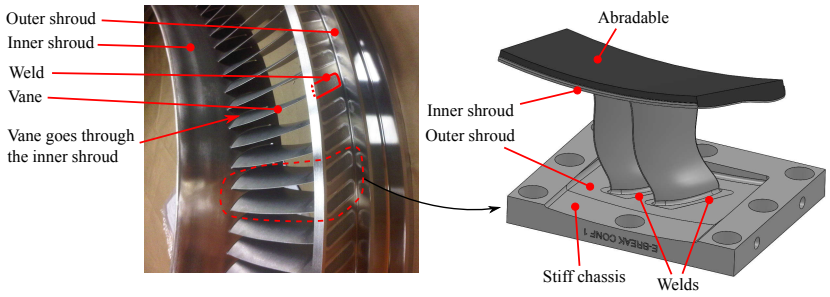

Figure 8.2: A subset of the IGV assembly is tested, containing a pair of vanes, a part of the inner and outer shroud and the abradable (picture SAB).

At the inner side of the inner shroud and covered by the abradable, each pair of vanes is connected with a retaining plate (Figure 8.3). This is a steel plate that is positioned through the dedicated sleeves at the end of the vanes. One of the main purposes of the retaining plate is to prevent the vanes from pulling out from the inner shroud when impacted.
The choice to use two vanes can be justified by two reasons. First and most of all, the retaining plate connects each pair of vanes in the booster. This connection is very likely to have a big influence on the impact resistance of the booster. Secondly, the diameter of the 300 gram bird is approximately 60 mm. The momentum will therefore mainly be experienced by two vanes. The developed fixture also allows to test the weld in the outer shroud (see Figure 8.2 and 8.3).

Simulations showed that testing only one pair of vanes without lateral reinforcements would result in very large and unrealistic deformations of the vanes. In a complete booster, the inner and outer shroud ring together with the other vanes provide a lot of stiffness which would not be present when

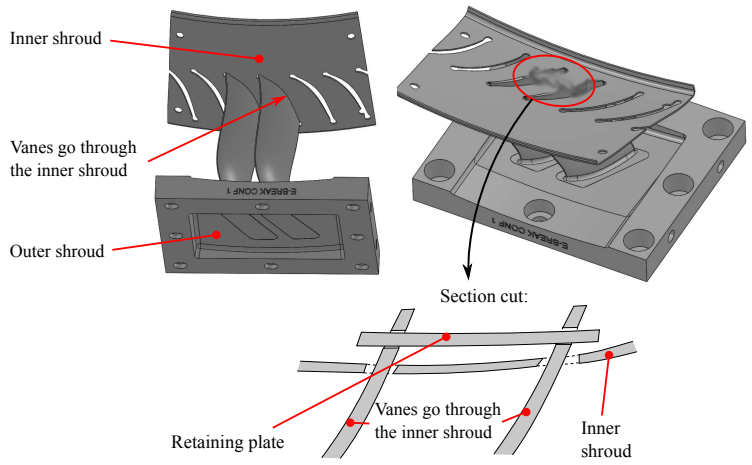

Figure 8.3: Each pair of vanes is connected with a retaining plate (CAD images without abradable).

excluding a small part. Therefore, lateral reinforcements are developed as a substitute for the stiffness of the remainder of the booster. For the two vane sizes that will be considered (a smaller reference configuration and a bigger configuration), the booster vane fixture with lateral reinforcements and without abradable is shown in Figure 8.4.

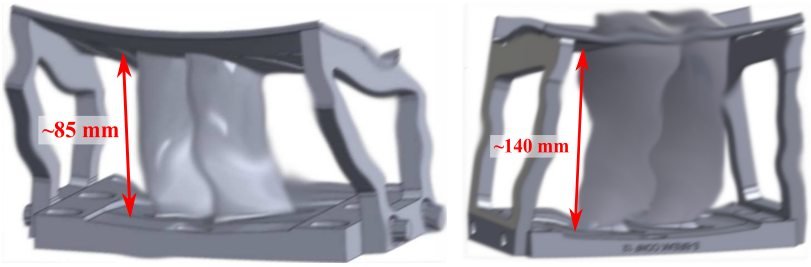

(a) Reference configuration. **(b)** Bigger configuration.

Figure 8.4: CAD view of the smaller reference configuration and a bigger configuration, including the lateral reinforcements.

Figure 8.5 shows one of the booster vane fixtures used in the experiments. It can be noticed that the abradable is not entirely covering the inner shroud (two cavities can be observed in the left picture of 8.5). This is an inaccuracy of the manufacturing process, which needs to be taken into account when looking at the results. Beneath the black abradable, there is another (grey)

silicon material which encapsulates an area just above the inner shroud, including the vanes and the retaining plate and fills up the gaps in the inner shroud where there are no vanes (right picture in Figure 8.5). The blue chalk will be used to reveal the trajectory of the bird, as was introduced in chapter 5. Blue chalk powder is applied to the vanes and occasionally also to the chassis and the inner shroud.

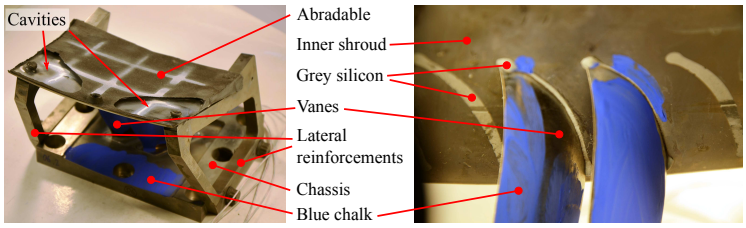

Figure 8.5: Booster vane fixture.

To assure that valuable quantitative data is obtained from the booster vane experiments, a lot of work is done to develop a good experimental set-up. This will be covered in the first part of this chapter. In this process, the most important part is the development of a method to measure the transferred momentum in multiple directions. This will be covered in section 8.3. After that, section 8.4 will elaborate on the complete experimental set-up and the performed data acquisition. In section 8.5, the correlation of the steel vane experiments with the simulations will be discussed. These results will serve as a validation of the entire set-up. In the second part of the chapter, the results of the booster vane experiments will be covered first in section 8.6. The performed tests will be summarized and the results of the different tests will be covered. Finally, in section 8.7, the results of the simulations are discussed.

8.3 Measurement of multi-axial momentum

In this section, the set-up to measure the multi-axial momentum or force will be introduced. The first subsection will cover some initial concepts, which will lead to the final concept and the working principle in section 8.3.2. Similar to the rigid target experiments, the momentum will be obtained by allowing movement. This movement is derived from an optical measurement,

which will be explained in section 8.3.3. Finally, the verification of the method to derive the rotational speeds will be covered in 8.3.4.

8.3.1 Initial concepts

The main requirement of the set-up is the capability to measure the momentum in multiple directions, transferred during a very short high force impact event. Apart from this requirement, the following aspects also have to be kept in mind:

- The influence of the set-up on the measurement should be small.
- It must be possible to position the vane such that the desired impact location of the bird and the orientation of the target with respect to the impact direction is achieved.
- It should be possible to apply the instrumentation in a straightforward way.
- Different vane geometries need to be tested.
- The set-up needs to be able to cope with impact energies of roughly 1.8 kJ.
- Any energy in the set-up should be efficiently absorbed after finishing the experiment.

Many concepts were considered to measure the transferred multi-axial momentum. One of the first concepts was the **instrumented rod**. The vane fixture would be mounted on top of a well dimensioned tube that is fixed at the bottom. From several strain measurements on this tube, the impact forces would be determined. The very short force pulse however would excite a lot of Eigen frequencies of the set-up. These would be measured in the strain signals, making it difficult to conclude something about the actual force. Increasing the stiffness and therefore Eigen frequencies of the tube would require very stiff boundary conditions to avoid the influence of the surrounding.

In a more challenging concept, the vane assembly would be attached to some well chosen mass and **suspended from a wire** that would break at impact. By recording the free movement of this mass and deriving the kinematics, the reaction forces and moments would be derived. After impact the assembly

would be caught to avoid damage when falling down). This concept however contains too many practical difficulties: to position the vane before the test, to maintain the position of the vane just before impact, the derivation of the kinematics, etc.

In chapter 5, the benefits of allowing movement of the set-up to measure the force was already mentioned. To achieve momentum or force in multiple directions, multiple degrees of freedom are necessary. This can be achieved with **multiple translational DOFs, rotational DOFs or even a combination of both**. The idea to use rotational DOFs originates from the work of (Premont and Stubenrauch, 1974; Steinhagen and Salemme, 1973), which was introduced in chapter 5. Several concepts were developed, from which four are shown in Figure 8.6. The degrees of freedom are indicated with the arrows. In each case, the vane should be mounted on the top surface.

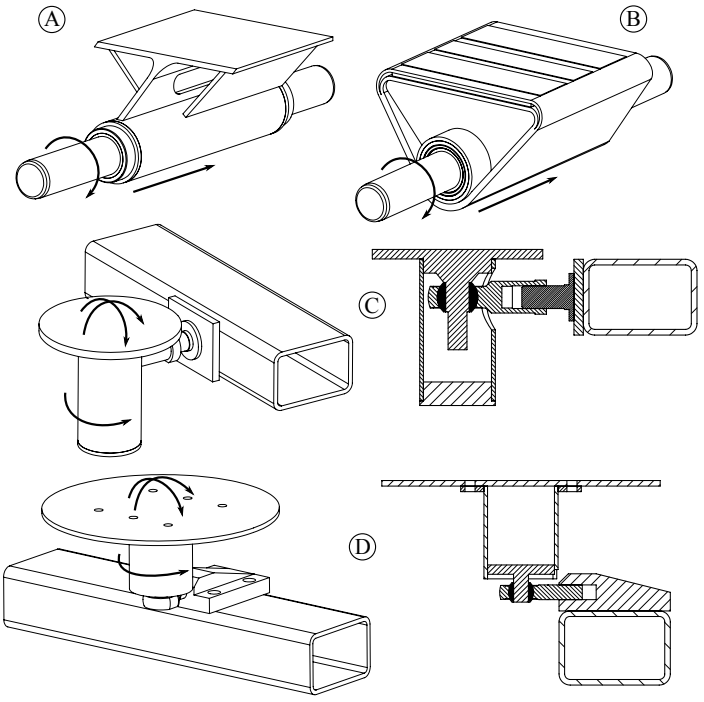

Figure 8.6: Four developed concepts to measure the multi-axial momentum from multiple DOFs.

The concepts in Figure 8.6 were numerically subjected to impact to investigate the response of the structure. In concept A and B the fixture is able to translate along and rotate about a thick solid axle (this concept therefore only measures the momentum in the two main directions). The movement is realized by two ball bearing cages. Concept A and B are respectively a steel and composite version. The main counter argument for these concepts is the inability of ball bearings to perform well when subjected to very high (shock) accelerations. The impact on the vane would also generate a moment which presses the ball bearing on the axle which could further impede the desired operation of the bearings. The mass of the bearings is also relatively large compared to the total mass of the set-up including the vane (especially for the composite version). The high inertia of these bearings would result in oscillations of the set-up at impact.

In concept C and D, three rotational degrees of freedom are obtained by using a ball and socket joint (further referred to as ball joint). Contrary to concept A and B, the influence of friction in the bearing is relatively smaller (the radius of the ball bearing is much smaller than the distance of the rotation centre to the impact location). An advantage of concept C specifically is that in theory, a stable equilibrium is achieved in the upward position, contrary to concept D. The major disadvantage of concept C on the other hand are the high oscillations that occur during impact (due to the high mass above and beneath the ball joint). The final concept therefore is derived from concept D.

8.3.2 Principle rotational momentum measurement

The final concept is shown in Figure 8.7. The rotating part consists of a turned cone shape with a mounting plate welded to the top. Some material of the inner part is removed to slightly decrease the mass of the structure. The rectangular shaped protrusions on each side of the flange are used for the optical measurements. The idea is similar to concept D from the previous section, but the shape is optimized to obtain a stiffer structure. The final structure has a cone shape. A cone has a triangular cross section (Figure 8.7c), which can optimally resist the loads induced by the booster vane fixture.

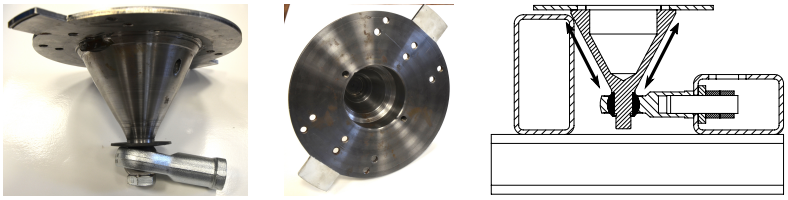

(a) Cone structure. **(b)** Mounting plate. **(c)** Section cut.

Figure 8.7: Final concept: the cone set-up.

At impact, the cone structure with the vane fixture starts rotating around the ball joint. From this movement the momentum can be calculated. For the impact momentum of roughly $30 - 40\,\mathrm{Ns}$, the rotational inertia is designed in such a way that the displacement of the flange during impact is in the order of millimetres (1-5 mm), which minimizes the influence of the set-up on the experiment. This way the experiment is also decoupled from the environment as much as possible (the structure to hold the ball joint sees no moment) and is therefore less dependent on supporting structures. Contrary to the work of Premont and Steinhagen, our set-up is more compact, likely reducing the influence of Eigen frequencies of the force measurement tool.

Euler introduced the following equation for rotational systems, equivalent to Newton's equation for translational motion:

$$\tau = I\alpha \tag{8.1}$$

With τ, the torque in Nm, α, the rotational acceleration in rad/s^2 and I, the mass moment of inertia in kg.m^2, which can be obtained from CAD software (containing the parts with the actual dimensions and material densities):

$$I = \begin{bmatrix} I_{xx} & I_{xy} & I_{xz} \\ I_{xy} & I_{yy} & I_{yz} \\ I_{xz} & I_{yz} & I_{zz} \end{bmatrix} \tag{8.2}$$

The angular momentum L can be calculated by integrating the torque:

$$L = \int \tau dt \tag{8.3}$$

in kg.m^2 or also Nms.

The idea is to have a tool that does not influence the experiment. This means that, if the vane would be mounted on a rigid surface, the same impact forces should be measured. Applying this to the equations above, the angular momentum measured with the cone (from the rotational movement together with the mass moment of inertia in equation 8.1) should be the same as for the scenario where the vanes are fixed (when integrating the reaction torque with 8.3):

$$L = \int I\alpha dt = I \int \alpha dt = I\omega \tag{8.4}$$

This is only valid when I is not dependent on time, or also, that the entire structure is rigid and fixed. This is why the displacement during impact should be limited. For deforming objects such as a booster vane, I is not exactly constant. But, simulations showed that the average transferred momentum is equal in both situations with and without cone, as well as the amplitude of the oscillations superimposed on this average value. Small delays in the momentum signals showed to have the biggest influence of the cone. The influence of the cone will be further discussed in the section 8.3.4.

The fact that a well-designed inertial tensor (a stiff fixture which makes the approximation of I=cte valid in equation 8.4) does not influence the momentum transfer can ease the comparison with the simulations. It allows to make abstraction from the actual geometry in the simulation (bolts, accelerometers, stiffeners, little plates with optical patterns, etc.) to speed up the process of meshing and reduce the model size. While boundary and initial conditions are acquired from the actual experiment, the geometry of the cone can be approximated in the numerical analysis, as schematically shown in Figure 8.8.

The rotational momentum is a measure for the impact force and will be used to compare simulations and experiments because it is fairly independent of the set-up. If the actual impact forces would have to be calculated, the lever arm would need to be known which (i) is an estimation but worse, (ii) is not constant through time and will therefore introduce another unknown and error in the process. Therefore, the momentum will remain the parameter

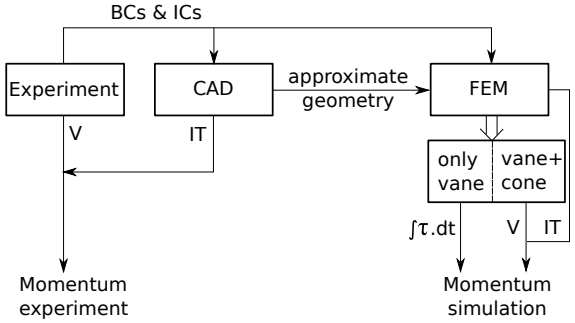

Figure 8.8: Comparison between experiment and simulation (IT: inertial tensor, V: rotation speed, τ: torque, BC: boundary condition, IC: initial condition).

for comparison throughout the remainder of this chapter.

The rotational speeds are essential to obtain the momentum (Equation 8.4). In the next section, the developed method to derive the rotational speeds will be covered.

8.3.3 Deriving the rotational speeds

The rotational movement of the cone is derived from an optical measurement, contrary to the accelerometers used in the work of Premont and Steinhagen. Optical measurements have several advantages compared to accelerometers (see also chapter 3) and the HSC is already necessary anyway to acquire the horizontal offset of the bird.

Initially, experiments were performed using DIC. Optimized speckle patterns were applied to the two protrusions of the cone (Figure 8.7b). The major disadvantage of DIC in this kind of application however is the fact that pieces of bird, foam and other debris disturb the view, making it very difficult to find subsets that correlate throughout the entire experiment. Even if several subsets do correlate, generally a lot of noise is superimposed on the actual displacement signal. The choice is therefore made to use the line patterns discussed in chapter 3. To get multiple data points during the impact interval, a sufficiently high frame rate is needed. For most of the simplified vane and booster vane experiments, a frame rate of 27.000 fps is used. This corresponds with a resolution of 448×288 (compared to the

full resolution of 1024×1024). Because of this relatively low resolution, a relatively large pattern is needed to correctly sample the sines in the optical pattern. The used pattern has a diameter of 80 mm, which corresponds with a pitch of 4 mm. The two optical patterns attached to the cone are shown in Figure 8.9a. To avoid oscillations of these optical patterns, the cone is reinforced between the flange of the cone and the cone itself (Figure 8.9b).

Figure 8.9a also shows several indications on the flange of the cone. These are used to set the initial position of the cone and serve as a reference to obtain the offset of the bird with respect to the cone.

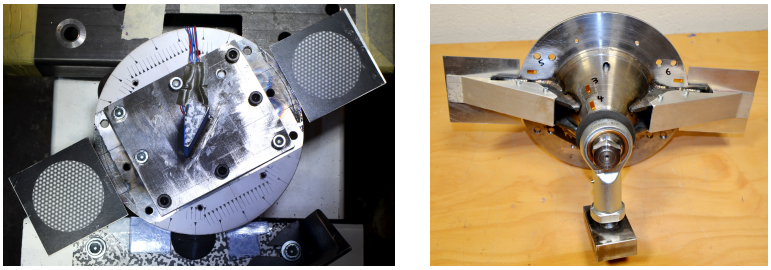

(a) Optical patterns. **(b)** Extra reinforcements.

Figure 8.9: Optical patterns on the cone set-up.

8.3.3.1 Overview

The patterns move on a spherical path, which is a boundary condition to the problem and makes it possible to derive the kinematics with only one camera. Practically, the patterns will not move exactly on a spherical path, which will therefore introduce an error (the total error will be assessed in section 8.3.4). The use of two cameras could eliminate this error as it does not require this assumption, but it does require an additional high speed camera dedicated to the measurement of the momentum which can be an unnecessary waste of resources. A simplified schematic overview of how the kinematics are derived is shown in Figure 8.10.
In a first step, the images are processed using the 2D line pattern processor software introduced in chapter 3. Because the patterns are not aligned with the spherical plane in which they move, the second correction option is used or also, the displacements perpendicular to the line of sight are

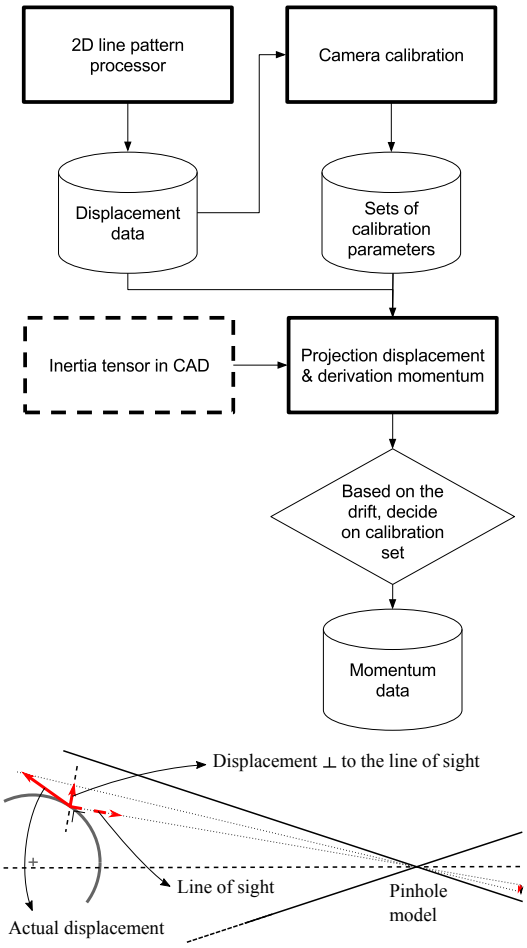

Figure 8.10: Schematic overview derivation cone kinematics.

obtained (section 3.4.4). The calculated displacements are therefore only a projection of the actual displacements of the patterns of the cone, so some transformation needs to be done (schematically shown at the bottom of Figure 8.10). To be able to do this correct, the extrinsic and intrinsic camera parameters need to be defined through camera calibration. The solution space proves to be very noisy with a lot of local optima, multiple sets of calibration parameters are therefore generated after which an additional parameter called the drift (which will be introduced further on) will decide on the final calibration set. Once this is done, the displacements can be

projected onto the sphere (the spherical path on which the patterns move) and the rotational speeds and momentum can be calculated. In the following sections, first, more details about the calibration of the camera will be given. After that, the projection of the displacements on the spherical path of the patterns will be explained. Three accelerometers were attached to the cone as well. These are not used to obtain momentum data because (*i*) something went wrong with the calibration of these sensors and (*ii*) a relatively large drift was obtained on the signals. For future reference however, the derivation of the momentum via these sensors will be covered briefly as well.

8.3.3.2 Calibration of the camera

When calibrating the camera, several calibration points are needed to link the world with the image coordinates (see also chapter 3). To calibrate the camera and obtain its position with respect to the cone, 15 calibration points are considered that are fixed with respect to the cone (Figure 8.11), from which 12 are derived from the pattern information and three points are chosen on the flange. From the pitch in pixels and the orientation of the different line gratings in the pattern, a hexagon-like pattern of points can be constructed that contains the information of the entire pattern. Each pair of opposite points in the hexagon corresponds with one line grating and is constructed by taking the orientation of the line grating and equating the distance to the centre of the pattern to five times the pitch (to acquire points that lie more or less on a circle with a diameter equal to half the diameter of the pattern itself). This hexagon can be constructed in the image (on subpixel level) and in world coordinates. The other three points can be distinguished easily from the indications on the flange of the cone.

For the Photron SA-4 cameras, the position of this reduced resolution (which will be further referred to as the region of interest or ROI) on the CCD is vertically in the middle of the CCD, while the position of the ROI in the horizontal direction can be chosen in steps of 32 pixels. This parameter was not known to be important at the time of the experiments. It was never noted in the the booster vane experiments and is therefore an additional optimization parameter.

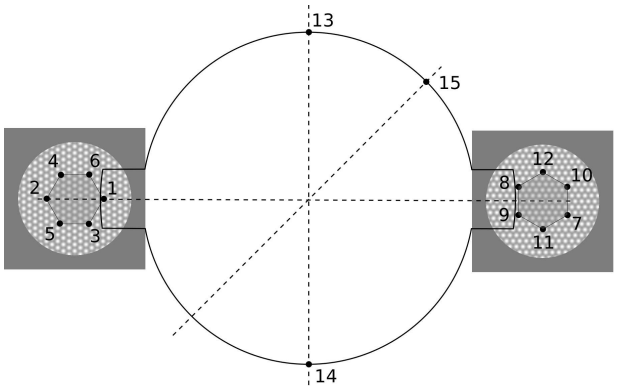

Figure 8.11: 15 calibration points.

In chapter 3, the local and global optimization techniques to determine the calibration parameters are introduced. In general, local optimization schemes are used for the calibration of the camera. Multiple experiments however showed that the solution of the local optimization is very dependent on the initial guess. Also with a global optimization scheme, different solutions were found each run, indicating that the solution space is very noisy with a lot of local optima. This phenomenon is partly the result of a poor set of almost coplanar calibration points, but also because of the nature of the problem. This can be observed in other software as well (using a different set of calibration images in the DIC software MatchID™ for example results in quite different calibration parameters). For each experiment, therefore, multiple calibration sets are generated. An additional parameter introduced in the next section is used to decide on the final calibration set.

For the optimization, the sum of the squares of the differences between the world coordinates projected on the image plane, and the corresponding actual image coordinates for each of the 15 points is minimized using a genetic algorithm in Matlab™.

8.3.3.3 Calculation of the actual displacements

The displacements of the patterns are only a projection of the actual displacements (see also Figure 8.10). How the actual displacements are determined, is schematically shown in Figure 8.12. In this figure, $\overrightarrow{cv}$, $\overrightarrow{pdv}$ and $\overrightarrow{pv}$ have an

abbreviated name, all the other vectors are derived from these three known vectors:

- $\overrightarrow{cv}$ stands for *camera vector*. $\overrightarrow{cv}$ starts from the centre of the pattern and points in the direction of the pinhole of the camera. The camera vector can directly be derived from the calibration parameters.
- $\overrightarrow{pdv}$ stands for *projected displacement vector*. This is the vector calculated by the 2D line pattern processor software. $\overrightarrow{pdv}$ lies in the plane defined by $\overrightarrow{cv}$, with an orientation which is also defined by the calibration parameters.
- $\overrightarrow{pv}$ stands for *position vector*. This vector points from the centre of rotation to the centre of the pattern. The initial position vector is defined by the initial position of the cone. The actual displacement vector lies in the plane defined by $\overrightarrow{pv}$ (for small displacements, the displacement can be assumed tangential to the sphere's surface).

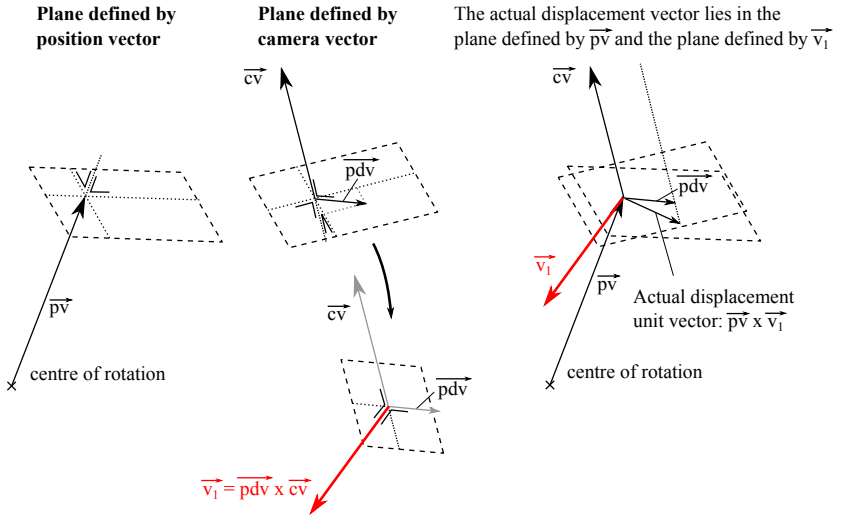

Figure 8.12: Calculation of the actual displacements.

The actual displacement vector lies in the plane defined by $\overrightarrow{pv}$, but also in the plane defined by $\overrightarrow{pdv} \times \overrightarrow{cv}$. Therefore, first a vector $\overrightarrow{v_1}$ is created, after which the wanted unit vector is obtained from the cross product of $\overrightarrow{pv}$ and $\overrightarrow{v_1}$.

This procedure can be repeated for each time step to obtain the actual displacements of the centre of both patterns. The mean of those displacements (from both patterns) gives the displacement of the centre of the flange of the cone, from which the two main rotation components can be derived. The calculation of the third rotation component along the axis of the cone makes use of the fact that this rotation is very small. The difference between the displacement of both patterns in the direction perpendicular to the axis of the cone and the vector between the patterns divided by the distance between the patterns gives a good estimate of the rotation about the cone's axis.

The calculation is separately done for each pattern. The rigid motion of the cone implies that the vector between both patterns should remain constant, which is practically never the case. Multiple tests however showed that the drift on the norm of this vector is a good measure for the quality of the calibration. From the different calibration sets that are generated with the global optimization scheme, the set with the least drift is therefore chosen. Figure 8.13a shows the drift for 150 runs of the genetic algorithm in case of an impact test. It can be observed that the drift does not decrease below a certain value around 0.3 mm. Figure 8.13b shows the norm of the vector for the smallest drift from all these runs. The minimum drift typically ranges between 0.2 and 1.5 mm.

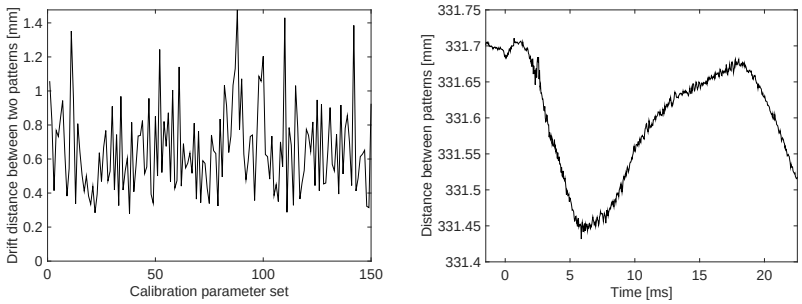

(a) Drift for different optimized calibration sets.

(b) Drift for an impact test.

Figure 8.13: The drift on the norm of the vector between both patterns as a measure for the quality of the calibration.

The error that does not decrease below a certain value for different runs of the genetic algorithm indicates that there are other errors that influence the

results as well (apart from the calibration of the camera). Multiple error sources can be identified:

- The most important error source is definitely the non-rigid boundary condition and oscillations that occur during impact. As a result, the patterns do not move in the spherical path in which they are assumed to move.
- The definition of the calibration points also introduces an error. This includes the orientations and location of the patterns in world coordinates and the pixel approximation of calibration points 13-15.
- The error on the displacements derived from the 2D line pattern software. This error source however should be negligible compared to the first two.

How much the drift error influences the obtained momentum is difficult to predict. Therefore several tests will be done to characterize the error on the obtained results. This will be done in section 8.3.4.

From the displacements and rotations, the rotation speeds can be calculated. Together with the inertia tensor obtained from the CAD drawing, the momentum can be determined. To obtain the inertial tensor, first the dimensions of the cone and the steel vane are measured and the weight of both parts is matched as good as possible with the CAD drawing. After that, the correct material densities are assigned to each part, after which the inertia tensors are requested. Figure 8.14a shows the CAD drawing that provided the inertia tensor for the steel vane experiments. The obtained momentum in the following sections is defined according to the coordinate system shown in Figure 8.14b. The z-axis is aligned with the impact direction, the y-axis is aligned according to the axis of the cone in its initial position or also the vertical upward direction and the x-axis completes the orthogonal right-handed coordinate system. This convention for the coordinate system will be used in the remainder of this chapter.

8.3.3.4 Rotations determined from the accelerometers

Two methods to derive the kinematics of the cone from the accelerometers are developed and validated. Three accelerometers are used, which give

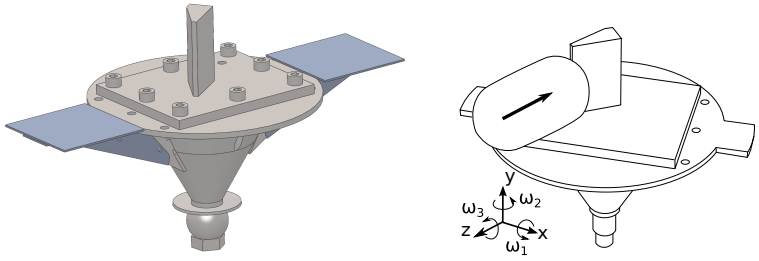

(a) CAD drawing to determine Inertia tensor.

(b) Convention coordinate system.

Figure 8.14: CAD drawing to determine the inertia tensor of the steel vane experiments and the used convention for the coordinate system.

accelerations A1, A2 and A3. The locations and directions are shown in Figure 8.15.

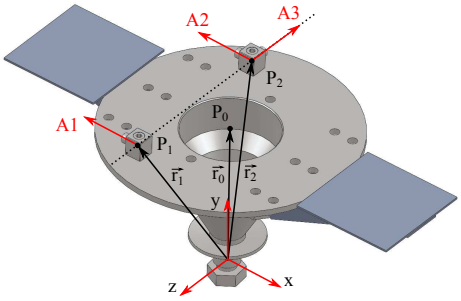

Figure 8.15: Position of the accelerometers on the cone.

The main steps for both methods are summarized in Table 8.1. Both methods make use of a reference system attached to the cone. For each time step, the next position relative to the cone in the previous time step is determined (using a coordinate system fixed to the cone). The absolute kinematics for each time step are obtained by adding the transformed relative displacements to the current absolute coordinate system.
To validate these methods, a sequence of rotation angles were considered, from which the corresponding displacements and accelerations are derived and the accelerations are projected on the accelerometer directions. Both methods proved to be capable of reconstructing the initial set of angles. The influence of random noise on both methods also showed to be limited for

Table 8.1: How to derive the momentum from the accelerometer signals (A1, A2 and A3 represent the acceleration signals from the three accelerometers also defined in Figure 8.15).

Method 1	**Method 2**
• $a_{0,x} = -(A1 + A2)/2$ • $\alpha_y = (A2 - A1)/(\|\|\overrightarrow{r_2} - \overrightarrow{r_1}\|\|)$ • $a_{0,y} = -\|\|\overrightarrow{r_0}\|\|(\omega_{0,x}^2 + \omega_{0,z}^2)$ • $a_{0,z} = -A3 - \|r_{0,x} - r_{2,x}\|\alpha_y$	• $\overrightarrow{a_1} = -[A1, 0, A3]$ • $\overrightarrow{a_2} = -[A2, 0, A3]$ • Project $\overrightarrow{a_1}$ and $\overrightarrow{a_2}$ on a sphere similar to the method described in section 8.3.3.3

both methods. Transverse sensitivity however can be a considerable error source (see also section 2.2.2.1).

8.3.4 Verification of the method to derive the rotation speeds

The methodology to derive the momentum, including the calculation of the displacements of the patterns, the calibration of the cameras and the projection on the sphere is validated using a set of quasi-static and bird impact tests. For these experiments, speckle patterns are attached to the cone and vane and tracked with a stereo DIC set-up. The orientations derived from these DIC measurements are a reference to calculate the errors, because DIC is a well-known technique that can be used in a stereo set-up to directly acquire 3D displacements and includes a distortion model (see also chapter 3). For the static tests, a pattern is applied at the centre of the flange of the cone (Figure 8.16a), while for the dynamic tests, DIC patterns are applied to the vane and to the line patterns at both sides of the cone (Figure 8.16b). Debris ruins the correlation so eventually, the outer speckle patterns attached to the plates with the line patterns had to be used. The centre displacement is obtained from the mean coordinates of P_1 and P_2. This displacement is then transformed to the desired coordinate system (using $\overrightarrow{P_0P_1}$ and $\overrightarrow{P_0P_2}$ for the static tests and $\overrightarrow{P_0P_t}$ and $\overrightarrow{P_0P_1}$ for the dynamic tests).

Three quasi-static and three dynamic experiments are performed. For the static experiments, the cone is rotated manually. The ROI with reduced resolution is once placed in the centre of the CCD, once 32 pixels shifted to

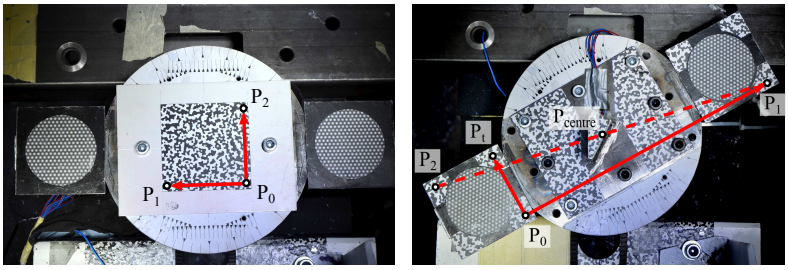

(a) Static tests. **(b)** Dynamic tests.

Figure 8.16: Set-up for the static and dynamic validation tests.

the right and once 64 pixels to the right. To test the influence of this shift parameter, the optimization is performed once with a fixed or known shift value (7 calibration parameters) and once with a free or unknown value (8 calibration points). An example of the error on the displacement of P_{centre} (for displacements larger than 1 mm) and the obtained rotational speeds around the x- and z-axis respectively is shown for a quasi-static test with an optimized shift parameter in Figure 8.17. The time scale for the quasi-static test is a fictitious one corresponding with one image per second. The rotation speed corresponds very well. Figure 8.18 shows the displacement and the error on these displacements for a dynamic test with an optimized shift parameter. The rotational speeds obtained from the DIC measurement are very noisy (due to the debris), which is why only the displacement is shown. It can be observed that the errors are rather small.

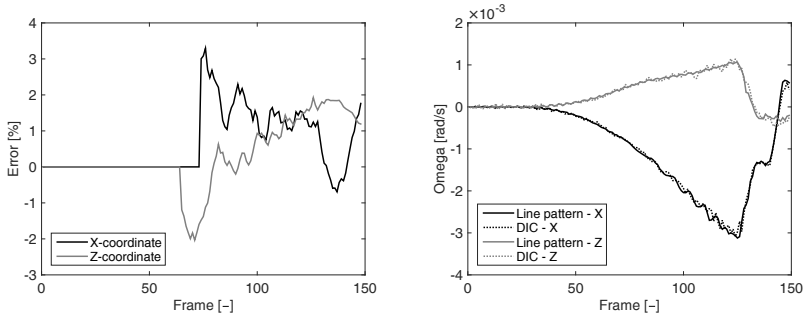

(a) Displacement errors. **(b)** Rotational speeds.

Figure 8.17: Errors and rotational speeds of a quasi-static test.

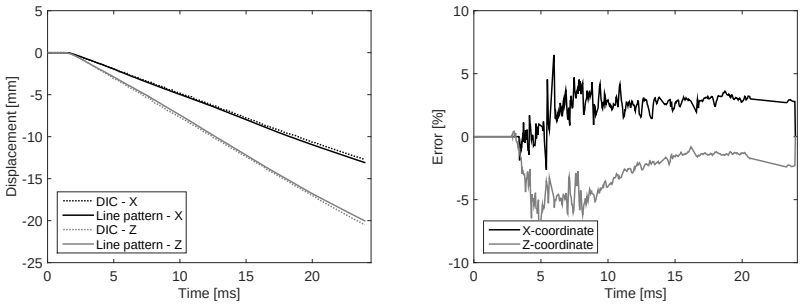

(a) Displacements. **(b)** Displacement errors.

Figure 8.18: Displacement values and errors of a dynamic test.

The errors on the x- and z-displacement of the static and dynamic tests are summarized respectively in Table 8.2 and 8.3, for the considered shifts of the ROI and the type of calibration that is performed (considering a known or unknown shift parameter in the optimization procedure). It can be deduced that the errors are in general less than 5%. Even for experiments with an error of several percent, the curves should allow to make good qualitative comparisons between different momentum curves.

Table 8.2: Displacement errors for the static force measurement set-up validation tests.

Shift [pix]	**Optimized shift**	**Max. x-error [%]**	**Max. z-error [%]**
0	no	-1	-0.5
0	yes	-4.5	2
32	no	6	-1
32	yes	1.5	-1
64	no	1	-1
64	yes	-0.5	1

Table 8.3: Displacement errors for the dynamic force measurement set-up validation tests.

Max. x-error [%]	**Max. z-error** [%]
0.5	-4
-1.5	-3
3	-5

8.4 Experimental set-up

8.4.1 Overview set-up

An overview of the whole set-up is depicted in Figure 8.19. The ball joint of the cone structure (2) is mounted onto a stiff structure of rectangular tubes (3). The main purpose of the big tube just before the cone (4) is to protect the cone from air waves and impact of debris (see also Figure 8.7c), which could influence the reaction force measurement. Additionally, it can also be used to balance the cone when necessary (in most cases, the friction as a result of the self-weight of the cone and the target is sufficient to keep the cone in an upwards position). The two "obstructions" (5) are used to limit foam and debris from disturbing the optical measurements. The height of the set-up can be regulated using sleeves and threads (6). Rubber stops (7) are mounted on the tube structure to dissipate the kinetic energy of the cone after the experiment is finished. They are positioned to allow a maximum deflection of approximately 15-20 mm. The rigid plate set-up (8) is placed just behind the vane set-up to measure the residual energy. Before each experiment, the steel vane or booster vane fixture (1) is mounted onto the cone.

8.4.2 Optical measurements

Several configurations of the high speed cameras and combinations with optical methods were considered and tested (DIC, regular patterns, camera positions, etc.). The final configuration is depicted in Figure 8.20. Two high speed cameras (1 and 3) will be placed on top of the test chamber and high speed camera 2 will record images from the side. The yellow arrow indicates

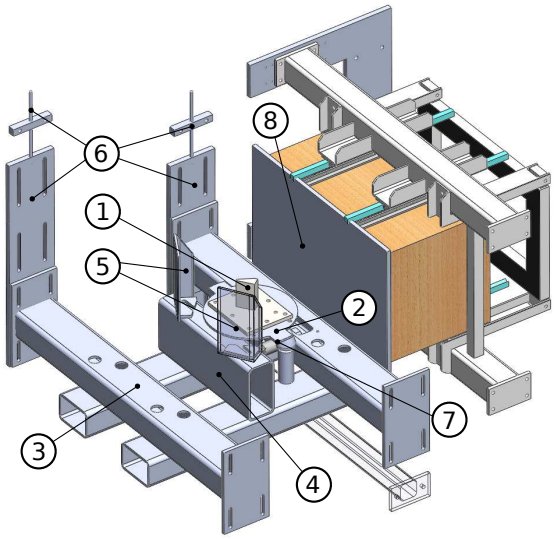

Figure 8.19: Experimental set-up to test vanes.

the impact direction of the bird (with a yellow contour). The red lines show the main geometry of the steel vane.

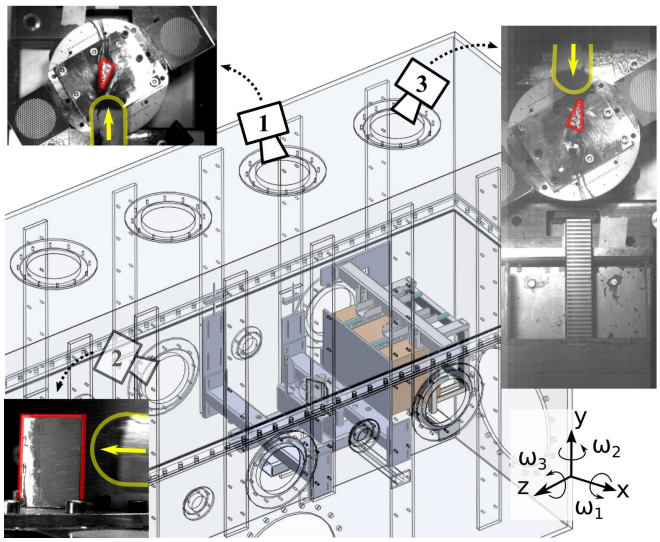

Figure 8.20: High speed camera set-up.

The purpose and properties of each camera are the following:

Camera 1:

- Record two regular 4 mm pitch line patterns (0°, +60°, -60°) to acquire a projection of the displacement of the patterns (the movement of the cone can be derived from this information).
- Maximum achievable zoom on the two gratings.
- Used to determine the offset and rotation of the bird in the XZ plane.
- Framerate: 27.000 fps.

Camera 2:

- Higher resolution image of the bird and the vane fixture from the side.
- The purpose of this camera is to determine the actual impact height and rotation of the bird in the YZ plane.
- Framerate: 10.000 fps.

Camera 3:

- Higher resolution image of the impact on the vane and the rigid plate.
- Recording the linear grating on the top of the rigid plate set-up (with a pitch of 6 mm).
- Get a general overview of the experiment.
- Framerate: 10.000 fps.

8.4.3 Residual energy measurement

Contrary to the rigid plate experiments, the mass distribution at impact on the rigid plate is not symmetric any more. For the booster vanes, the centre of mass of the bird is entirely out of centre of the rigid plate. Initial tests showed that this eccentric impact induces rotations of the rigid plate set-up (while only translational momentum is wanted). The rigid plate is therefore repositioned just behind the vanes, bringing the centre of impact closer to the centre of the plate. Also, the clearance in the linear needle bearings is reduced as much as possible.

A line grating pattern is added to the centre top of the box to serve as the main technique to determine the momentum of the bird after impact (see also chapter 5 and 6). Because of the central location of the grating, it is much less prone to vibrations due to the eccentric impact. The results of the line grating proved to be the most reliable.

Before each test, blue chalk powder is wetted and wiped onto the impact surfaces to track the position of impact of the bird (see also chapter 5), on the rigid plate as well as on the vanes. The powder has a negligible influence on the experiment, while it gives information about the distribution of the bird mass throughout the experiment.

8.4.4 3D scanning and Eigen frequency measurements

3D scanning of the vanes before and after each test together with Eigen frequency measurements has only been done for the booster vane experiments.

The titanium vanes are scanned by Argon (*Argon: Measuring solutions*, 2016) to get an idea of the plastic deformations (or rather displacements) after impact. In the simulations, a static springback analysis analysis can be performed after the explicit impact simulations to compare the final deformations with the results of these 3D measurements.

8.5 Steel vane experiments and simulations

Throughout the PhD, the set-up to test the vanes has been optimized. The three dynamic tests to quantify the error (covered in the section 8.3.4) are part of a final test campaign where four tests were executed on the steel vane set-up. The results obtained from these tests will be used to make a comparison with the simulations. Table 8.4 summarizes the considered tests, containing the test ID, the impact mass, speed and impact offset of the bird (the y-coordinate is relative to the top of the flange of the cone), the initial rotation of the cone (along the axis of the cone) and the residual energy of the bird derived from the linear transducer on the rigid plate (two cameras are necessary for the DIC measurement). $\alpha_{0,y} = 0$ means that the vector

between the two patterns is perpendicular to the impact direction. All the tests are executed with a 1:6 gelatine MR.

Table 8.4: Steel vane experiments (SV stands for steel vane).

Test	m [kg]	v [m/s]	Offset x [mm]	Offset y [mm]	$\alpha_{0,y}$[°]	$E_{res,z}$ [J]
SV-1	0.2978	114.1	-2.1	41.1	30	1750
SV-2	0.2970	114.3	-16.7	41.5	25	1477
SV-3	0.2956	113.4	-2.2	40.3	20	1467
SV-4	0.2970	114.3	-1.1	40.2	30	1606

8.5.1 Results experiments

SV-1 and SV-4 have nearly identical input conditions. These two tests show the consistency of the results. First of all, a qualitative comparison is made in Figure 8.21, which shows three subsequent high speed images of test SV-1 and SV-4 (the total ROI of 448x288 pixels from camera 1). Little extra space is foreseen to make sure that the patterns are always in the ROI throughout the entire movement of the cone. In the third image, the bird has travelled through its own length, while the movement of the cone can barely be seen. The deformation of the bird throughout the experiment is very similar: the direction and the speed at which the bird is deviated to the left and to the right are alike.

For all the tests (SV-1 to SV-4), multiple calibration sets are generated, from which the one with the least drift is chosen (for SV-1 to SV-4 respectively 0.25, 0.28, 0.41 and 0.27 mm peak to peak). The displacements from the patterns are projected on the spherical path and the rotational speeds are calculated. From the rotational speeds and the inertial tensor, the momentum is calculated. To get a better overview of the results, a low pass filter of 3 kHz is applied. The result of this process is shown in Figure 8.22. The two tests with nearly identical input conditions (SV-1 and SV-4) give very similar results, for all the three axes. Most of the mass is deflected to the right (positive x-axis), which makes the cone move to the left and back (the negative x- and z-axis). This corresponds with a positive and negative rotational momentum around the z-axis and x-axis respectively.

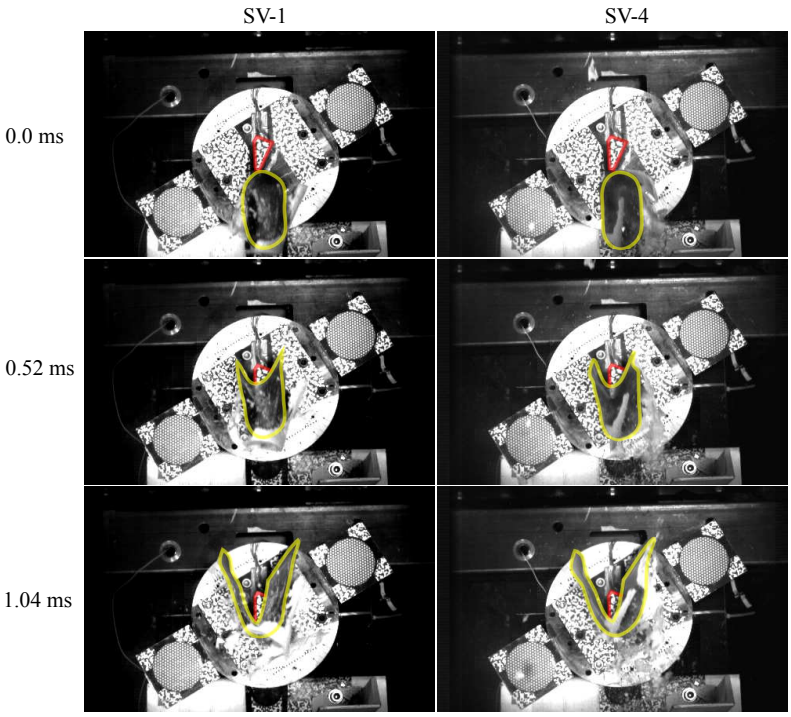

Figure 8.21: High speed images of two bird strikes with similar impact conditions on the steel vane mounted on the cone set-up.

The magnitude of the momentum around the z-axis is smaller than around the x-axis because some mass is also deflected to the left (negative x-axis). The rotational momentum around the y-axis is a lot smaller because the lever arm of the impact force with respect to the axis of the cone is a lot smaller than for the other axes. The sign is negative because most of the deviation of the bird happens at the front of the steel vane, which is positioned slightly to the left of the axis of the cone from the point of view of the bird.

The experiments with a lower initial rotation angle of the cone naturally have a higher momentum transfer about the z-axis and x-axis, because the main surface of the vane gets more orthogonal to the impact direction. The magnitude of the momentum about the y-axis also seems to increase for lower initial rotation angles.

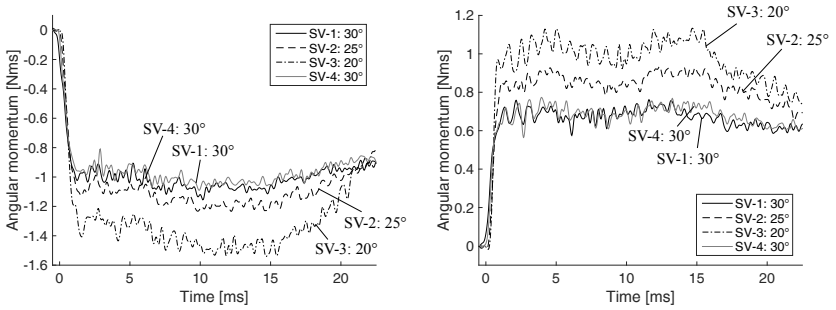

(a) Momentum x-axis.

(b) Momentum z-axis.

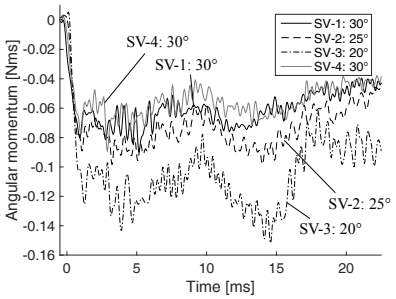

(c) Momentum y-axis.

Figure 8.22: Rotational momentum versus time for experiment SV-1 to SV-4 with different initial rotation angles $\alpha_{0,y}$ of the cone (see also Table 8.4).

8.5.2 Results simulations

Explicit simulations are ran with the same impact conditions as test SV-2, SV-3 and SV-4 (SV-1 is omitted because the impact conditions and results are similar to SV-4), where the bird is modelled with SPH. A structured mesh is generated based on the shape of the mould, with a slight offset to exactly match the mass with the experiments.

For the numerical model, the cone is modelled as a deformable object, able to rotate around the tip of the cone (Figure 8.23). The vane is modelled as accurately as possible, including a coarse representation of the welds between the vane and the plate of the vane. To acquire the strain at the location of the strain gauges, membranes are attached to the element that best corresponds with the centre of the strain gauges (the gradients of the strain are relatively low). More details about deriving surface strains from

a solid part will be given in the section comprising the development of the numerical booster vane model (section 8.7.1). Both the cone and the vane are modelled with reduced integration hexahedral elements.

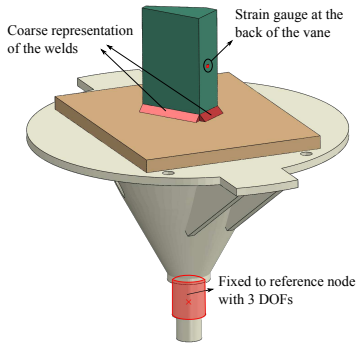

Figure 8.23: Numerical model steel vane set-up.

The linear Mie-Grunesen EOS from Sherpherd is used for the bird (Shepherd et al., 2009), with bulk viscosity reduced to 20%. A tensile failure criterion of 1 MPa is set as well. For experiment SV-2 and SV-4, the bird is respectively rotated 14.9° in the horizontal plane and 8° in the vertical plane, to have a better match with the impact conditions of the experiments.

In the next sections, subsequently a qualitative comparison is made between the experiments and simulations and the correlation of the transferred momentum, strain and residual energy is investigated.

8.5.2.1 Qualitative comparison

Figure 8.24 shows a qualitative comparison of test SV-4 from the side and Figure 8.25 compares test SV-2, SV-3 and SV-4 with the simulation from the top of the cone, 1 ms after impact. The difference in time should be 0.05 ms maximum. The green line in Figure 8.25 resembles the impact direction, based on the indications of the cone. The red line indicates the orientation of the main front surface of the vane.
The global behaviour correlates very well with the experiment. Both the direction in which the mass is deviated as the speed of the deviated mass after impact. It can be observed that for smaller initial angles of the cone

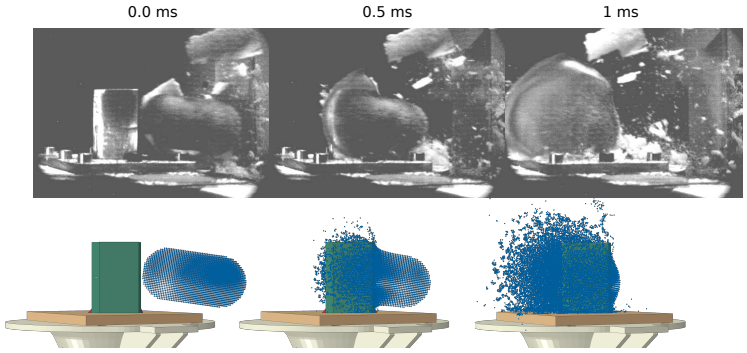

Figure 8.24: Qualitative comparison of test SV-4 with the simulation - side view.

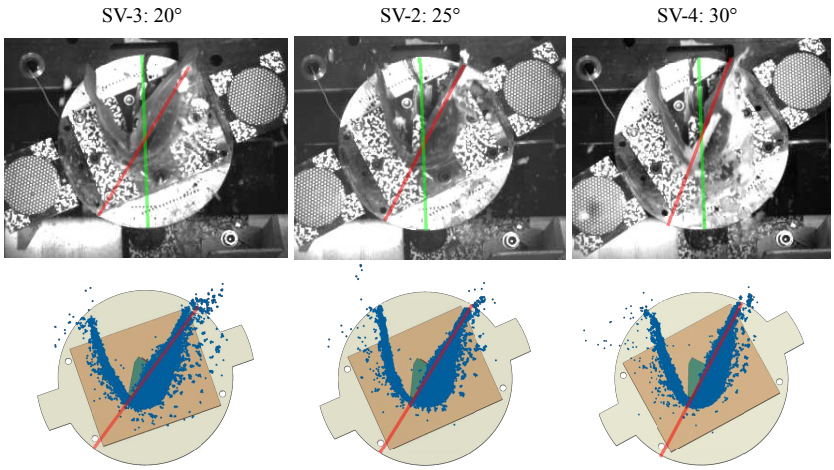

Figure 8.25: Qualitative comparison of test SV-2, SV-3 and SV-4 with the simulation, 1 ms after impact - top view.

(i.e. higher deviation angles according to the front surface of the vane), the bird does not follow the orientation of the vane any more (mainly in the experiments).

8.5.2.2 Transferred momentum

Figure 8.26 shows a comparison between the momentum obtained from experiment SV-4 and from the simulation, including a 2 mm offset on the estimation of the impact location both in the negative as the positive x-direction in the simulation. For the momentum of the simulation, the speeds

extracted at a point on each protrusion of the cone is used to determine the rotational speed about the two main axes, while the rotation speed about the y-axis is directly obtained from the rotation in the rotation point. Together with the inertia tensor from the model, the momentum is calculated.

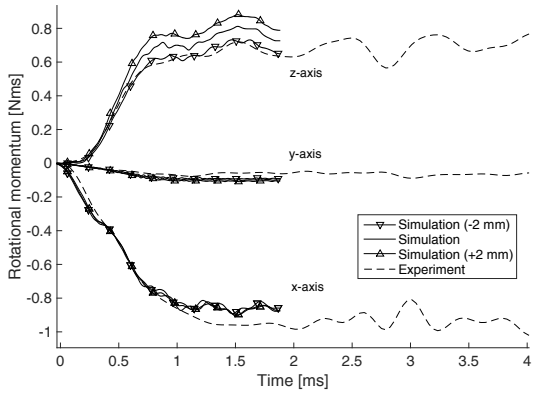

Figure 8.26: Comparison of the rotational momentum of experiment SV-4 with the simulation (including different runs with horizontal offsets of 2 mm).

The impact location of the bird is crucial. A 2 mm offset error for example, which can be easily made, corresponds with 4.5% of the bird mass that is deviated in the other direction. This kind of error is therefore most represented in the momentum around the z-axis. The order of magnitude of momentum transfer is approximated well, but some differences can be observed. In the simulation, the momentum transfer to the x-axis is slightly lower. The graphs also show that possibly, an error of approximately 2 mm was made in the estimation of the x-offset. The momentum transfer around the x-axis also takes slightly longer in the experiment. These two observations are possibly linked to the underestimation of the momentum transfer seen in the wedge simulations.

The momentum for experiment SV-2 and SV-3 is shown in Figure 8.27. Again the momentum about the z-axis is overestimated. Possibly, as a result of perspective in the image, the offset along the x-axis is consistently overestimated. Nevertheless, the shape of both curves again resemble quite well with the experiment. The correlation of the momentum about the x-axis is much better than for SV-4. A possible explanation is that the surface of

the vane is more orthogonal to the impact direction. As a result, the impact scenario resembles more to a flat plate impact, which is approximated well by the simulation. The momentum about the y-axis is much higher in the simulation. It could be that the force that generates the moment lies at a very close distance to the axis of the cone, relatively to the radius of the ball bearing. If that is the case, then the friction can have a significant influence on the momentum about the y-axis.

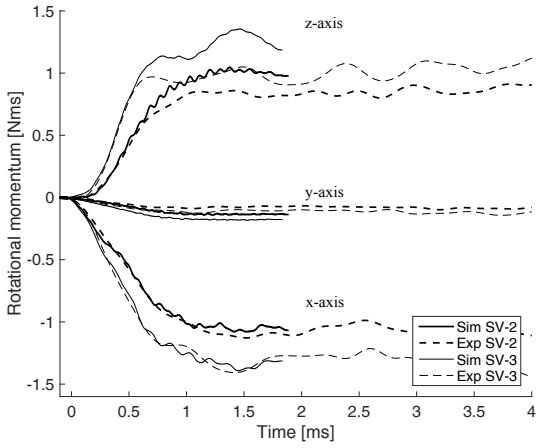

Figure 8.27: Comparison of the rotational momentum in the simulation and the experiment of SV-2 and SV-3.

8.5.2.3 Strain

A comparison between the strain at the back and the left side of the vane for experiment SV-4 and the correlation with the simulations is shown in Figure 8.28. The influence of the offset is less pronounced in the strain signals. The left strain gauge measures the deformation along the weak axis of the steel vane and therefore sees more strain. For the left strain gauge, the strain amplitude is 15-20% higher in the simulation. And after 0.6 ms, the correlation with the strain gauge at the back gets worse. Apart from that, the response of the vane is capture quite well.
Also for experiment SV-2 and SV-3, the correlation of the strains is quite well (Figure 8.29). Especially for the left strain gauge, the response of the vane is predicted very well. The linear decrease in strain at 1-1.5 ms in

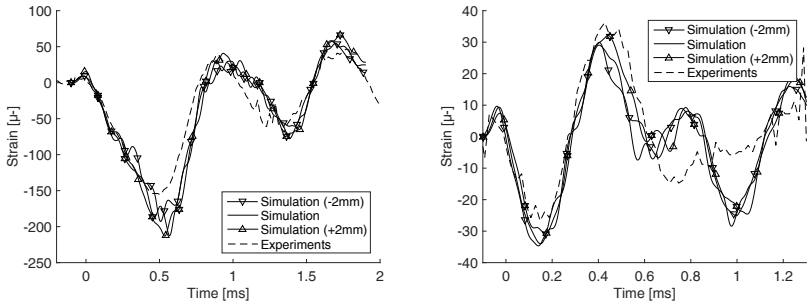

(a) Left side of the vane. **(b)** Back of the vane.

Figure 8.28: The strain at the left side (left) and the back (right) of the vane in experiment SV-4 and the correlation with the simulations (including different runs with horizontal offsets of $2\,\mathrm{mm}$).

experiment SV-2 for example can also be observed in the simulation. The much lower strain at the back of the vane is slightly underestimated in the simulation, but the overall response is quite good.

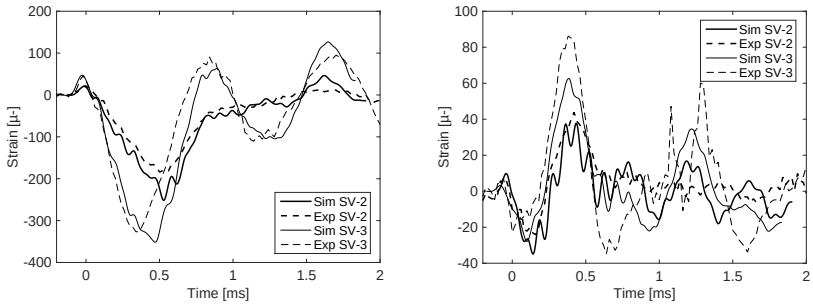

(a) Left side of the vane. **(b)** Back of the vane.

Figure 8.29: The strain at the left side (left) and the back (right) of the vane in experiment SV-2 and SV-3 and the correlation with the simulations.

8.5.2.4 Residual energy

Table 8.5 shows the residual energy in the impact direction for the experiment and the simulation, both absolute and relative to the impact energy. First of all, it can be observed that contrary to the comparable momentum and strain results of SV-1 and SV-4, the residual energy does differ quite a lot.

Table 8.5: Residual energy in the steel vane experiments.

Test	$\alpha_{0,y}[^\circ]$	$E_{res,z}$ exp [J]	$E_{res,z}$ exp [%]	$E_{res,z}$ sim [J]	$E_{res,z}$ sim [%]
SV-1	30	1750	90.3	/	/
SV-2	25	1477	76.1	1392	71.8
SV-3	20	1467	77.2	1214	63.9
SV-4	30	1606	82.8	1463	75.4

Disregarding the possible high inaccuracy of the experimentally measured residual energy, it can be observed that the residual energy in the simulation is always lower than the one from the experiment. This is unexpected, because the wedge experiments showed that the dissipation in the bird is underestimated. The high speed images however show that the bird deviates slightly more in the simulations. This is shown in Figure 8.30 for experiment SV-3, 2 ms after impact. In Figure 8.30, the contours of the bird are drawn in red using the HSC frame, after which the contour is superimposed on the same view in the simulation. The red contour of the mass deviates less in the experiment than in the simulation (for the mass that deviates to the right). This could be an explanation for the lower residual energy in the impact direction for the simulations.

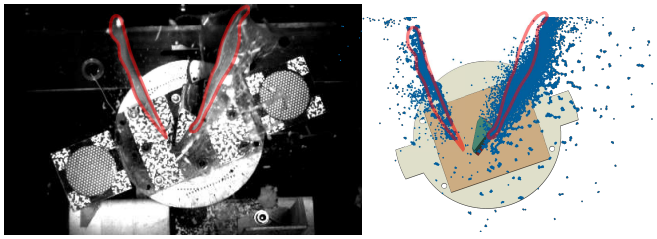

Figure 8.30: The deviation of the bird in experiment SV-3 compared to the simulation, 2 ms after impact. The red contours are from the experiment.

8.5.3 Influence of the cone

To show that the influence of the cone is negligible, a simulation with and without cone is performed. For the simulation without cone, all the elements of the cone are removed except for the top (shell) surface of the cone. The

same tie is defined, the remaining surface of the cone is defined rigid and coupled to a fixed reference point. The forces and moments acting on this reference node are recorded throughout the simulation, filtered with a cut-off frequency of 10 kHz, transformed to moments at the rotation point and integrated over time. A comparison between the obtained momentum from this integration and the one from the cone kinematics together with the strain in both situations is shown in Figure 8.31.

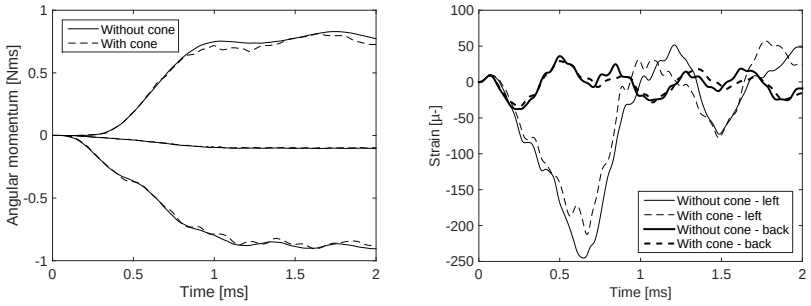

(a) Momentum. **(b)** Strain.

Figure 8.31: Influence of the cone on the transferred momentum and strain.

The momentum transferred to the cone matches very well. The strain is slightly lower in the simulation with the cone. This is likely the result of the deformation of the cone where the vane is mounted to the cone.

8.6 Booster vane experiments

In this section, the results of the booster vane experiments will be discussed. First, the performed test matrix will be covered after which the results of the experiments will be discussed.

8.6.1 Test matrix

In Table 8.6, the different configurations can be found, with the configuration ID, the amount of tests, the aimed velocity, the amount of strain measurements and the aim or sensitivity to be tested. In all the booster vane experiments, a 300 gram gelatine bird with a mixing ratio of 1:6 is used.

Table 8.6: Considered configurations in the booster vane experiments.

Conf.	**Amount of tests**	**v [m/s]**	**SGs**	**Aim**
1	3	ref.	12	Reference model
2	2	ref.	4	Thickness reduction
3	2	ref.	4	Radius reduction
4 (=1)	2	faster	4	Velocity increase
5	2	ref.	4	Stacking modification
6 (=1)	2	ref.	4	Inclined impact
12	1	faster	12	Bigger vane configuration

In general, two models are tested: a smaller and a bigger set of vanes. Configuration 1 and 12 is respectively the reference model for the smaller and the bigger model (see also Figure 8.4). For the smaller model, the influence of a reduced vane thickness (configuration 2), a decrease in radius (configuration 4), an increased speed (configuration 4), a reduced stacking (configuration 5) and an incidence angle (configuration 6) is tested as well. The geometry of configuration 4 and 6 is therefore identical to configuration 1. In this chapter, each test will get a unique ID (BV-1.2 for example stands for the second test on configuration 1, where BV stands for booster vane).

For each test, at least four strain gauges are attached to the vanes (two on the left and two on the right vane). For the fixture in test BV-1.3 and BV-12, 8 additional strain gauges are attached to one vane. For test BV-1.1, the other 8 strain gauges are attached to the inner shroud and for test BV-1.2, to the lateral reinforcements.

The location of the strain gauges for the reference model of the smaller vane (configuration 1) is shown in Figure 8.32. The strain gauges KD1B03, 04, 11 and 12 are four strain gauges that can be found on each configuration.

Figure 8.33 shows the location of the strain gauges for configuration 12.

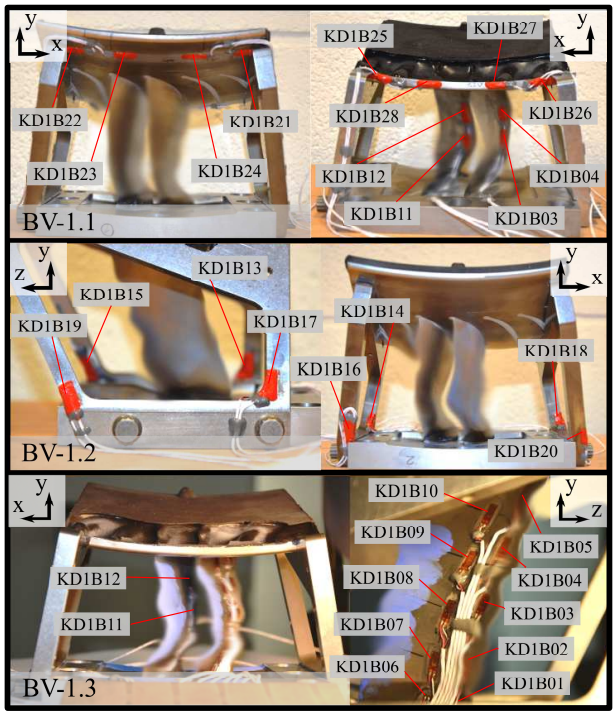

Figure 8.32: Location of the strain gauges for configuration 1 (BV-1.1 BV-1.2 and BV-1.3).

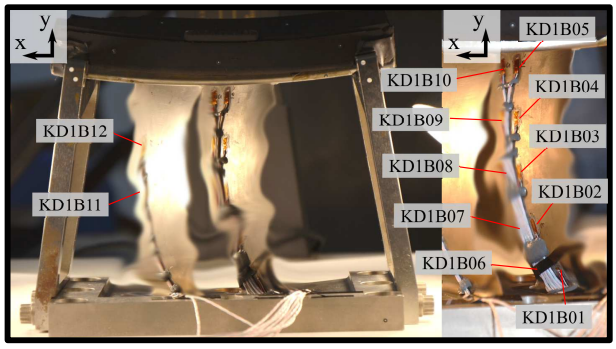

Figure 8.33: Location of the strain gauges for configuration 12.

8.6.2 Results

In this section, an overview of the results will be given and general observations will be discussed. A lot of data is gathered during the experiments.

Most of the acquisition will be used to determine input parameters and serve as validation for the numerical models, which will be discussed in the second last section of this chapter.

In this section, first the results of several Eigen frequency measurements will be covered. After that, the observed damage will be summarized. The transferred momentum and strain will be discussed and finally, the measured residual energy will be covered.

8.6.2.1 Eigen frequency measurements

For each titanium vane fixture, multiple Eigen frequency measurements are performed using a force sensor attached to a hammer and two accelerometers. For each hit, frequency response curves are created and Eigen frequencies are extracted. Cubic spline interpolation is used to get an accuracy smaller than the frequency resolution. The reliable measurements (returning consistent frequencies) can be used to validate the numerical model.

The geometry of configuration 1 (including 4 and 6 because they are identical) is used to investigate the Eigen frequencies. In total, 279 ping tests have been processed to achieve a reliable estimate of the Eigen frequencies. During the test series, the amount of ping tests gradually increased as a result of the gained experience. Ping tests are performed on the left and right reinforcement, the inner and outer shroud and the left and right vane. Multiple locations are struck to get bending modes as well as torsion modes. Eigen frequency simulations helped to reveal some interesting measurements points.

Only Eigen frequencies that are observed more than once are considered. The ping tests on the reinforcement are the most consistent. There are multiple reasons why the other ping tests do not give good results. A first one is that a lot of material damping is present in the fixture (the silicon and the abradable), which damps out the vibrations very quickly. The bolts connecting the inner shroud with the reinforcements also impede the Eigen frequency measurements. Another reason is unquestionably the weight of the accelerometer (2 gram), which is, compared to the vanes for example, relatively large (according to the numerical mesh, one vane weighs around

32.6 gram). In future work, a non-contact measurement using e.g. a laser Doppler vibrometer would be better to measure the response of the fixture.

The difference between the Eigen frequencies for different configurations can be a result of the fact that the abradable is not always completely covering the inner shroud, resulting in different mass and stiffness for each configuration. The frequencies for the symmetric left and right reinforcement in the same configuration on the other hand are always quite comparable.

8.6.2.2 Observed damage

This section will give a qualitative overview of the damage and deformation that is visually observed. After inspecting the different configurations, the abradable is cut away by Safran Aero Boosters to reveal the condition of the retaining plate.

Damage types

In general, four damage or deformation types can be observed in all the configurations, not necessarily occurring in its enumerated order:

1. Small cracks in the grey silicon, mostly at the tip of the vane.
2. Grey silicon pulled out from the inner shroud by the vane.
3. Cracks in the black abradable, visible from the top of the fixture.
4. Vanes entirely pulled out from the inner shroud.

The first two damage types typically occur together.

In the next paragraphs, the tests are divided in two groups according to the amount of observed damage: the configurations with limited damage and the ones with more severe damage. Every configuration is assigned to one of these paragraphs according to the test with the most damage, which is not always consistent.

Limited damage

In all the three tests on configuration 1, no excessive damage is found at first sight. Figure 8.34 shows some pictures of test BV-1.3. The upper left picture shows configuration 1 before the test. The upper right shows the vanes after the test. The blue chalk shows the edge of the area which came into contact with the bird. The bottom left picture shows a bottom view of the inner shroud after the test, taken from the front. The red circle shows a typical crack at the tip. A gap can also be observed between the inner shroud and the vane which was not present before the test (at least not that pronounced). During bird impact, the vanes are pulled out from the inner shroud which likely tears the grey silicon and possibly even the black abradable. The right bottom picture shows a lot of detached and deformed strain gauge wires. The deformation of these wires will also be present in the strain gauge signals.

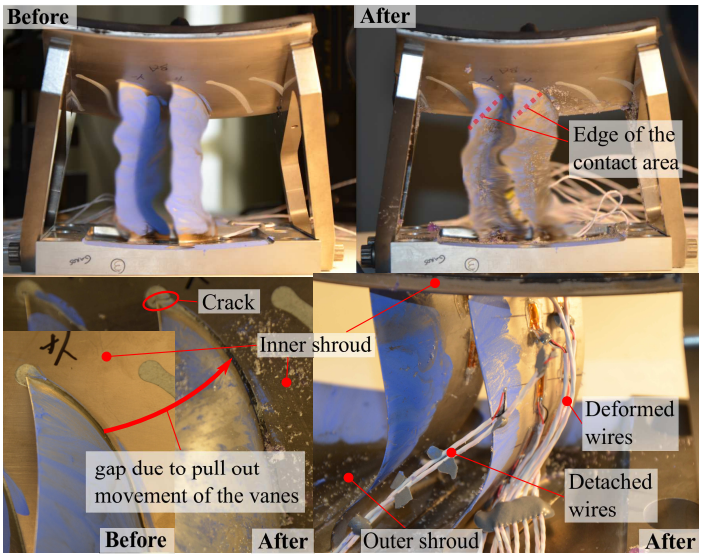

Figure 8.34: Test BV-1.3 - before the tests (upper left), after the test (upper right), typical damage (bottom left) and problem detaching strain gauges (bottom right).

For all the three tests, small cracks could be observed in the silicon, probably due to the vanes that are pulled out from the inner shroud (Figure 8.35).

When the vanes are pulled down during impact, they also pull down the retaining plate where it passes through the sleeves of the vanes. Because there is abradable and silicon material beneath the retaining plate, the

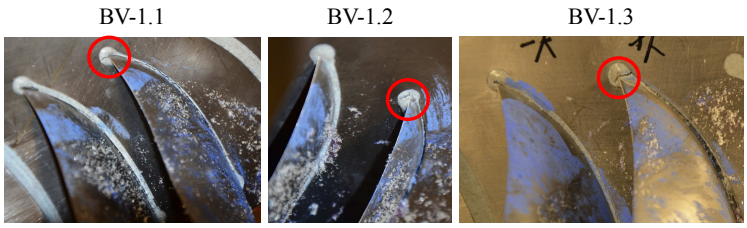

Figure 8.35: Typical cracks in the silicon where the vane goes through the inner shroud.

retaining plate shows a lot of bending deformation (the retaining plate is pulled over the abradable material). For each test on configuration 1, a similar shape of the retaining plate is obtained. The initially flat retaining plate is bended, with the most deformation closest to the right vane.

The vanes that suffered the least damage are the ones from configuration 6. As the splitter experiments also indicated, splitter forces are relatively low compared to scenarios with more change of momentum such as the wedge or the rigid plate. For configuration 6, almost no damage is visible (pictures are not shown). The cracks that are typically found in the reference tests (configuration 1) are not found. Except for the silicon, no damage can be observed for both tests on configuration 3 as well.

Configuration 12 is another configuration which shows limited damage, even though the impact speed was higher than expected. Small cracks though, as in configuration 1, are again present.

More severe damage

Cracks are visible in the abradable in test BV-2.2, BV-4.2 and BV-5.2. For BV-4.2, one vane is even entirely pulled out from the inner shroud. The damage is not consistently found for each configuration (for BV-2.1, BV-4.1 and BV-5.1, no cracks were found in the abradable).

Figure 8.36 shows some pictures from the damage found in test BV-2.2, BV-4.2 and BV-5.2. For BV-2.2, the damage was limited. The shot on test 4.2 was very destructive. The left vane is entirely pulled out from the inner

shroud. The right one is only partly maintained at the back, but the front is also pulled out. In test BV-5.2, there is big gap in the IS, silicon and the abradable. But, since the other tests on the same configuration did not experience this amount of damage, it is difficult to conclude something about the influence of the different parameters shown in the test matrix.

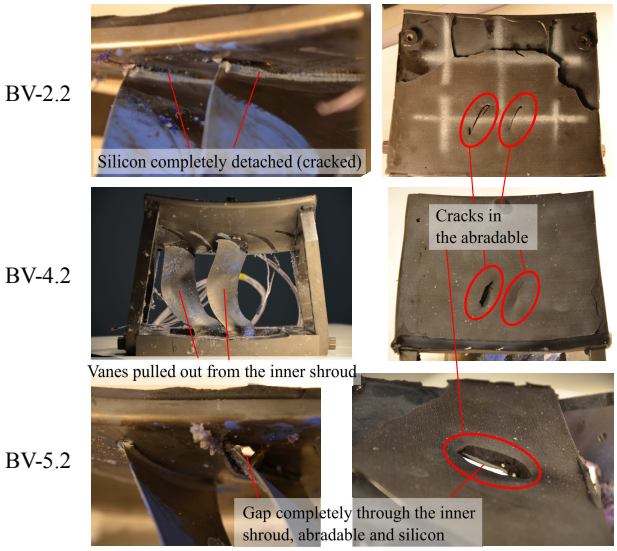

Figure 8.36: Configurations with severe damage.

8.6.2.3 Momentum

For each configuration, the mass of the CAD part is adapted to the average weight of the tests performed on that configuration. This is done by eliminating some of the abradable because this is the only part that does not correspond exactly to the CAD drawing. The influence on the inertia tensor of this operation however is limited (0.5-1%). The CAD drawing that was used to generate the inertia tensor for configuration 1 is shown in Figure 8.37a. The corresponding inertia tensor is shown in Table 8.37b.
The rotational momentum for the three axes of configuration 1, 4 and 6 is shown in Figure 8.38.
The momentum in configuration 6 is much lower than the other configurations because the impact angle almost coincides with the chord of the vane. Because the bird in the tests on configuration 4 impacted too low for one of

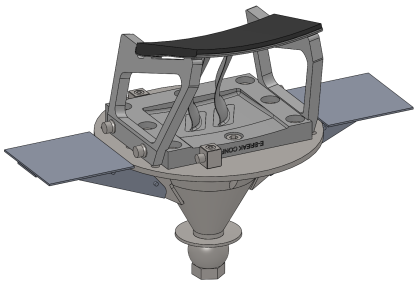

Inertia [$\mathbf{kg.m^2}$]	
I_{xx}	0.191973
I_{yy}	0.053891
I_{zz}	0.208212
I_{xy}	-0.00065
I_{yz}	0.008858
I_{xz}	5.55E-06

(a) Corresponding CAD drawing. **(b)** Actual data.

Figure 8.37: The inertia tensor of configuration 1.

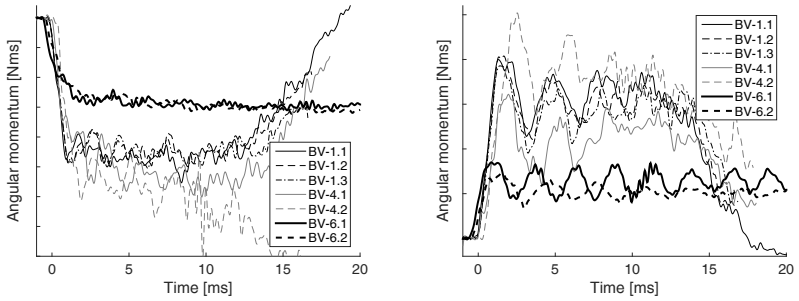

(a) Momentum x-axis. **(b)** Momentum z-axis.

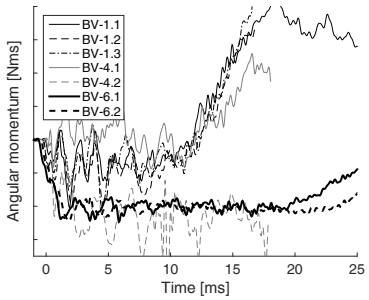

(c) Momentum y-axis.

Figure 8.38: Rotational momentum versus time for all the tests on configuration 1, 4 and 6.

the two tests, the momentum of this configuration is worse (less consistent). Additionally, one of the patterns detached during impact in test BV-4.2, which might explain the magnitude of the momentum around the x-axis that starts increasing between 7-15 ms. The momentum of configuration 1 on the

other hand shows quite consistent results for the three experiments. Even for the y-axis, the obtained momentum is very consistent for configuration 1 and 6. These momentum curves can be compared with the numerical model.

The momentum for configuration 2, 3 and 5 is shown in Figure 8.39. The order of magnitude is the same for the three configurations. But the momentum around the x-axis is slightly higher for both tests on configuration 5. The momentum around the z-axis shows much higher oscillations. The amplitude of these oscillations is not consistent between each pair of configurations, so it might be better to consider the momentum data of these three configurations as the spread that can occur for each of these configurations.

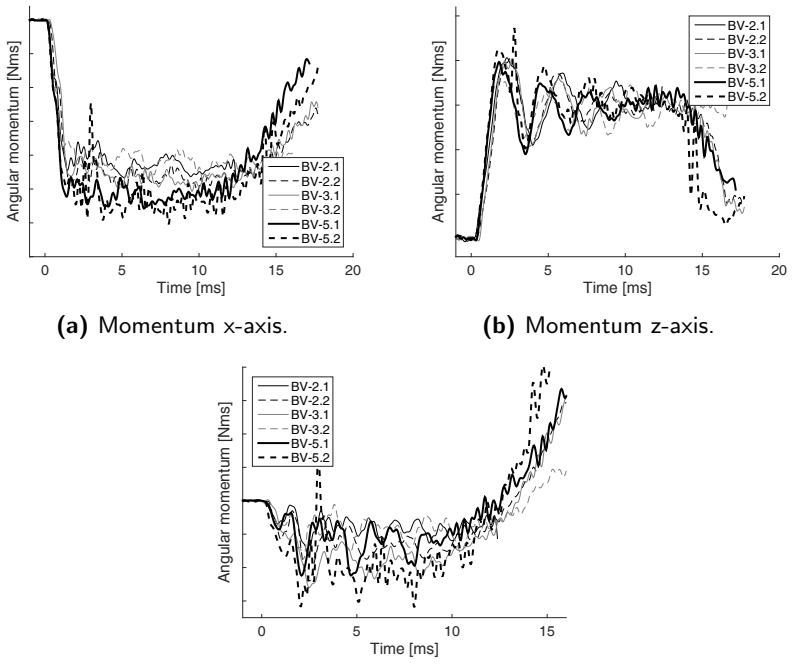

(a) Momentum x-axis.

(b) Momentum z-axis.

(c) Momentum y-axis.

Figure 8.39: Rotational momentum versus time for all the tests on configuration 2, 3 and 5.

8.6.2.4 Strain

In this section, several (unfiltered) strain gauge signals will be discussed. It is not possible to cover everything, therefore a selection is made to get an overview of the results.

Configuration 1 is extensively instrumented and will serve as a reference for the correlation with the numerical model. Figure 8.40 shows the strain signals of the four main strain gauges on the vanes for the three tests on configuration 1. Not all signals were recorded well. At impact, the bird is squeezed between the two vanes and has a high chance of disturbing the measurement on strain gauges KD1B11 and KD1B12. KD1B12 for example is only recorded well in test BV-1.3. It is important to always keep in mind that the deformation of cables can alter the measured resistance and therefore calculated strain.

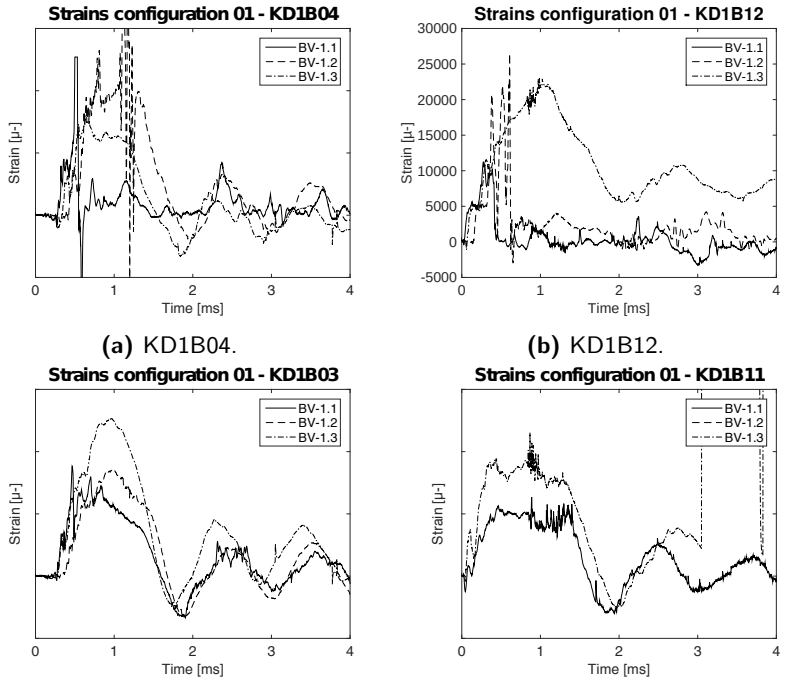

(a) KD1B04. **(b)** KD1B12.

(c) KD1B03. **(d)** KD1B11.

Figure 8.40: Four main strain gauge signals measured in the configuration 1 experiments.

The strain gauge signals of the reinforcements and the inner shroud will be introduced in the simulation section, where the correlation with the numerical model will be covered.

Figure 8.41 shows the strain signals on the vanes for configuration 2, 3 and 5. For some configurations the strains are clearly higher (KD1B04 for example with an order of magnitude double the one of the reference configuration 1).

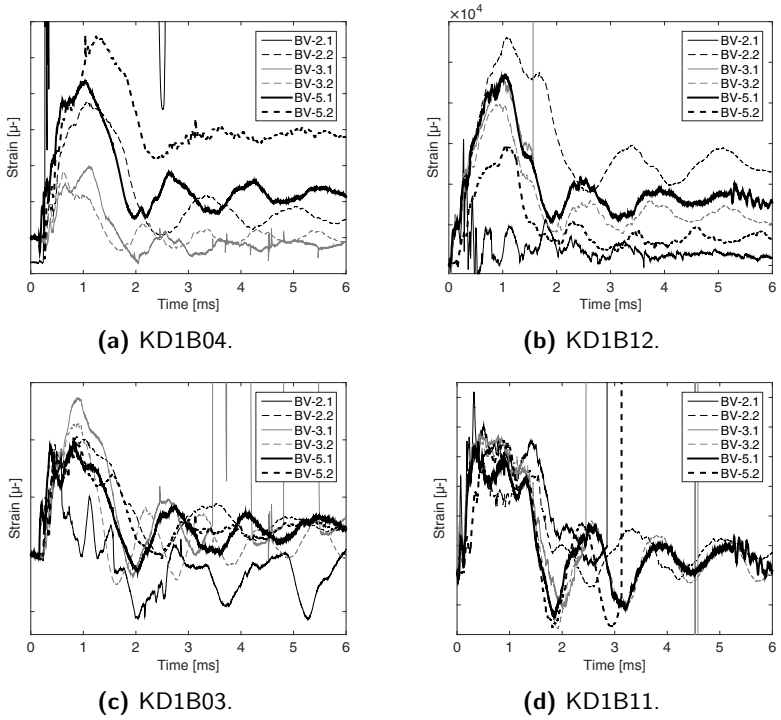

(a) KD1B04. **(b)** KD1B12.

(c) KD1B03. **(d)** KD1B11.

Figure 8.41: Four main strain gauge signals measured in the configuration 2, 3 and 5 experiments.

For configuration 6, the strains are, as expected, lower because of the impact angle which is very close to the incidence angle. Almost all the strain gauge signals for the bigger vanes (configuration 12) broke down before reaching a maximum. For the right vane, the signals were recorded well. Despite the higher velocity, the amplitude is still limited. The bigger vanes clearly show a higher bird strike robustness.

8.6.2.5 Residual energy

The residual energy in the impact direction ($E_{res,z}$) as well as an estimation of the total residual energy E_{res} based on the angle between the impact direction and the bird trajectory after impact is determined. The estimated angle is the mean of the angle derived (1) from high speed images and (2) from the disturbed chalk pattern on the rigid plate after impact. There was a lot of deviation on the calculated angles. Therefore, the results based on this angle should only be used for general observations. For the simulations, $E_{res,z}$ can/should be used.

For configuration 1 to 3, the total residual energy fluctuates around 49% approximately. A considerably higher residual energy is found for configuration 6 and 12. Configuration 6 has an impact angle close to the angle of attack of the vane, resulting in much less energy transfer to the vane and cone and dissipation in the bird. The chalk on the rigid plate for configuration 12 shows that the bird does not deviate a lot from its impact direction. The higher vanes tend to allow the bird to continue its trajectory much easier, resulting in a higher residual energy. For configuration 4, the impact on the plate is also quite central. Here, damage could have dissipated a lot of energy. The residual energy for the vanes with reduced stacking (configuration 5) is remarkably lower. This is an interesting observation which should be verified in the simulations.

8.7 Booster vane simulations

In this section, the development and the performance of the numerical model will be discussed. In section 8.7.1, the numerical model will be covered, focussing on the mesh convergence and the influence of the bird to vane mesh size ratio. After that, the overall behaviour, momentum, strains and residual energy of several simulations with configuration 1 and 6 will be investigated in section 8.7.2.

8.7.1 Development of the numerical model

8.7.1.1 Convergence of the vane mesh

Solid elements are used for the booster vanes, to ensure correct 3D stress states at the root and at the location where the vanes interact with the inner shroud. This is computationally still feasible because the in-plane dimensions relative to the thickness are considerably lower than the fan blade discussed in literature.

The stable time increment is linearly related to the smallest characteristic length of all the deformable elements in the simulation. In order to keep this as high as possible, the performance of different mesh sizes (in-plane and through the thickness) is investigated. The critical part in the whole assembly are the vanes. Multiple elements are needed through the thickness of the vane to correctly simulate the bending and torsion behaviour, which results in elements with a thickness several times lower than the thickness of the vanes, being roughly 1.5 mm.

The influence of the mesh size is investigated with a rectangular flat plate with similar dimensions as the vane (a length and a width of respectively 100 mm and 30 mm and a thickness of 1.5 mm). In the booster vane simulations, it was observed that full integration elements are necessary to limit the artificial strain energy dissipation so also in this preliminary study, full integration elements are used. Multiple meshes are considered, with different elements through the thickness and different in-plane mesh sizes. For each simulation, the error on the obtained strain, relative to the theoretical result (if any) or a fine shell mesh is defined. Bending, torsion and frequency analyses are done. Additionally, it is investigated how the strain on the surface of the vane can be measured correctly. From this exercise, it can be concluded that 3 elements through the thickness with a sufficiently fine in-plane mesh size suffices. The torsional Eigen frequencies specifically require a fine in-plane mesh size of down to 0.5 mm. The strain at the surface sampled at the nodes on the surface of the mesh is not accurate at all. Therefore, strain gauges are modelled with dummy shell elements (with a negligible thickness and stiffness). The strains measured in these elements proves to be an extrapolation of the strains measured at the integration

points.

The mesh convergence of the vane geometry was investigated with a frequency analysis as well, with Eigen frequencies up to 2 kHz. This approach showed that for a fine mesh, the frequency for the first five unique modes (Figure 8.42) converge within 5% for a fully integrated mesh with 3 elements through the thickness and an in-plane mesh size of 0.5 mm.

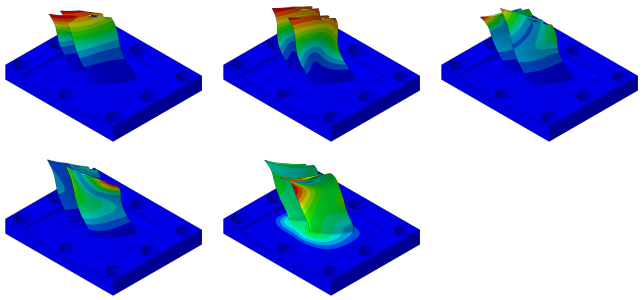

Figure 8.42: First five unique Eigen frequency modes booster vane mesh.

A similar convergence study was done for the inner shroud and the reinforcements. For the converged meshes, for each strain gauge, the element closest to the centre of the strain gauge in the experiment is used to create a shell element strain gauge with the measurement direction aligned with the edge of the element, which is quite accurate because the mesh direction is aligned with the leading edge, the inner shroud, etc.

8.7.1.2 Influence of the bird to vane mesh size ratio

The bird to vane mesh size ratio can have a significant influence on the simulation (disregarding convergence). Two phenomena occurred in the simulations, both at element level:

1. Unrealistic discrete plastic strains on the vanes.
2. Unrealistic discrete deformations at the leading edge of the vane.

The first phenomenon is the result of the way the contact is enforced. For particles with a relatively large mass (even for a 2 mm mesh), high stresses are induced by the penalty contact definition. The stresses in the vane

exceed the yield strength and result in very local plastic strains. The effect is similar to shot peening. Luckily, this does not deteriorate the stiffness of the vane, because the event only occurs during a couple of increments. The only disadvantage of this phenomenon is the dissipation of energy. For the $0.5 \times 0.5\text{mm}^2$ in-plane mesh in the configuration 1 simulation for example, for a 1.5 mm bird mesh, roughly 70 J is dissipated in plastic strain energy, good for 4% of the total energy. Several simplified simulations showed that at least half of this plastic dissipation can be the result of such discrete plastic strains (apart from the global plastic strains). This will be translated partly in a decreased residual energy of the bird.

The second phenomenon is more problematic. For a too high bird to vane mesh size ratio, the leading edge distorts drastically, which results in more material that hits the vane, which makes the deformation become worse, and so on (it could be an unstable situation). Figure 8.43 shows this phenomenon for a 2 mm bird mesh and the 0.5 mm vane mesh. A distorted leading edge can be observed. For higher mesh size ratios, the distortion is much worse.

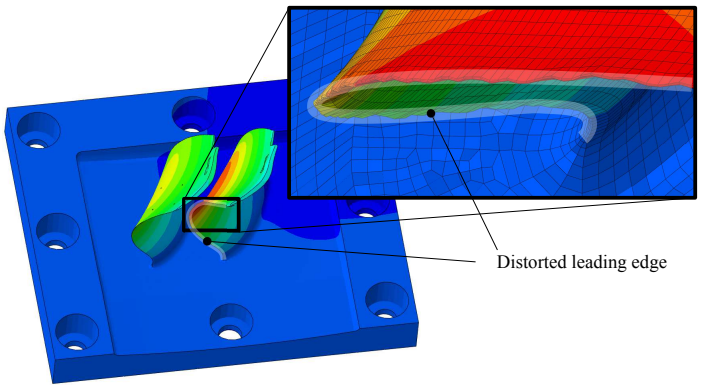

Figure 8.43: Distorted leading edge for a $2\,\text{mm}$ bird mesh impacting a $0.5\,\text{mm}$ vane mesh (at the end of the simulation).

8.7.1.3 The booster vane model

The final model is shown in Figure 8.44, showing a configuration with and without abradable. All the meshes are provided by Safran Aero Boosters as they have a lot of experience in meshing vane geometries.

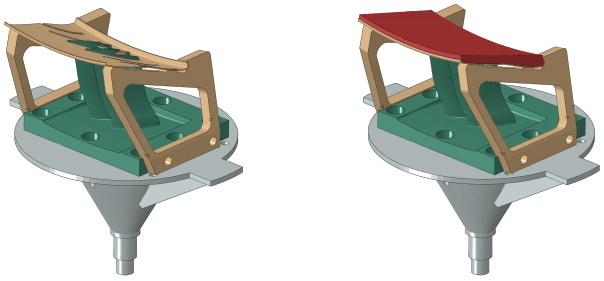

(a) Without abradable. **(b)** With abradable.

Figure 8.44: Vane model without and with abradable.

Modelling the abradable is important for three reasons:

- It contributes to the inertia and stiffness of the inner shroud and therefore should improve the correlation of the strain signals on this part.
- The deformation of the retaining plate will also be more realistic, because in the experiment the abradable between the retaining plate and the inner shroud results in a characteristic bending deformation of the retaining plate when the vanes are pulled down due to the bird impact.
- The retaining plate proved to be the weakest link in the design. So in order to predict the failure of the entire assembly, modelling the deformation and dynamics of the retaining plate is very important.

Modelling the abradable is not straightforward. The abradable is a rubber-like material which experiences large deformations during impact. These large deformations make it difficult to maintain a computationally realistic stable time increment throughout the simulation. On top of that, the abradable generally tears close to the vane. In the simulation, the abradable is modelled with a hyperelastic Mooney-Rivlin law with $C_{10} = 0.474\,\mathrm{MPa}$, $C_{01} = 0.118\,\mathrm{MPa}$ and $D_1 = 0.02\,\mathrm{MPa}^{-1}$, based on the shore hardness of the abradable. The entire volume including the silicon and the abradable is modelled with this material law because there is no information about the geometry of the silicon. Because of the complex geometry, this part is meshed with tetrahedral elements. The performance of a model without

abradable is investigated as well.

The cone (grey in Figure 8.44) is identical to the one of the steel vane simulations (see section 8.5.2). The vane (green) is tied to the flange of the cone close to the locations of the bolts. The reinforcements (brown) are tied to the vane chassis and the inner shroud over the entire contacting surface. A Johnson Cook strain hardening and strain rate model from (Lesuer, 2000) is used for both the vanes (including the chassis that connects the vane fixture with the cone) and the inner shroud (see Table 8.7). Including a damage model would require a much finer bird mesh to avoid very high mesh distortions at the leading edge. For the simulation with the abradable (red), the abradable is tied to the inner shroud over the entire contacting surface. An elastic model is assigned to the retaining plate in the simulations without abradable (the deformation of the retaining plate would not be realistic anyway). In the simulations with abradable, an elastic-plastic material law is used.

Table 8.7: Parameters for the Johnson Cook material model for Ti-6Al-4V (Lesuer, 2000).

A [MPa]	**B** [MPa]	**n** [-]	**C** [-]
1098	1092	0.93	0.014

An attempt was made to obtain numerical Eigen frequencies. A huge amount of Eigen frequencies however were obtained (mostly deformations of the inner shroud and the abradable). Because it is impossible to determine the dominant Eigen modes from this analysis, a comparison with the experiments is not made.

Apart from the plastic strain energy dissipation of the titanium and the retaining plate, there is no physical mechanism that dissipates energy. The correlation of the residual energy therefore will again tell something about the underestimation of the dissipation in the numerical model. The residual energy in the simulation is computed from the velocity vectors of the SPH particles.

8.7.2 Results

This section contains the results of the numerical simulations on the booster vane model. The results on configuration 1 and 6 will be covered. For each configuration, the impact conditions of the performed tests are averaged to obtain the input conditions for the numerical simulation.

8.7.2.1 Configuration 1

Simulation with abradable

An overview of the impact from the left side is shown in Figure 8.45. Red contours are drawn on the leading and trailing edge of the left vane. It can be observed that the global deformation is captured correctly. The yellow line in the image from the experiment at 0.9 ms is a contour of the back of the bird, which is hardly visible on the recorded images. The behaviour of the bird also corresponds quite well. In the image from the experiment at 1.8 ms however, some gelatine can be observed at the back of the vane which is not visible in the simulation.
The momentum obtained from the cone is compared to the experiments in Figure 8.46. To improve the visibility of the graph, a cut off filter of 5 kHz is applied to the experimental curves and a cut-off frequency of 10 kHz to the numerical ones (the noise in the experiments and the simulations is quite different, therefore different cut-off frequencies are chosen).

The momentum is quite well captured by the model. There is a small overestimation and underestimation respectively of the momentum about the z-axis and the x-axis. The momentum about the y-axis is also overpredicted. The kinetic energy of the entire fixture calculated from the cone displacement in the experiment and the simulation is shown in Figure 8.47 (this is not equal to the actual kinetic energy because it assumes a constant inertia tensor). The maximum kinetic energy is captured quite well, but the slope of the curve is slightly steeper in the simulation before 1 ms and decreases more quickly than the experiment after 1 ms.
A comparison of the four strains KD1B03, KD1B04, KD1B11 and KD1B12, from the experiments with the simulations is shown in Figure 8.48. Except for KD1B12, a very good correlation is obtained for these four strain gauges.

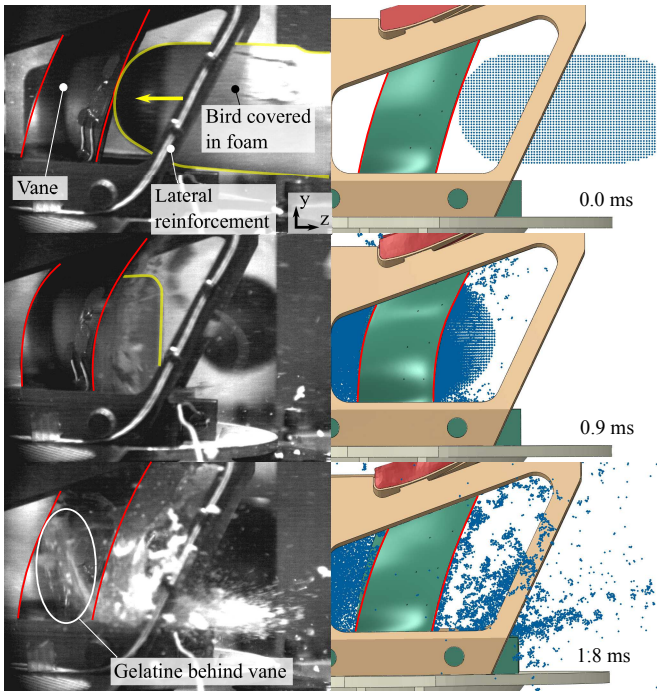

Figure 8.45: Comparison between the images of test BV-1.1 and the simulation (yellow contours for the bird and red contours for the left vane).

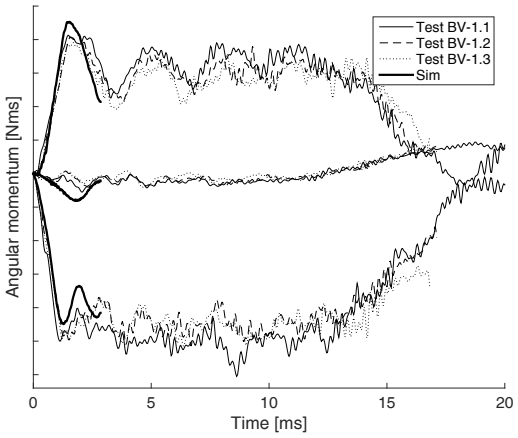

Figure 8.46: Momentum configuration 1 simulation with abradable.

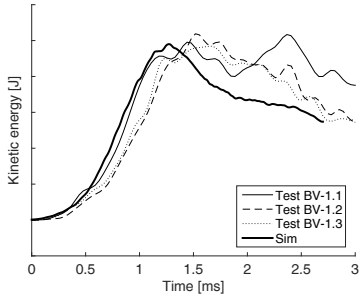

Figure 8.47: Kinetic energy cone configuration 1 simulation with abradable.

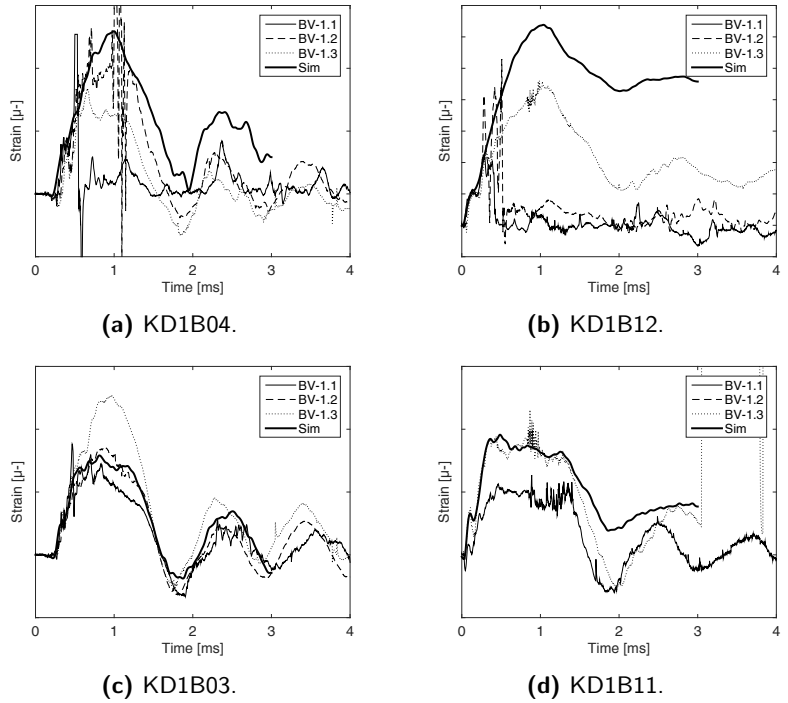

(a) KD1B04.

(b) KD1B12.

(c) KD1B03.

(d) KD1B11.

Figure 8.48: Correlation main strain gauges on the vane KD1B03, KD1B04, KD1B11 and KD1B12 in the experiments on configuration 1 with the simulation including the abradable.

The correlation of the strain gauges of components further away from the vane is worse. This is shown for the first four strain gauges on the inner shroud and for the first four strain gauges on the reinforcements in Figure

C.1 and Figure C.2 respectively in appendix C. All the reinforcements are loaded in tension first as expected. The strains in the simulation however give an indication that the reaction of the fixture is too stiff (the frequency of the strain gauge signals is too high), which could also be observed in Figure 8.46, where the momentum about the z-axis in the simulations starts decreasing sooner than in the experiments. This might be the result of a too stiff abradable or even more likely, the absence of damage of the silicon and the abradable. The sign of the strain for strain gauge KD1B25 is the opposite in the simulation (also for KD1B26 and KD1B27). These are strain gauges at the back of the inner shroud (see Figure 8.32) and will likely be the result of the release of an unstable buckling state which is predicted wrong in the simulation.

Four additional simulations are performed with offsets of 4 mm in four directions: the negative and positive, horizontal and vertical direction. Figure 8.49 shows the momentum and kinetic energy over time for the horizontal offsets, because these prove to have the biggest influence on the results.

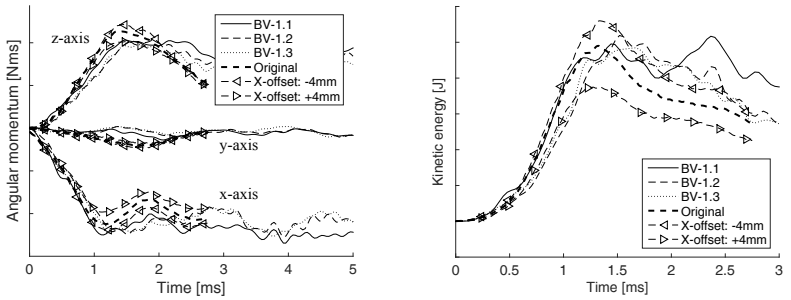

(a) Momentum. **(b)** Kinetic energy.

Figure 8.49: Influence of a 4 mm offset on the impact location in the negative and positive horizontal direction on the transferred momentum and kinetic energy of the cone.

The impact location has a big impact on the transferred momentum and energy. This again shows how important it is to achieve a good or at least well-known shape of the bird and to determine the impact location as accurate as possible. In contrast with the steel vane simulations, a horizontal offset does have a considerable influence on the momentum about the x-axis

as well (see also Figure 8.26).

Except for a large influence on strain gauge KD1B04, the influence on the strain signals of the vane is much less (Figure 8.50). For the strain signals on the IS and the reinforcements, small changes in amplitudes can be observed as well (these strain signals are not included). As can be observed in Figure 8.49 and 8.50, the offset mainly has an influence on the amplitude and not so much on the frequencies in the signal.

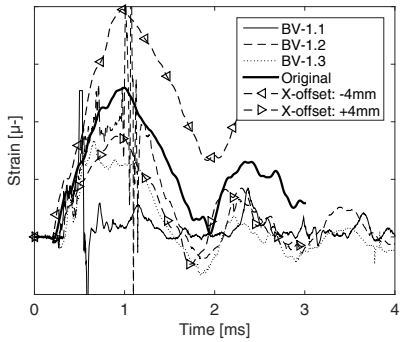

Figure 8.50: Influence of a $4\,\mathrm{mm}$ offset of in the negative and positive horizontal direction on strain signal KD1B04.

The deformation of the retaining plate is shown for four time frames in Figure 8.51 (only the material beneath the retaining plate is shown). The deformation at 0.6 ms corresponds very well with the experiments. The high bending deformation close to the right vane for example is also observed in the experiments. But, in the end, the vanes pull the retaining plate through the inner shroud. The following aspects are missing in the model to accurately simulate the retaining plate behaviour:

- The stiffer grey silicon material which encapsulates the vanes in the experiment for example is not modelled (see also section 8.7.1.3). The complete constitutive behaviour of this material would have to be characterized.

- The material model and its related parameters of the black abradable are an estimation. Damage is also not modelled in the abradable.

- There is no information about the contact conditions between the abradable and the metallic parts.

Adding the abradable increases the accuracy of the model, but it is not sufficient. In fact, except for the abradable beneath the retaining plate, there is nothing keeping the vanes and the retaining plate from being pulled down.

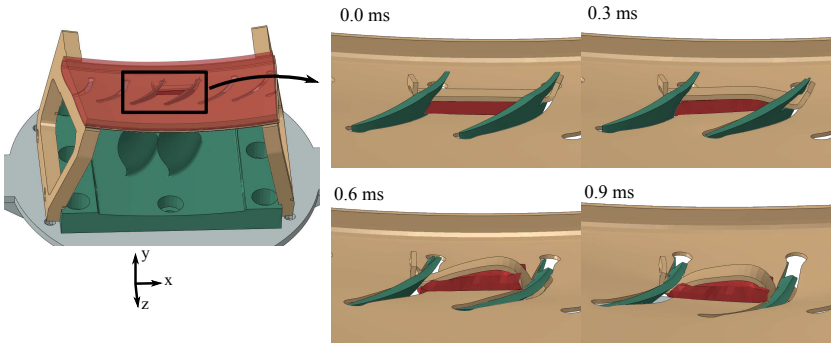

Figure 8.51: Deforming retaining plate (only the abradable beneath the retaining plate is shown).

The residual energy is determined for all the particles with a negative z-coordinate or also, for each particle behind the rotation centre of the cone with respect to the impact direction. This is done to exclude the particles flying in the opposite direction.

The residual energy in the impact direction of this selection of SPH particles at the last frame (at 3 ms after impact) is 62.1%. Compared to the residual energy of 40.7% in the experiments, this is quite an overestimation. The correlation is much worse compared to the steel vane experiments and simulations. The missing damage mechanisms in the abradable definitely will be one reason for this underestimation. Possibly, the bird also dissipates more energy in this situation.

It is interesting to note that throughout the entire simulation, the total energy mainly originates from the kinetic energy of the bird. At 1 ms, still 84% of the total energy is kinetic energy, from which the movement of the cone and the booster vane fixture is only a very small part (the kinetic energy in Figure 8.47 is 1.62% of the total energy). The next dominant energy

levels are respectively the artificial dissipation (7%), the plastic dissipation (5%) and the strain energy (3%).

Simulation without abradable

This section will briefly cover a simulation without abradable. This simulation is performed with a bird mesh size of 2 mm. The material model for the retaining plate is also purely elastic. Compared to the simulation with abradable, the momentum is slightly higher for the three axes (Figure 8.52). The momentum about the x-axis therefore correlates better, but the momentum about the z-axis is overestimated, resulting in an overestimation of the kinetic energy, contrary to the simulation with abradable.

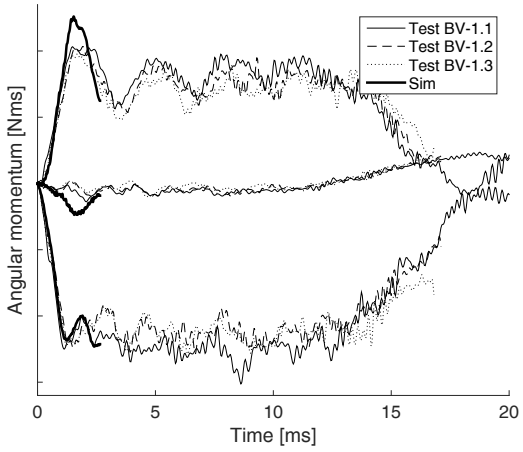

Figure 8.52: Momentum configuration 1 simulation without abradable.

The strains in the IS do not improve or get worse. The strains on the reinforcements get higher and therefore make the correlation worse. The strains on the vane also get slightly higher. Figure 8.53 shows the comparison of strain KD1B11 for the simulation with and without abradable.

The residual energy in the impact direction decreases slightly to 59.9%.

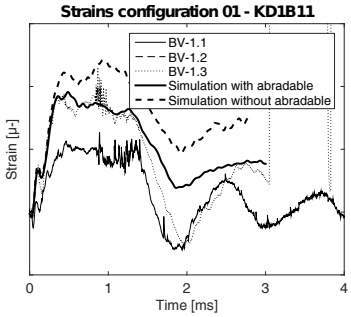

Figure 8.53: Strain KD1B11 simulation without abradable.

8.7.2.2 Configuration 6

Similar to the simulation of configuration 1 with abradable, a simulation is performed using the mean input conditions of configuration 6, with a 1.5 mm mesh for the bird. A comparison of the deformed bird roughly 1.5 ms after impact is shown in Figure 8.54. Three separate mass flows can be observed clearly for the experiment and simulation (a contour is drawn for the experiment). Similar mass flows can be observed in the simulation.

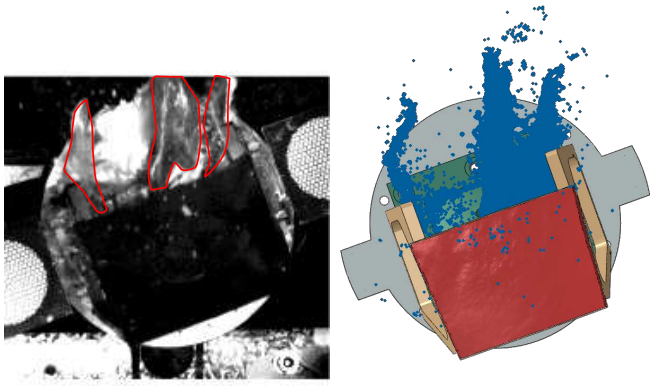

Figure 8.54: Comparison test BV-6.1 with simulation roughly 1.5 ms after impact (including abradable).

The momentum however is not captured very well in the simulation. Figure 8.55 compares the momentum from the simulation with the momentum from the two experiments.

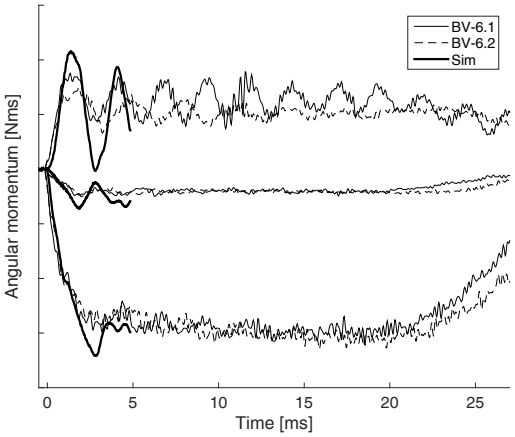

Figure 8.55: Transferred momentum in the simulation of configuration 6 (including abradable).

The amplitude is much larger for the simulation. The overestimation in momentum can also be observed in the kinetic energy of the fixture (Figure 8.56). In the simulations on the splitter, a very high mesh dependency could be observed as well. A significant refinement of the mesh size down to 1.0 mm improves the result. Further refining the mesh probably further improves the correlation. However, simulating a time interval of 2 ms with 1 CPU already takes up to one month of simulating time.

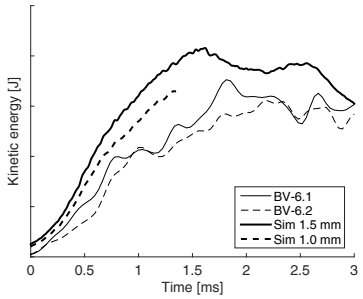

Figure 8.56: Kinetic energy of the cone in the simulation of configuration 6 with a 1.5 mm and 1.0 mm bird mesh (including abradable).

For each of the four strain gauges, the strain is also overestimated (Figure 8.57). The mesh refinement greatly improves the result. The plastic strain

in the simulation also reduces for a finer bird mesh (the strain that does not oscillate around zero after impact), which corresponds better with the experiments.

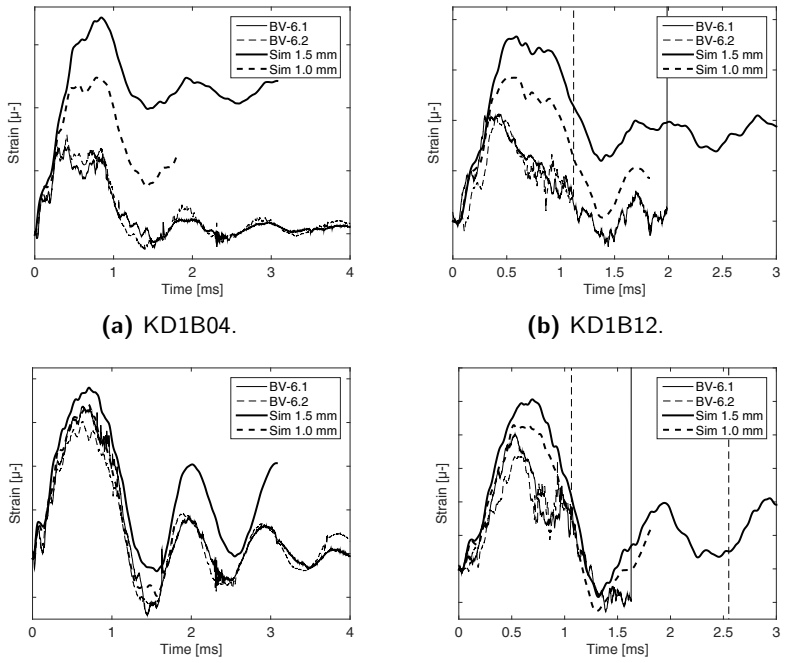

(a) KD1B04. **(b)** KD1B12.

(c) KD1B03. **(d)** KD1B11.

Figure 8.57: Correlation of the four strain gauges on the vane KD1B03, KD1B04, KD1B11 and KD1B12 in the experiments on configuration 6 with the simulation (including abradable).

The residual energy in the direction of impact is 69.7% in the numerical model, compared to 77.6% in total in the experiment. The correlation is better in this case. Decreasing the bird mesh size likely will increase the residual energy.

8.8 Conclusion

In this chapter, first a method is developed to measure the multi-axial impact momentum during impact on a vane. After considering and testing multiple concepts, the concept to use 3 rotational DOFs from (Steinhagen

and Salemme, 1973; Premont and Stubenrauch, 1974) is chosen. The final concept consists of a stiff cone structure. When a vane fixture mounted on this cone is impacted by a bird, the entire structure starts to rotate, from which the rotational momentum about three axes is obtained. Contrary to the work of (Steinhagen and Salemme, 1973; Premont and Stubenrauch, 1974), the rotational speeds are derived from an optical measurement. The developed technique comprises one of the implementations of the 2D line pattern technique from chapter 3, the calibration of the camera and the transformation of the obtained displacement data. The error on the momentum obtained from the optical measurement has been quantified with DIC measurements in static and dynamic experiments. The error on the obtained momentum showed to be less than 5%.

The dynamic experiments to quantify the error consisted of bird impact tests on a simplified steel vane, with multiple initial rotations of the cone set-up. The corresponding simulations correlate very well in terms of momentum and strain. The residual energy in the impact direction on the other hand is slightly underpredicted, which can be the result of an overestimated bird deviation angle in the simulations.

A parametric study on the booster vanes is performed, where the influence of stacking and the radius of the vanes, the impact speed and angle of the bird and the size of the vanes is investigated. Different damage types can be observed after the tests. Starting from small cracks or a pull out movement of the grey silicon up to cracks in the black abradable and vanes entirely pulled out from the inner shroud. For the tests at higher speed, the retaining plate failed to keep the vanes from pulling out from the inner shroud. The momentum is quite consistent, even for the different test parameters (except for the impact speed and angle variation). It therefore might be better consider the momentum data as the spread that can occur for each of these configurations. The total residual energy is mostly around 50%. A slightly higher residual energy is obtained for configuration 6 and 12. For both configurations, the bird is allowed to continue its trajectory much easier. The test campaign generated very valuable data for the validation of numerical models. It is important to keep in mind that only a section of the booster is tested. Therefore the results of the weak link in the assembly may not

directly be extrapolated to a full booster.

The performance of the numerical model is investigated using global (momentum transfer, bird mass flows and residual energy) and local (strain measurement) parameters and compared to the obtained experimental data. The global and local behaviour of the bird and the vane is captured quite well by the model for configuration 1, and less good for configuration 6.

For configuration 1, the momentum and the strains on the vane correlate well with the experiments. The implementation of the abradable results in more realistic deformation of the retaining plate. An offset of 4 mm has a tremendous influence on the achieved momentum and kinetic energy. This again shows that the impact location is of utmost importance to achieve good results in the simulations. For configuration 6, the mass flow of the bird is realistic compared to the experiments, but the momentum transfer is overestimated. A mesh refinement can improve this result in the future.

In future research, following attempts can be made to improve the correlation:

- The abradable material model (black and grey abradable) and the interaction with the retaining plate, vane and inner shroud can be characterized.
- The bird mesh size can be decreased drastically for impact angles closely aligned with the chord of the vanes, beyond the current computational limits.
- The material model of the bird can be improved. Dissipation inside the bird and deviatoric stiffness is missing to improve the correlation.

8.9 Bibliography

Argon: Measuring solutions (2016), `http://www.argon-ms.com/`. [Online; accessed 1-August-2016].

Bertke, R. S. and Barber, J. P. (1979), Impact damage on titanium leading edges from small soft body impacts, Technical Report AFML-TR-79-4019, University of Dayton Research institute.

Boehman, L. and Challita, A. (1982), A model for predicting bird and ice impact loads, Technical Report AFWAL-TR-82-2046, University of Dayton Research Institute.

Castelletti, L. and Anghileri, M. (2008), Birdstrike onto structures in rotational motion, *in* 'Proceedings of the 26th ICAS congress', pp. 1–11.

Chevrolet, D., Audic, S. and Bonini, J. (2002), 'Bird impact analysis on a bladed disk', *RTO-MP-089* .

Chuan, Z., Xiang-hua, J., Xiang-hai, C. and Tong-cheng, S. (2015), 'TC4 hollow fan blade structural optimization based on bird-strike analysis', *Procedia Engineering* **99**, 1385 – 1394.

Friedrich, L. (1974), Impact resistance of hybrid composite fan blade materials, Technical report, Pratt & Whitney Aircraft Division of United Aircraft Corporation.

Graff, J., Stolze, L. and Varholak, E. (1973), Impact resistance of spar-shell composite fan blades, Technical Report NASA CR-134521, Hamilton Standard.

Graff, J., Stolze, L. and Varholak, E. (1976), Fiber composite fan blade impact improvement, Technical Report NASA CR-135001, Hamilton Standard Division.

Hirschbein, M. S. (1982), Bird impact analysis package for turbine engine fan blades, Technical Report Nasa-TM-82831, NASA, Lewis Research Center.

Jain, R. and Ramachandra, K. (2003), 'Bird impact analysis of pre-stressed fan blades using explicit finite element code', *Proceedings of the International Gas Turbine Congress* .

Johns, R. (1974), 'FOD impact testing of composite fan blades', *19th National SAMPE Symposium and Exhibition* .

Kim, M., Zammit, A., Siddens, A. and Bayandor, J. (2011), 'An extensive crashworthiness methodology for advanced propulsion systems, part I: Soft impact damage assessment of composite fan stage assemblies', *49th*

AIAA Aerospace Sciences Meeting including the New Horizons Forum and Aerospace Exposition .

Lesuer, D. R. (2000), Experimental investigations of material models for Ti-6Al-4V titanium and 2024-T3 aluminium, Technical Report DOT/FAA/AR-00/25, Federal Aviation Administration.

Liu, J. and Li, Y. (2013), 'Numerical simulation of a rotary engine primary compressor impacted by bird', *Chinese Journal of Aeronautics* **26**(4), 926 – 934.

Mao, R. H., Meguid, S. A. and Ng, T. Y. (2008), 'Transient three dimensional finite element analysis of a bird striking a fan blade', *International Journal of Mechanics and Materials in Design* **4**(1), 79–96.

Meguid, S., Mao, R. and Ng, T. (2008), 'FE analysis of geometry effects of an artificial bird striking an aeroengine fan blade', *International Journal of Impact Engineering* **35**(6), 487 – 498.

Orlowski, M. (2015), Experimental and Numerical Investigation on the Bird Impact Resistance of Novel Composite Sandwich Panels, PhD thesis, Cranfield University.

Premont, E. and Stubenrauch, K. (1974), Impact resistance of composite fan blades, Technical Report NASA CR-134707, Aircraft Engine Group, General Electric Co.

Ryabov, A. A., Romanov, V. I. and Kukanov, S. S. (2007), 'Fan blade bird strike analysis using lagrangian, SPH and ALE approaches', *6th European LS-DYNA Users Conference* .

Selezneva, M., Stone, P., Moffat, T., Behdinan, K. and Poon, C. (2012), 'Modeling bird impact on a rotating fan: The influence of bird parameters', *11th European LS-DYNA Users Conference* .

Shepherd, C. J., Appleby-Thomas, G. J., Hazell, P. J. and Allsop, D. F. (2009), 'The dynamic behaviour of ballistic gelatin', *AIP Conference Proceedings* **1195**(1), 1399–1402.

Shmotin, Y., Chupin, P., Gabov, C., Ryabov, A., Romanov, V. and Kukanov, S. (2009), 'Bird strike analysis of aircraft engine fan', *7th European LS-DYNA Users Conference* .

Siddens, A. and Bayandor, J. (2013), 'Multidisciplinary impact damage prognosis methodology for hybrid structural propulsion systems', *Computers & Structures* **122**, 178 – 191. Computational Fluid and Solid Mechanics

2013, Proceedings Seventh MIT Conference on Computational Fluid and Solid Mechanics.

Siddens, A., Bayandor, J. and Celestina, M. L. (2014), Detailed post-soft impact progressive damage assessment for hybrid structure jet engines, Technical Report NASA/TM-2014-218397, NASA Glenn Research Cente.

Sinha, S. K. and Turner, K. E. (2011), 'Dynamic loading on turbofan blades due to bird-strike', *Journal of Engineering for Gas Turbine and Power* **133**, 1017–1031.

Steinhagen, C. and Salemme, C. (1973), The impact resistance of current design composite fan blades tested under short haul operating conditions, Technical report, General Electric Company.

Vasko, T. J. (2000), 'Fan blade bird-strike analysis and desgin', *6th International LS-DYNA Users Conference* .

Vignjevic, R., Orlowski, M., De Vuyst, T. and Campbell, J. C. (2013), 'A parametric study of bird strike on engine blades', *International Journal of Impact Engineering* **60**, 44–57.

Zammit, A., Kim, M. and Bayandor, J. (2010), Bird-strike damage tolerance analysis of composite turbofan engines, *in* 'Proceedings of the 27th ICAS congress', pp. 1–17.

CHAPTER 9

Conclusion and future work

Abstract: This final chapter will take a step back to elaborate on the results that were achieved, how these results answer the initial objectives stated in the introduction and how it contributes to the state-of-the-art of the current bird strike research. Finally some suggestions for future work will be given as well.

9.1 Conclusion

The ultimate goal of this PhD is to perform a parametric study on the booster vane subjected to bird strike and to develop a numerical model capable of predicting the damage caused by bird strike.

To assure that qualitative information is achieved from the parametric study and to understand the behaviour of the model in the simulations, these goals are extended to three main research topics:

- **Understanding the behaviour of the bird:** A better understanding of the bird impact phenomenon is obtained. This required the consideration of multiple (simplified) impact conditions and situations which tells something about the requirements of the numerical aspects, the importance of certain impact regimes and eventually the performance of the numerical model. The majority of the PhD focusses on this topic (chapter 4 to 7).
- **Development of the set-up to test booster vanes:** The experimental tests on multiple booster vane configurations are expensive and require a qualitative and extensively tested and validated test set-up to obtain valuable data for the numerical simulations. Different concepts are considered and the optimal use of the available equipment is assured. This is discussed in the first part of chapter 8.
- **Parametric study on the booster vanes and validation of the numerical model:** The parametric test campaign is executed and the obtained results are analysed. The performance of the numerical model is investigated by comparing the results with the data from the experiments. This is discussed in the second part of chapter 8.

The results in these three research domains required extensive experimental testing. To derive useful information from the performed experiments, two optical techniques were improved (chapter 3): a 3D shape map technique and a 2D line pattern technique. In the 3D shape measurement technique, a stereo vision technique is developed that is able to calculate 3D shape maps from specimens containing a line pattern. The main focus was to enhance the images to some extent, when excessive blurring occurs. A 2D line pattern

technique developed at the department is further enhanced to extract more data from the refined Fourier transform and improve the accuracy of the method in certain conditions. Some of these techniques were essential to obtain the necessary data from the experiments.

Together with the experimental set-up, these optical techniques lead to several contributions to the bird strike research. In the subsequent sections below, the results will be discussed according to the three main research topics.

9.1.1 Understanding the behaviour of the bird

This first part of the research elaborated on the pressures exerted during bird strike, characterized by the shock and steady state regime (chapter 4), the impact on rigid targets (chapter 5 and 6) and the impact on deformable targets (chapter 7).

The impact of a bird on a structure can, in the first place, be characterized by the pressure exerted on that structure. The first step towards bird strike modelling is therefore often the investigation of these impact pressures. The shock and steady state regime and the regime in between is considered and compared to the analytical models that are extensively described in the work of (Wilbeck, 1978*a*,*b*; Wilbeck and Rand, 1981). In this dissertation, numerical simulations are performed using SPH to model the bird and the results of several experimental impact pressure measurements are covered.

The main part focussed on the shock regime. Firstly, specific conditions are created to zoom in at the short shock pressure pulse by using very fine flat cylinder meshes and deliberately decreased time increments. This showed that the pressure pulse amplitude and duration corresponds very well with the analytical model from literature. Secondly, it is shown that depending on the front surface of the bird, pressures above the analytical pressure can be reached. Slightly tilting a flat cylinder mesh can lead up to 190% of the analytical pressure, in contrast to the model of Wilbeck. The increase above the analytical pressure is also observed in one experimental pressure measurement. For hemispherical ended projectiles, a pressure equal to the

flat ended projectiles is measured, as predicted by the theory. Thirdly, the elastic energy as a measure for the shock regime is introduced. An analytical model is developed for flat ended projectiles and compared to the simulations. The shape of the curve predicted by the analytical model is comparable, but the amplitude is underestimated (mainly due to the simplified representation of the release waves). The elastic energy is compared between hemispherical and flat ended projectiles, which showed that the presence of the shock regime for hemispherical ended projectiles is negligible. For the simulation on the booster vanes, the shock regime therefore does not have to be taken into account. Lastly, the influence of the mass and deformability of the target is investigated. It can be concluded that only for very low masses or thin plates, the shock regime starts to decrease significantly and that local failure indeed can occur during the shock regime.

During the transition to the steady state regime, a tensile wave is formed close to the target. As a result, the mesh bounces back from the target in the simulation, as there is no vacuum that keeps the mesh from doing so. In the pressure signal, this translates to a short decrease to zero pressure, which is occasionally also observed in the experiments. Also in literature, this phenomenon can be observed in the numerical pressure signals. Both in the experiments (for porous and non-porous gelatine substitute birds as well as for pigeons) and the simulations, the steady state pressure corresponds well with the analytical model. This first fundamental case study gave insight about the importance of the impact regimes and gave a first idea about the performance of the numerical model.

Next, the impact of a bird is studied in a broader sense using three rigid targets: a plate, a wedge and a splitter. The idea is that a combination of the effects seen in these rigid target experiments (change of momentum direction, friction, splitting) are also present in the experiments on the booster vanes. Substitute birds with different mixing ratios (1:4, 1:6 and 1:9) and ducks are tested and compared. In this study, the momentum transferred to these structures is used as the measure for the force. A 1:9 MR bird proved to perform too liquid, while a 1:4 and 1:6 MR bird often disintegrated into several big lumps. But in general, these experiments showed that the impactor material has a negligible influence in terms of momentum transfer.

For the plate, wedge and splitter experiments, the momentum transfer is respectively 100%, 50-60% and 2-6%. The main difference between gelatine and real birds was found for the splitter, where the real bird material is more likely to get stuck on the splitter and increases the momentum transfer (and therefore also force) by a large extent, as a result of its high kinetic energy.

Analytical models are developed based on the momentum balance. For wedge-like structures specifically (valid for the wedge but also for the splitter), a new formulation for the momentum transfer is developed. The fundamental difference with a flat plate or a rotated plate is that the momentum transfer depends on the momentum of the bird after impact, which means that the constitutive behaviour of the bird has much more influence on the momentum transfer. The wedge therefore comes forward as a tool to assess the behaviour of substitute birds and the performance of a material model. The current state-of-the-art material model which only includes hydrostatic stiffness underestimates the momentum transfer (37% in the simulations instead of 50-60% in the experiments). The momentum is also transferred over a much shorter time. Most likely, deviatoric and/or dissipating constitutive behaviour is missing to increase the elasticity of the bird and decrease the velocity of the bird after impact.

Simulations on the plate target also showed that the artificial viscosity by default dissipates too much energy, leading to an underestimation of the momentum transfer. For the splitter, a very high dependency of the mesh size is observed. Even for very fine mesh sizes, the momentum transfer did not converge. Likely also here, deviatoric and/or dissipating constitutive behaviour is required to improve the correlation with the experiments. The CEL method performs very similar to SPH, in terms of momentum transfer and general behaviour. This is an indication that both methods are worthy of simulating bird strike.

Whereas most research (including literature) tries to investigate the momentum transfer in case of a rigid plate (which should be 100% according to the analytical model), it can also be applied the other way around: the analytical momentum transfer can be used to determine the momentum of the bird before impact. This concept can therefore serve as a method to

measure the residual energy. This concept is validated by the performed experiments, the analytical model and multiple numerical simulations.

Finally, a transition is made towards deformable targets such as a booster vane. Four tests were performed where the bird hits a thin at aluminium plate in front of a thick steel frame with a square opening. The high deformation of the bird and the plate over time and the final shape at the end of test correlates well between the experiment and simulation. The influence of several input conditions were investigated, which gave a first indication that the impact location has a large influence on the final shape of the plate.

9.1.2 Development of the set-up to test booster vanes

Most of the work in the development of the set-up to test the booster vanes focussed on the development, designing and validation of a set-up to measure the transferred multi-axial momentum during impact. Several concepts were considered and tested, from which several contain a combination of translational and rotational degrees of freedom (the idea to use rotational DOFs originates from the work of (Steinhagen and Salemme, 1973; Premont and Stubenrauch, 1974)). The final concept consists of a cone structure with three rotational degrees of freedom. From the rotational speeds of this cone structure, the multi-axial momentum can be derived.

Contrary to the work of (Steinhagen and Salemme, 1973; Premont and Stubenrauch, 1974)), the rotational speeds are derived from an optical measurement. The developed technique comprises a specific implementation of a Fourier based 2D line pattern technique, the calibration of the camera and the transformation of the obtained displacement data. The error on the momentum obtained from the optical measurement has been quantified with DIC measurements in quasi-static experiments and dynamic bird impact experiments. The error on the obtained momentum showed to be less than 5%. A simplified steel vane is used to test the set-up dynamically and to serve as an intermediate step towards the booster vane experiments and simulations. A very good correlation of these experiments with the simulations is achieved, in terms of momentum transfer and measured strain. The residual energy in the impact direction is slightly underpredicted, which can

be the result of an overestimated bird deviation angle in the simulations.

The final set-up to test the booster vanes consists of the validated cone set-up to measure the multi-axial momentum of the bird, the rigid plate positioned right behind the booster vanes to measure the residual energy of the bird, provisions to measure up to 12 strain gauges and an optimized configuration of the three available high speed cameras (to obtain the offset of the bird in two directions, record the optical measurement to derive the cone momentum, get an overview of the experiment and obtain the velocity signal of the rigid plate to derive the residual energy).

9.1.3 Parametric study on the booster vanes and performance of the numerical model

A parametric study is performed on the booster vanes, where the influence of the stacking and the radius of the vanes, the impact speed and angle of the bird and the size of the vanes is investigated. For each of these parameters, two tests are performed. Additionally, three tests on a reference configuration are performed. These tests on the reference configuration were instrumented with 12 strain gauges each, once on the vanes, once mainly on the inner shroud and once mainly on the reinforcements. The data obtained from the reference tests is used to validate numerical models.

From the parametric study, different damage types can be identified. Starting from small cracks or a pull out movement of the grey silicon up to cracks in the black abradable and vanes entirely pulled out from the inner shroud. These damage types are all the result of the vanes that are pulled down during impact. The retaining plate that connects the two vanes after they pass through the inner shroud deformed in the tests on the reference configuration. For the tests at higher speed, the retaining plate failed to keep both vanes from pulling out from the inner shroud. The momentum is quite consistent, even for the different parameters considered in the parametric study (except for the bird impact speed and angle variation). It therefore might be better to consider the momentum data as the spread that can occur for each of these configurations. The reference configuration specifically gives consistent momentum and strain data, which is very useful for the

correlation with the simulations. The total residual energy is mostly around 50%. A slightly higher residual energy is obtained for configuration 6 and 12. For these impact conditions, the bird is allowed to continue its trajectory much easier. It is important to keep in mind that only a section of the booster is tested. Therefore the results of the weak link in the assembly may not directly be extrapolated to a full booster.

For the numerical model, solid elements are chosen for all the parts in the assembly. An extensive mesh convergence study showed that for the vanes, 3 elements through the thickness with an in-plane mesh size of 0.5 mm is sufficiently refined to obtain good results. It is shown that the bird to vane mesh size ratio can have a significant impact on the result, as the particles induce very high plastic strains during the very short time they come into contact with the vane. A too high ratio can result in an unrealistic distorted leading edge and high mesh distortions when damage is modelled. A significant mesh refinement can eliminate this issue. The performance of the numerical model is investigated using momentum transfer, strain signals and residual energy and compared with the experimental data. The global and local behaviour of the bird and the vane is captured quite well by the model for configuration 1, and less good for configuration 6.

For configuration 1, the momentum and the strains on the vane correlate well with the experiments. The implementation of the abradable improves the strains and results in more realistic deformation of the retaining plate. An offset of 4 mm proved to have a tremendous influence on the achieved momentum and kinetic energy. This again shows that the impact location is of utmost importance to achieve good results in the simulations. For configuration 6, the mass flow of the bird is quite realistic when compared to the experiments, but the momentum transfer is overestimated. In the splitter simulations, a high mesh dependency was observed as well. A mesh refinement of the bird improves the result significantly.

To conclude, the major contributions to the current state-of-the-art can be summarized as follows:

- Several new insights are obtained regarding the shock regime. The elastic energy can be used to quantify the presence of the shock regime. For hemispherical ends for example, the elastic energy shows that the shock regime is negligible. It has also been shown that for flat ends, shock pressures up to 190% of the analytical pressure can occur, this is experienced in the experiments and is shown in the simulations.

- The wedge can serve as a tool to assess the behaviour of substitute birds and the performance of a material model in the simulations, as the momentum transfer proves to be highly dependent on the momentum of the bird after impact. Therefore, the constitutive behaviour of the bird has a large influence on the momentum transfer.

- The residual energy of the bird after impact can be a very valuable parameter for validating the numerical models. Multiple experiments and simulations showed that the rigid plate can be used to obtain the residual energy, because the momentum transfer is always 100%, independent from the shape, impact speed or mass of the bird.

- A procedure is developed to measure the multi-axial momentum during an impact event. This is done by allowing a stiff cone structure to rotate according to 3 rotational degrees of freedom. The movement of this cone is obtained from a very robust optical measurement.

- The experimental and numerical work on a simplified steel vane and a series of booster vanes is presented. For the booster vane, a fixture is developed which allows Safran Aero Boosters to test a subset of the entire booster including the inner and outer shroud, the welds in the outer shroud, the silicon, abradable and the retaining plate. The correlation and validation of these experiments and simulations are unique and also contributes to the fan blade research found in literature.

9.2 Future work

During the PhD, several concepts and ideas arose that can or may be worthwhile to investigate or consider in future work. In this section, these ideas are summarized.

- **Measure the friction during impact:** In chapter 5, the assumptions was made that the friction of a substitute or real bird during impact on a target is negligible. This assumption is based on the results of the rotated surface experiments from Wilbeck. However, there is a large deviation on the data provided by Wilbeck. It would be very interesting to perform a test series on a rotated plate (rotated over 45° degrees for example) to confirm this assumption. This can be done using the same principle to measure the momentum transfer as introduced in chapter 5. The situation however is slightly different as problems might arise due to the high reaction forces that are generated in this kind of test (only a projection of the reaction force is measured). A solution can be to use a combination of the splitter and the wedge (Figure 9.1). When the two halves impact the wedge (assuming that a negligible amount of energy is dissipated during the impact on the splitter), the scenario is twice equivalent to the impact on a rotate plate.

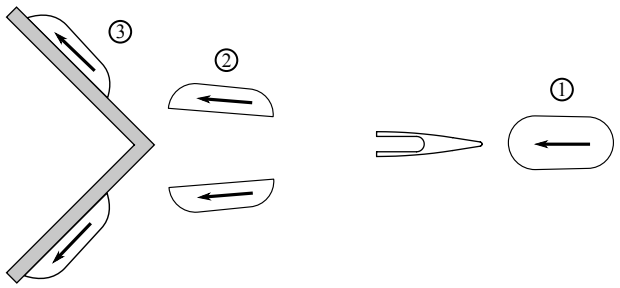

Figure 9.1: Combination of the splitter and the wedge as an equivalent for the rotated plate without unwanted reaction forces.

  Theoretically, this set-up will not experience a reaction force except for the measurement direction. If there would truly be no friction involved, for both a substitute as a real bird, the momentum transfer for a plate rotated over 45° degrees should be 50%.

- **Validating the wedge momentum balance experimentally:** In chapter 5, the analytical momentum transfer for wedge-like structures is developed (Equation 5.11). According to this formulation, the momentum transfer depends on the momentum of the bird after impact. To assure that this formulation is also valid in the experiments, both

for real as substitute birds, it can be interesting to measure the residual energy after impact on the wedge. This can be done by using two rigid plate set-ups (Figure 9.2).

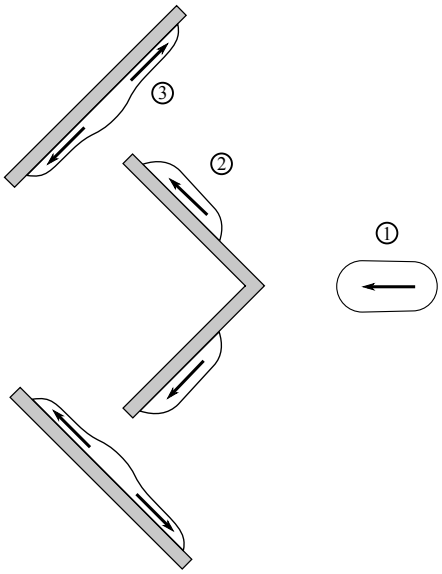

Figure 9.2: Rigid plate set-ups to measure the residual energy after impact on the wedge.

- **Develop a set-up to measure the total residual energy (and not just a projection):** For the simplified steel vane and booster vane experiments in chapter 8, the residual energy after impact was measured in the impact direction. Since the bird mass after impact was not flying along the initial impact direction, only a projection of the total residual energy was measured. On top of that, the highly asymmetric impact resulted in large oscillations in the momentum measurement, which has a negative influence on the achieved accuracy. For large test campaigns, it therefore might be worthwhile to extent the set-up to be able to measure the total residual energy with multiple plates, as shown in Figure 9.3. Two concepts are shown: one with rotated plates (chapter 5 and 6 indicated that also for a rotated plate, the momentum transfer can be predicted quite well analytically) and one with non-rotated plates.

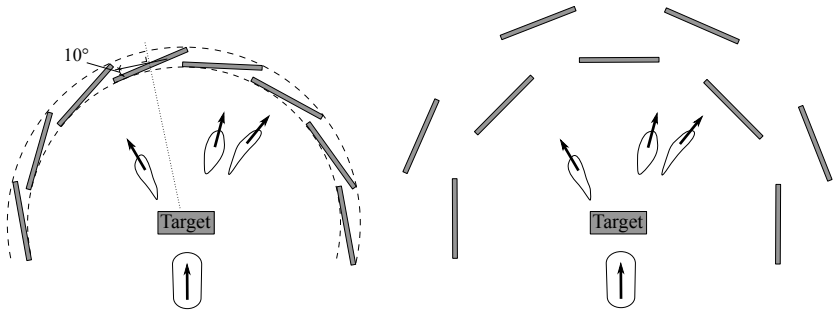

Figure 9.3: Multiple rigid plate set-ups to accurately measure the total residual energy of the bird after impact.

Likely it would not be possible any more to measure the transferred momentum by allowing movement of the set-up. Therefore it might be necessary to measure the momentum using force transducers. Also, additional simulations need to be performed to investigate what happens if a piece of bird hits the edge of a plate.

- **Investigate the performance of substitute birds in confined spaces:** In the development process of the method to measure the residual energy of a bird, a concept was designed where the bird would be decelerated in a box full of metal grids (see chapter 5). This concept was tested with ducks and gelatine substitute birds, which revealed that gelatine much easier flows through the confined spaces of the metal grids (see Figure 5.28). In case of the ducks, a lot of bird material got stuck just before the first grid. A test campaign studying the forces of a real and substitute bird on a target with confined spaced therefore might be interesting.

- **Build a better rigid plate set-up to acquire force-time signals:** The plate set-up to measure the momentum transfer was not rigid enough to achieve valuable force-time signals. Building a much stiffer set-up will be necessary to resolve this issue.

- **Material characterization of the silicon, abradable and gelatine bird:** The material model of the silicon and abradable in the booster vane assembly and the gelatine bird itself can be improved significantly. For the bird, it is important to maintain the hydrostatic

stiffness, while adding deviatoric behaviour and the ability to rupture at high deformations.

- **Optimize the set-up for tests at higher speed:** Currently, 300 gram birds can be launched precisely up to 130 m/s. For higher speeds, the bird starts to deform severely. One of the plausible causes is the foam that starts crushing at higher speeds (the equivalent weight of the bird during launch is enormously, see also chapter 2). Some optimization of the launching procedure is needed here. One step in the right direction is the use of filled cell foam (instead of the open cell foam used so far).

9.3 Bibliography

Premont, E. and Stubenrauch, K. (1974), Impact resistance of composite fan blades, Technical Report NASA CR-134707, Aircraft Engine Group, General Electric Co.

Steinhagen, C. and Salemme, C. (1973), The impact resistance of current design composite fan blades tested under short haul operating conditions, Technical report, General Electric Company.

Wilbeck, J. S. (1978*a*), 'Bird impact loading', *The shock and vibration bulletin* **48**, 115–120.

Wilbeck, J. S. (1978*b*), Impact behavior of low strenght projectiles, Technical Report AFML-TR-77-134, Air Force Materials Laboratory, Wright-Patterson Air Force Base.

Wilbeck, J. S. and Rand, J. L. (1981), 'The development of a substitute bird model', *Transactions of ASME Journal of Engineering for Gas Turbine and Power* **103**(4), 725–730.

APPENDIX A

Proof that the spatial frequencies of a line pattern with at least 3 line gratings coincide on one characteristic ellipse in the frequency domain

Or the obtained frequencies lie on an ellipse, or the corresponding pitches, or neither of both. It is not possible that both the frequencies and the corresponding pitches lie on an ellipse as the inverse of an ellipse (the inverse of the radius for each angle in a polar coordinate system) does not result in an ellipse. Figure A.1 shows a normal ellipse with the big axis at 60° on the left and the inverse of that ellipse on the right. It can easily be observed that this is not at all an ellipse. The radius does continuously increase from the small axis to the big axis, but the shape is not an ellipse.
In what follows, perspective and distortion are not considered.

A.1 The pattern in a well-chosen coordinate system

The proof will be given for a random line grating, oriented in any direction, which is rotated out-of-plane about any axis. First of all, a well-defined

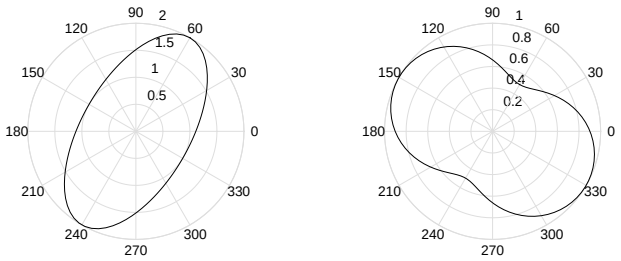

(a) Original ellipse. **(b)** Inverse of the ellipse.

Figure A.1: The inverse of an ellipse.

coordinate system is chosen. A pattern with a pitch p is created in the x-z plane, with an initial in-plane orientation (the gradient direction) with the x-axis equal to θ, before out-of-plane rotation. The x-axis is chosen in the direction of the out-of-plane rotation axis. The camera is assumed to be viewing from the top (from a positive y-axis value), with pixels oriented in the x and z directions. Having the pixels oriented along the axis should still be a general case as changing it would just add a simple rotation of the projections around the y-axis.

The scenario is shown in Figure A.2. With a so called pitch vector in the gradient direction and a line vector in the direction of the lines, perpendicular to the pitch vector.

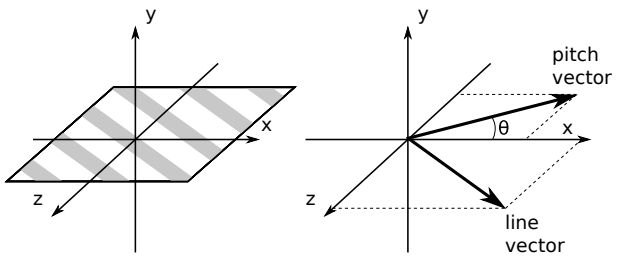

Figure A.2: Coordinate system with the pattern before out-of-plane rotation.

The magnitudes of the line vector projected on the three axes before out-of-plane rotation are the following:

$$v_x = t\sin(\theta); \quad v_y = 0; \quad v_z = t\cos(\theta) \tag{A.1}$$

In the next step, the out-of-plane rotation (α) is applied. The grating is rotated out-of-plane. Only the projection of those lines on the x-z plane are seen by the camera. This is shown in the Figure A.3.

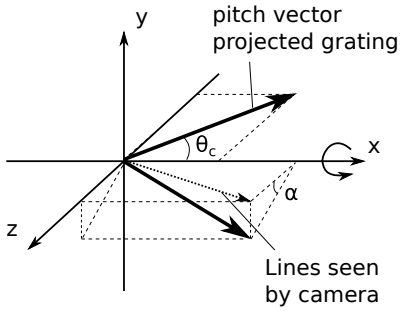

Figure A.3: Coordinate system with the pattern after out-of-plane rotation.

The magnitudes of the line vector on the three axes after out-of-plane rotation are:

$$v_x = t\sin(\theta); \quad v_y = t\cos(\theta)\sin(\theta); \quad v_z = t\cos(\theta)\cos(\theta) \tag{A.2}$$

The cosine and sine of the angle of the pitch seen by the camera with the x-axis can be calculated as follows:

$$\cos(\theta_c) = \frac{\cos(\theta)\cos(\alpha)}{\sqrt{\sin(\theta)^2 + \cos(\theta)^2\cos(\alpha)^2}} \tag{A.3}$$

$$\sin(\theta_c) = \frac{\sin(\theta)}{\sqrt{\sin(\theta)^2 + \cos(\theta)^2\cos(\alpha)^2}} \tag{A.4}$$

Note that it would not be correct to rotate the pitch vector out-of-plane. Imagine a large out-of-plane rotation and one would see that the pitch vector seen from the camera viewpoint is not perpendicular any more to the line vector seen from the camera viewpoint (which should of course always be the case). This can also be seen when solving the dot product of the two

vectors (this is not zero).

The pitch viewed by the camera (p_p) can easily be calculated for a line grating in the direction of the x-axis ($\theta = 0$), here the pitch viewed by the camera is equal to the original pitch p, or for a line grating perpendicular to the x-axis ($\theta = \pi/2$), where the pitch viewed by the camera is equal to the original pitch multiplied with the cosine of α, as also shown in Figure A.4. The frequency would respectively be equal to the original frequency and the original frequency divided by the cosine of α.

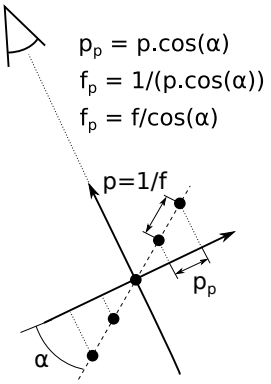

Figure A.4: Projection of the pitch for a rotation vector along the lines of the line grating.

With p the original pitch and p_p the pitch viewed by the camera. For other angles the projected pitch can be calculated making use of the sketch in Figure A.5. The figure shows two lines before and after out-of-plane rotation. The information along the rotation axis (the x-axis in this case) stays constant during rotation. This means that also the pitch or distance p_a stays constant during rotation.
The following relations can be made:

$$p_a = \frac{p}{\cos(\theta)}; \quad p_p = p.\cos(\theta_c) \tag{A.5}$$

Combining those two gives a relation between the projected pitch and the angle of the pitch viewed by the camera:

$$p_p = p\frac{\cos(\theta_c)}{\cos(\theta)} \tag{A.6}$$

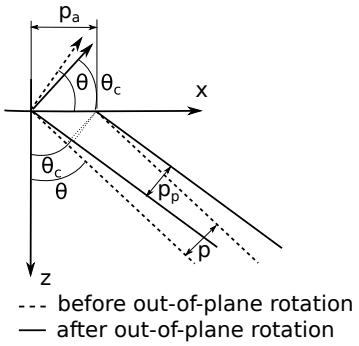

Figure A.5: Two lines before and after out-of-plane rotation.

Filling in the equation for $\cos(\theta_c)$ gives the following:

$$p_p = p\frac{\cos(\alpha)}{\sqrt{\sin(\theta)^2 + \cos(\theta)^2\cos(\alpha)^2}} \tag{A.7}$$

Or for the frequency:

$$f_p = \frac{\sqrt{\sin(\theta)^2 + \cos(\theta)^2\cos(\alpha)^2}}{p\cos(\alpha)} \tag{A.8}$$

A.2 Proof that the frequency of a pattern rotated in any direction lies on an ellipse

An ellipse can be constructed from the extreme scenarios: a pattern with $\theta = 0$ and a pattern with $\theta = \pi/2$ (calculated in the previous section). The frequency corresponding with these extremes of course could only be the small and the big axis of the ellipse. This ellipse is sketched in Figure A.6.

To prove that any other grating, with any other direction lies on the ellipse defined by these two axes, the corresponding projection on the x- and z-axis (respectively f_x and f_z) should fit in the following ellipse equation for each angle θ:

$$\frac{f_x^2}{f^2} + \frac{f_z^2\cos(\alpha)^2}{f^2} = 1 \tag{A.9}$$

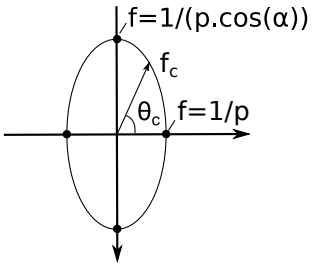

Figure A.6: Ellipse in the frequency domain of a pattern with lines co-oriented with a coordinate axis.

This can also be written in terms of pitches:

$$f_x^2 p^2 + f_z^2 p \cos(\alpha)^2 = 1 \tag{A.10}$$

The frequency seen by the camera, projected on axes x and z can be calculated from the information derived in the previous section:

$$\begin{aligned} f_x = f_p \cos(\theta_c) &= \frac{\sqrt{\sin(\theta)^2 + \cos(\theta)^2 \cos(\alpha)^2}}{p \cos(\alpha)} \frac{\cos(\theta)\cos(\alpha)}{\sqrt{\sin(\theta)^2 + \cos(\theta)^2 \cos(\alpha)^2}} \\ &= \frac{\cos(\theta)}{p} \end{aligned} \tag{A.11}$$

$$\begin{aligned} f_z = f_p \sin(\theta_c) &= \frac{\sqrt{\sin(\theta)^2 + \cos(\theta)^2 \cos(\alpha)^2}}{p \cos(\alpha)} \frac{\sin(\theta)}{\sqrt{\sin(\theta)^2 + \cos(\theta)^2 \cos(\alpha)^2}} \\ &= \frac{\sin(\theta)}{p \cos(\alpha)} \end{aligned} \tag{A.12}$$

Putting these in the ellipse equation gives the following:

$$\frac{\cos(\theta)^2}{p^2} p^2 + \frac{\sin(\theta)^2}{p^2 \cos(\alpha)^2} p^2 \cos(\alpha)^2 = 1 \tag{A.13}$$

Or also

$$\cos(\theta)^2 + \sin(\theta)^2 = 1 \tag{A.14}$$

Which is valid for each θ.

A.3 Proof that the pitch of a pattern rotated in any direction does not lie on an ellipse

The same can be done for the pitch, starting from the ellipse equation based on the data from a pattern oriented according to $\theta = 0$ and $\theta = \pi/2$:

$$\frac{p_x^2}{p^2} + \frac{p_z^2}{p^2 \cos(\alpha)^2} = 1 \tag{A.15}$$

And the pitch seen by the camera, projected on the axes x and z:

$$p_x = \frac{p \cos(\theta) \cos(\alpha)^2}{\sin(\theta)^2 + \cos(\theta)^2 \cos(\alpha)^2} \tag{A.16}$$

$$p_x = \frac{p \sin(\theta) \cos(\alpha)}{\sin(\theta)^2 + \cos(\theta)^2 \cos(\alpha)^2} \tag{A.17}$$

Filling in the projected pitches in the ellipse equation and working out the cosines and the sines only has three solutions: $\alpha = 0$ and/or $\theta = 0$ and/or $\theta = \pi/2$. This means that for out-of-plane rotation, the pitches at angles different than the ones of the main axes (the one of the rotation axis and the axis perpendicular to the rotation axis), do not lie on an ellipse.

APPENDIX B

Test matrices plate, wedge and splitter experiments

Table B.1, B.2 and B.3 summarize respectively the plate, wedge and splitter experiments (in the order the tests are performed).

Table B.1: Test matrix rigid plate experiments.

Test	**Bird**	**m [kg]**	**v [m/s]**	**MT [%]**	**F [kN]**	**panel**
RP-1	1:4 MR	1.7844	60.7	100.9	39.0	Sandwich
RP-2	1:9 MR	1.7242	85.7	105.8	65.1	Sandwich
RP-3	1:4 MR	1.8066	81.8	103.9	61.4	Sandwich
RP-4	1:9 MR	1.7888	112.4	100.8	72.4	Sandwich
RP-5	1:4 MR	1.8119	112.6	99.2	126.5	Sandwich
RP-6	1:9 MR	1.7790	111.8	103.1	113.9	Sandwich
RP-7	1:4 MR	1.8188	84.8	102.6	68.9	Sandwich
RP-8	1:4 MR	1.8160	114.6	101.5	124.3	Sandwich
RP-9	1:6 MR	1.8244	88.5	100.2	95.1	Sandwich
RP-10	1:6 MR	1.7602	114.9	96.2	129.8	Sandwich
RP-11	duck	1.3867	95.3	98.4	46.4	Sandwich
RP-12	duck	1.2854	110.0	95.2	48.1	Sandwich
RP-13	1:6 MR	1.6000	86.7	101.8	67.3	Sandwich
RP-14	1:6 MR	1.5806	113.7	103.3	97.7	Sandwich
RP-15	1:6 MR	0.2948	133.4	102.3	43.4	Al plate
RP-16	1:6 MR	0.3028	135.4	98.9	44.0	Al plate
RP-17	1:6 MR	0.2918	94.8	104.5	21.5	Al plate
RP-18	1:6 MR	0.2928	100.6	102.4	24.4	Al plate

Table B.2: Test matrix wedge experiments.

Test	**Bird**	**m [kg]**	**v [m/s]**	**MT [%]**	**F [kN]**
WE-1	1:6 MR	0.2928	85.0	59.3	10.4
WE-2	1:6 MR	0.2956	99.1	55.5	13.3
WE-3	1:6 MR	0.2906	127.7	54.4	21.3
WE-4	1:6 MR	0.2958	126.8	51.4	20.3
WE-5	1:6 MR	0.2964	108.5	55.0	15.9
WE-6	1:6 MR	0.3008	127.5	50.3	20.4
WE-7	1:6 MR	0.2962	147.5	53.7	28.7
WE-8	1:6 MR	0.2966	123.6	51.6	19.3
WE-9	1:6 MR	0.2936	142.0	51.9	25.4
WE-10	1:6 MR	0.2956	115.5	55.8	18.2
WE-11	1:6 MR	0.2962	103.3	55.8	14.6
WE-12	1:6 MR	0.2922	121.5	56.0	20.0
WE-13	1:9 MR	0.2884	110.7	55.4	16.2
WE-14	1:9 MR	0.2920	125.0	56.8	21.4
WE-15	1:4 MR	0.2954	109.9	60.9	18.0
WE-16	1:4 MR	0.3072	123.6	57.0	22.2
WE-17	Pigeon	0.3836	108.0	59.2	9.1
WE-18	Pigeon	0.4378	112.2	55.7	9.1
WE-19	Pigeon	0.4220	126.5	62.2	12.8

Table B.3: Test matrix splitter experiments.

Test	**Bird**	**m [kg]**	**v [m/s]**	**MT [%]**	**F [kN]**	$\boldsymbol{\alpha}[^\circ]$
SP-1	1:6 MR	1.533	88.0	2.18	0.95	5.0
SP-2	1:6 MR	1.450	116.0	2.05	1.50	5.8
SP-3	duck	1.435	87.6	5.77	1.61	1.9
SP-4	duck	1.281	104.5	5.29	1.86	1.8
SP-5	1:4 MR	1.500	81.5	3.11	1.23	5.0
SP-6	1:4 MR	1.518	105.5	1.83	1.09	6.2

APPENDIX C

Test matrix and results booster vane experiments

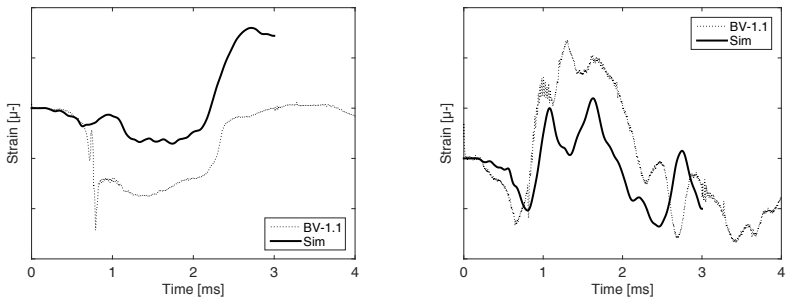

(a) KD1B22.

(b) KD1B23.

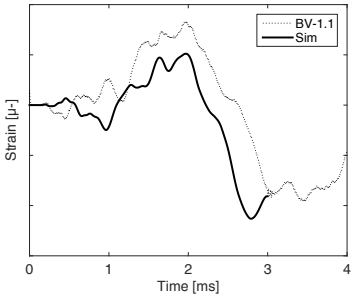

(c) KD1B24.

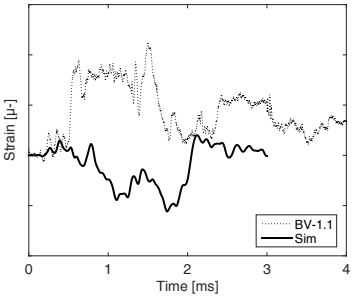

(d) KD1B25.

Figure C.1: Correlation first four strain gauges on the inner shroud KD1B22, KD1B23, KD1B24 and KD1B25 with the simulation including the abradable.

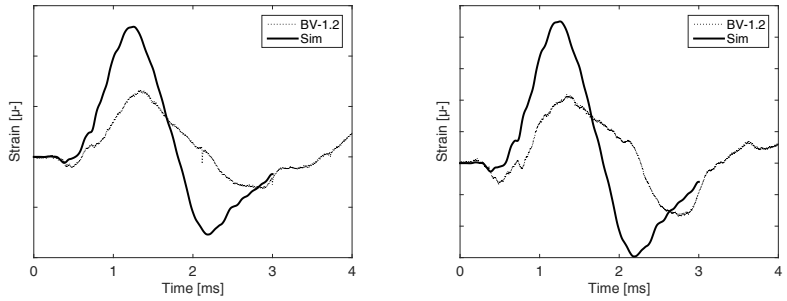

(a) KD1B13.

(b) KD1B14.

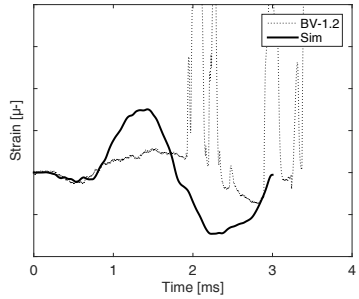

(c) KD1B15.

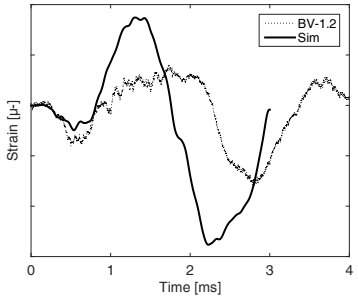

(d) KD1B16.

Figure C.2: Correlation first four strain gauges on the reinforcements KD1B13, KD1B14, KD1B15 and KD1B16 with the simulation including the abradable.